TRANSPORTATION RESEARCH

# RECORD

No. 1504

*Pavement Design, Management, and Performance; Soils, Geology, and Foundations*

---

# Modeling and Model Verification; Testing Pavement Layers and Materials; and Low-Cost Drainage Structures

*A peer-reviewed publication of the Transportation Research Board*

TRANSPORTATION RESEARCH BOARD
NATIONAL RESEARCH COUNCIL

NATIONAL ACADEMY PRESS
WASHINGTON, D.C. 1995

**Transportation Research Record 1504**
ISSN 0361-1981
ISBN 0-309-06172-5
Price: $27.00

Subscriber Category
2B pavement design, management, and performance
3A soils, geology, and foundations

Printed in the United States of America

**Sponsorship of Transportation Research Record 1504**

**GROUP 2—DESIGN AND CONSTRUCTION OF TRANSPORTATION FACILITIES**
*Chairman: Michael G. Katona, U.S. Air Force Armstrong Laboratory*

**Soil Mechanics Section**
*Chairman: Verne C. McGuffey*

Committee on Modelling Techniques in Geomechanics
*Chairman: Deborah J. Goodings, University of Maryland*
*Sreenivas Alampalli, Sangchul Bang, Richard D. Barksdale, Richard J. Bathurst, Joseph A. Caliendo, Jack I. Clark, K. P. George, Mary E. Hynes, William M. Isenhower, Ilan Juran, Victor N. Kaliakin, Stephen Ketcham, Kenneth J. Larsson, Rita B. Leahy, Glen E. Miller, Victor A. Modeer, Jr., Reed L. Mosher, Yacoub M. Najjar, Clifford J. Roblee, Raymond L. Sterling, Harry E. Stewart, Tien H. Wu*

Committee on Subsurface Drainage
*Chairman: L. David Suits, New York State Department of Transportation*
*Silvan Andrei, Thomas R. Baas, John S. Baldwin, Walter R. Barker, Ryan R. Berg, George R. Cochran, Jack E. Cowsert, Andrew R. Dawson, Gregory A. Dolson, Ervin L. Dukatz, Jr., L. John Fleckenstein, James B. Goddard, Michael J. Hall, William M. Hawkins, John Owen Hurd, Robert M. Koerner, Larry Lockett, Richard P. Long, Michael McDonnell, Bruce M. McEnroe, Victor E. Mottola, Emile A. Samara, Clinton E. Solberg, Malcolm L. Steinberg, David C. Wyant*

**Geology and Properties of Earth Materials Section**
*Chairman: Robert D. Holtz, University of Washington*

Committee on Soil and Rock Properties
*Chairman: Mehmet T. Tumay, Louisiana Transportation Research Center*
*Roy H. Borden, Dario Cardoso de Lima, Umakant Dash, Andrew R. Dawson, Don J. DeGroot, Eric C. Drumm, David J. Elton, Kenneth L. Fishman, An-Bin Huang, Mary E. Hynes, Hilary I. Inyang, Steven L. Kramer, Rodney W. Lentz, Emir Jose Macari, Paul W. Mayne, Kenneth L. McManis, Victor A. Modeer, Jr., Priscilla P. Nelson, Peter G. Nicholson, Norman I. Norrish, John W. Oglesby, Samuel G. Paikowsky, Sibel Pamukcu, Nader S. Rad, Kaare Senneset, Sunil Sharma, Timothy D. Stark, Ramzi Taha*

**GROUP 5—INTERGROUP RESOURCES AND ISSUES**
*Chairman: Patricia F. Waller, University of Michigan*

Committee on Low-Volume Roads
*Chairman: Ronald W. Eck, West Virginia University*
*Abdullah Al-Mogbel, Gerald T. Coghlan, Santiago Corro Caballero, Larry Emig, Richard B. Geiger, Anthony R. Giancola, Jacob Greenstein, Edward H. Hall Sr., Henry Hide, John L. Hopkins II, Stuart W. Hudson, Robert L. Martin, John B. Metcalf, Neville A. Parker, Bryan Dale Pidwerbesky, James L. Pline, John D. Riverson, Richard Robinson, Andrea L. Smith, Eileen S. Stommes, Walter J. Tennant, Jr., Alex T. Visser, Michael C. Wagner, Anthony F. Welch*

**Transportation Research Board Staff**
*Robert E. Spicher, Director, Technical Activities*
*G. P. Jayaprakash, Engineer of Soils, Geology, and Foundations*
*Nancy A. Ackerman, Director, Reports and Editorial Services*

Sponsorship is indicated by a footnote at the end of each paper. The organizational units, officers, and members are as of December 31, 1994.

# Transportation Research Record 1504

## Contents

# Foreword

The 12 papers included in this volume represent three general groups. They contain information for those who are interested in numerical and centrifuge modeling, testing and evaluation of pavements, and low-cost drainage structures.

In the first group of five papers the authors present innovative modeling approaches aimed at solving some major concerns of the transportation agencies. These papers contain information on full size prototype rockfall barrier test results that provide tools for design modifications and improvements; centrifuge model tests on liquefaction of saturated loose sands that result in flowslides, seismic stability of sand foundations, and studies that simulate chemical movement through soils surrounding underground fuel storage tanks; and finite element analysis of sheetpile cell filling.

The second group of five papers focuses on issues related to pavements. These papers include descriptions of a comparative study of dynamic nondestructive tests of flexible and rigid pavements using the falling weight deflectometer and spectral analysis of surface waves; bender element, a rapid method of determining resilient modulus of subgrade soils; effects of moisture variations on resilient modulus of subgrade soils; and permeability of asphalt-treated pavement base layers.

The third group contains two papers on drainage of low-volume roads. In the first paper the authors quantify the extent of overtopping and provide a functional design method for the selection of low level river crossings. The authors of the second paper describe portable, temporary, reusable, low-cost stream crossings.

# Testing and Modeling of Two Rockfall Barriers

GEORGE HEARN, ROBERT K. BARRETT, AND H. HENRIE HENSON

Testing, evaluation, and analysis of two types of rockfall barriers are reported. Rockfall barriers are designed to withstand impacts by falling boulders and are used to protect roadways and structures. Among several types of barriers in use by transportation departments, two designs–a flexible cable-fence barrier and a freestanding mechanically stabilized earth (MSE) barrier–have been developed by the Colorado Department of Transportation in a program of prototype testing and dynamic analysis. In tests, full-size prototype barriers were subject to impacts by boulders falling freely down a natural slope. The velocity and kinetic energy of the rockfall and the performance of the barrier are basic findings of tests. Simulation of test impacts in dynamic analysis provides information about the load demand on components of barriers. Test data are used to calibrate analytical procedures. Three prototype cable fences have been tested. The fences have proven rockfall capacities up to 129 kJ (95,000 ft-lb) and can halt boulders as heavy as 2,950 kg (6,500 lb). Three prototype MSE barriers have been tested. One prototype was repaired after initial testing and then retested to examine the performance of repairs. MSE barriers offer rockfall capacities in excess of 1,360 kJ (106 ft-lb) and have been observed to halt boulders as heavy as 13,700 kg (30,100 lb).

Rockfall has been defined as the rapid movement, by rolling, sliding, and leaping, of one or a few boulders down a slope (*1*). Once freed from its position on a slope, a boulder acquires significant kinetic energy as it travels, and it can have a long runout beyond the slope (*2*). Rockfall hazards exist along many highways. The severity of rockfall hazard is a function of the frequency of rockfall events as well as traffic levels, sight distances, and traffic speeds. Several state transportation departments employ hazard rating practices that recognize both the geotechnical and operational characteristics of a site (*3–5*).

Rockfall hazard can be mitigated by barriers such as ditches, walls, fences, and other means (*6*). Rockfall barriers are suitable where (*a*) boulders are of moderate size, (*b*) source material consists of many individual cobbles, (*c*) boulders and blocks are distributed over a wide area, (*d*) boulders are expected to fall individually, and (*e*) a barrier can be periodically cleared of debris. Barriers are the preferred method of mitigation when the disturbance of a slope must be kept to a minimum, as is the case with scenic or environmentally sensitive sites.

There are two categories of rockfall barriers: slope features such as berms and catch ditches (*7*) and barrier structures such as fences and walls. Barriers must be of adequate size and must be designed for strength. Impacts by boulders are severe events and exert high forces on barrier components. The commonly used measure of rockfall barrier capacity is the kinetic energy of falling boulders. The design of barriers for a hazard site employs data on kinetic energies and bounding heights of boulders and a computation of forces on components, using explicit dynamic analysis. Bounding heights and kinetic energies of falling boulders at a site can be determined in computer simulations (*8,9*).

The rockfall capacity of barriers is established in tests of prototypes. Tests have been reported for rockfall attenuators (*10*), steel mesh fences (*11*), cable net fences (*12,13*), and mechanically stabilized earth (MSE) barriers (*14,15*). Rockfall capacities of barriers range from 41 kJ (30,000 ft-lb) for steel mesh fences, to 700 kJ (500,000 ft-lb) for cable net systems, to more than 1,360 kJ (106 ft-lb) for MSE barriers. Tests demonstrate the rockfall capacity of a barrier in terms of a maximum kinetic energy of boulders and often as a limit on maximum boulder size or weight.

Methods for the dynamic analysis of rockfall barriers have been developed. Analysis of impact response of cable fences is reported by Hearn (*11*). Analysis of a rockfall attenuator is reported by Mustoe and Huttlemaire (*16*). The use of dynamic analysis in the development of new designs for cable fences is reported by Hearn (*17*). The rockfall capacities of new cable fences were subsequently demonstrated in prototype tests reported in this paper. Preliminary results of a discrete element analysis of impact response of MSE walls are also reported in this paper, and the results are compared with data from prototype tests conducted by the Colorado Department of Transportation in 1990 and 1993 (*14,15*).

## PROTOTYPE TESTING OF ROCKFALL BARRIERS

The method of prototype testing is straightforward. A boulder of known weight and size is released at the top of a slope and is allowed to hit a barrier at the bottom of the slope. The impact conditions are stated in terms of boulder speed and kinetic energy, and the performance of the barrier is evaluated in terms of its success in stopping the boulder and in terms of the damage sustained.

Prototype tests approximate the real service conditions of rockfall barriers. Prototypes are full-size barriers. Boulders fall freely down a natural slope. Boulder path and speed are not constrained, though the severity of the rockfall event is bounded approximately by the size of the boulder. All prototypes are tested with repeated impacts. Boulders are cleared after each impact, but prototypes are left unrepaired unless disabled. Boulder weight, speed, bounding height at impact, kinetic energy, and the location of the impact on the barrier characterize each test. Each test yields a determination of whether the kinetic energy is within or beyond the capacity of the barrier.

G. Hearn, Department of Civil, Environmental, and Architectural Engineering, University of Colorado, Boulder, Colo. 80309. R.K. Barrett, Colorado Department of Transportation, Denver, Colo. 80222. H.H. Henson, Parsons DeLeuw, Denver, Colo. 80290.

**TABLE 1 Range of Boulder Weights and Speeds in Tests of Prototype Barriers**

| | | Boulder | | | | | |
|---|---|---|---|---|---|---|---|
| | No. of | Weight, kg | | Velocity, m/s | | Kin. Energy, kJ | |
| | Tests | Min | Max | Min | Max | Min | Max |
| Flexpost Fence | | | | | | | |
| Prototype I | 11 | 270 | 2,134 | 6.9 | 14.5 | 6 | 225 |
| Gabion Mesh Prototype | 15 | 118 | 2,742 | 3.3 | 15.3 | 4 | 179 |
| Cable Net Prototype | 10 | 590 | 4,077 | 3.8 | 19.2 | 6 | 747 |
| Mechanically Stabilized Earth Barrier | | | | | | | |
| Prototype 6x10 | 11 | 200 | 8,354 | 3.7 | 19.5 | 8 | 1,391 |
| Repaired 6x10 | 8 | 1,952 | 12,213 | 6.1 | 16.8 | 51 | 1,416 |
| Prototype 8x12 | 9 | 3,768 | 13,665 | 4.9 | 18.3 | 44 | 1,410 |

Tests of prototype barriers were executed at a slope near Rifle, Colo. The slope has a difference in elevation of 82 m (270 ft) from the point of release of boulders to the location of barriers. The slope has a nearly constant grade of 66 percent. Boulders travel about 153 m (500 ft) from release to impact. The surface of the slope is sandy, with isolated rock ledges, some cobbles, widely spaced small brush, and little grass. There are no trees in the boulder path. A level construction site for barriers has been prepared at the bottom of the slope, but otherwise the slope has not been modified. Boulders run down a natural, undisturbed slope.

Boulders that have been used in tests range in mass from 120 to 13,700 kg (260 to 30,100 lb). Boulder speeds at impact have been as high as 19 m/sec (62 ft/sec), and kinetic energy of translational velocity have been as high as 1,420 kJ (1,044,000 ft-lb). Speeds and weights of boulders in tests are summarized in Table 1.

## FLEXPOST FENCE ROCKFALL BARRIER

The flexpost fence rockfall barrier is constructed of flexible steel posts that support steel cables and steel mesh (Figure 1). Flexposts are constructed of two sections of steel pipe; the upper section is the visible post, and the lower section is the foundation. The two sections are joined by a group of 19 seven-wire steel strands that are grouted into both pipe sections. Between the two sections, a height of 0.5 m (1.5 ft) of the group of strands is exposed. This exposed height forms a leaf spring, which makes flexposts capable of large elastic rotations about their bases. Posts can be bent to touch the ground and will rebound to a vertical position when released. Flexible posts make this barrier very compliant and therefore very strong. Its strength stems from the tensile strength of its cables and steel mesh. Flexpost fences are flat; all cables lie in a single plane. No stays or other components are out of plane.

Tests of three prototypes 3.10 m (10 ft) tall were conducted in 1990 on the slope at Rifle. These prototypes led to a standard design of a flexpost fence using a gabion mesh and rated at 41 kJ (30,000 ft-lb) rockfall capacity (*18*). This design has been used in more than 2 dozen installations along Interstate 70 in Glenwood Canyon. The 1990 tests provided the data for verifying an explicit dynamic analysis program for flexible barriers (*11*). A fourth prototype using cable nets was tested in 1993. Tests of the prototype verified the predicted capacity of the 129 kJ (95,000 ft-lb) design.

Data from tests of prototype fences is presented in two sets: the 1990 prototype for 41-kJ (30,000-ft-lb) gabion mesh fences and the 1993 prototype for 129-kJ (95,000-ft-lb) cable net fences. The gabion mesh flexpost can halt boulders as heavy as 1,630 kg (3,600 lb). The cable net flexpost fence has a rockfall capacity of 129 kJ (95,000 ft-lb) and can halt boulders as heavy as 2,950 kg (6,500 lb).

### Tests of Gabion Mesh Fences

Three prototype flexpost fences using gabion mesh were tested in 1990. Boulder impacts ranged in weight from 118 kg (260 lb) to 2,740 kg (6,040 lb) at velocities from 3.3 m/sec (10.9 ft/sec) to 15.3 m/sec (50 ft/sec) and translational kinetic energies as high as 225 kJ (166,000 ft-lb). Prototype tests are summarized in Tables 2 and 3.

Prototype tests were carried into a range of rockfall kinetic energies sufficient to damage the fence. In tests of gabion mesh prototypes, failures of the mesh, splices in the mesh, stay cables, and top cables were observed. In addition, a direct impact bent one flexpost, though the function of the post was not impaired. Two boulders rolling along the ground at slow speeds passed under the fence but halted a few feet beyond the fence.

Prototype gabion mesh fences halted all boulders with translational kinetic energies below 40 kJ (29,700 ft-lb). The prototypes did not stop boulders at energies of 80 kJ (58,700 ft-lb) and 179 kJ (132,000 ft-lb). Both impacts damaged the fence. Boulder weights and speeds are plotted in Figure 2, and the impacts are identified as being within or beyond the capacity of the fence. Also plotted in Figure 2 is a constant kinetic energy curve at 41 kJ (30,000 ft-lb). The 41 kJ (30,000 ft-lb) curve excludes all damaging impacts, and on the basis of these prototype tests, the 41 kJ (30,000 ft-lb) limit is the rockfall capacity for this gabion mesh fence.

### Tests of Cable Net Fences

A prototype flexpost fence using cable nets 20 x 20 x 20 cm (8 x 8 x 16 in.) was tested in 1993. Impacts included boulders that weighed

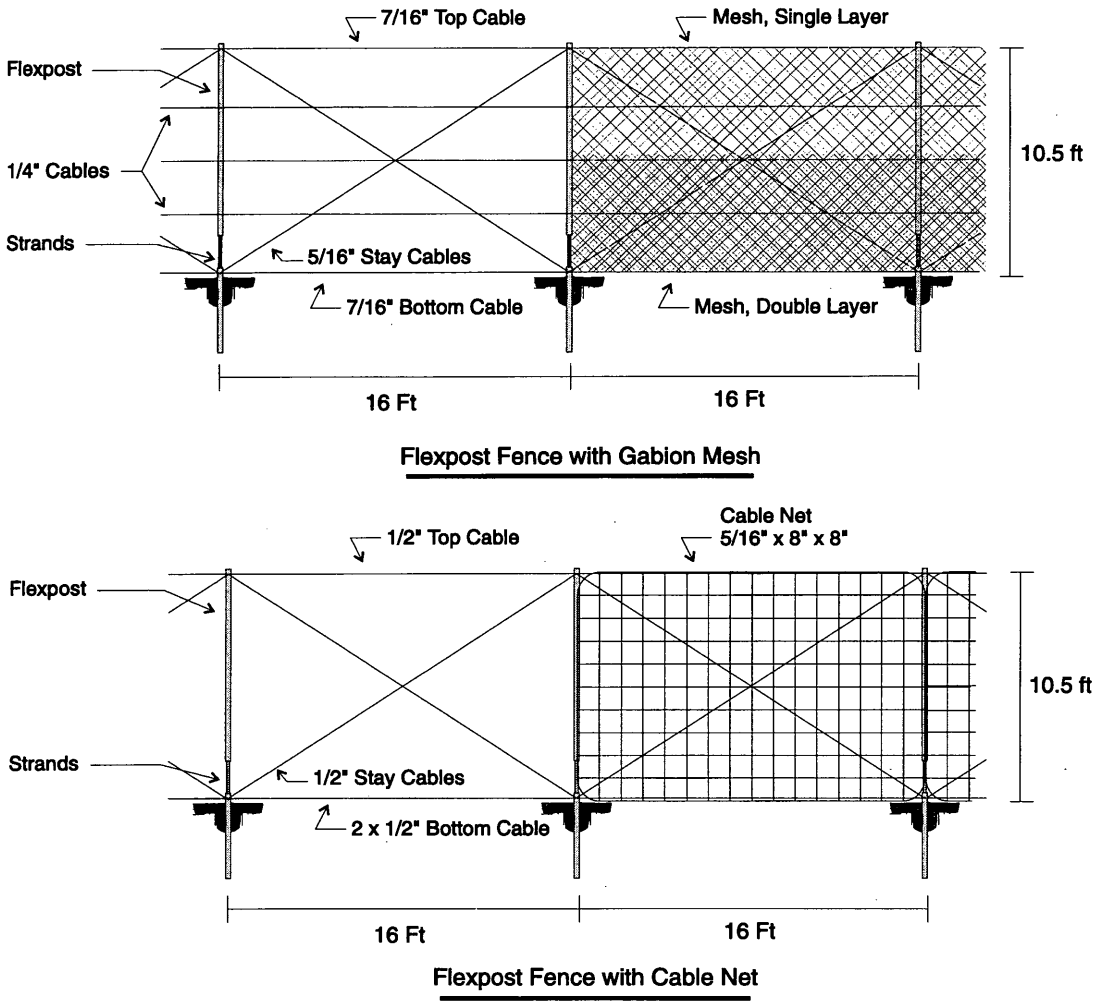


**FIGURE 1 Flexpost fences.**

from 590 kg (1,300 lb) to 4,080 kg (8,980 lb) and boulder translational velocities that ranged from 3.8 m/sec (12.6 ft/sec) to 19.2 m/sec (62.9 ft/sec). Translational kinetic energy was as high as 747 kJ (551,000 ft-lb). The prototype halted a boulder with a translational kinetic energy of 369 kJ (272,000 ft-lb), but the impact ruptured one of the stay cables. The prototype halted a boulder at a translational kinetic energy of 119 kJ (88,000 ft-lb) without damage. The prototype also stopped a boulder at an energy of 103 kJ (76,000 ft-lb) and suffered only minor damage; a crimp splice in a cable net opened. The prototype was severely damaged by a boulder with a translational kinetic energy of 748 kJ (552,000 ft-lb). Tests are summarized in Table 3. Flexpost fences using cable nets are rated at a rockfall capacity of 129 kJ (95,000 ft-lb). Boulder weights and speeds from prototype tests are plotted in Figure 2.

## Dynamic Analysis of Flexpost Fences

The response of flexpost fences to boulder impacts are simulated in an explicit dynamic analysis. Analysis provides data on forces on components and allows a simulation of impact conditions not observed in prototype tests. This is useful because tests of prototypes provide a limited set of data despite a substantial effort. In addition, analysis can be used to study new fence designs. This process of simulation, design, and subsequent verification of rockfall capacity was followed in the development of the 129-kJ (95,000-ft-lb) cable net fence.

The analysis response of fences to boulder impact employs an iterative, time-marching technique. In each time step, a new equilibrium position for the fence is sought–one that is consistent with the contact forces imposed by the boulder and with the current position and velocities of fence components. The boulder is a discrete element in the analysis. Geometric interference of the boulder with the fence is used to compute a set of normal and tangential contact forces. Details of the analysis are provided in Hearn and Akkaraju (*19*).

The position of the contact zone within the fence changes as the impact progresses. For analysis, a dense grid of nodes is used in the fence model in the vicinity of the impact of the boulder. The dense grid facilitates the computation of contact forces and accommodates the migration of the contact zone during impact.

Impact response is nonlinear. Cables and mesh in a fence are initially slack. Impact by a boulder drives these components to high tensions and imposes large changes in fence geometry. As the

**TABLE 2 Comparision of Tests and Analysis of Flexpost Fence Gabion Mesh Prototype**

41 kJ Gabion Mesh Fences

| Test No. | Boulder Mass kg | Boulder Velocity m/s | Trans. Kin. En. kJ | Lin. Mom. kg-m/s | Outcomes: Prototype Testing | Outcomes: Dynamic Analysis |
|---|---|---|---|---|---|---|
| 1 | 116 | 8.0 | 3.7 | 925 | Boulder stopped. No damage. | All components within breaking strength. |
| 2 | 2742 | 11.4 | 179.0 | 31,363 | Boulder not stopped. Mesh rupture. | Mesh at 4 times breaking strength. Top and bottom cables at 1.4 & 1.9 times breaking strength |
| 3 | 272 | 10.2 | 14.0 | 2,767 | Boulder passed through rend in mesh. | All components within breaking strength. |
| 4 | 631 | 4.0 | 4.9 | 2,502 | Boulder rolled under fence. No damage. | All components within breaking strength. Analysis shows escape of boulder under the fence. |
| 5 | 361 | 10.8 | 21.0 | 3,897 | Boulder stopped. No damage. | All components within breaking strength. |
| 6 | 686 | 15.3 | 79.6 | 10,454 | Boulder not stopped. Mesh rupture. | Mesh at 1.4 times breaking strength. |
| 7 | 268 | 10.8 | 15.6 | 2,892 | Boulder stopped. No damage. | All components within breaking strength. |
| 8 | 735 | 4.6 | 7.8 | 3,387 | Boulder rolled under fence. No damage. | All components within breaking strength. Analysis shows escape of boulder under the fence. |
| 9 | 617 | 11.4 | 40.3 | 7,062 | Boulder stopped. No damage. | All components within breaking strength. |
| 10 | 361 | 13.4 | 32.1 | 4,822 | Boulder stopped. No damage. | All components within breaking strength. |
| 11 | 138 | 10.2 | 7.1 | 1,406 | Boulder stopped. Post bent. | All components within breaking strength. |
| 12 | 581 | 10.2 | 29.8 | 5,902 | Boulder stopped. No damage. | Mesh at 1.4 times breaking strength. |
| 13 | 341 | 8.7 | 12.9 | 2,970 | Boulder stopped. No damage. | All components within breaking strength. |
| 14 | 1634 | 6.5 | 34.7 | 10,668 | Boulder stopped. Remained in fence. | Mesh at 1.1 times breaking strength. |

**TABLE 3 Comparison of Tests and Analysis of Flexpost Fence Cable Net Prototype**

129 kJ Cable Net Fence

| Test No. | Boulder Mass kg | Boulder Velocity m/s | Trans. Kin. En. kJ | Lin. Mom. kg-m/s | Outcomes: Prototype Testing | Outcomes: Dynamic Analysis |
|---|---|---|---|---|---|---|
| 15 | 590 | 5.1 | 7.6 | 3,006 | Boulder stopped. No damage. | All components within breaking strength. |
| 16 | 790 | 6.3 | 15.5 | 4,939 | Boulder stopped. No damage. | All components within breaking strength. |
| 17 | 844 | 3.8 | 6.2 | 3,245 | Boulder stopped. No damage. | All components within breaking strength. |
| 18 | 840 | 12.4 | 65.0 | 10,452 | Boulder stopped. No damage. | All components within breaking strength. |
| 19 | 790 | 16.2 | 103.1 | 12,770 | Boulder stopped. Crimp splice in net pulled open. | All components within breaking strength. |
| 20 | 1,875 | 15.3 | 218.3 | 28,651 | Boulder rolled over fence at post. | Top cable at 1.2 times breaking strength. Bottom cable at 1.3 times breaking strength. |
| 21 | 2,111 | 18.7 | 368.8 | 39,535 | Boulder stopped. Stay cable broken. | Stay cable at 1.1 times breaking strength. Top and bottom cable also beyond breaking strength. |
| 22 | 2,974 | 9.0 | 119.3 | 26,665 | Boulder stopped. No damage. | All components within breaking strength. |
| 23 | 4,050 | 13.9 | 389.2 | 56,199 | Boulder rolled over fence at post. | Top, bottom and stay cables overstressed. |
| 24 | 4,077 | 19.2 | 748.5 | 78,214 | Boulder not stopped. Top cable broken. | Top cable at 3.4 times breaking strength. Bottom and stay cables also overstressed. Net not overstressed. |

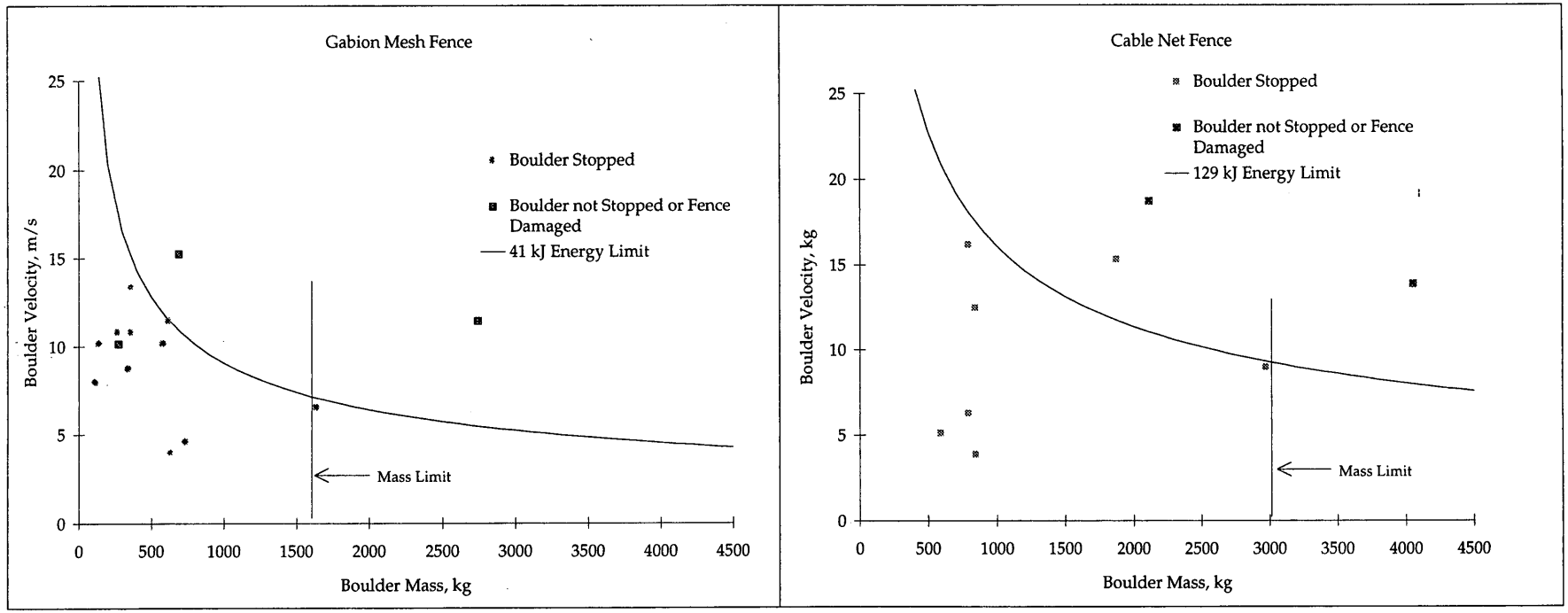


**FIGURE 2 Test impacts and energy limits for flexpost fences.**

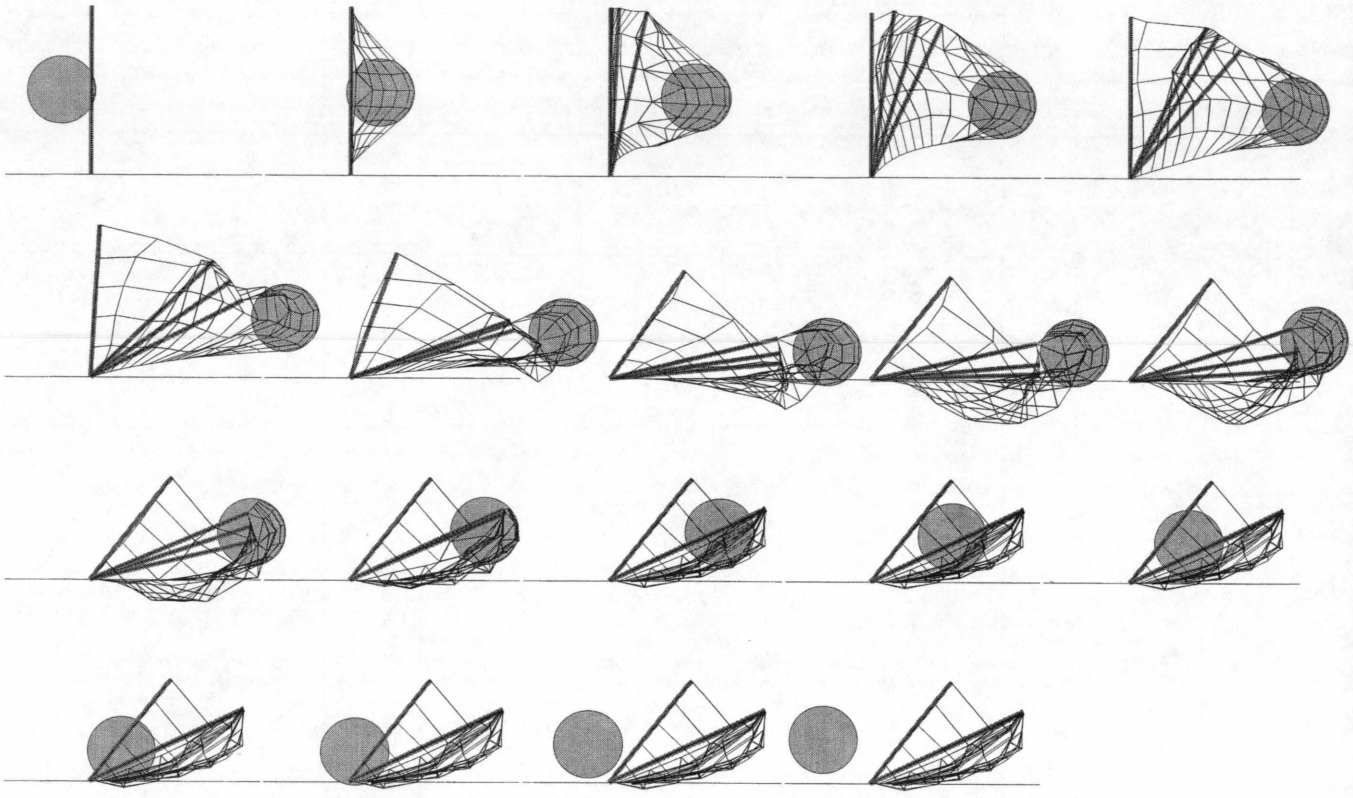

**FIGURE 3 Deformed shapes of flexpost fence after 54-kJ impact (images at .01 sec).**

impact progresses, the boulder is slowed, but momentum of the posts carries the fence forward, allowing regions of the fence to slacken. The analysis must be able to accommodate large changes in contact forces, evolution of the position of the contact between the fence and the boulder, large changes in fence geometry, and the occurrence of slack regions of the fence with nonzero velocity.

Dynamic analysis yields time histories of the following: contact forces, the position and velocity of the boulder, forces on components of the fence, and the deformed geometry of the fence. Typical deformed geometries obtained in analysis are shown in Figures 3 and 4. Figure 3 shows a side view of a gabion mesh fence under impact by a 908-kg (2,000-lb) boulder with a translational velocity at impact of 11 m/sec (36 ft/sec). Beginning at the upper left, the 19 images show the deformed shape of the fence at 0.1-sec intervals. The boulder first pushes the mesh forward and then pulls posts forward. At 0.7 sec (the eighth image), cables and mesh are pulled taut

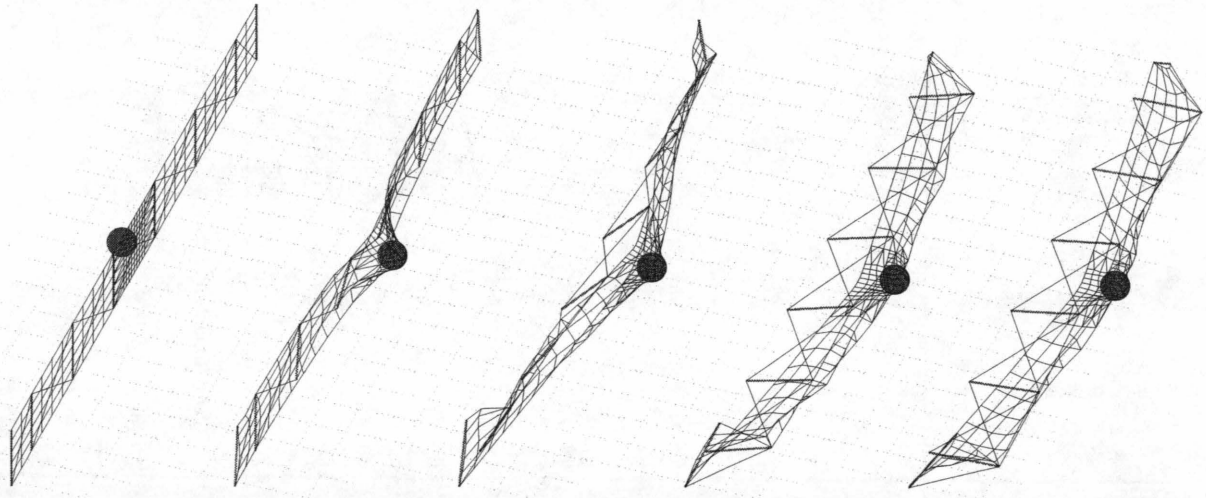

**FIGURE 4 Deformed shapes of flexpost fence after 54-kJ impact (images at 0.2 sec).**

TRANSPORTATION RESEARCH BOARD
National Research Council

# ERRATA
## TRB Publications
(January 1997)

*Transportation Research Circular 456*

The original list of task force members in the Foreword includes names other than members of the task force. The list should read as follows:

Members of the task force included Salvatore J. Bellomo [now deceased], Jerry Gluck, Herbert S. Levinson, Vergil G. Stover, and Gail Yazersky-Ritzer.

*Transportation Research Record 1483*

*pages 97 through 101*

Figures 4–6 are incorrectly labeled in the volume. The correct arrangement is shown here on pages 2–5.

*Transportation Research Record 1504*

*pages 1, 7, 8*

In the abstract and on pages 7 and 8, the conversion for 1,360 kJ should be $10^6$ ft-lb.

and the boulder is stopped. The release of cable tension forces ejects the boulder from the fence. The images span a period of only 1.8 sec. The recovery of posts is slower, even though, as demonstrated in the last images, the fence has begun to return to an upright position. Note also that the boulder bounces on the ground twice; once at 0.7 sec and again at 1.6 sec. The combined effects of tension in the fence fabric and deflection of the posts leads the boulder to impacts with the ground surface, and these impacts dissipate the boulder's kinetic energy. Figure 4 shows a general view of the fence for the same boulder impact. These five images present fence geometry at 0.2-sec intervals. The view is from above and in front of the fence.

Figure 5 shows a simulation of Test No. 8 for the gabion mesh prototype. In the test, the boulder escaped the fence by rolling under it. The analysis correctly simulates this behavior. The boulder, which had been bouncing as it reached the fence, slips under the bottom of the mesh. The images show the impact at 0.1-sec intervals.

Results of dynamic analysis are verified against prototype tests through comparisons of deformed geometries and the disposition of the boulder and through a comparison of peak forces in components with breaking strength and observed damage in tests. In Tables 2 and 3, observations on damage to components from tests and from analysis are listed in the two columns labeled "Outcomes." Analyses used the same weight, speed, and position of impact of boulders that were observed in prototype tests. For all impacts that produced damage in a prototype, the analysis indicates an overstress condition. No damaging impacts are missed or omitted.

In all but one case, an overstress condition in analysis of an impact corresponds to observed failure of at least one component of a prototype. The exception is Test No. 14 for a gabion mesh prototype. Dynamic analysis indicates that the mesh is at 1.1 times its breaking strength for this impact. The mesh did not break in the test, though it did deform.

Overall, analysis results agree with the performance of prototype flexpost fences. The analysis identifies impacts that can be damaging to fences and yields data on forces on components. Such data are needed for fence design. The analysis confirms the 41-kJ (30,000-ft-lb) and 129-kJ (95,000-ft-lb) energy limits for gabion mesh and cable net fences, respectively.

## MECHANICALLY STABILIZED EARTH ROCKFALL BARRIERS

Very high rockfall capacities are offered by MSEs. The Colorado Department of Transportation's design for MSE rockfall barriers uses a granular fill and nonwoven geotextile reinforcement in a free-standing, wrapped face wall (Figure 6). MSE rockfall barriers have halted boulders weighing as much as 13,700 kg (30,100 lb) with translational kinetic energies in excess of 1,360 kJ (106 ft-lb). In 29 impacts of three prototypes, no boulder has breached an MSE rockfall barrier.

Permanent deformations of prototypes are measured after each impact in tests. A series of 19 steel reference posts spaced at 1.2 m (4 ft) are installed on the downhill face of prototypes (Figure 6, lower right). Three sliding tubes are supported by each post and are placed with their tips imbedded in the face of the barrier. Deformations of the wall push the slide tubes forward, and this movement is recorded.

Three prototypes have been tested. The first was a barrier 1.8 m (6 ft) thick, 3.1 m (10 ft) tall, and 27.5 m (90 ft) long. This prototype underwent 11 impacts by boulders ranging in weight from 200 kg (440 lb) to 8,330 kg (18,400 lb). Boulder speeds ranged from 3.7 m/sec (12 ft/sec) to 20 m/sec (64 ft/sec), and translational kinetic energy was as great as 1,400 kJ (1,030,000 ft-lb). Rockfall tests left this barrier with permanent deformations of 0.76 m (2.5 ft) on the downhill face. The most severe impact damaged timber facing, ripped geotextile reinforcements locally and allowed some of the fill to spill out. Damage occurred almost entirely on the impact (uphill) face of the barrier. The downhill face showed large, permanent deformations and some dislocation of timbers, but no rupture of geotextile and no loss of fill. Impacts and permanent deformations of the 1.8- x 3.1-m (6- x 10-ft) prototype are summarized in Table 4.

The 1.8- x 3.1-m (6- x 10-ft) prototype was repaired and retested. Approximately 11 lineal meters (36 ft) of the barrier were reconstructed. The repairs restored the 1.8- x 3.1-m (6- x 10-ft) prototype to its original configuration. The repaired prototype was tested. In these tests, boulder weights ranged from 1,950 kg (4,300 lb) to 12,200 kg (26,900 lb). Boulder speeds ranged from 6.1 m/sec (20 ft/sec) to 17 m/sec (55 ft/sec). Translational kinetic energy was as

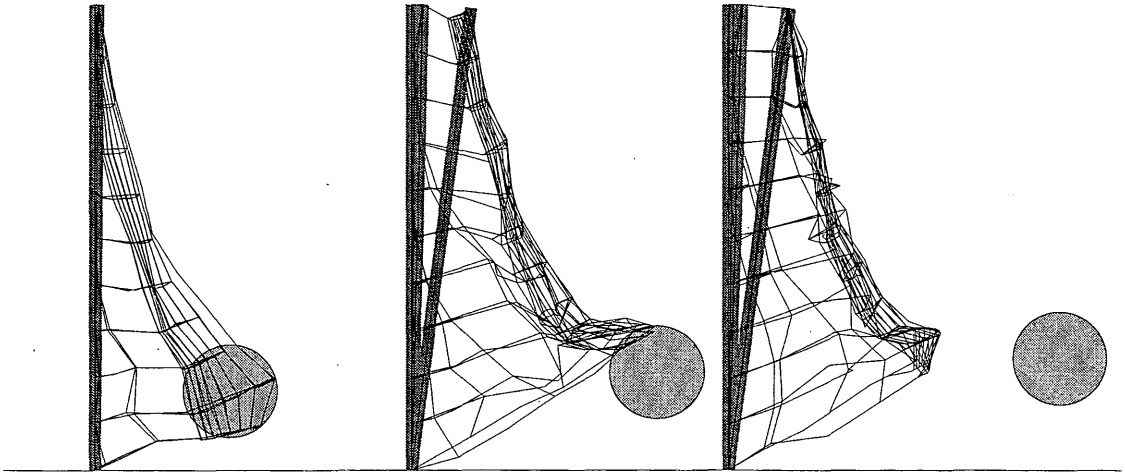

**FIGURE 5 Simulated boulder escape in Test No. 9.**

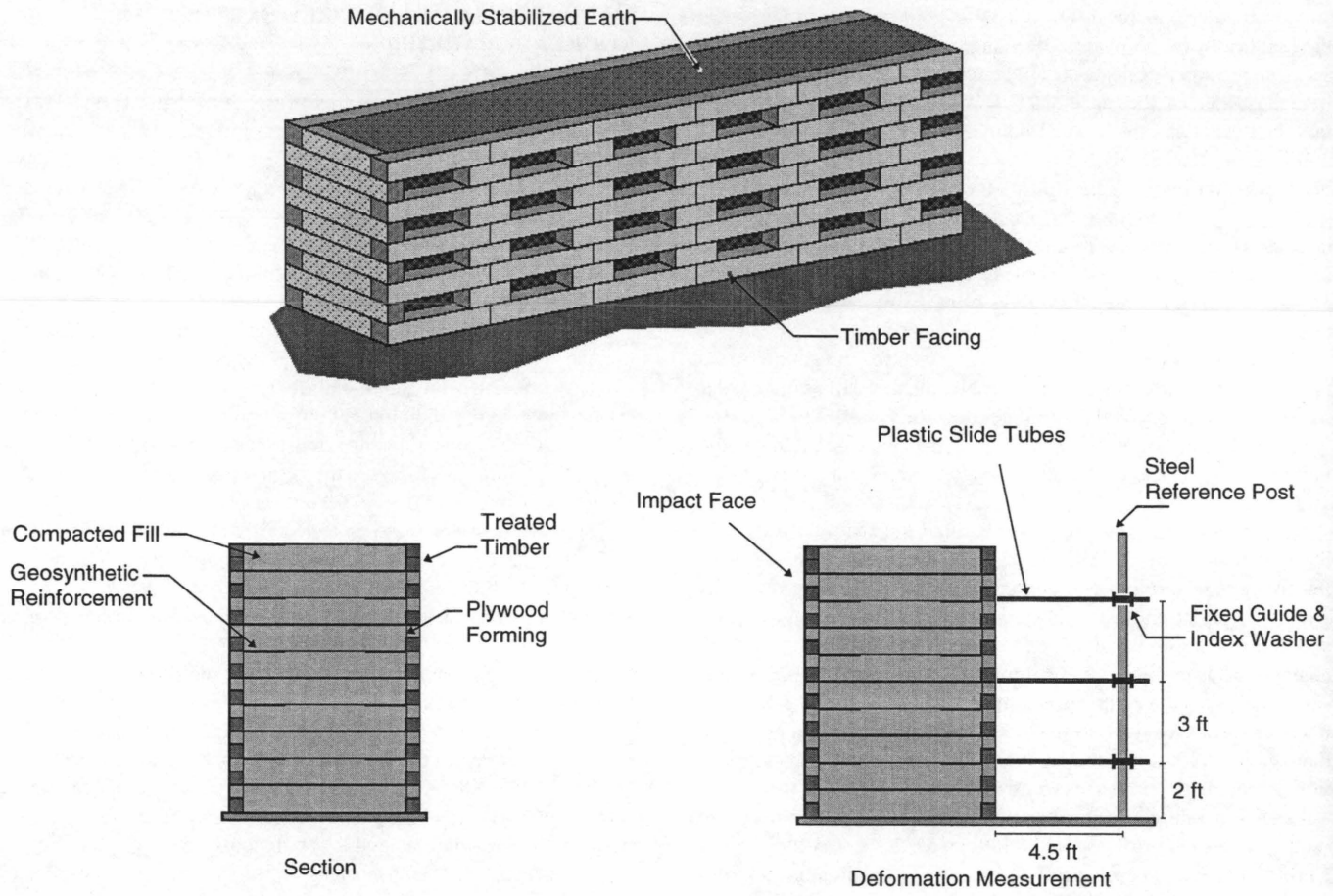


**FIGURE 6 Mechanically stabilized earth rockfall barrier.**

high as 1,420 kJ (1,044,000 ft-lb). The repaired prototype had a rockfall capacity that equaled the original construction. Permanent deformation under extreme impacts was 0.76 m (2.48 ft). The disruption of facing, fill, and geotextile reinforcement was similar to that observed in the test of the original barrier.

In the third set of tests, a larger MSE barrier, 3.7 m (12 ft) tall and 2.4 m (8 ft) thick, was constructed. Tests of this barrier used boulders that ranged in weight from 3,770 kg (8,300 lb) to 13,700 kg (30,100 lb). Boulder translational velocities ranged from 4.9 m/sec (16 ft/sec) to 18 m/sec (60 ft/sec). Translational kinetic energy was as great as 1,410 kJ (1,040,000 ft-lb). It should be noted that the maximum translational kinetic energy stopped by this barrier is perhaps as great as 1,630 kJ (1,200,000 ft-lb), but the boulder translational velocity could not be recovered from videotapes.

The performance of this larger barrier was similar to that of the other prototypes. Extreme impacts disrupted the timber facing and damaged the geotextile reinforcement. The 2.4- x 3.7-m (8- x 12-ft) barrier has a greater resistance to deformation. At a translational kinetic energy of 1,410 kJ (1,040,000 ft-lb), the barrier showed a permanent deformation at the downhill face of only 0.34 m (1.1 ft)–less than half that of the 1.8- x 3.1-m (6- x 10-ft) barrier.

Translational kinetic energies of boulders and the corresponding permanent deformations of MSE barriers follow a power law relationship for translational kinetic energies greater than 271 kJ (200,000 ft-lb). Figure 7 plots the kinetic energies and permanent deformations observed in tests and the power laws. These relationships follow:

| | |
|---|---|
| 1.8- x 3.1-m (6- x 10-ft) barrier | $KE = 1{,}700d^{0.697}$ |
| 2.4- x 3.7-m (8- x 12-ft) barrier | $KE = 2.940d^{0.626}$ |

where $KE$ is the translational kinetic energy of the boulder in kJ and $d$ is the maximum permanent deformation of the wall in meters. The equations indicate that for similar deformations, the larger barrier, which is 2.4 x 3.7 m (8 x 12 ft), can withstand about twice the translational kinetic energy that the smaller barrier can.

A discrete element method has been applied in a preliminary development of dynamic analysis for MSE barriers. Analyses have been attempted for impacts with translational kinetic energies between 949 kJ (700,000 ft-lb) and 1,360 kJ (106 ft-lb) for both the 1.8- x 3.1-m (6- x 10-ft) and 2.4- x 3.7- m (8- x 12-ft) barriers. The analysis is stable and yields estimates of permanent deformation that agree with the power laws developed from test data. Models for MSE barriers consist of through-thickness prisms of rectangular cross sections. The prisms are discrete elements. They interact through normal and frictional forces, but are free to translate independently, to slide along and across each other.

Deformed shapes of the MSE barrier for one impact are shown in Figure 8. At the top of the figure, a cross section at the middle of the barrier is shown at intervals of 0.05 sec. The boulder pushes prisms

**TABLE 4 Summary of Tests of Prototype MSE Rockfall Barriers**

Prototype Tests - 1.8m x 3.1m (6'x10') MSE Rockfall Barrier

| Test No. | Boulder Weight kg | Trans. Velocity m/s | Kinetic Energy kJ | Linear Momentum kg m/s | Permanent Deformation m |
|---|---|---|---|---|---|
| 1 | 200 | 9.2 | 8 | 1832 | 0.000 |
| 2 | 622 | 8.8 | 23 | 5497 | 0.003 |
| 3 | 686 | 15.3 | 80 | 10461 | 0.018 |
| 4 | 677 | 9.2 | 28 | 6198 | 0.009 |
| 5 | 772 | 5.5 | 12 | 4240 | 0.000 |
| 6 | 3457 | 13.7 | 324 | 47444 | 0.146 |
| 7 | 2653 | 17.1 | 386 | 45308 | 0.146 |
| 8 | 3824 | 8.5 | 140 | 32653 | 0.061 |
| 9 | 5318 | 19.5 | 1010 | 103802 | 0.214 |
| 10 | 4017 | 3.7 | 27 | 14702 | 0.000 |
| 11 | 8333 | 18.3 | 1397 | 152489 | 0.717 |

Prototype Tests - Repaired 1.8m x 3.1m (6'x10') MSE Rockfall Barrier

| Test No. | Boulder Weight kg | Trans. Velocity m/s | Kinetic Energy kJ | Linear Momentum kg m/s | Permanent Deformation m |
|---|---|---|---|---|---|
| 1 | 2769 | 6.1 | 5 | 16893 | 0.052 |
| 2 | 1952 | 11.6 | 127 | 22626 | 0.095 |
| 3 | 4041 | 16.8 | 557 | 67781 | 0.329 |
| 4 | 3723 | 16.8 | 514 | 62450 | 0.262 |
| 5 | 4222 | 13.1 | 359 | 55374 | 0.098 |
| 6 | 5584 | 16.8 | 770 | 93675 | 0.177 |
| 7 | 3632 | 14.0 | 359 | 50957 | 0.113 |
| 8 | 12213 | 15.3 | 1410 | 186242 | 0.756 |

Prototype Tests - 2.4m x 3.7m (8'x12') MSE Wall

| Test No. | Boulder Weight kg | Trans. Velocity m/s | Kinetic Energy kJ | Linear Momentum kg m/s | Permanent Deformation m |
|---|---|---|---|---|---|
| 1 | 3768 | 4.9 | 44 | 18389 | 0.000 |
| 2 | 4222 | 14.0 | 418 | 59237 | 0.058 |
| 3 | 4767 | 8.8 | 180 | 42164 | 0.024 |
| 4 | 4177 | 12.2 | 311 | 50957 | 0.034 |
| 5 | 5584 | 10.1 | 287 | 56205 | 0.012 |
| 6 | 6901 | 16.8 | 952 | 115761 | 0.113 |
| 7 | 8399 | 18.3 | 1410 | 153702 | 0.308 |
| 8 | 9398 | 16.8 | 1296 | 157648 | 0.247 |
| 9 | 12213 | 15.3 | 1410 | 186242 | 0.336 |
| 10 | 13665 | - | - | - | 0.336 |

forward by contact and pulls other prisms along by friction within the wall. The cross section at the right of the figure is at the extreme deformation of 2.42 ft. A general view of the deformed barrier is presented in the lower half of the figure. The permanent deformation is distributed along the length of the barrier and therefore appears to be moderate. Permanent deformations obtained in four trials of the analysis procedure are listed in Table 5. The agreement between power law results and the discrete element model is good.

## SUMMARY

Prototype testing is a direct method of establishing the rockfall capacity of barriers. Rockfall capacity is stated to be a limiting translational kinetic energy. This form of rating is convenient for the selection of barriers based on the expected sizes and velocities of boulders at a hazard site. Two types of barriers are reported. The first is a flexible cable fence that can be constructed with gabion mesh or cable nets and has a proven rockfall capacity as great as 129 kJ. Rockfall capacity of the fence is limited by tensile strengths of components. The second barrier is an MSE wall barrier with a rockfall capacity in excess of 1,360 kJ. Rockfall capacity of this barrier is determined by a limit on permanent deformations in the barrier.

Three prototypes of each barrier have been tested. Test conditions approximated the service conditions of rockfall barriers. Test data are the primary measure of barrier capacity and performance. A quantitative analysis method has been developed for flexible fence barriers. The analysis agrees with the observed performance

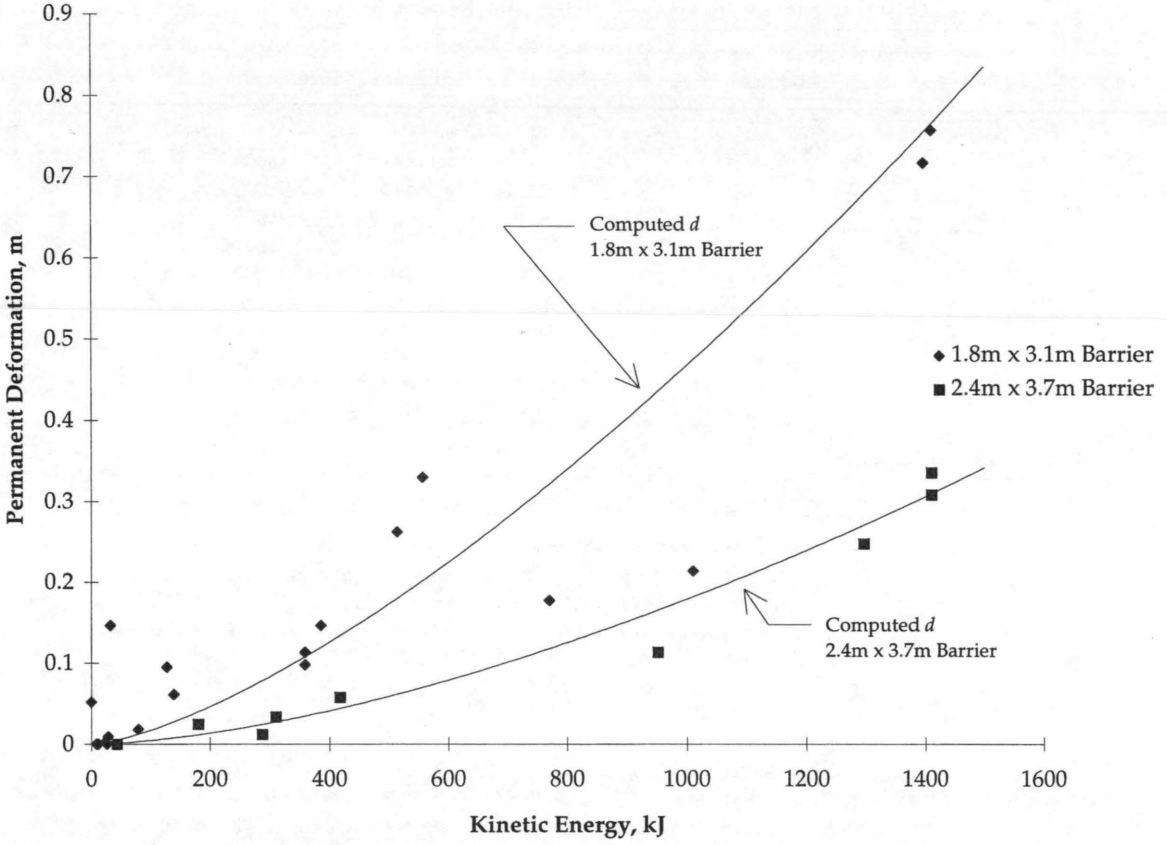


**FIGURE 7 Test impacts and power law relationships for MSE rockfall barriers.**

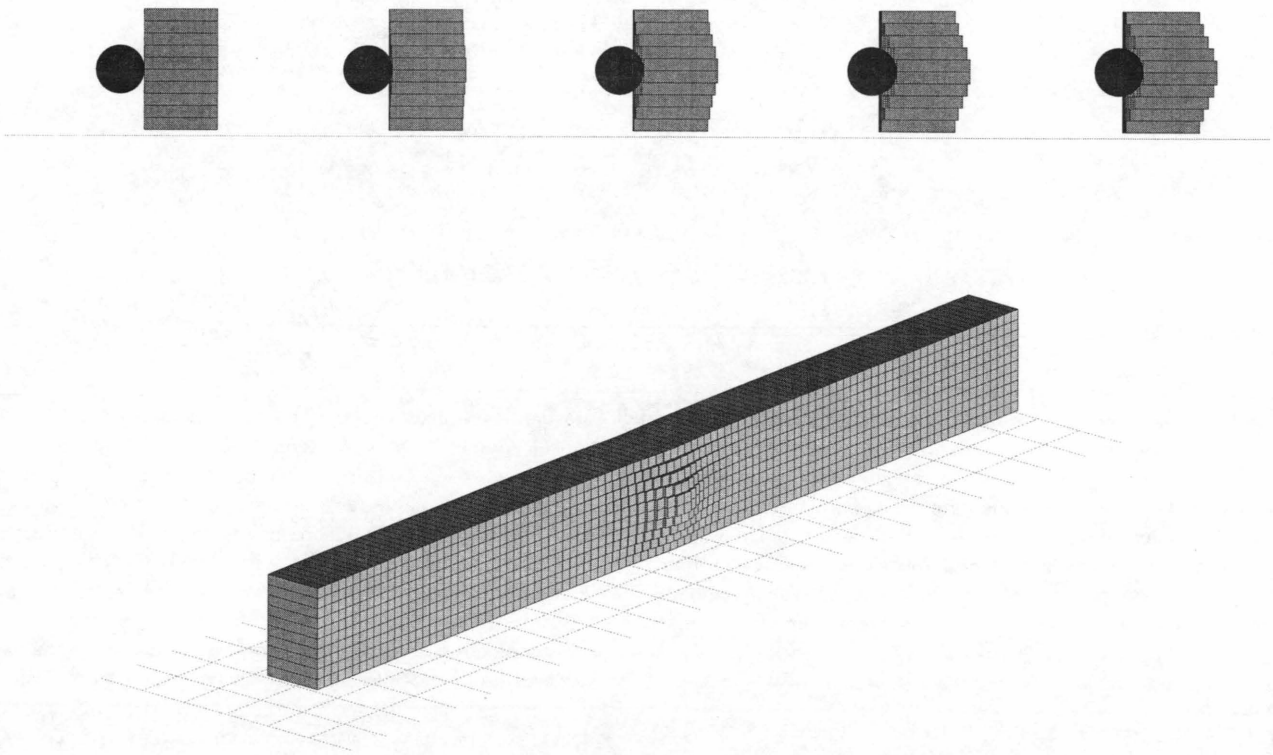

**FIGURE 8 Deformed shapes of MSE rockfall barrier after 1,400-kJ impact (images at 0.05 sec).**

**TABLE 5 Comparison of Deformations from Power Law and Discrete Element Analyses**

| Boulder Weight | Velocity | Energy | Permanent Deformation Power Law | Analysis |
|---|---|---|---|---|
| kg | m/s | kJ | m | m |
| 1.8m x 3.1m (6x10) Prototype | | | | |
| 5318 | 19.5 | 1010 | 0.48 | 0.48 |
| 8333 | 18.3 | 1397 | 0.74 | 0.74 |
| 2.4m x 3.7m (8x12) Prototype | | | | |
| 6901 | 16.8 | 952 | 0.17 | 0.20 |
| 12213 | 15.3 | 1410 | 0.31 | 0.30 |

of prototype fences. The analysis was used in the design development of cable net fences, and subsequent prototype testing verified analytical predictions. A discrete element analysis has been developed for MSE barriers. The work demonstrates that the method is feasible and that reasonable predictions of deformations in barrier can be obtained. It is not yet a quantitative analysis method for MSE barriers.

## ACKNOWLEDGMENTS

This work was supported by the Colorado Department of Transportation and Colorado Transportation Institute. Their support is gratefully acknowledged.

## REFERENCES

1. Varnes, D. J. Slope Movement Types and Processes. In *Landslides Analysis and Control*, R. L. Schuster and R. J. Krizek, eds. Special Report 176. TRB, National Research Council, Washington, D.C., 1978, pp. 11–33.
2. Kobayashi, Y., E. L. Harp, and T. Kagawa. Simulation of Rockfalls Triggered by Earthquakes. *Rock Mechanics and Rock Engineering*, Vol. 23, No. 1, 1990, pp. 1–20.
3. Badger, T. C., and S. M. Lowell. Rockfall Control in Washington State. In *Transportation Research Record 1343*, TRB, National Research Council, Washington, D.C., 1992, pp. 14–19.
4. Pierson, L. A. Rockfall Hazard Rating System. In *Transportation Research Record 1343*, TRB, National Research Council, Washington, D.C., 1992, pp. 6–13.
5 Rock Slope Hazard Rating Procedure. Working draft. New York State Department of Transportation, Albany, 1993, 41 pp.
6. McCauley, M. L., W. W. Byron, and S. A. Naramore. *Rockfall Mitigation*. Report FHWA/CA/T-85/12. California Transportation Department, Sacramento, 1985, 147 pp.
7. Ritchie, A. M. Evaluation of Rockfall and Its Control. In *Highway Research Record 17*, HRB, National Research Council, Washington, D.C., 1963, pp. 13–28.
8. Barrett, R. K., T. Bowen, T. Pfeiffer, and J. Higgins. *Rockfall Modeling and the Colorado Rockfall Simulation Program: Version 2.1 Users Manual*. Report CDOT-DTD-ED3/CSM-89-2B. Colorado Department of Transportation, Denver, 1991, 164 pp.
9. Pfeiffer, T. J., and J. D. Higgins. Rockfall Hazard Analysis Using the Colorado Rockfall Simulation Program. In *Transportation Research Record 1288*, TRB, National Research Council, Washington D.C., 1990, pp. 117–126.
10. Barrett, R. K., T. Bowen, T. Pfeiffer, and J. Higgins. Rockfall Modeling and Attenuator Testing. Report CDOH-DTD-ED3/CSM-89-2. Colorado Highway Department, Denver, 1989, 141 pp.
11. Hearn, G. *CDOT Flex-Post Rockfall Fence*. Report CDOH-R-UCB-91-6, Colorado Highway Department, Denver, 1991, 105 pp.
12. Duffy, J. D., and B. Haller. Field Tests of Flexible Rockfall Barriers. In *Transportation Facilities Through Difficult Terrain*, J. T. H. Wu and R. K. Barrett, eds., Balkema, 1993, pp. 465–474.
13. Kane, W. F., D. Q. Fletcher, and J. D. Duffy. Low-Impact Rock Net Testing, Performance, and Foundation Design. In *Transportation Facilities Through Difficult Terrain*, J. T. H. Wu and R. K. Barrett, eds., Balkema, 1993, pp. 453–464.
14. *Full-Scale Geotextile Rock Barrier Wall Testing, Analysis, and Prediction*. Report for Colorado Department of Transportation. Parsons DeLeuw, Denver, 1992.
15. *Full-Scale Geotextile Rock Barrier Wall Testing, Analysis, and Prediction: Addenda I and II*. Report for Colorado Department of Transportation. Parsons DeLeuw, Denver, 1993.
16. Mustoe, G. G. W., and H. P. Huttlemaier. Dynamic Simulation of a Rockfall Fence by the Discrete Element Method. *Microcomputers in Civil Engineering 8*, 1993, pp. 423–437.
17. Hearn, G. High-Capacity Flexpost Rockfall Fences, with Addendum on Prototype Testing. Report CDOT- UCB-94-4. Colorado Department of Transportation, Denver, 1994.
18. Hearn, G., and D. Hinzman. *Analysis and Design Recommendations for the CDOH Flexpost Fence*. University of Colorado, Boulder, 1991.
19. Hearn, G., and L. Akkaraju. Analysis of Cable Nets for Boulder Impact. Proc., *ASCE 10th EMD*, Boulder, Colo., ASCE, Washington, D.C., 1995, pp. 289–292.

*Publication of the paper sponsored by Committee on Modeling Techniques in Geomechanics.*

# Modeling Flowslides Caused by Static Loading

R. PHILLIPS AND P. M. BYRNE

The phenomenon of liquefaction can occur in saturated loose sands and is characterized by a large strength or stiffness loss resulting in substantial deformation or a flowslide when subjected to rapid static or cyclic loading. To study this phenomenon, the Canadian geotechnical engineering community has started the Canadian Liquefaction Experiment (CANLEX), which has planned to include a large, controlled liquefaction event in the field. Numerical predictions of the response of this full-scale event will be compared with the field measurements. Centrifuge model tests are being conducted to aid in the design of the field event and to allow for calibration of the numerical models. These tests could serve as a substitute for calibration of numerical models in the event that a dynamic field event is not possible or not conducted at the site. The first of these tests ascertained that a gravitational flowslide event could be induced under undrained static loading. A surcharge dropped on the crest of an equivalent 16-degree submerged 8.8-m-high slope of loose oil sand tailings caused the slope to liquefy and flow with deep-seated lateral movements throughout the soil slope to an angle of 7 degrees. A finite difference numerical model, calibrated against laboratory element test data, captured the essence of the observed undrained response of the centrifuge test in terms of pore pressure rise and deformation pattern. These modeling techniques will be used to evaluate other triggering mechanisms for the field event.

The Canadian geotechnical engineering community has started a major $1.8 million (Canadian) sand liquefaction study entitled the Canadian Liquefaction Experiment (CANLEX) through the collaborative efforts of industry, engineering consultants, and university participants, and with support from the Natural Sciences and Engineering Research Council of Canada (NSERC). The study will examine the characterization of sand for dynamic and static liquefaction. The phenomenon of liquefaction occurs in saturated loose sands and is characterized by a large strength loss resulting in substantial deformation when the sand is subjected to rapid static or cyclic loading. The objectives of sand characterization are as follows (*1*):

1. To obtain high-quality undisturbed samples through in situ freezing techniques.
2. To calibrate and verify in situ testing techniques including those under the influence of high overburden stress.
3. To obtain greater understanding of the mechanism of liquefaction-induced displacement through the development and evaluation of analytical models.
4. To investigate other factors such as influence on liquefaction of fines content, fabric, direction of loading, shape of state boundaries, and triggering mechanisms.

R. Phillips, C-CORE, Memorial University of Newfoundland, St. John's, Newfoundland, A1B 3X5 Canada. P. M. Byrne, Department of Civil Engineering, University of British Columbia, Vancouver, British Columbia, V6T 1W5 Canada.

CANLEX comprises three phases over 3 years. Phases 1 and 2 are concerned with characterization of loose sand to determine its in situ state and elemental stress-strain response. These phases will involve both in situ tests and recovery of high-quality samples for laboratory testing. The purpose of such characterization is to understand further the liquefaction phenomenon and to specifically evaluate triggering resistance, residual strength, and liquefaction-induced displacement of embankments and slopes under static and earthquake loading conditions. The Phase 1 field characterization of hydraulically deposited sand at the Syncrude Canada Limited Mildred Lake Settling Basin, Fort McMurray, Alberta, has been successfully completed. Phase 2 has commenced with test sites in the Fraser River Delta in Richmond, British Columbia (*2*).

In Phase 3, a controlled liquefaction event will be initiated at the Syncrude tailings disposal site and will involve construction of a loose sand berm and the triggering of a static flow liquefaction event. Numerical modelers will predict the response of this full-scale event and compare the numerical response with the field measurements.

In the project entitled Verification of Liquefaction Analysis Using Centrifuge Studies, the relevance and effectiveness of existing numerical and constitutive models used in the analysis of soil liquefaction were also evaluated (*3*). It was concluded that centrifuge modeling was a reliable tool for studying the mechanisms of soil behavior in such boundary-valued problems and that fully coupled effective stress-based numerical procedures using plasticity-based constitutive models were most promising for the prediction of deformation.

The CANLEX project includes centrifuge testing of reduced-scale physical models of potential full-scale events. The objectives of these tests have been described. In Stage 1 of these tests, described by Phillips and Byrne (*4*), the feasibility of modeling static liquefaction in the centrifuge was ascertained. Subjecting a submerged loose sand slope to a crest loading applied at an appropriate rate brought about an undrained flowslide. In this paper the characteristics of this flowslide are compared with a Class B prediction from a numerical model.

## MATERIAL PROPERTIES

### Laboratory Measurements

The sand used was moist oil sand tailings supplied by Syncrude Canada Limited. Table 1 presents properties of this fine subangular to subrounded sand determined in accordance with ASTM Schedule D procedures, except the trace oil content. The grain size distribution is shown in Figure 1. The response of undrained triaxial extension and compression tests and drained compression tests are

**TABLE 1 Properties of Oil Sand Tailings**

| | | |
|---|---|---|
| Specific gravity, $G_s$ | | 2.64 |
| Maximum void ratio, $e_{max}$ | | 0.96 |
| Minimum void ratio, $e_{min}$ | | 0.53 |
| Mean grain size, $d_{50}$ | mm | 0.17 |
| Effective grain size, $d_{10}$ | mm | 0.092 |
| Uniformity coefficient, $C_u$ | | 2.12 |
| Natural water content, w | % | 7 - 9 |
| Oil content | % | 0.27 |
| Permeability to Canola oil @ 21°C | m/s | 3.3e-07 |
| at relative density, Dr | | 0.40 |
| Permeability to water @ 21°C | m/s | 1.6e-05 |
| at relative density, Dr | | 0.48 |

summarized in Figure 2. The samples tested were of water-saturated oil sand with an average relative density of 40 percent. These were tested at an axial strain rate of about 2 percent/min. The normal and deviator stresses $s'$ and $t$ in Figure 2(*b*) are $(\sigma'_1 + \sigma'_3)/2$, and $(\sigma_1 - \sigma_3)/2$, respectively. The projection of the critical state or constant volume line in stress space has a friction angle, $\varphi \leq {}_{cv}$, of about 36 degrees. The instability line in triaxial extension, taken as the locus of maximum deviator stress, has a mobilized friction angle of 13 degrees.

Typical stress-strain responses from both undrained triaxial compression and extension tests are shown in Figure 2(*a*). In compression, the material is strain hardening, and such a material would not be expected to undergo static liquefaction. In extension, however, a strain-softening liquefaction response is noted, and such a material could undergo static liquefaction.

## CENTRIFUGE MODELING

Centrifuge modeling is a technique for reduced-scale physical modeling of gravity-dependent phenomena, such as soil slope behavior. Because a full-scale soil structure is in equilibrium under the Earth's gravitational field, $g$, a reduced-scale model on a centrifuge, at radius $R$, is in equilibrium under an acceleration field of $R\omega^2$, where $\omega$ is the rotational speed. The model will then have its weight increased $N$ times, where $N = R\omega^2/g$.

For a typical value of $N = 100$, if a model is made at 1/100th scale and is accelerated to $100g$, the stresses caused by self weight will be similar to the stresses in the prototype at homologous points. The model can then reproduce the phenomena of cracking, rupture, or flow that would be observed in the prototype because the stress dependency of soil behavior has been correctly simulated. The principles, scaling laws, and some applications of centrifuge modeling are described by Schofield (*5*) and Leung et al. (*6*).

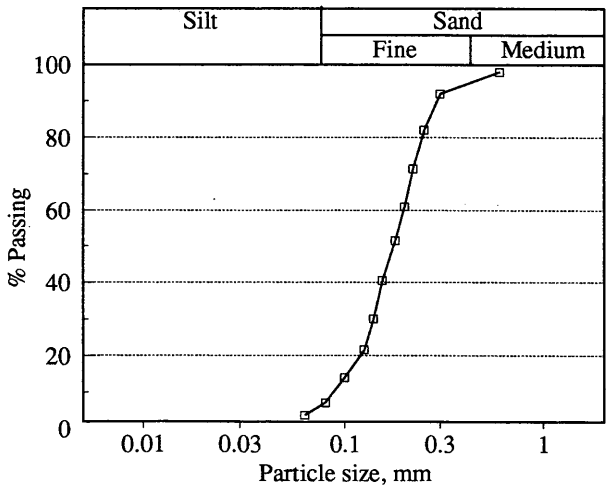


**FIGURE 1 Oil sand particle size distribution.**

### Centrifuge Model Test

The centrifuge model test comprised an instrumented plane-strain submerged loose sand with 16-degree slope at a relative density of about 30 percent, as shown in Figure 3. The test was conducted at $50g$ for a scaled slope height of 8.75 m. Two pore pressure transducers (PPT 1 and PPT 2) were placed within the sand model under the center of the crest and at the midpoint of the slope, respectively, as shown. The model tests were conducted at the C-CORE Centrifuge Centre, St. John's, Newfoundland (*7*).

The sand slope was saturated with a viscous pore fluid, namely, Canola vegetable oil with a dynamic viscosity of 57 centipoise at 21°C. Comparison of both water-saturated and oil-saturated drained triaxial tests confirmed that the oil did not affect the skeletal response of the sand. For water-saturated sand, the coefficient of consolidation, $c_v$, at 50 kPa is about 200 cm²/sec, which is possibly too large to control the escape of water and cause a liquefaction event in the centrifuge test. The more viscous pore fluid retards pore pressure dissipation, permitting liquefaction to develop. The oil viscosity is approximately 50 times that of water, which will reduce $c_v$ by a factor of 50. The use of such a viscous pore fluid ensures synchronous time scaling of inertial and consolidation events (*8*).

Preliminary analyses indicated that even with oil rather than water as a pore fluid, the crest load would have to be applied in a few seconds to prevent significant dissipation of pore pressures. Such dissipation would prevent the triggering of static liquefaction. For this reason, a drop weight approach was used. The weight was composed of a steel surcharge suspended above the slope crest. The sand slope was subjected to Loading Sequences A and B, as described in the next two sections.

### Loading Sequence A

For Sequence A, the surcharge had a static bearing pressure of 43 kPa and was suspended 11 mm above the initial slope crest. The slope crest settled 6 mm during acceleration of the centrifuge to $50g$ at middepth of the sand slope. The surcharge struck the sand surface with a velocity of more than 0.6 m/sec. Both PPTs recorded an instant increase of about 32 kPa, which is 74 percent of the static bearing pressure (Figure 4). The pore pressure at PPT 1 continued to increase by 8 kPa for another 2.5 sec because of pore pressure redistribution under the impermeable surcharge. No significant movements of the sand slope were observed by a video monitoring system. This observation was confirmed by the PPTs as the pore pressures eventually dissipated to their initial equilibrium values.

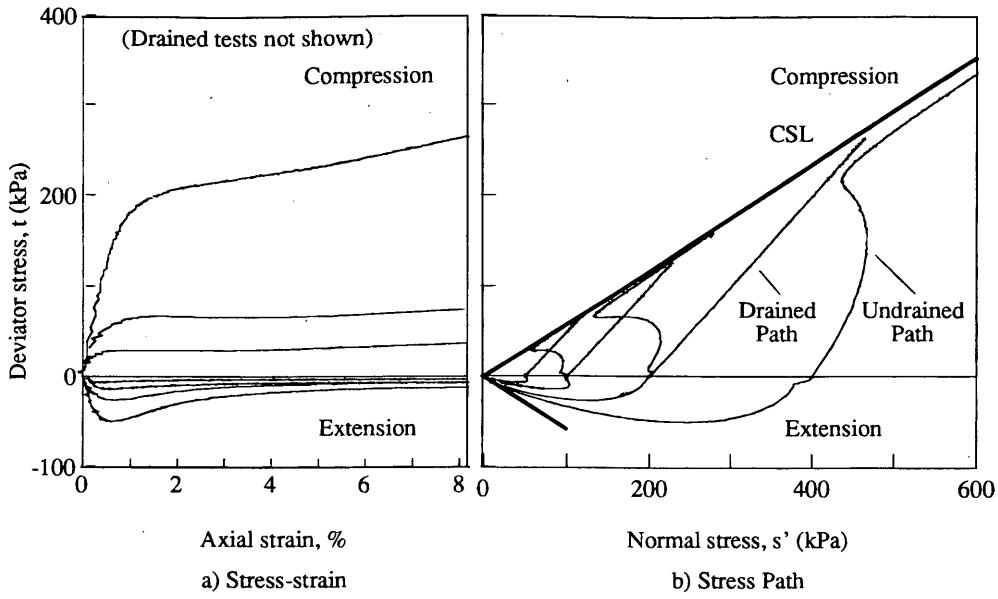


**FIGURE 2 Oil sand triaxial response.**

### Loading Sequence B

The centrifuge was stopped and the surcharge increased to a static bearing pressure of 87 kPa suspended 18 mm above the compressed slope crest. The centrifuge was accelerated again to 50*g* and the surcharge dropped. The actual drop height exceeded 21 mm because of embedment of the surcharge into the crest of the slope. The measured impact velocity exceeded 0.1 m/sec and probably exceeded 0.6 m/sec, as measured in Loading Sequence A. The 42-kPa step rise at PPT 1 was 48 percent of the surcharge static bearing pressure (Figure 5). The continued rise at PPT 1 of 27 kPa for 4 sec after impact is partly because of downward movement of PPT 1 during embedment of the surcharge. The initial total stress above PPT 2 was about 106 kPa. The pore pressure at PPT 2 rose to 90 percent of this value, indicating the potential for liquefaction adjacent to this transducer.

The video record matches the events recorded by PPT 1. After dropping of the weight, no gross distortion of the slope was observed for a short period of about 1/4 sec. The surcharge then punched vertically down into the crest of the slope and large deep-seated lateral soil flow movements were observed throughout the soil slope toward the slope toe. These movements stopped after a 3-sec period. A shear plane developed vertically down from the edge of the drop weight adjacent to the shoulder of the slope. The final slope profile with the positions of the surcharge and the PPTs is shown in Figure 6. The slope came to rest at an angle of about 7 degrees. The lateral slope movement was constrained by the end wall of the test section.

## NUMERICAL MODELING

The numerical simulation of the centrifuge test uses a finite difference solution of the governing equations incorporating an elastic-plastic stress-strain model that captures the fundamental drained or skeleton behavior of sand. The undrained behavior is predicted by imposing the volumetric constraint that arises from the presence of the water. Details of the stress-strain law used in the analysis are

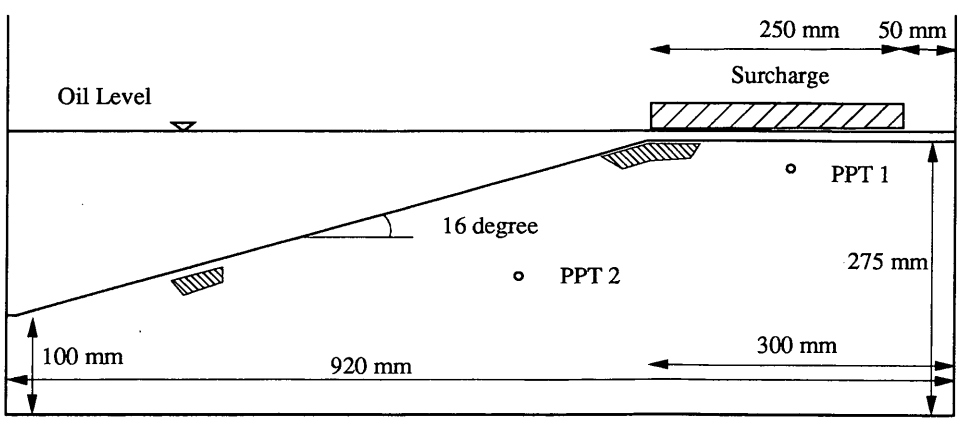


**FIGURE 3 Centrifuge test geometry.**

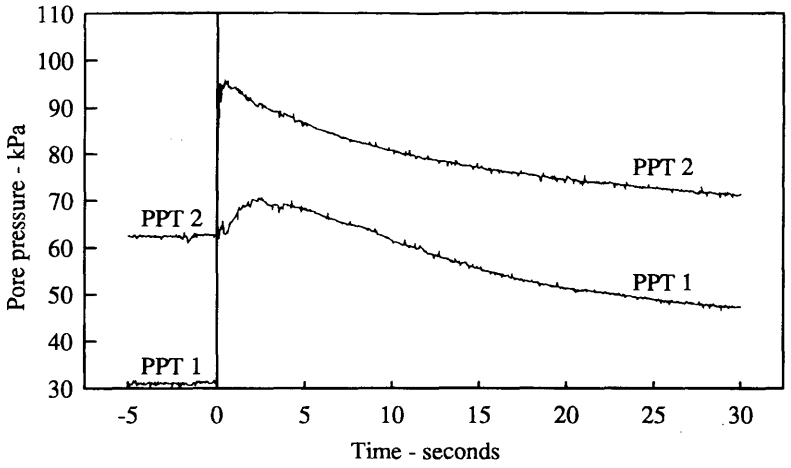


**FIGURE 4 Pore pressure response to loading sequence A.**

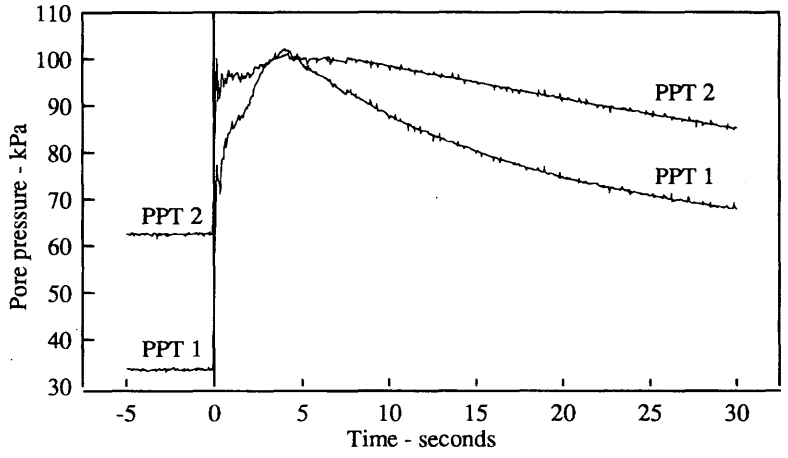


**FIGURE 5 Pore pressure response to loading sequence B.**

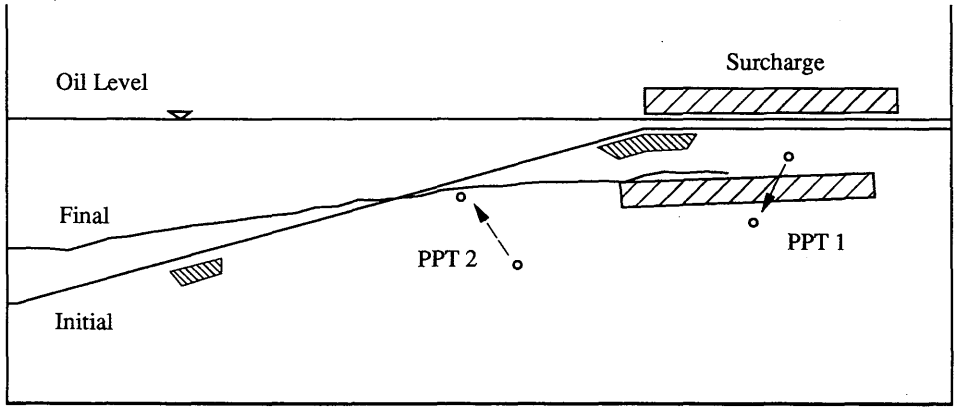


**FIGURE 6 Initial and final slope configurations.**

presented in the following section. The numerical model is first used to capture the laboratory stress-strain response of test elements and then applied to predict the response of the centrifuge model.

## Stress-Strain Model

Both the drained and the undrained responses of granular material are controlled by the skeleton behavior. The effective stress ratio $t/s'$ and the density basically control the shear response as shown in Figure 7(*a*). Shear strains induce volumetric strains as shown in Figure 7(*b*). Basically, loose material is contractive when sheared to any effective stress ratio state, whereas dense material is contractive for stress ratio states below the phase transformation or constant volume friction angle and dilative for stress ratio states above [Figure 7(*d*)]. At very low confining stress, loose material may behave as a dense material and may be dilative at large strains. Unloading and reloading during shear (not shown) would promote a stiff, essentially elastic response. Thus the major portion of the observed strain during first loading is plastic rather than elastic, and these plastic strains dominate the response. The elastic-plastic stress-strain model used to capture such behavior is discussed in the following section.

### *Elastic Properties*

The elastic properties are assumed to be isotropic and defined by two stress-level-dependent elastic parameters, a shear modulus $G_e$ and bulk modulus $B_e$ as follows:

$$G_e = K_{ge} \cdot P_a \cdot (s'/P_a)^{ne} \quad (1)$$

where

$K_{ge}$ = the shear modulus number,
$ne$ = shear modulus exponent, and
$P_a$ = atmospheric pressure in the units selected.

$$B_e = K_{be} \cdot P_a \cdot (s'/P_a)^{me} \quad (2)$$

where $K_{be}$ is the bulk modulus number, and $me$ is the bulk modulus exponent.

The values of the parameters $K_{ge}$, $K_{be}$, $ne$, $me$ can be obtained from unloading tests. In the absence of such data for the Syncrude sand, values of $K_{ge} = 300$, $K_{be} = 300$, $ne = 0.5$, and $me = 0.5$ were selected. The bulk modulus parameters $K_{be}$ and $me$ were based on isotropic drained unloading tests on other loose granular material. The shear exponent parameter $ne$ was set to 0.5. The shear modulus number $K_{ge}$ was set equal to $K_{be}$ to conform with that of Hardin (*9*), who determined Poisson's ratio for sand to be in the range 0 to 0.2 and recommended a value of about 0.12. The increments of elastic strain for any stress increment are determined from these two stress-level-dependent elastic moduli, $G_e$ and $B_e$.

### *Plastic Properties*

The variation of deviator stress ratio $\eta$ ($t/s'$) with plastic shear strain [Figure 7(*a*)] is assumed to be hyperbolic. The slope of this line is the normalized plastic tangent modulus $G_p^* = G_p/s'$, where the tangent plastic shear modulus $G_p$ is given by

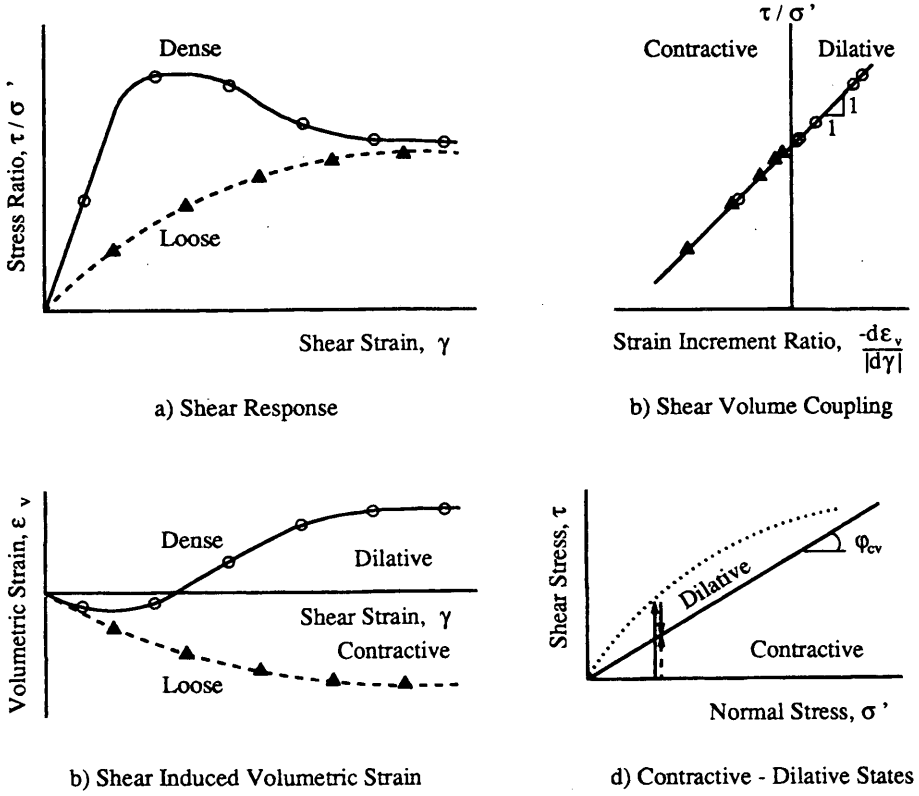


**FIGURE 7 Response of granular skeleton to monotonic shear loading.**

$$G_p = K_{gp} \cdot P_a \cdot (s'/P_a)^{np}(1 - t/t_f \cdot R_f)^2 \quad (3)$$

where

$K_{gp}$ = plastic shear modulus number,
$np$ = plastic shear modulus exponent,
$t_f$ = shear strength = $s' \sin(\varphi)$
$R_f$ = failure ratio, $t_{ult}/t_f$, generally in the range of 0.5 to 1.0, and
$t_{ult}$ = ultimate stress from the best-fit hyperbola.

This approach is similar to that of Duncan and Chang (*10*) except that solely plastic strains, rather than the combination of elastic and plastic strains, are considered. An increment of plastic shear strain, $d\epsilon_\gamma^p$, is caused by an increase in stress ratio, $d\eta$, where

$$d\varepsilon_\gamma^p = d\eta/G_p^* = d\eta/(G_p/s') \quad (4)$$

since $\eta = t/s'$

$$d\eta = dt/s' - tds'/s'^2 \quad (5)$$

Hence,

$$d\varepsilon_\gamma^p = \frac{1}{G_p}\left[dt - \frac{t}{s'}ds'\right] \quad (6)$$

An increase in stress ratio can be brought about by an increase in shear stress or a decrease in normal effective stress. Either change will cause an increment of plastic shear strain, $d\epsilon\gamma^p$, as may be seen from Equation 6. If $ds' = 0$, as it would be for a drained simple shear test, then the usual definition of $G_p$ is obtained. If $dt = 0$, then a reduction in effective stress ($-ds'$) will still cause a plastic shear strain increment $d\epsilon_\gamma^p$ as shown in Figure 8. For undrained tests in which a significant pore water pressure rise occurs, $ds'$ will be negative and lead to a significant increase in plastic shear strain. Positive values of $ds'$ are neglected in Equation 6 because they cause a reduction in stress ratio, which causes an elastic (not plastic) strain. The second term inside the bracket of Equation 6 is a key feature of the model and is not generally considered in stress-strain modeling of sand. Equation 6 gives the plastic shear strains. To complete the picture, the associated plastic volume changes are also needed.

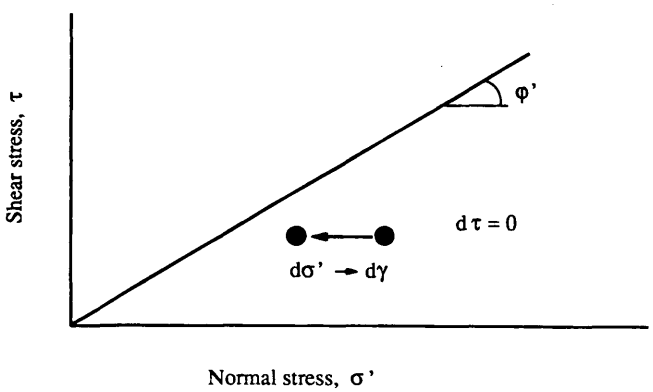


**FIGURE 8 Strain increment because of reduction in normal effective stress.**

The increment of plastic volumetric strain $d\epsilon_\gamma^p$ is related to the increment of plastic shear strain and is obtained from energy considerations following the concepts of Taylor (*11*), Schofield and Wroth (*12*), and Matsuoka and Nakai (*13*) that the plastic work increment is dissipated solely in friction against the plastic shear strain increment:

$$d\varepsilon_v^p = d\varepsilon_\gamma^p(\sin\varphi_{cv} - t/s') = d\varepsilon_\gamma^p \cdot Dt \quad (7)$$

where

$d\epsilon_v^p$ = plastic volumetric strain increment
$\varphi_{cv}$ = constant volume friction angle, and
$t/s'$ = deviator stress ratio on the plane of maximum shear stress, taken here to be the mobilized plane.

The term $D_t(\sin\varphi_{cv} - t/s')$ controls the shear-induced volumetric contraction or dilation. Contraction occurs for stress ratios less than $\sin\varphi_{cv}$ and dilation for stress ratios greater than $\sin\varphi_{cv}$. Because planes of principal stress and strain increment are assumed to coincide, the normal plastic strain $d\epsilon_n^p$ on the mobilized plane is half the plastic volumetric strain $d\epsilon_v^p$. Hence, from Equations 6 and 7 the plastic stress-strain relationship on the mobilized plane is

$$\begin{Bmatrix} d\varepsilon_n^p \\ d\varepsilon_\gamma^p \end{Bmatrix} = \frac{1}{G_p}\begin{bmatrix} -t/s' \cdot D_t/2 & D_t/2 \\ -t/s' & 1 \end{bmatrix}\begin{Bmatrix} ds' \\ dt \end{Bmatrix} \quad (8)$$

In general, the direction of the mobilized plane does not correspond with the reference coordinate system, and the stress-strain response is transformed into the following form:

$$\begin{Bmatrix} d\epsilon_x^p \\ d\epsilon_\gamma^p \\ d\gamma_{xy}^p \end{Bmatrix} = [C_p]\begin{Bmatrix} d\sigma'_x \\ d\sigma'_y \\ d\tau_{xy} \end{Bmatrix} \quad (9)$$

in which $C_p$ is the plastic strain matrix linking the $x,y$ Cartesian coordinates of the stress and plastic strain increment vector. The elastic and plastic strains are then added, and the matrix is inverted to give the stress increments in terms of the strain increments.

$$\{\Delta\sigma'\} = \begin{Bmatrix} d\sigma'_x \\ d\sigma'_y \\ d\tau_{xy} \end{Bmatrix} = [D_{ep}]\begin{Bmatrix} d\epsilon_x \\ d\epsilon_\gamma \\ d\gamma_{xy} \end{Bmatrix} = [D_{ep}]\{d\epsilon\} \quad (10)$$

Coaxiality of the plastic strain increments and the associated principal stresses is assumed in performing this transformation. The effective stress-strain response of the soil skeleton to loading under drained conditions is thus described in Equation 10. In classical plasticity terms, the yield loci comprise lines of constant stress ratio with a nonassociated flow rule given by Equation 8 and a hardening law defined in terms of plastic shear strain in Equation 6.

*Undrained Response*

For undrained conditions the increment of pore fluid pressure, $du$, is given by

$$du = B_f/n \cdot d\epsilon_v^f \tag{11}$$

where

$B_f$ = bulk modulus of the pore fluid,
$n$ = porosity of the skeleton, and
$d\epsilon_v^f$ = volumetric strain of the fluid expressed in terms of the total volume of the element.

For undrained conditions, volume compatibility requires that the volumetric strain of the soil skeleton, $d\epsilon_v$, must equal the volumetric strain of the fluid, $d\epsilon_v^f$, thus

$$d\epsilon_v^f = d\epsilon_v = d\epsilon_x + d\epsilon_y = \begin{Bmatrix} 1 \\ 1 \\ 0 \end{Bmatrix}^T \begin{Bmatrix} d\epsilon_x \\ d\epsilon_y \\ d\gamma_{xy} \end{Bmatrix} \tag{12}$$

Hence

$$du = \frac{B_f}{n} = \begin{Bmatrix} 1 \\ 1 \\ 0 \end{Bmatrix}^T \begin{Bmatrix} d\epsilon_x \\ d\epsilon_y \\ d\gamma_{xy} \end{Bmatrix} \tag{13}$$

and

$$\{du\} = \begin{Bmatrix} du \\ du \\ 0 \end{Bmatrix} = \frac{B_f}{n} \begin{Bmatrix} 1 \\ 1 \\ 0 \end{Bmatrix} \begin{Bmatrix} 1 \\ 1 \\ 0 \end{Bmatrix} \{d\epsilon\} = \frac{B_f}{n} \begin{bmatrix} 1 & 1 & 0 \\ 1 & 1 & 0 \\ 0 & 0 & 0 \end{bmatrix} \quad \{d\epsilon\} = [D_f]\{d\epsilon\} \tag{14}$$

now

$$d\sigma = d\sigma' + du \tag{15}$$

Hence

$$\{d\sigma\} = \{d\sigma'\} + \{du\} = [[D_{ep}] + [D_f]]\{d\epsilon\} \tag{16}$$

The stress-strain model for the special case of undrained conditions is thus obtained in terms of total stresses by adding the effective and pore fluid contributions to stiffness. At each step of the analysis, the change of pore fluid pressure is obtained from the computed element strains using Equation 11. The stress-strain model is therefore a fully coupled effective stress model.

## Numerical Analysis Procedure

In general, stress-deformation response is governed by the laws of mechanics, which require that equilibrium and compatibility be satisfied for the given boundary conditions and the appropriate stress-strain law. Finite element or finite difference techniques are routinely used to reasonably satisfy these con-ditions.

The analysis was carried out using the computer code Fast Lagrangian Analysis of Continua (FLAC), Version 3.2 (*14*). This program uses a finite difference technique. The domain is discretized into a quadrilateral grid in which each grid zone or element comprises four triangles. The stiffness contribution of each zone is essentially the same as if it were represented by four constant strain finite elements. Dynamic equilibrium, rather than static equilibrium, is satisfied using a step-by-step explicit time domain procedure. Large strains and displacements are approximated by upgrading the nodal coordinates.

This approach has the advantage that the solution is numerically stable even when the problem is not statically stable. In this way, development of large strains and displacements before failure can be examined. The code allows the user to input the specific stress-strain model. The modified Matsuoka model [after Matsuoka and Nakai (*13*)] discussed in the previous section was used for the analyses described hereafter.

## Numerical Simulation of Triaxial Tests

The undrained response observed in the triaxial tests was first captured using the FLAC code and the stress-strain model described previously. The predicted and observed responses for undrained triaxial compression and extension tests for a confining stress of 100 kPa are compared in Figure 9. The predicted undrained triaxial compression response [Figure 9(*a*)] is strain-hardening, whereas the

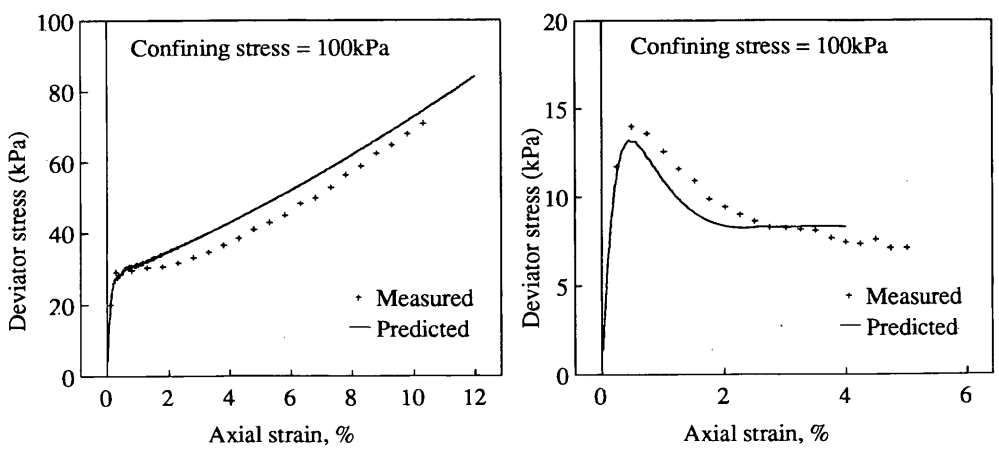


a) Triaxial Compression b) Triaxial Extension

**FIGURE 9 Comparison of oil sand undrained response.**

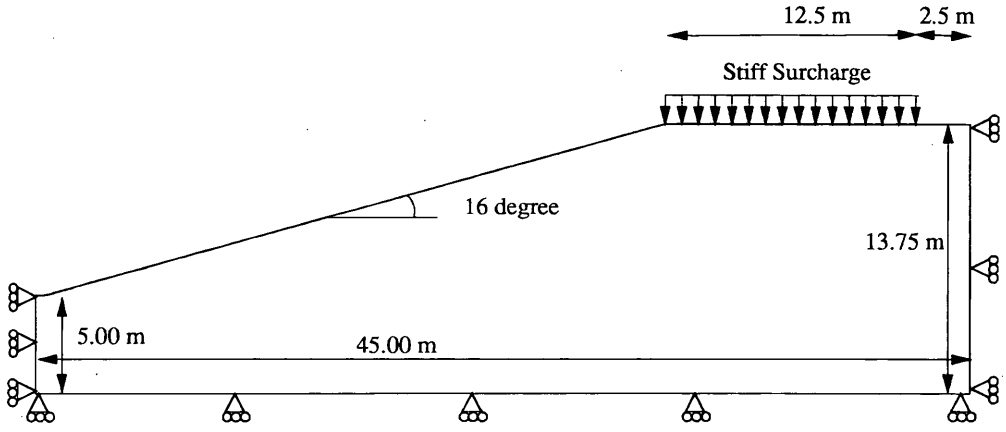


**FIGURE 10 Slope geometry and boundary conditions simulated in numerical model.**

extension response [Figure 9(*b*)] is strain-softening. This stress path dependency or anisotropy is captured in the modeling procedure by making the plastic shear modulus a function of the direction of the major principal compressive stress, $\sigma'_1$. The model parameters were selected to provide the best fit to the observed data. The elastic parameters used were stated previously.

The plastic parameters used to capture the undrained extension ($\sigma'_1$ horizontal) behavior were $K_{gp} = 100$, $np = 0.5$, $R_f = 0.95$, $\epsilon = 30$ degrees, $\varphi_{cv} = 30$ degrees. The stiffer response in vertical compression ($\sigma'_1$ vertical) was captured using a stiffer $K_{gp} = 300$ and $\varphi = 31$ degrees. Because $\varphi > \varphi_{cv}$, this will cause dilation and strain hardening at large strains.

In the centrifuge analysis, the stress path followed will range from vertical compression beneath the applied load to vertical extension (horizontal compression) in the toe area. To allow for this stress rotation, it was assumed that $K_{gp} = 100$ and $\varphi = 30$ degrees for $0 < \alpha < 45$ degrees, $K_{gp} = 100\,(1 - 2\cos 2\alpha)$ and $\varphi = (30 - \cos 2\alpha)$ degrees for $45 < \alpha < 90$ degrees, where $\alpha$ is the angle between the direction of major principal stress and the horizontal axis. Thus for $0 < \alpha < 45$ degrees representing horizontal compression through simple shear conditions $K_{gp}$ and $\varphi$ are constant. For $45 < \alpha < 90$ degrees representing simple shear to vertical compression there is a continuous increase in $K_{gp}$ and $\epsilon$ from 100 to 400 and 30 to 31 degrees, respectively. The numerical model is used in the following section with these calibrated parameters to predict the response of the centrifuge model test.

### Numerical Simulation of Centrifuge Test

The scaled model or prototype having the dimensions shown in Figure 10 was used for analysis purposes. The discretized grid or element mesh is shown in Figure 11. The effective stresses in the model before the application of the loads were computed using a submerged unit weight of 9.0 kN/m$^3$ and a drained analysis.

The responses to Loading Sequences A and B were obtained by applying pressures of 43 and 87 kPa, respectively, at the surface. The inertia effect of dropping the weight was not completely simulated. However, because FLAC uses a dynamic solution technique, inertia effects corresponding to the sudden application of load under zero drop are simulated.

The predicted and observed excess pore pressures at PPT 1 and 2 for the two loading sequences are compared in Table 2. The predicted pore pressures at PPT 1 are in reasonable agreement with those observed for both load cases. The predicted pore pressures at PPT 2 are lower than those observed. This may be because of the impact loading, which was not completely simulated in the analysis. Contours of excess pore pressure are shown in Figure 12.

The predicted deformations for Loading Sequence A were small and are not shown. The predicted displacements for Loading Sequence B (Figure 13) show a deep-seated pattern of movements, which is in general agreement with the observed pattern. The predicted movements are slightly smaller than those observed, which may be because of the effect of impact loading, which was not completely simulated in the analysis.

## CONCLUSIONS

In Stage 1 of the CANLEX centrifuge testing, conducted on the C-CORE centrifuge, it was determined that a static liquefaction

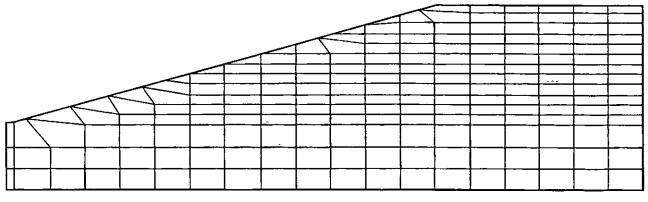

**FIGURE 11 Finite difference mesh.**

**TABLE 2 Comparison of Excess Pore Pressures after Surcharging**

| | Load case A | | Load case B | |
|---|---|---|---|---|
| (kPa) | Measured | Predicted | Measured | Predicted |
| PPT1 | 38 | 36 | 68 | 70 |
| PPT2 | 32 | 14 | 42 | 28 |

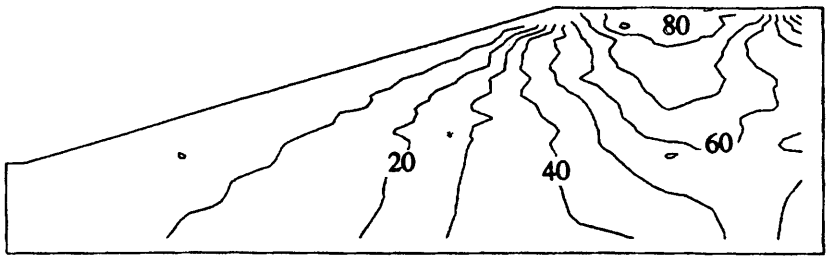


Contours at 10 kpa intervals from 0 to 90 kPa.
Contour for 0 kPa is on left hand side.

**FIGURE 12 Contours of excess pore pressure, load case B.**

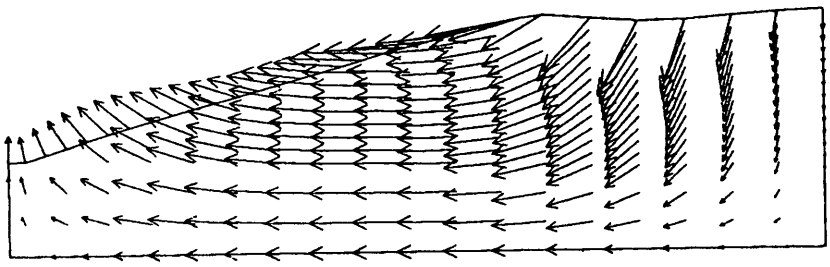

Displacement vector magnification factor: 4.6.

**FIGURE 13 Displacement vectors, load case B.**

event could be induced in a centrifuge test. The centrifuge test involved construction of a 16 degrees submerged slope of oil sand tailings at a relative density of about 30 percent. During the centrifuge test, the prototype slope height was equivalent to 8.8 m. A steel surcharge dropped on the slope crest caused the slope to liquefy and flow to an angle of 7 degrees. Stage 2 of the centrifuge testing will simulate more closely the proposed field event, for which a number of triggering mechanisms are under consideration.

The numerical model presented enables us to capture static liquefaction behavior in loose sand. The numerical modeling was based on the initial capturing of the observed element behavior in both triaxial compression and extension. This behavior was used to predict the centrifuge tests. The predicted pore pressures at PPT 1 under the load were in good agreement with those measured, whereas the prediction of PPT 2 was too low. The pattern and magnitude of predicted displacements were in general agreement with those observed. The larger pore pressures measured may have been because of the impact loading, which was not simulated in the numerical analysis.

## ACKNOWLEDGMENTS

The authors acknowledge the support provided through the CANLEX project from a NSERC Collaborative Research and Development Grant. C-CORE's provision of centrifuge facilities and technical assistance is also acknowledged. The authors are grateful to Yi Ning Zeng of the University of British Columbia for her assistance with the numerical analysis.

## REFERENCES

1. CANLEX. *CANLEX Newsletter*, Vol. 1, No. 1, June 1993.
2. CANLEX. *CANLEX Newsletter*, Vol. 2, No. 1, June 1994.
3. Arulanandan, K., and R. F. Scott. *Verification of Numerical Procedures for the Analysis of Soil Liquefaction Problems, Vol. 2*. A. A. Balkema, Rotterdam, The Netherlands, 1994.
4. Phillips, R., and P. M. Byrne. Modelling Slope Liquefaction Due to Static Loading. Preprints of 47th Canadian Geotechnical Conference, Halifax, Nova Scotia, Canada, September 1994.
5. Schofield, A. N. Cambridge Geotechnical Centrifuge Operations. Twentieth Rankine Lecture. *Geotechnique*, Vol. 30, No. 3, 1980, pp. 227–268.
6. Leung, C. F., F. H. Lee, and T. S. Tan. Centrifuge 94. *Proc., International Conference on Geotechnical Centrifuge Modelling*, Singapore, A.A. Balkema, Rotterdam, The Netherlands, September 1994.
7. Phillips, R., J. I. Clark, M. J. Paulin, R. Meaney, D. E. L. Millan, and K. Tuff. Canadian National Centrifuge Centre with Cold Regions Capabilities. *Proc., International Conference on Geotechnical Centrifuge Modelling*, Singapore, A.A. Balkema, Rotterdam, The Netherlands, September 1994.
8. Lambe, P. C., and R. V. Whitman. Scaling for Earthquake Shaking Tests on a Centrifuge. *Proc., Soil Dynamics and Earthquake Engineering Conference*, Southampton, U.K., Vol. 1, 1982, pp. 367–378.
9. Hardin, B. O. Stress-Strain Behaviour. Earthquake Engineering and Soil Dynamics. *Proc., ASCE Geotechnical Engineering Division Special Conference*, Pasadena, Calif., 1978.
10. Duncan, J. M., and C. Y. Chang. Non-linear Analysis of Stress and Strain in Soils. *Journal of Soil Mechanics and Foundations Division, Proc.*, ASCE, Vol. 96, 1970, pp. 1629–1653.

11. Taylor, D. W. *Fundamentals of Soil Mechanics*. John Wiley & Sons, New York, 1948.
12. Schofield, A. N, and C. P. Wroth. *Critical State Soil Mechanics*. McGraw-Hill, London, 1968.
13. Matsuoka, H., and T. Nakai. Stress-Strain Relationship of Soil Based on S.M.P. *Proc., 9th International Conference on Soil Mechanics and Foundation Engineering*, 1977, pp. 153–162.
14. Cundall, P. A. *FLAC User's Manual*. ITASCA Consulting Group, Inc. Minneapolis, Minn., 1993.

---

*Publication of this paper sponsored by Committee on Modelling Techniques in Geomechanics.*

# Modeling the Stability of Sand Foundations During Earthquakes

XIANGWU ZENG

Many of the damages caused to structures during earthquakes are due to the failure of sand foundations. Experience in past earthquakes showed that poorly designed sand foundations can cause large vertical settlement and tilting to buildings. However, research efforts are complicated by the lack of field data about the responses of foundations during earthquakes. Centrifuge modeling has the advantage of being able to replicate field events in a controllable environment. For earthquake centrifuge tests, the boundary effects imposed by a model container need to be addressed carefully. A group of dynamic centrifuge tests was conducted at Cambridge University to study the seismic stability of sand foundations. The tests were conducted in a specially designed model container that could simulate a soil layer of infinite lateral extent. A large data base was established, which can be used for the verification of design calculations and validation of numerical procedures. Failure mechanism similar to that which occurred in the field was observed in the tests. When sand in the foundation was saturated, the risk of failure was significantly increased. There was clear indication of deterioration of the stiffness of sand under cyclic loading and with pore pressure increase. Implications for design are discussed.

Failure of structures based on sand foundations, such as block buildings and bridge foundations, was widely observed during earthquakes. For instance, during the Niigata Earthquake in 1964, the Mexico City Earthquake in 1985, the Loma Prieta Earthquake in 1989, and the Northridge Earthquake in 1994, extensive damage to block buildings was reported. An example of the field failure observed during the Loma Prieta Earthquake is shown in Figure 1. Typical failure of such structures involved excessive settlement and tilting of the foundation.

The frequent occurrence of such failure and the severe damage it caused have provoked widespread research interests among geotechnical engineers, and different types of analyses have been suggested. For example, Seed and Idriss (*1*) conducted a comprehensive analysis of the failure of block buildings during the Niigata Earthquake. To verify the results of these analyses, it is necessary to compare them with the data recorded in the field. However, as an earthquake in the field is unpredictable, recording the response of earth structures and foundations during earthquakes is difficult, time-consuming, and expensive. What is available in most cases is the pre- and post-earthquake information. The most critical information for the analysis, the response of earth structures and foundations during earthquakes, is lacking. For instance, regarding the failure of block buildings in the field, the following critical questions need to be answered in order to improve the design in the future. What were the accelerations on the building? Did the displacement occur during the largest cycles of ground vibration or did it accumulate during the entire duration of the earthquake? What was the magnitude of excess pore pressure in the ground? Was acceleration amplified or attenuated in the foundation soils? Unfortunately, in most cases there are no field data to provide answers to these questions.

This problem has been realized by researchers in many countries and tremendous efforts have been made to instrument sites in the field. In recent years, there have been some cases of success in recording field data during earthquakes. One of the examples is the recording of acceleration and excess pore pressures at the Wildlife site during the Imperial Valley Earthquake, as described by Youd and Holzer (*2*). However, given the infrequent occurrence of earthquakes at a particular site, a number of instruments would have to be installed on a wide range of structures to have a fair probability of recording some data eventually. The considerable cost involved in the installation and maintenance of instruments means that this technique can only be used on limited and highly selective structures. This cannot satisfy the requirements for the development of earthquake-resistant design.

In earthquake-resistant design, it is very important to choose effective and economical engineering countermeasures if a structure is found to be inadequately designed. However, it is difficult and expensive to prove the effectiveness of an engineering countermeasure in the field, especially when there are a number of options available. Different types of designs using a variety of engineering countermeasures would have to be adopted so as to find the most desirable solution. This could be costly and perhaps even risky. It is even more undesirable that the proof would be available only after a major earthquake has occurred at the locations where the engineering countermeasures have been used.

One of the effective methods of analyzing earthquake problems in geotechnical engineering is numerical simulation. Over the past two decades, considerable progress has been made in modeling the behavior of soils under cyclic loading and numerical implementation. There are quite a few established numerical codes available that are specially designed for dynamic problems. Numerical simulation has the advantage of being able to operate easily and identify the influence of individual parameters. The application of numerical simulation has been greatly expanded in recent years with the introduction of fast personal computers. However, it is well understood that the behavior of soils under cyclic loading is very complicated. Therefore, numerical simulation needs to be ver-

Department of Engineering, Cambridge University, United Kingdom. Current affiliation: Department of Civil Engineering, University of Kentucky, Lexington, Ky. 40506-0281.

**FIGURE 1 Failure of block building during Loma Prieta Earthquake.**

ified against experimental results before it can be applied in the field.

## ROLE OF CENTRIFUGE MODELING

In the absence of field data, physical modeling techniques have an important role to play in geotechnical earthquake engineering. Physical modeling techniques have been used in the research of geotechnical earthquake engineering since the beginning of this century. Because a model test can be conducted in a controllable environment and transducers can be used at different locations to record the required data, physical modeling provides an effective way to generate experimental results. Data from such tests can be used to verify numerical codes, to improve design procedures, and to help the design in the field.

There are two types of physical modeling techniques widely used in geotechnical earthquake engineering: shaking table tests at normal gravity and shaking table tests mounted on a centrifuge. Shaking table tests conducted at normal gravity ($1g$ tests) have the advantage of being able to make detailed models at a relatively low cost. However, in a $1g$ test the stresses arising from the weight of the soil are much less than those in the field. It is well known that the behavior of soil is stress- and strain-dependent. Certain aspects of soil behavior, such as crushing of soil particles and dilatancy, are highly stress-dependent. Therefore the behavior of soil in a $1g$ test may be quite different from that in the field under high stresses. Although this does not invalidate the $1g$ test, interpretation of the data is difficult, especially if the strain in soil is high.

This difficulty can be avoided by using centrifuge modeling. In a centrifuge test the dimensions of earth structures are reduced while the body force is increased by the ratio of centrifugal acceleration over gravitational acceleration, resulting in the same stress and strain in the model as in the prototype. The principles of centrifuge modeling are well understood now, as demonstrated by Schofield (*3*). It has become a popular research tool in geotechnical engineering (see Corte [*4*] and Ko and McLean [*5*]). Since the early 1980s, a number of centrifuge centers have acquired the capability of earthquake centrifuge modeling, as discussed by Steedman (*6*). With the help of advanced data-acquisition systems and miniature transducers, centrifuge model tests can make valuable contributions by permitting general observations concerning the behavior of soil masses during simulated ground shaking and by providing experimental data against which theoretical analysis can be checked.

In recent years, several research groups have conducted centrifuge simulation on the behavior of shallow foundations during earthquakes. Liu and Dobry (*7*) conducted centrifuge tests on circular shallow foundations based on saturated sand foundations. It was reported that redistribution of excess pore pressure after base shaking played an important role in the displacement of the foundation. Krstelj and Prevost (*8*) carried out centrifuge tests on a square footing based on a saturated sand layer, overlaid by a thin layer of saturated silt. The data were used to verify numerical predictions.

Reported here are some results of centrifuge tests conducted at the Cambridge Geotechnical Centrifuge Center. The operation of the beam centrifuge was described by Schofield (*3*). A series of dynamic centrifuge tests was conducted on block buildings based on sand foundations. All the data in this paper are presented in prototype scale. The soil used in the model tests was Hostun RF sand, a field sand from France. The particle size of this sand ranges between 0.1 and 1 mm, and the average particle size is 0.4 mm. The specific gravity of the sand is 2.677, and the maximum and minimum void ratios are 0.976 and 0.607, respectively. All of the tests were conducted at a centrifugal acceleration of $50g$. The details of the tests and all of the data were reported by Zeng (*9*).

## REDUCING BOUNDARY EFFECTS IN EARTHQUAKE TESTS

Although earthquake centrifuge modeling is very useful, it is difficult to model field conditions properly in an earthquake centrifuge test. As a centrifuge model is much smaller than the corresponding prototype structure, the scaling factor may be influential in some tests. For instance, the number of soil particles in contact with a footing would be much lower for the model test than for the corresponding prototype if the same soil is used. While it is possible to change the particle size of soil in the model test to reduce this influence, doing so would create other problems, because some properties of a soil depend on its particle size. A common problem in earthquake tests is to satisfy the scaling relationship for time. While for a dynamic event the model time is reduced by $N$, the scaling factor of time for consolidation is $N^2$. This conflict between scaling factors can be solved by increasing the viscosity of the pore fluid.

The unique problem in earthquake centrifuge modeling is how to reduce boundary effects. In the field most geotechnical problems are associated with a soil stratum of large lateral extent, which can be idealized as being of infinite lateral extent. Under base shaking, cyclic shear stresses are imposed on soil elements that are in equilibrium under static loading. A typical loading condition on a section of such a soil stratum is shown in Figure 2*a*. The base shaking would induce shear stresses on both vertical and horizontal planes. The inertial force on soil mass would induce a rocking moment on

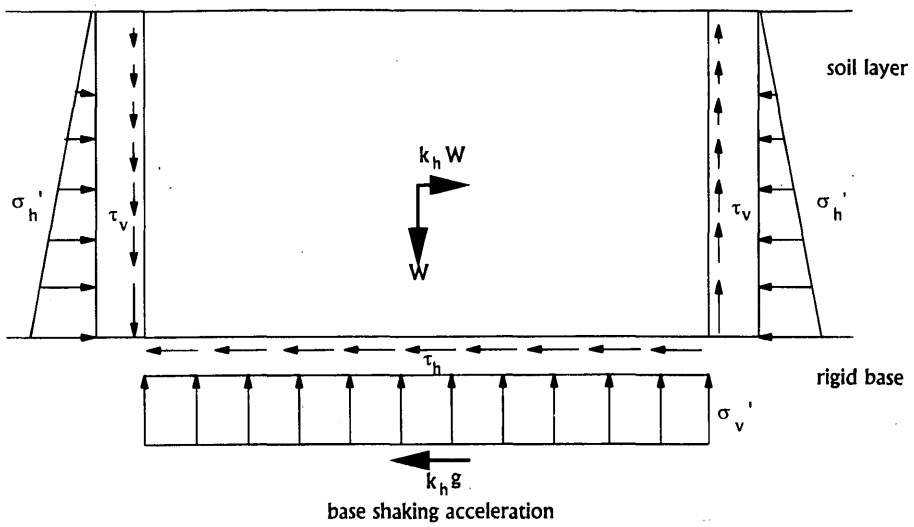


**FIGURE 2*a*** **Distortion in stress field due to smooth end walls: distribution of stresses in a soil layer of infinite lateral extent.**

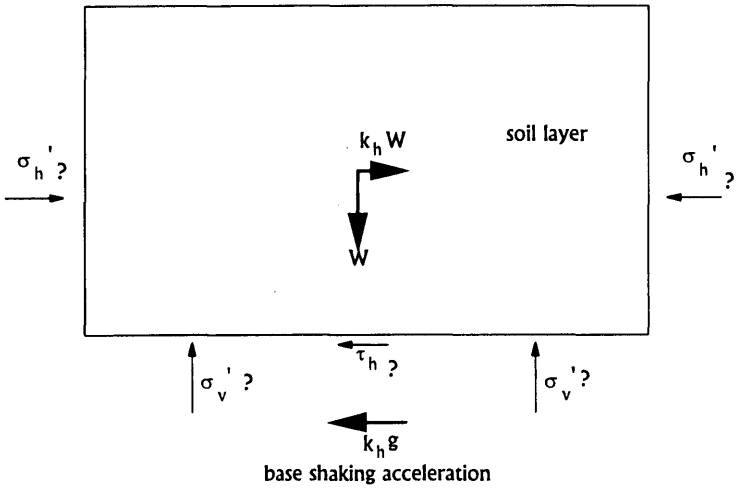


**FIGURE 2*b*** **Distortion in stress field due to smooth end walls: distribution of stresses in model with smooth rigid end walls.**

the mass, which would be balanced by the moment of complementary shear stresses on the two vertical planes. However, in a centrifuge test a model is constructed in a model container, and thus artificial boundaries are imposed. If the model container is not properly designed, severe boundary effects may be induced, which can lead to differences in stress and strain distributions between the model and the field conditions. These boundary effects are discussed in detail by Schofield and Zeng (*10*). For instance, if the model container has smooth and rigid end walls, complementary shear stresses cannot be sustained on the vertical end walls. The rock moment induced by the inertial force has to be balanced by the redistribution of stresses on the boundaries, as shown in Figure 2*b*. This complicates the analysis of soil behavior in the model container. Although this effect does not invalidate the results of dynamic centrifuge tests conducted in a rigid model container, the data must be interpreted carefully, especially if the model container is small. For a relatively long model container, it may be suggested that in the central region of the container the influence of boundary effect is small. However, it is difficult to determine the extent to which the boundary effects will affect the data.

To reduce the boundary effects, an equivalent-shear-beam (ESB) model container was designed and tested at the Cambridge Geotechnical Centrifuge Center. The design criteria and the performance of the model container were described by Schofield and Zeng (*10*). A three-dimensional view of the model container is shown in Figure 3. The model container is made of rectangular frames of dural spaced by rubber layers. Under base shaking, the model container moves together with the soil contained, and was designed to have the same lateral deflection and natural frequency

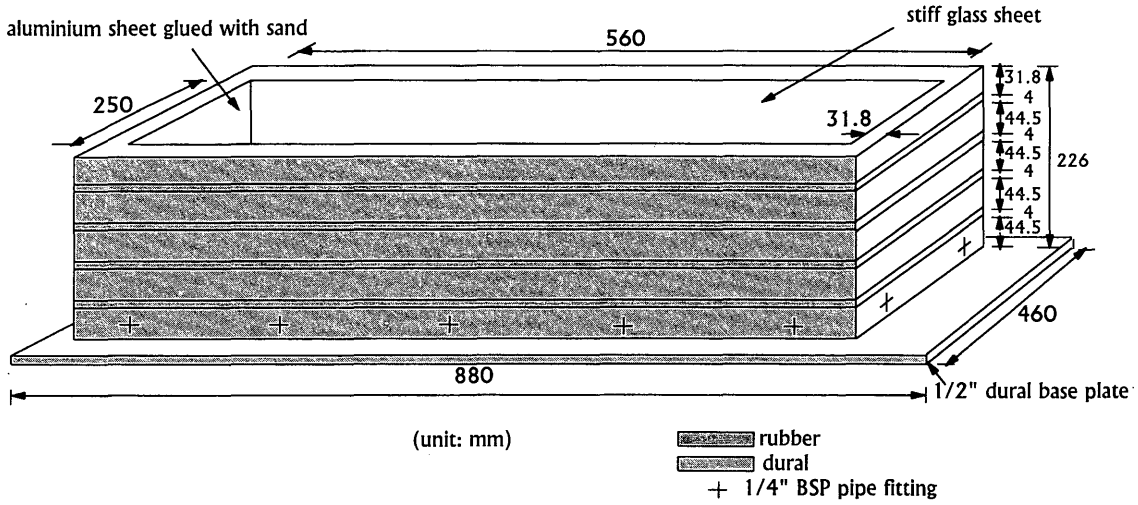


**FIGURE 3 A three-dimensional view of the ESB container.**

as the soil contained. To sustain complementary shear stresses induced by base shaking, a flexible and inextensible frictional sheet was attached at each end wall and the base of the box was glued with local sand.

A group of centrifuge tests was conducted to study the performance of the ESB container under earthquake loading. One of the centrifuge models is shown in Figure 4. It is a dry sand bed 10 m thick. Two layers of accelerometers were placed across the sand bed and on the model container to check whether a uniform acceleration field is achieved in the model. If the boundary effects are small, accelerations at the same height in the model should be identical. The recording of the accelerometers during one model earthquake is shown in Figure 5. It is clear that accelerations recorded in the sand and on the model container at the same height were almost identical, proving that the design criteria were met. There were other measurements that showed that the performance of the ESB container was satisfactory, as described by Schofield and Zeng (*10*).

## BLOCK BUILDING ON DRY FOUNDATION

Test SERC7 was conducted on a block building slightly embedded in a flat, dry sand bed. A cross-sectional view of the centrifuge model and the location of some of the transducers used are shown in Figure 6. The block building was 5 m high and 1.67 m wide, made of steel. The embedment of the building was 0.5 m. The sand in the model had a dry density of 15.01 kN/m$^3$, which corresponded to a void ratio of 0.743, or a relative density of 63.1 percent. A sequence of earthquakes was applied to the model, with a gradual increase in intensity.

Data recorded by accelerometers during a large earthquake are shown in Figure 7. Accelerometer 1 (ACC1) was fixed at the base of the ESB model container and its recording can be regarded as the earthquake input. As shown in Figure 7, a typical earthquake contains a number of approximate sinusoidal vibrations. The peak horizontal acceleration for this earthquake was 0.31$g$. It is clear that the vibration in the soil was slightly amplified as the shear wave prop-

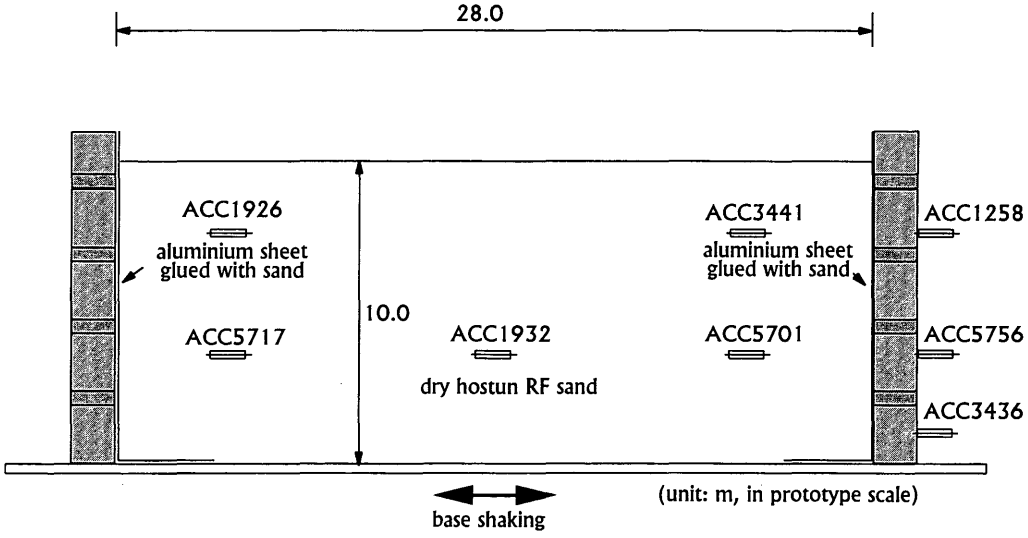


**FIGURE 4 Cross-sectional view of centrifuge model, test SERC8.**

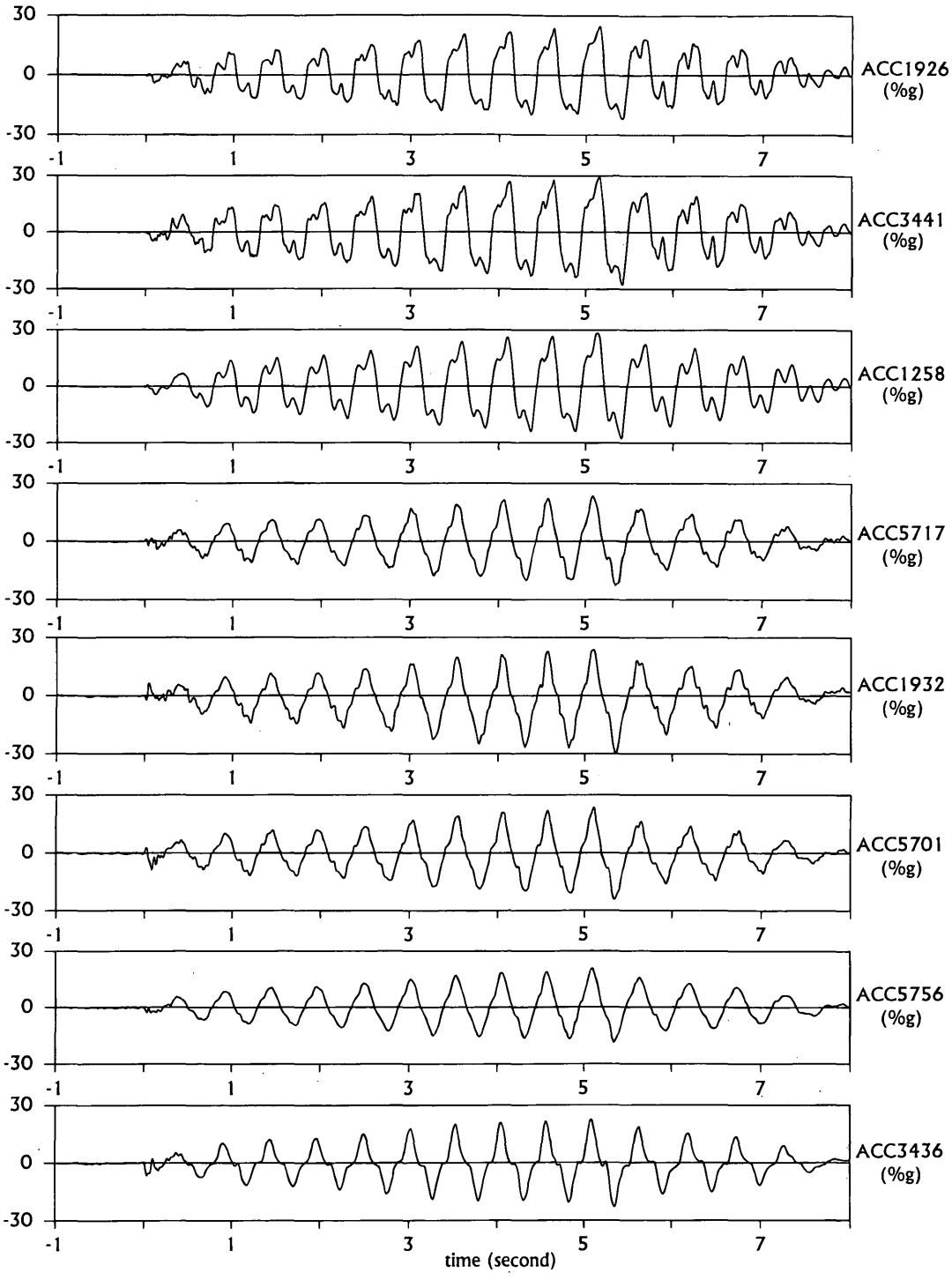


**FIGURE 5** Accelerations at two specific heights across the model during EQ2, test SERC8.

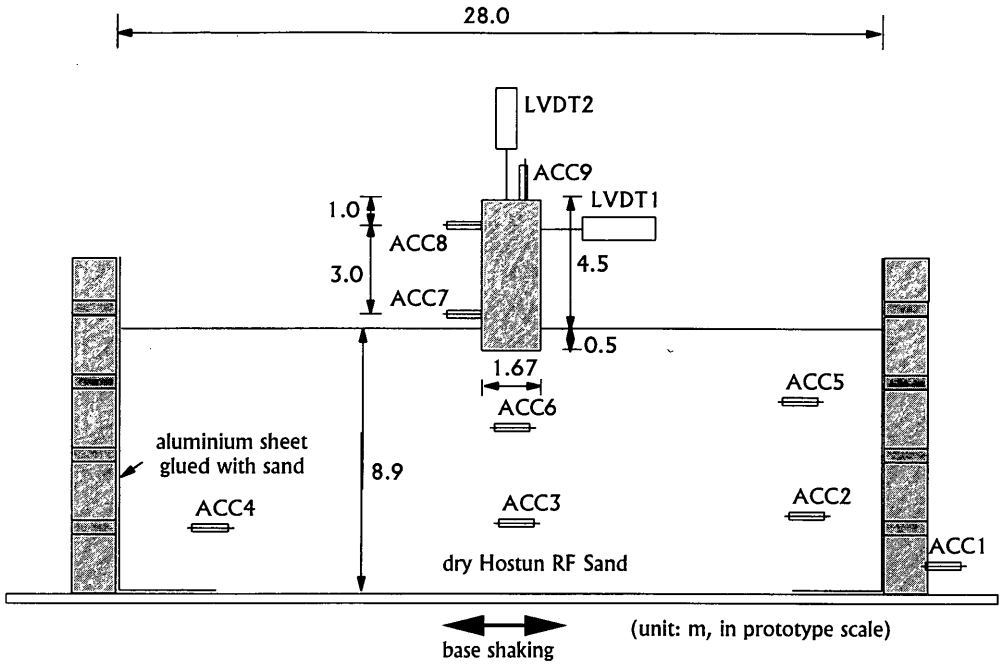


**FIGURE 6 Cross-sectional view of centrifuge model, test SERC7.**

agated upward. The peak acceleration recorded near the surface was significantly higher than the input motion.

Accelerometers 2, 3, and 4 were in the sand at the same height across the model container. The recordings of ACC2 and ACC4 were almost identical in both amplitude and phase, proving again that the performance of the ESB model container was satisfactory. However, the recording of ACC3 was quite different, showing the strong influence of the vibration of the building. It indicated that the large strain in the soil due to the vibration of the building was limited to the area close to the building. ACC6 was buried in sand underneath the block building. Its recording showed an amplification of nearly 100 percent. Both time history and amplitude were quite different from those recorded in the free field by ACC5.

Both accelerometers and linear variable differential transformers (LVDTs) were fixed on the block building to measure the response of the building. The recording of the transducers during the earthquake is shown in Figure 8. ACC7 was near the base of the structure, hence it predominantly recorded horizontal vibration of the building. As shown in Figure 8, the amplitude of the horizontal vibration was close to that of the base shaking. There was no phase shift indicating that the natural frequency of vibration in the horizontal direction was high. ACC9 was fixed in the vertical direction. Its recording showed that the amplitude of vertical vibration was small. ACC8 was placed near the top of the building, hence its recording included both lateral vibration and rocking motion of the building. ACC8's recording showed that it lagged behind ACC2 by nearly 180 degrees and the amplitude was lower than that of input motion. That was due to the fact that the natural frequency for rocking was lower than the dominant frequency of base shaking.

Two LVDTs were attached to the building to record displacement in the vertical and horizontal directions. As shown in Figure 8, both recorded large displacements during the earthquake. However, the time history showed quite different patterns. The vertical settlement of the building started during the high amplitude cycles and increased continually till the end of the earthquake. On the other hand, the lateral displacement of the building cyclically accumulated during the whole period of base shaking, and the direction of inclination was determined during the first cycle. After the test, measurement of the profile of the model showed that the building model suffered a foundation failure, Figure 9. The total settlement was about 0.3 m and the tilting angle was 6.3 degrees. On the opposite side of the tilting there was a clear heave on the ground. All these data indicate a bearing capacity failure. In the free field away from the structure, there was hardly any ground settlement.

## BLOCK BUILDING ON SATURATED FOUNDATION

The centrifuge model for test SERC6 was almost identical to that in test SERC7, except that the sand foundation was saturated with deaired water. A cross-sectional view of the centrifuge model and the locations of some transducers used are shown in Figure 10. The sand in the foundation had a void ratio of 0.774, or a relative density of 55 percent. The model was saturated using a vacuum system. When the model preparation was finished, the lid of the model container was put on and the model container was sealed. A vacuum was applied to the model. After the vacuum had been stabilized, deaired water was slowly introduced into the sand. The whole process

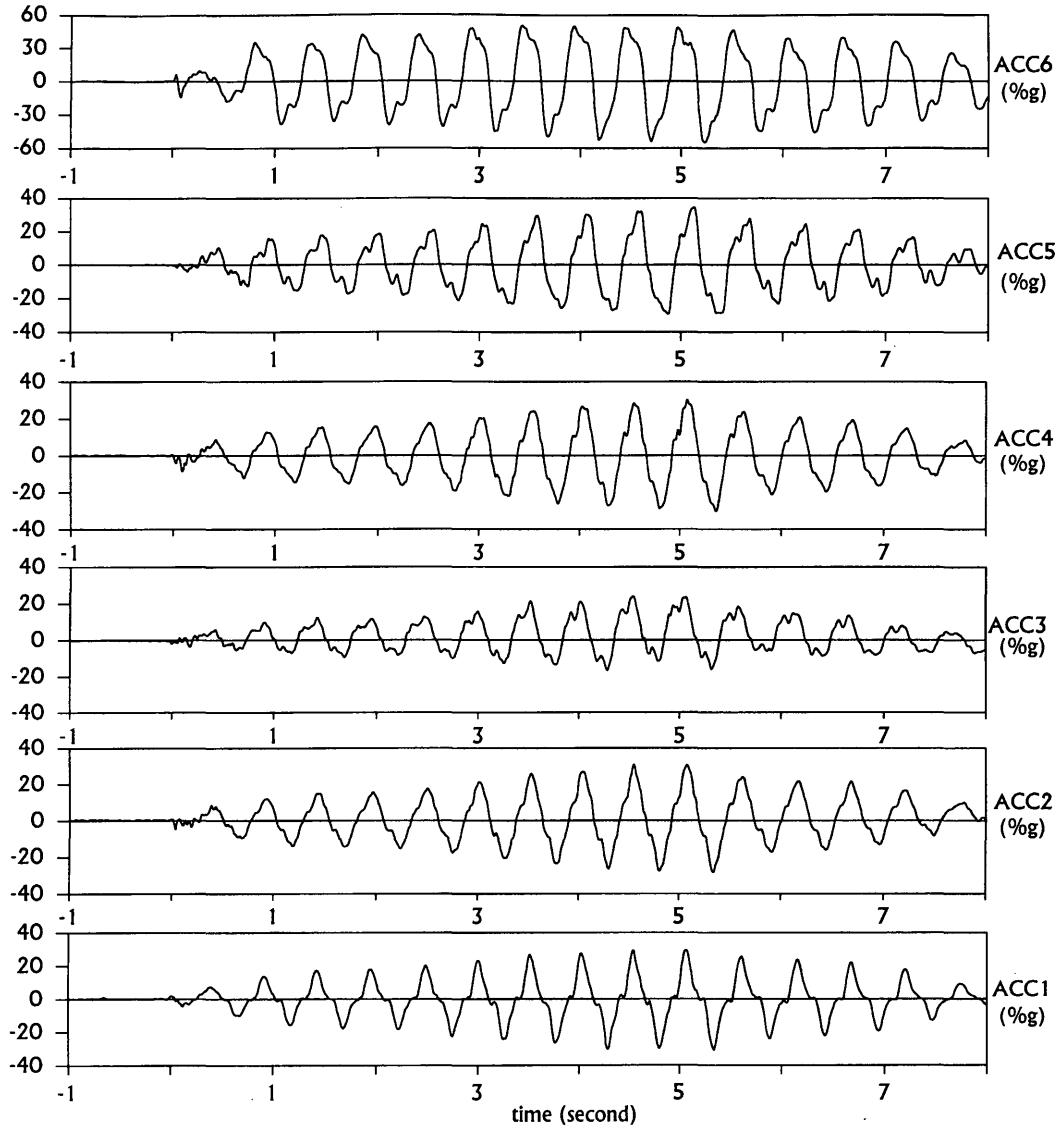


**FIGURE 7 Recording of accelerometers during an earthquake, test SERC7.**

of saturation took about 12 hours. Because water was used as pore fluid, the permeability of the sand was greatly increased. Therefore, excess pore pressure generated during earthquakes would dissipate fast and the accumulated excess pore pressure was expected to be low.

In this test a number of pore pressure transducers were used to monitor the excess pore pressure in the foundation. The recording of the transducers during a large earthquake is shown in Figure 11. All the transducers recorded cyclic variation of excess pore pressure but no accumulation of excess pore pressure. Pore Pressure Transducers 4 and 5 were in the sand near the two corners of the block building. Their recordings were out of phase with each other. This was due to the rocking motion of the structure, which caused sand on one side to contract while sand on the other side was expanding.

Accelerations recorded in the sand foundation are shown in Figure 12. The results were quite similar to those recorded in the dry test. ACC5, which was right underneath the block building, recorded amplification of vibration. Across the model at the same height, Accelerometers 2 and 4 recorded quite similar results, indicating that desirable boundary conditions were achieved.

The response of the model building to the base shaking is shown in Figure 13. The recordings of the three accelerometers on the building were similar to those during the dry test. A phase shift gradually built up between the lateral vibration of the building (recorded by ACC6) and the input motion, suggesting that the lateral stiffness of the foundation deteriorated under earthquake loading. The two LVDTs recorded large displacements of the structure. After the test the measurement of the profile showed a clear failure mechanism (Figure 14). The building settled 0.5 m and tilted 12

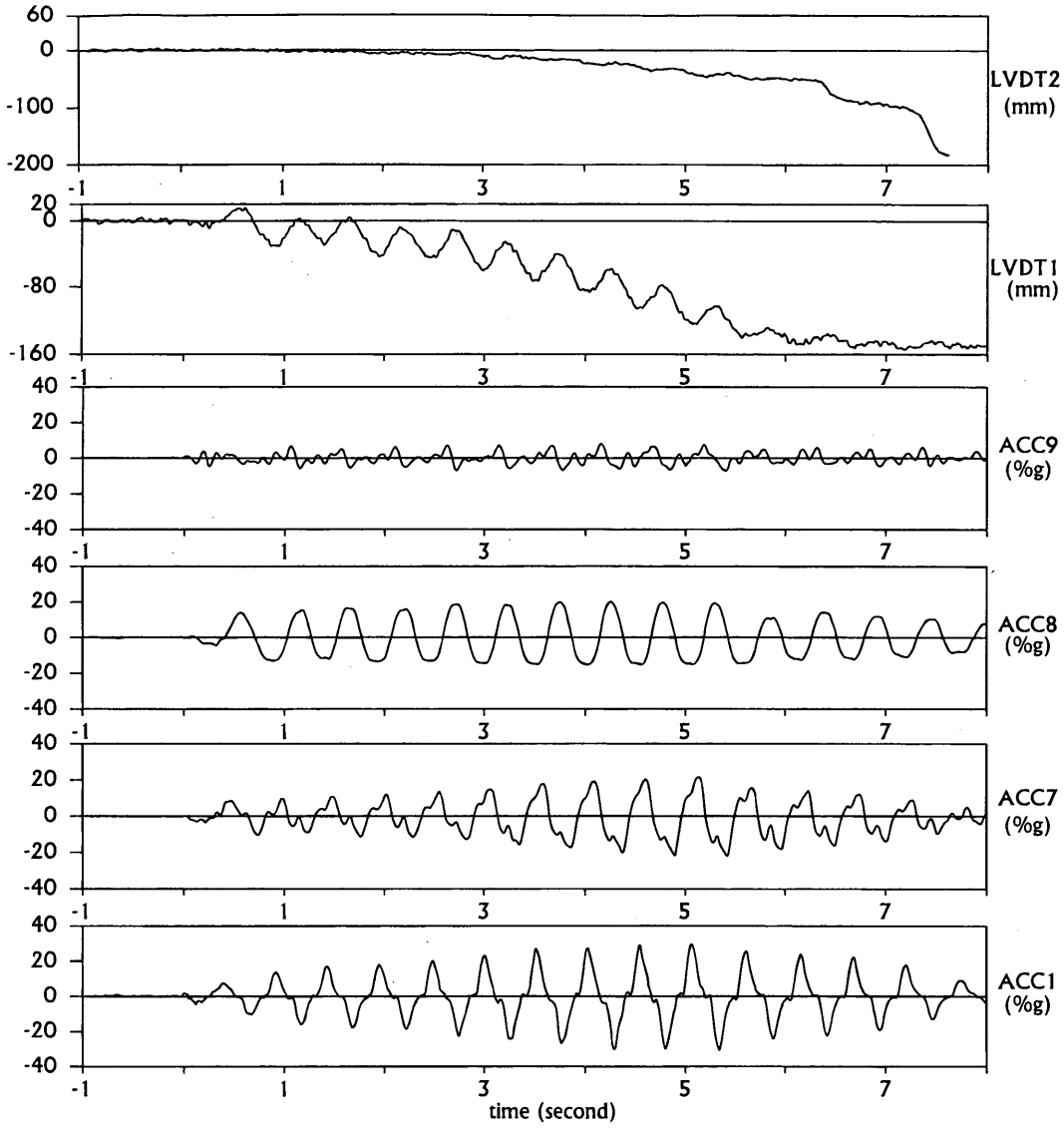


**FIGURE 8** Response of the block building during an earthquake, test SERC7.

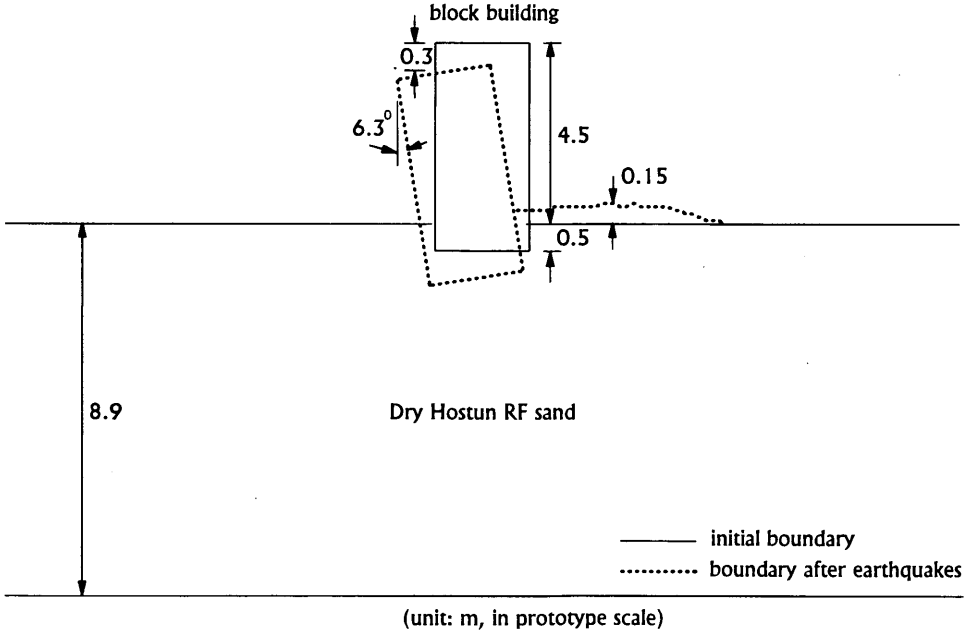


**FIGURE 9** Failure of the block building after earthquakes, test SERC7.

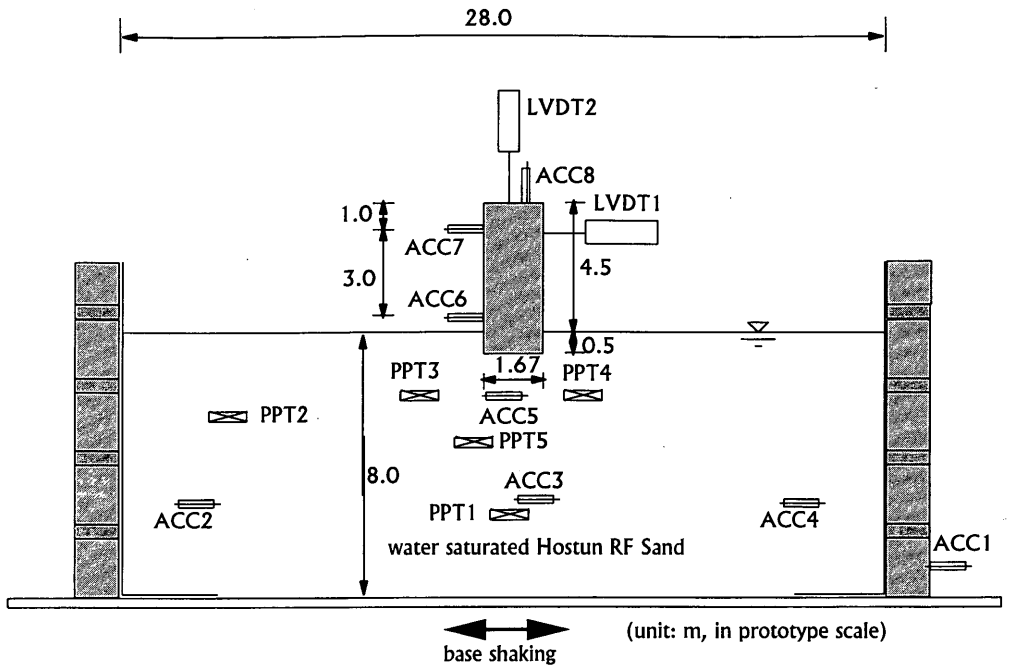


**FIGURE 10** Cross-sectional view of centrifuge model, test SERC6.

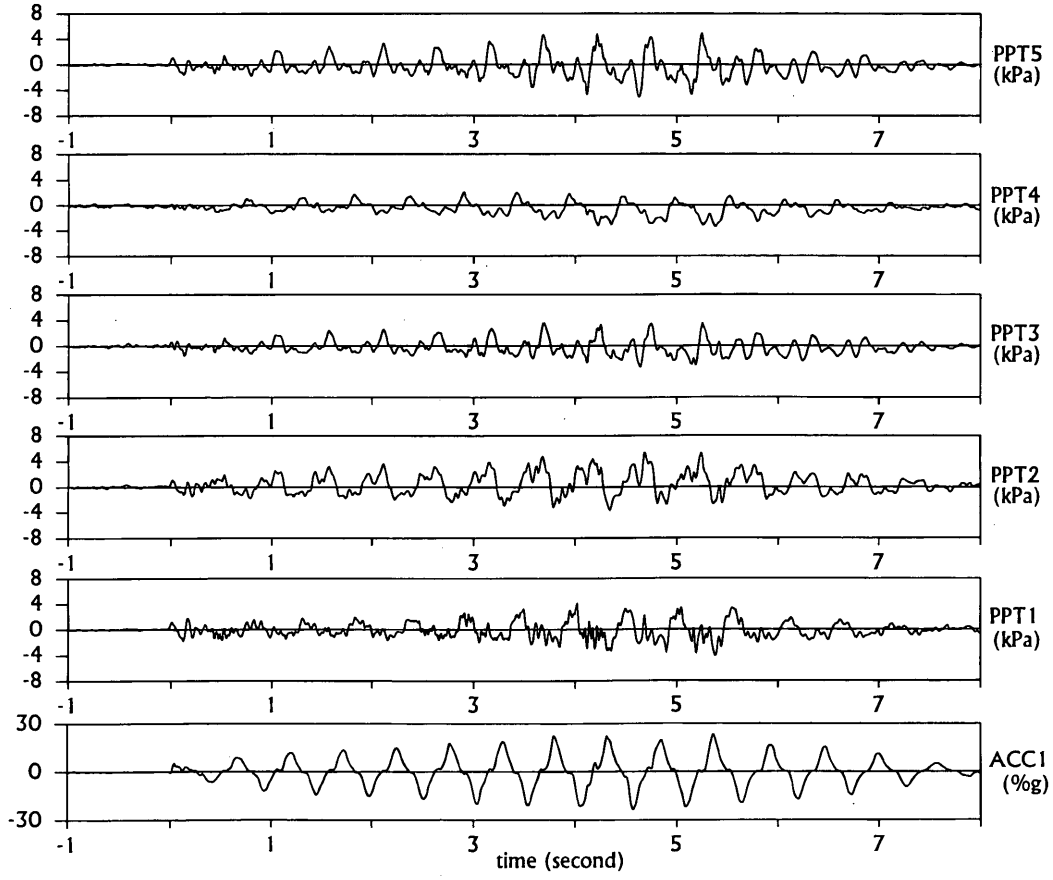


**FIGURE 11** Recording of pressure transducers during an earthquake, test SERC6.

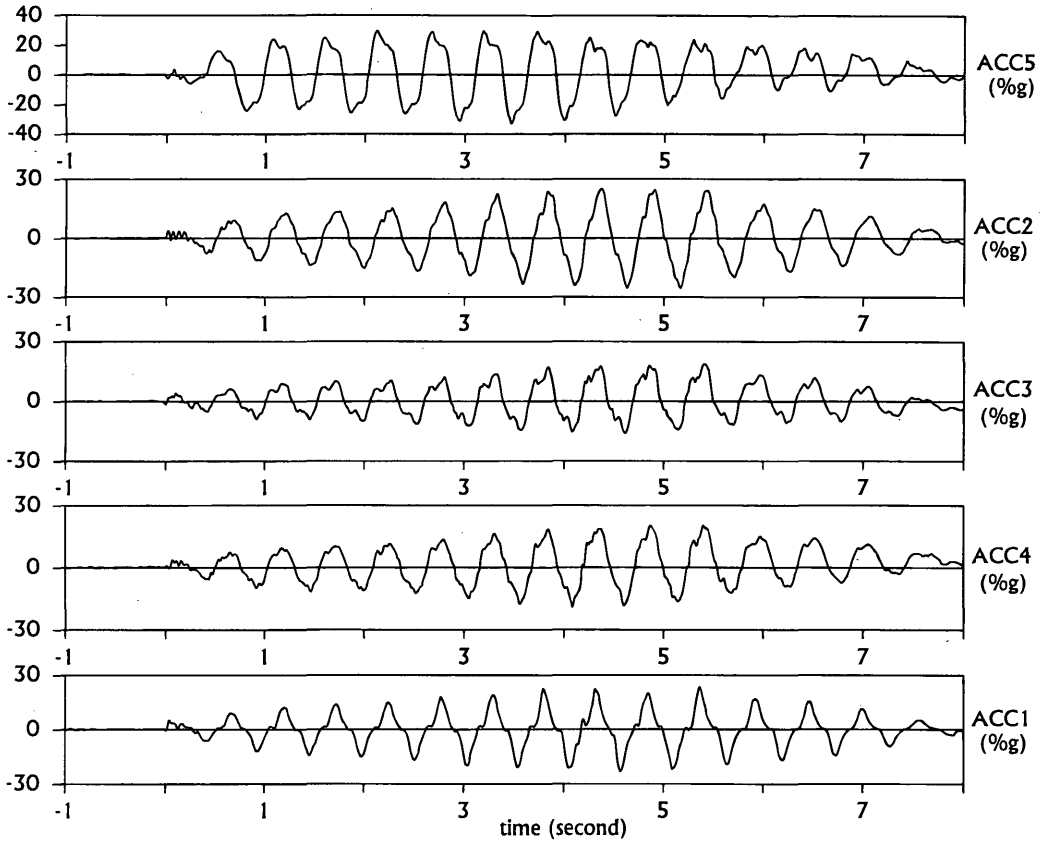


**FIGURE 12 Recording of accelerometers during an earthquake, test SERC6.**

degrees. On the side opposite of the tilting there was a clear ground heave. The ground away from the building suffered an average settlement of 0.15 m. The failure mechanism was similar to that observed in the field.

Compared with the test on dry foundation, although the amplitude of base shaking was much lower (0.24$g$ versus 0.31$g$), the displacement of the structure was significantly larger. Thus the effect of earthquakes on saturated foundations was much more severe than on dry foundations, even without significant accumulation of excess pore pressure. The decrease in effective stress due to both static and dynamic pore pressures reduces the strength and stiffness of the foundation. Moreover, the bearing capacity of the foundation is significantly reduced, which can lead to catastrophic failure.

Therefore, in the design of foundations in the field, special consideration is necessary if the foundation is saturated. Even if the top layer of the foundation is dry, migration of water due to excess pore pressure at lower depths can have a similar effect. To reduce such risks, the foundation can be compacted or installed with a drainage system.

## CONCLUSIONS

From the results of this study, the following conclusions can be drawn:

1. Centrifuge tests can generate useful physical data about seismic response of earth structures. These data can help engineers to understand the mechanism of seismic soil-structure interaction and to evaluate the risk of existing structures. In areas related to transportation engineering, centrifuge tests can be used effectively to study complicated problems such as the design of retaining walls and bridge abutments.
2. It is important to ensure that boundary conditions in earthquake centrifuge tests properly replicate the field situation. The concept and the application of the ESB model container proved able to achieve desirable boundary conditions for the type of tests described herein. This model containment can be used for centrifuge tests on models of other structures such as bridge abutments.
3. Foundations of block buildings can suffer bearing capacity failure under earthquake loading, especially when the foundations are saturated.

## ACKNOWLEDGMENTS

The research work reported here was supported by grant GR/F/88858 of the Science and Engineering Research Council of the United Kingdom. Professor Schofield and Dr. Steedman provided valuable advice throughout the project. Technicians at the Cambridge Geotechnical Centrifuge Center helped in model preparation and centrifuge tests.

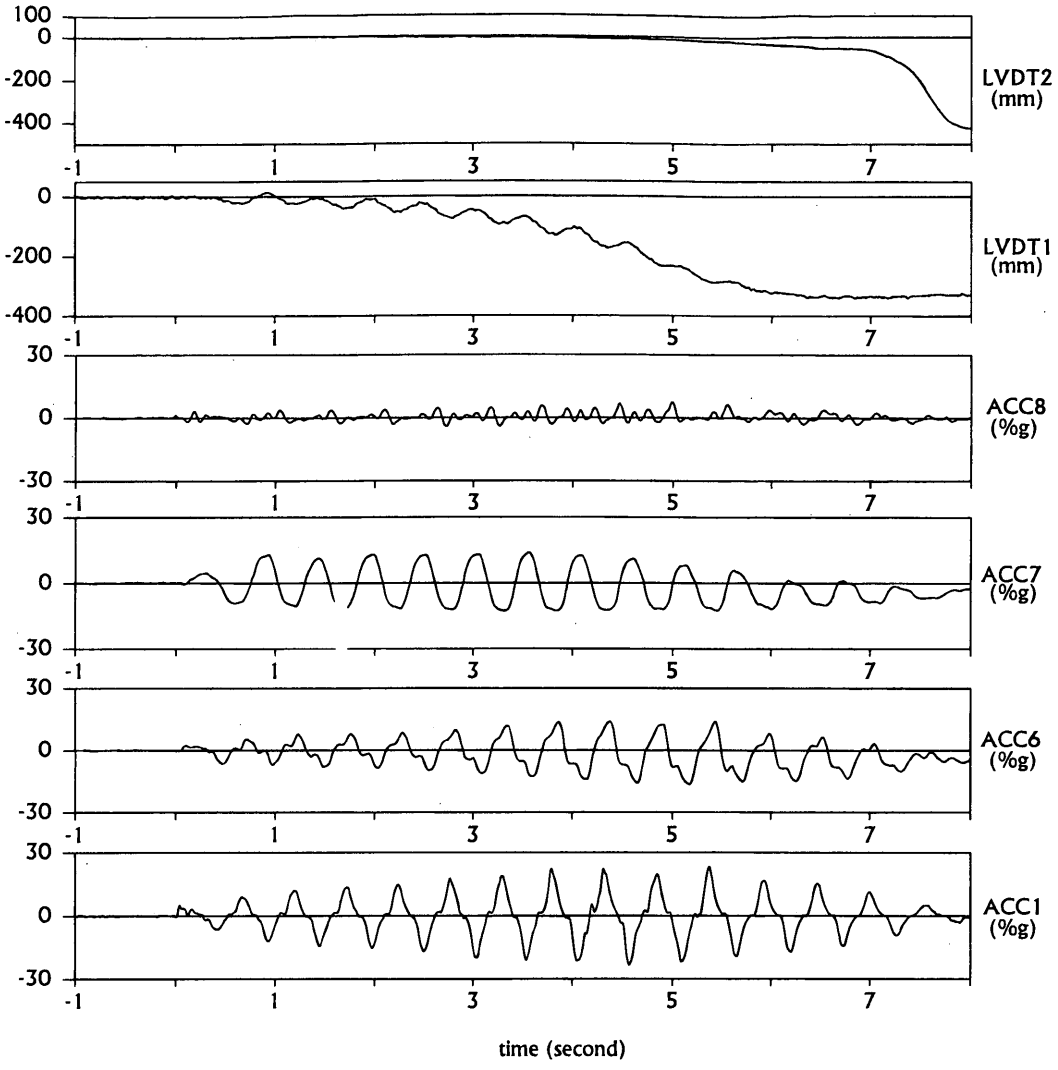


**FIGURE 13** Response of the block building during an earthquake, test SERC6.

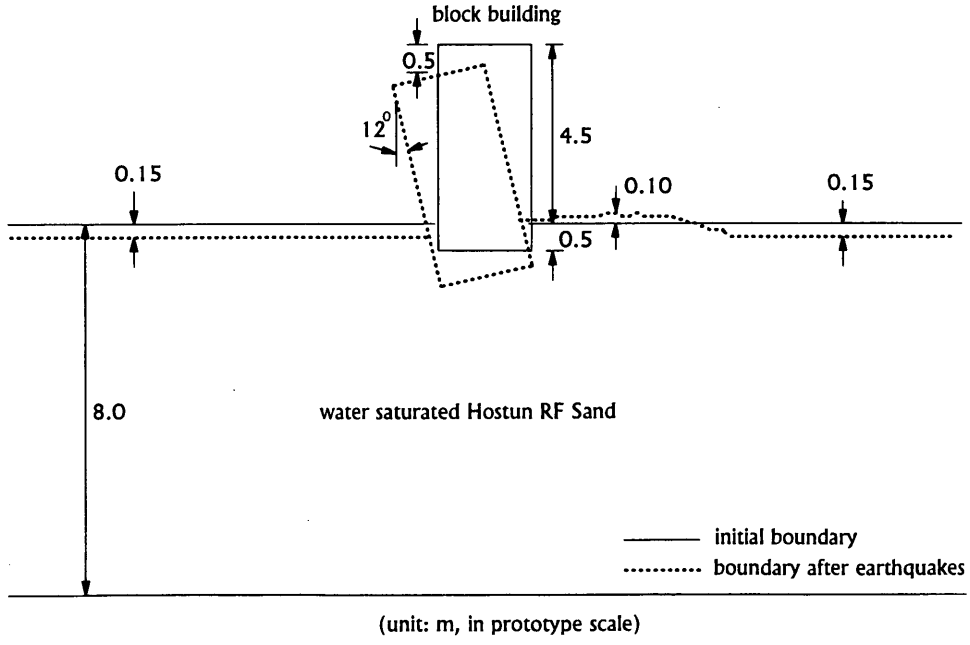


**FIGURE 14** Failure of the block building after earthquakes, test SERC6.

## REFERENCES


1. Seed, H. B. and I. M. Idriss. Analysis of Soil Liquefaction: Niigata Earthquake. *Journal of the Soil Mechanics and Foundation Division,* ASCE, SM6, June 1967, pp. 108–134.
2. Youd, T. L. and T. L. Holzer. Piezometer Performance at Wildlife Liquefaction Site. *Journal of Geotechnical Engineering,* ASCE, Vol. 120, No. 6, June 1994, pp. 975–995.
3. Schofield, A. N. Cambridge Geotechnical Centrifuge Operation. *Geotechnique,* Vol. 30, No. 3, June 1980, pp. 227–268.
4. Corte, J. F., ed. *Centrifuge 88,* Balkema, Rotterdam, 1988.
5. Ko, H.-Y. and F. G. McLean. *Centrifuge 91,* Balkema, Rotterdam, The Netherlands, 1991.
6. Steedman, R. S. Centrifuge Modeling for Dynamic Geotechnical Studies. *Proceedings of Second International Conference on Recent Advance in Geotechnical Earthquake Engineering and Soil Dynamics,* University of Missouri—Rolla, 1991.
7. Liu, L. and R. Dobry. Centrifuge Study of Shallow Foundations on Saturated Sand during Earthquakes. *Proceedings of the 4th U.S.-Japan Workshop on Soil Liquefaction Countermeasure Lifeline Facilities,* Honolulu, Hawaii, May 1992, pp. 493–508.
8. Krstelj, I. and J. H. Prevost. Experimental results of Model No. 12. *Proceedings of the International Conference on the Verification of Numerical Procedures for the Analysis of Soil Liquefaction Problems,* Vol. 1, Davis, Calif., October 1993, pp. 1007–1017.
9. Zeng, X. Modeling the Seismic Response of Block Buildings. *Technical Report 252.* Department of Engineering, Cambridge University, United Kingdom, 1992.
10. Schofield, A. N. and X. Zeng. Design and Performance of an Equivalent-Shear-Beam (ESB) Container for Earthquake Centrifuge Modeling. *Technical Report 245.* Department of Engineering, Cambridge University, United Kingdom, 1992.


*Publication of this paper sponsored by Committee on Modelling Techniques in Geomechanics.*

# Sheetpile Cell Filling: Finite Element Model Verification for Two Case Histories

K. J. WISSMANN, J. R. MARTIN II, AND G. M. FILZ

Cellular sheetpile structures are used as temporary cofferdams to keep construction activities dry and as permanent bulkheads. Successful design ensures that allowable sheetpile interlock tensions are not exceeded during cell filling operations. For two cellular cofferdam case histories, axisymmetric finite element analyses were performed to estimate main and arc cell fill pressures and arc cell tensions. Results of the analyses are compared with field strain gage data and conventional predictions of main and common wall interlock tensions.

Cellular sheetpile structures have been used both as temporary cofferdams to keep construction activities dry and as permanent bulkheads. Cells are composed of interlocking steel sheetpiles, which are commonly arranged in a circular configuration and usually filled with sand or gravel. Cellular structures are built by joining individual main cells with connecting arc cells to form a continuous retaining system. Successful design ensures that allowable sheetpile interlock tensions are not exceeded during cell filling operations and that the system is stable under applied external loads. Conventional methods for estimating sheetpile interlock tensions and stability under external loads are based largely on procedures developed by Terzaghi in the 1930s and 1940s (*1*). These methods generally do not consider soil-structure interaction effects and are thought to be conservative (*2*). The advent of the finite element technique and the instrumentation of constructed cells over the past 20 years have led to important new insights that can be used to develop improved design procedures for these structures.

This article describes the cell filling behavior of sheetpile structures constructed for the Lock and Dam 26 [Replacement (R)] and Trident Drydock case histories. For both projects, the results of axisymmetric finite element analyses are compared with project instrumentation data and predictions of interlock tensions from conventional methods.

This work is of particular significance because it introduces a new approach for predicting common wall behavior and confirms the importance of soil-structure interaction effects on cell filling behavior. Additionally, this work presents the first finite element analyses for the Trident Drydock cells known to the writers.

## BACKGROUND

Cellular structures are constructed by first driving a series of interlocking steel sheetpiles around a circular template to form individual cells. Sheetpile penetration depths generally range from no penetration for cells constructed on hard materials to significant penetration for cells constructed on relatively loose deposits. Cell construction is completed by initially filling each of the main cells, and then subsequently filling the adjacent connecting arc cells (Figure 1).

During main cell filling, main cell sheetpiles bulge radially outward in response to cell fill pressures. These radial deflections are characterized in part by the reduction of slack in the initially loose sheetpile assemblage and also by elastic tensioning of the sheetpiles. Near the dredgeline, outward sheetpile deflections are reduced by the passive resistance of the foundation soils. The combination of increasing cell fill pressure with depth and the constraining influence of the foundation soils results in a pattern of radial deflections that increase with depth from the top of the cell to some point near the dredgeline. Based on field observations, the point of maximum radial deflection is typically between one-fourth and one-third the cell free height above the dredgeline (*3*). Because tensions increase with increasing radial deflection, the point of maximum bulging corresponds to the point of maximum sheetpile interlock tension.

Main and arc cell maximum tensions ($t_{max}$) are commonly estimated using the hoop stress equation:

$$t_{max} = p_{max} \cdot \text{radius}, \quad (1)$$

where $p_{max}$ is the maximum lateral pressure acting against the sheetpile wall. The maximum lateral pressure is assumed to occur at the point of maximum bulging (*4*). Design for main and arc cell interlock tensions therefore requires that cell radius, soil unit weight, the coefficient of lateral earth pressure, and the point of maximum bulging be known. The coefficient of lateral earth pressure depends on both the sheetpile movements and on the amount of arching that occurs within the cell. Arc cell tensions are less than main cell tensions because arc cell radii are smaller than main cell radii, and because arching within the arc cells reduces the horizontal earth pressures acting against the sheetpiles to a greater extent than it does for the main cells.

Sheetpiles installed along the main/arc cell common wall (Figure 1) are loaded by several mechanisms. During main cell filling, common wall piles bulge radially outward in a manner similar to the other main cell piles. Then, during arc cell filling, the common wall is pushed back toward the main cell interior, causing a reduction in interlock tension. At the same time, tensions that occur in the arc cell piles because of filling are transmitted through the wye pile and increase common wall interlock tensions. The effect of these two mechanisms generally results in a net increase in common wall interlock tensions following arc cell loading (*5*).

## PROJECT DESCRIPTIONS

In the following, important aspects of the Trident Drydock and Lock and Dam 26 (R) projects are briefly summarized. Complete

Department of Civil Engineering, Virginia Polytechnic Institute and State University, Blacksburg, Va. 24060.

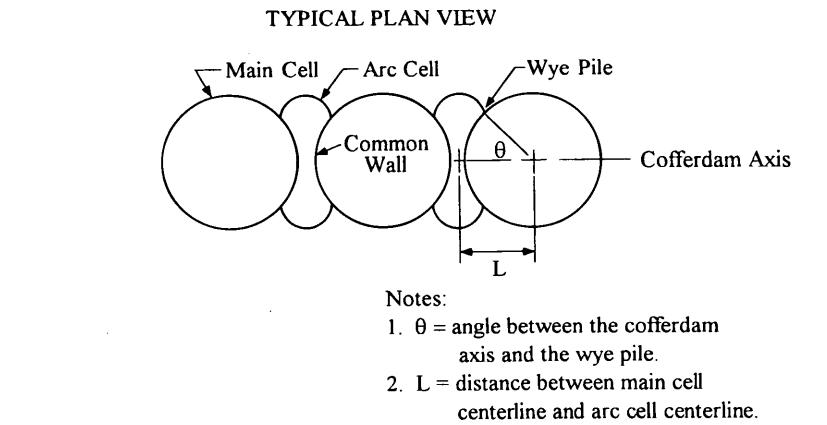


**FIGURE 1 Cellular structure description.**

project descriptions are provided by Sorota and Kinner (*6*), Sorota et al. (*7*), and Shannon and Wilson, Inc. (*8,9*).

### Trident Drydock

A cellular cofferdam was constructed for the Trident Drydock (Bremerton, Washington) to keep construction activities dry and to function as a permanent laydown area for dry-dock operations. Main cells are 23.2 m (76 ft) in diameter and extend 24.4 to 26.5 m (80 to 87 ft) above the dredgeline (Figure 2). Forty-degree wye piles were used to connect the main cells to the 4.9 m (16 ft) radius connecting arcs.

Cell construction started with sheetpiles being driven up to 1.21 m (4 ft) into the hard glacial till foundation soils. High strength PSX32 sheetpiles were used for all main cell, arc cell, and common wall sections. Cell fill consisted of gravelly sands placed with a clamshell bucket. Cells were filled to an elevation of 5.2 m (17 ft) before dewatering operations. Two cells were instrumented with strain gages, located on both main and common wall piles.

### Lock and Dam 26 (R)

Lock and Dam 26 (R) was constructed in three separate stages to replace existing Lock and Dam 26 on the Mississippi River near Alton, Ill. Stage 1 main cells were 19.2 m (63 ft) in diameter and extended 18.3 m (60 ft) above the river bottom (Figure 2). Thirty-degree wye piles were used to connect main cells with 4.9 m (16 ft) radius connecting arcs.

Construction activities started with sheetpiles driven 10.7 m (35 ft) into the medium-dense to dense alluvial foundation sands. Standard Penetration Test blowcounts in the sand indicated a fairly uniform relative density of about 70 percent (*10*). High strength PSX32 sheetpiles were used for the common walls; mild steel PS32 sheetpiles were used for the remaining main and arc cell sections. After pile driving, cells were filled with dredged sand placed with a clamshell bucket. Instrumentation installed to observe cell filling behavior consisted of strain gages and inclinoms (Figure 2).

## NUMERICAL MODELING

### Main Cell-Filling Analyses

The finite element modeling of main cell filling was performed with an axisymmetric formulation because of the inherent axisymmetric nature of the physical problem. In order to provide a realistic representation of the soil response, a nonlinear (hyperbolic), confining pressure-dependent model was used (*11*). Soil element stiffnesses ($E_t$) are given by

TRIDENT DRYDOCK CELL GEOMETRY

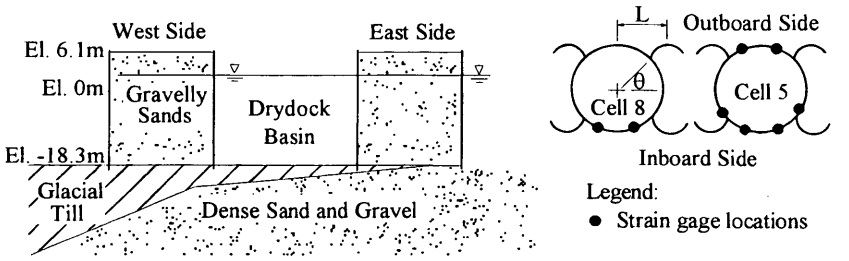


Profile Through Middle of Drydock

Plan View of Instrumented Cells

Notes:

| | |
|---|---|
| 1. Main cell diam. = 23.2m. | 5. Wye pile angle = 40 degr. |
| 2. Arc cell radius = 4.9m. | 6. θ = 36.5 degr. |
| 3. Pile embedment = 0 to 1.2m. | 7. L = 14.3m. |
| 4. Cell height = 24.4m. | 8. 1 meter = 3.28 ft. |

LOCK AND DAM 26 (R) CELL GEOMETRY

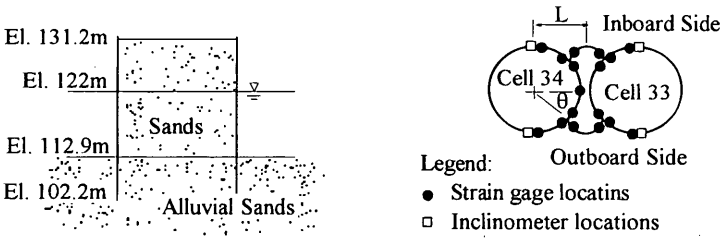


Profile Through Typical Cell

Plan View of Instrumented Cells

Notes:

| | |
|---|---|
| 1. Main cell diam. = 19.2m. | 5. Wye pile angle = 30 degr. |
| 2. Arc cell radius = 4.9m. | 6. θ = 30 degr. |
| 3. Pile embedment = 10.7m. | 7. L = 13.2m. |
| 4. Cell height = 18.3m. | 8. 1 meter = 3.28 ft. |

**FIGURE 2 Project descriptions.**

$$E_t = K_m P_a \left( \frac{\sigma_3'}{P_a} \right)^n (1 - R_f SL)^2, \quad (2)$$

where $K_m$, $n$, and $R_f$ are values developed from laboratory testing, $P_a$ is the atmospheric pressure, $\sigma_3'$ is the effective confining pressure, and SL is the soil element stress level. Soil element volume changes depend on the bulk modulus (B), which is given by Duncan et al. (*12*):

$$B = K_b P_a \left( \frac{\sigma_3'}{P_a} \right)^m, \quad (3)$$

where $K_b$ and m are values developed from laboratory testing and $P_a$ and $\sigma_3'$ are defined above. Interface elements were used to allow for the relatively large movements that can occur between the soil and sheetpile walls. Cell filling was modeled by establishing the initial stresses in the foundation soils, adding shell elements to represent the sheetpiles, and incrementally filling the cell interior with soil fill. Incremental loading is necessary because the response of the soil and interface elements is dependent on the magnitude and history of stresses in the system (Equation 2). For these analyses, a minimum of 120 load steps were used to model filling operations. The water level within the cell fill was assumed to be the same as the exterior water level because clamshell bucket filling is sufficiently slow to allow dissipation of excess pore water pressures in the fill.

### Common Wall Analyses

The response of the common wall to filling of the main and arc cells is a complex three-dimensional problem. Hardin (*5*) gained insight into the common wall problem by performing two-dimensional finite element analyses on a horizontal slice extending through the Lock and Dam 26 main and arc cells. Analyses were performed by applying out-of-plane loads (vertical "fill" loads) on the elements of the horizontal slice and examining the displacements and stresses generated in the sheetpile walls. Hardin's results indicated that although high localized stresses were induced at the wye pile, tensions along all other common wall piles were approximately the same. The results suggest that the combination of arc fill lateral

loading and the additional arc cell tensions transmitted through the wye pile result in a uniform common wall tension at any elevation. Mosher (*10*) performed three-dimensional finite element analyses for the Lock and Dam 26 cells. The three-dimensional analyses confirmed the predictions made by the horizontal slice analyses. Even though useful information can be obtained from the horizontal slice model and from three-dimensional analyses, there are important disadvantages to these approaches. The horizontal slice model provides information only at the elevation of the slice. Additional analyses must be performed at each elevation at which common tensions are desired. Additionally, when the horizontal slice model is used above the dredgeline, it does not include the effects of lateral restraint provided by the foundation materials. For this reason, the horizontal slice model does not work well near the dredgeline. In principal, three-dimensional analyses could provide a good model of cofferdam behavior. The major difficulty with three-dimensional analyses is that the engineering cost for performing analyses and interpreting the results is prohibitive.

For this research, we attempted to model the key mechanisms of common wall behavior while avoiding the disadvantages of the horizontal slice and three-dimensional approaches. The common wall problem was therefore modeled using the three step approach shown in Figure 3. Step 1 consists of an axisymmetric finite element analysis of main cell filling, as described previously. In Step 2, the axisymmetric analysis of main cell filling is carried further by simulating fill placement in an annular space around the outside of the main cell. The effect of this fill placement is to push the sheetpiles back toward the center of the main cell and to reduce main cell sheetpile tensions. In Step 3, the component of the arc cell tension (obtained from axisymmetric finite element analyses of arc cell filling), in the direction of the common wall at the wye, is added to the main cell tensions from Step 2. The proposed procedure is advantageous because it is believed to effectively simulate the actual loadings on the common wall during cell filling. Additionally, this procedure produces a uniform tension in the common wall at any elevation, in agreement with the results of Hardin's horizontal slice

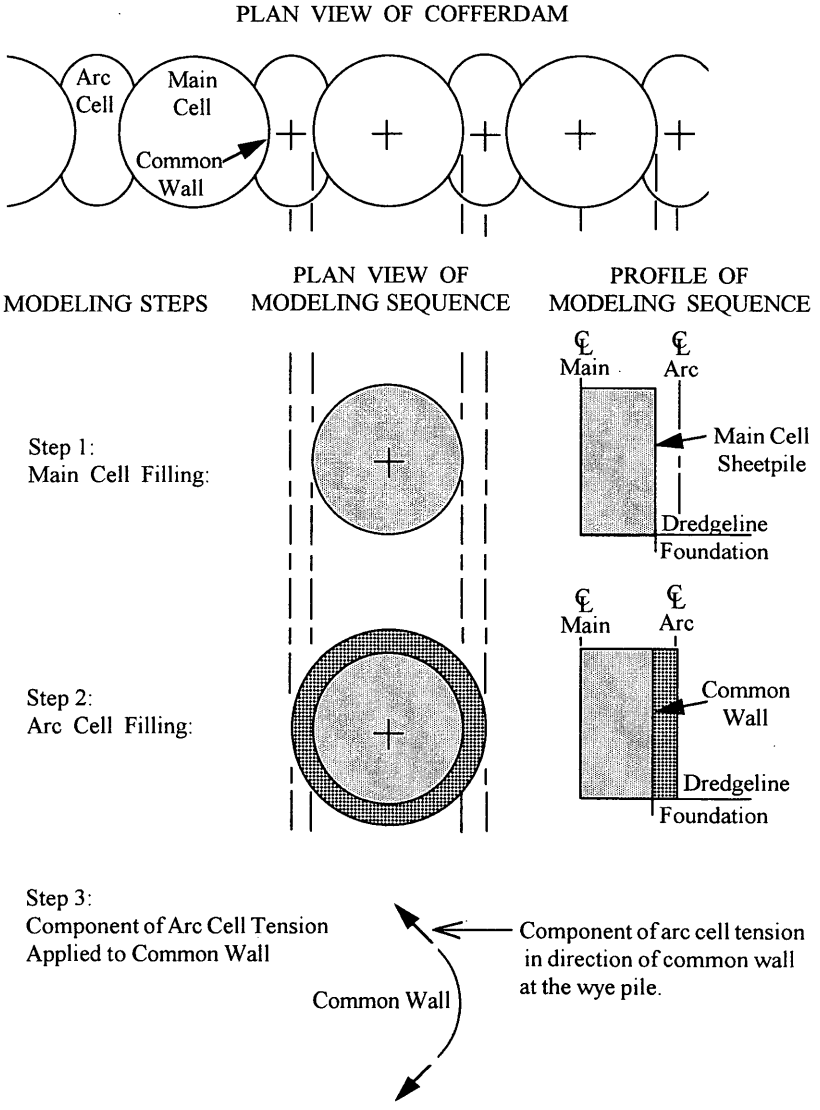


**FIGURE 3 Common wall construction sequence modeling.**

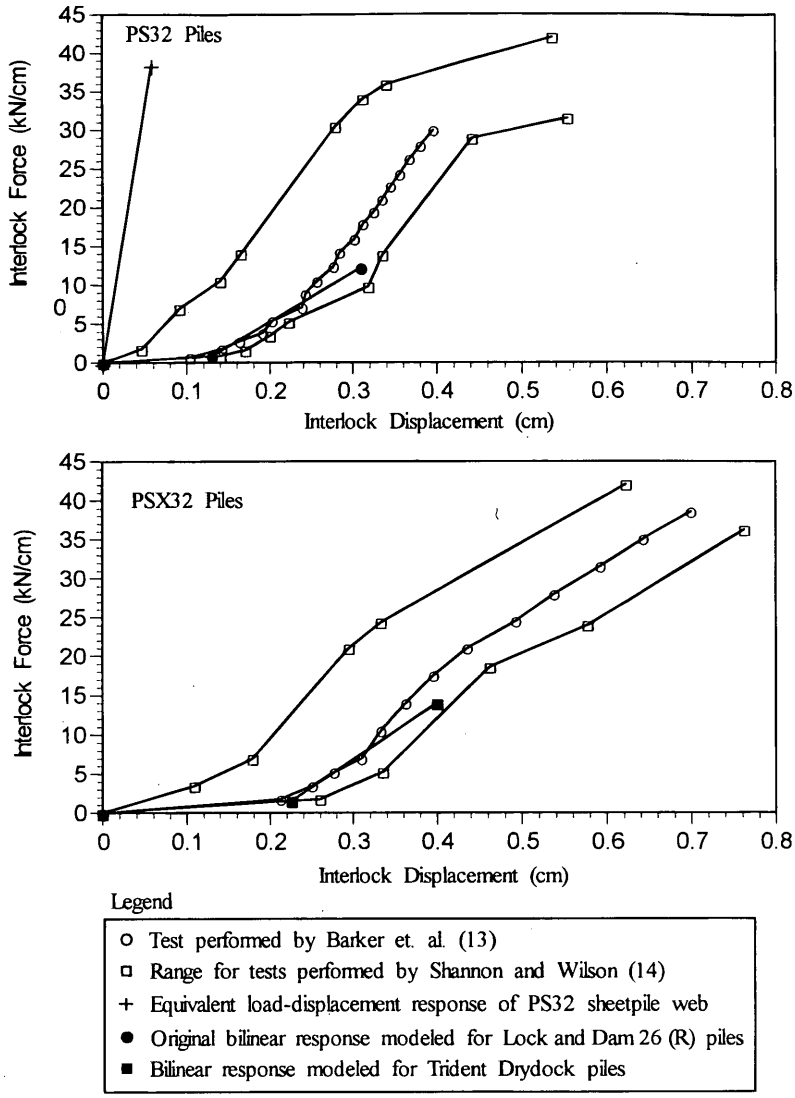


**FIGURE 4 Lock and Dam 26 (R): sheetpile load-displacement curves.**

analysis. The main drawbacks of this procedure are that not all of the three-dimensional effects are explicitly modeled and that loads are superpositioned although the system is nonlinear. The error associated with superposition in this case, however, is thought to be minimal because the load increment associated with the application of the arc cell tension is small and because the soil elements are at relatively low stress levels, corresponding to portions of the stress-strain curves that are not highly nonlinear.

## Sheetpile Response Modeling

In an effort to quantify sheetpile interlock load-displacement behavior at Lock and Dam 26 (R), two sets of sheetpile interlock pull tests were performed (*13,14*). The test results show that the interlock load-displacement responses for both PS32 and PSX32 piles are considerably softer than the elastic stiffness of the sheetpile web (Figure 4). This anisotropic system behavior is primarily attributed to the imperfect and initially slack fit between the thumb-and-forefinger interlocks that connect adjacent sheetpiles (Figure 1).

Sheetpile behavior is modeled within the code by assigning an orthotropic stiffness reduction factor, E-ratio, to the shell elements (E-ratio = circumferential stiffness divided by axial stiffness). Because of the predominantly bilinear response of the pull tests, bilinear E-ratio reduction factors were used to model stiffnesses for sheetpiles installed at both Lock and Dam 26 (R) and Trident Drydock.

**TABLE 1 Hyperbolic Soil Parameter Values Used in Analyses**

| Project | Material | Unit Weight ($kg/m^3$) | Friction Angle (degrees) | $K_m$* | n* | $R_f$* |
|---|---|---|---|---|---|---|
| Trident Drydock | Moist Fill | 2064 | 35 | 800 | 0.65 | 0.82 |
| | Buoyant Fill | 1162 | 35 | 800 | 0.65 | 0.82 |
| | Foundation | ** | ** | ** | ** | ** |
| Lock & Dam 26(R) | Moist Fill | 1968 | 35 | 800 | 0.65 | 0.82 |
| | Buoyant Fill | 1130 | 35 | 800 | 0.65 | 0.82 |
| | Foundation | 1130 | 41 | 1600 | 0.50 | 0.85 |

* Elastic Modulus = $E_t = K_m P_a (\frac{\sigma_3'}{P_a})^n (1-R_f SL)^2$,

where Pa = atmospheric pressure, and
SL = soil element stress level

** Linear elastic parameters used for Trident Drydock foundation materials.

### Soil Parameter Values

Laboratory tests were previously performed to select input parameters for earlier Lock and Dam 26 (R) finite element studies. Because of the similarities in the descriptions of the fill materials and placement methods at Lock and Dam 26 (R) and at Trident Drydock, similar fill parameter values were used in both analyses (Table 1). Because the Trident Drydock was founded on hard glacial tills, linear elastic parameter values, similar to those appropriate for lean concrete, were used for the foundation materials.

## ANALYSES RESULTS

### Trident Drydock

Calculated deflections and interlock tensions for Trident Drydock are presented on Figure 5. As expected, calculated cell deflections and interlock tensions increase from low values at the top of the cells to maximum values just above the dredgeline. The range and average measured interlock tensions are also shown in Figure 5. The location of maximum interlock tension shown in Figure 5 was interpreted using data from longer piles where strain gages were located at the point of maximum tension. It can be seen that there was good agreement between the calculated and measured tensions. Unfortunately, measured deflections are not available for Trident Drydock cell filling.

### Lock and Dam 26 (R)

Calculated and measured deflections for Lock and Dam 26 (R) are presented in Figure 6. The calculated deflections were significantly lower than the measured deflections, and the calculated tensions were significantly higher than the measured tensions.

One possible reason for these differences is that the sheetpile response at Lock and Dam 26 (R) may have been softer than the laboratory tests indicated. This possibility was investigated (*8*) by converting the average radial deflections from the inclinom data to tangential displacements per interlock with the relationship

$$u = \frac{dr \cdot L}{R}, \quad (4)$$

where $u$ is the interlock displacement, $dr$ is the sheetpile radial deflection, $L$ is the sheetpile width, and $R$ is the cell radius. The displacement per interlock is plotted versus the interlock tension from the average of the strain gage data on Figure 7. It can be seen that sheetpiles installed for the Lock and Dam 26 (R) cells were much looser than the laboratory pull tests indicate. The reasons for this softer response were not obvious, but may have been because of more interlock slack left in the pile assemblage during construction than during the laboratory tests.

Revised analyses for Lock and Dam 26 (see Figure 8) were performed with revised E-ratios obtained from the inclinom and strain gage data. It can be seen that the calculated deflections and tensions were in better agreement with the measured values when the E-ratios from the field data (Figure 7) were used. The agreement between calculated and measured values for the main cell and the common wall was good. For the arc cell, the calculated tensions were larger than most of the averages of the measured tension data. Some of this difference is thought to have been because of localized cell fill arching effects occurring near the wye piles.

## COMPARISONS WITH CONVENTIONAL PREDICTIONS

### Main Cell Interlock Tension

Conventional cellular design methods use the hoop stress approach to predict main cell interlock tensions. With the hoop stress equation, the maximum interlock tension is calculated by simply multiplying the maximum lateral cell fill pressure (which occurs at the point of maximum cell bulge) times the cell radius (Equation 1).

Three recognized design methods, Terzaghi (*1*), Tennessee Valley Authority (TVA) (*3*), and Schroeder and Maitland (*15*) provide alternate recommendations for the lateral earth pressure coefficient, $K$, (see Table 2) and for finding the point of maximum bulge. For finding the location of maximum tension, Terzaghi (*1*) recommended that the maximum lateral cell fill pressures be computed at the dredgeline where the overburden stresses within the cell are largest. Alternatively, the TVA procedure (*3*) suggests that the point of maximum tension occurs at one-fourth of the free cell height above the dredgeline. Schroeder and Maitland (*15*) recommend that the point of maximum tension is most likely to occur at one-third

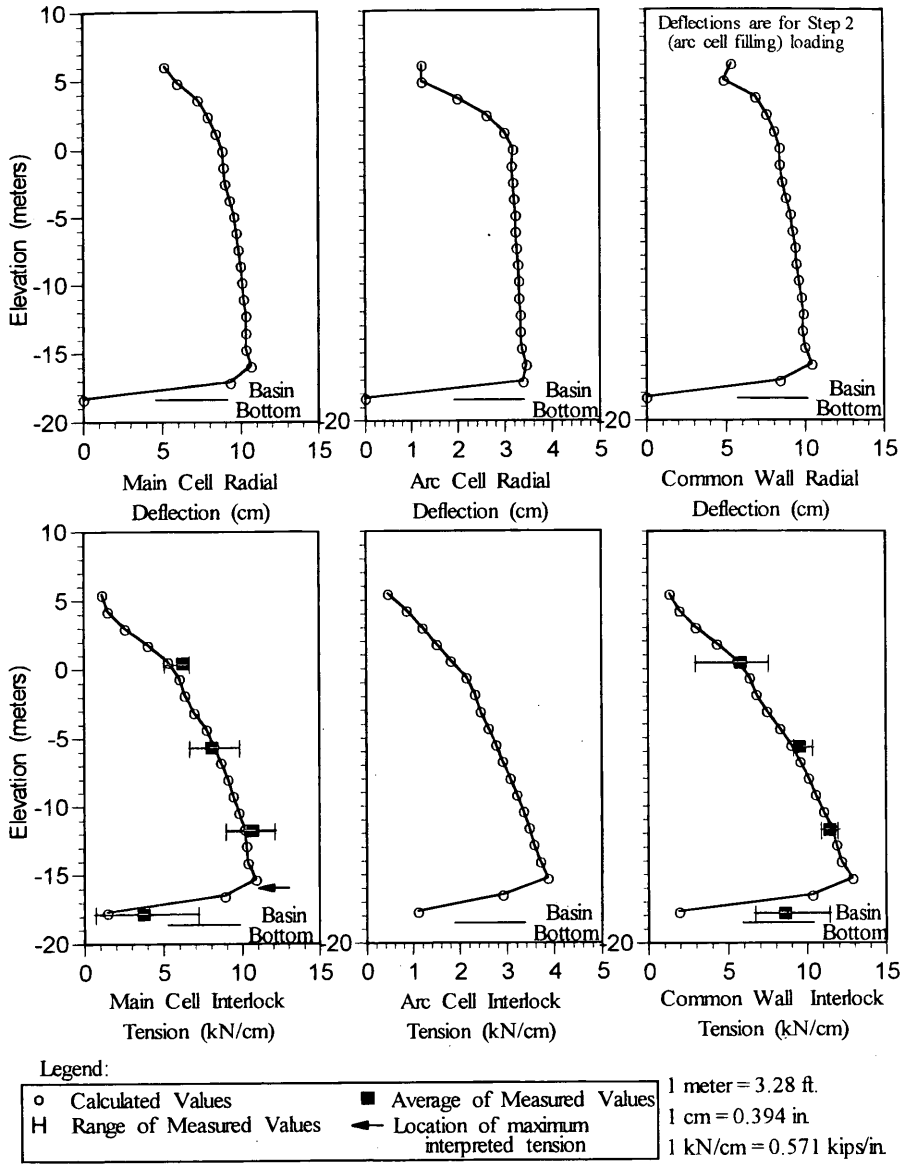


**FIGURE 5 Trident Drydock: sheetpile deflections and interlock tensions.**

the distance between the point of pile fixity within the foundation material and the top of the cell.

Main cell interlock tensions predicted with the three conventional procedures are compared with finite element results and strain gage data in Figure 9. For both the Trident Drydock and the Lock and Dam 26 (R) projects, the Terzaghi method overestimates the maximum interlock tensions by at least 40 percent because no provisions for tension reductions above the dredgeline are made. Maximum tensions calculated using the TVA method are less than the maximum tension at the Trident Drydock and approximately equal to the maximum measured tension at Lock and Dam 26 (R). Maximum tensions calculated using the Schroeder and Maitland method are approximately equal to the maximum measured tension at Trident Drydock and are greater than the maximum measured tension at Lock and Dam 26 (R). For both the TVA method and the Schroeder and Maitland method, the location of maximum tension is higher than the observed location for Trident Drydock and approximately at the observed location for Lock and Dam 26 (R).

## Common Wall Interlock Tensions

The TVA secant method (*3*) and the Swatek method (*4*) are commonly used to predict interlock tensions in the common wall. These methods are illustrated in Figure 10. The maximum lateral earth pressure ($p_{max}$) value used in both methods is evaluated by the procedures described above for the main cells.

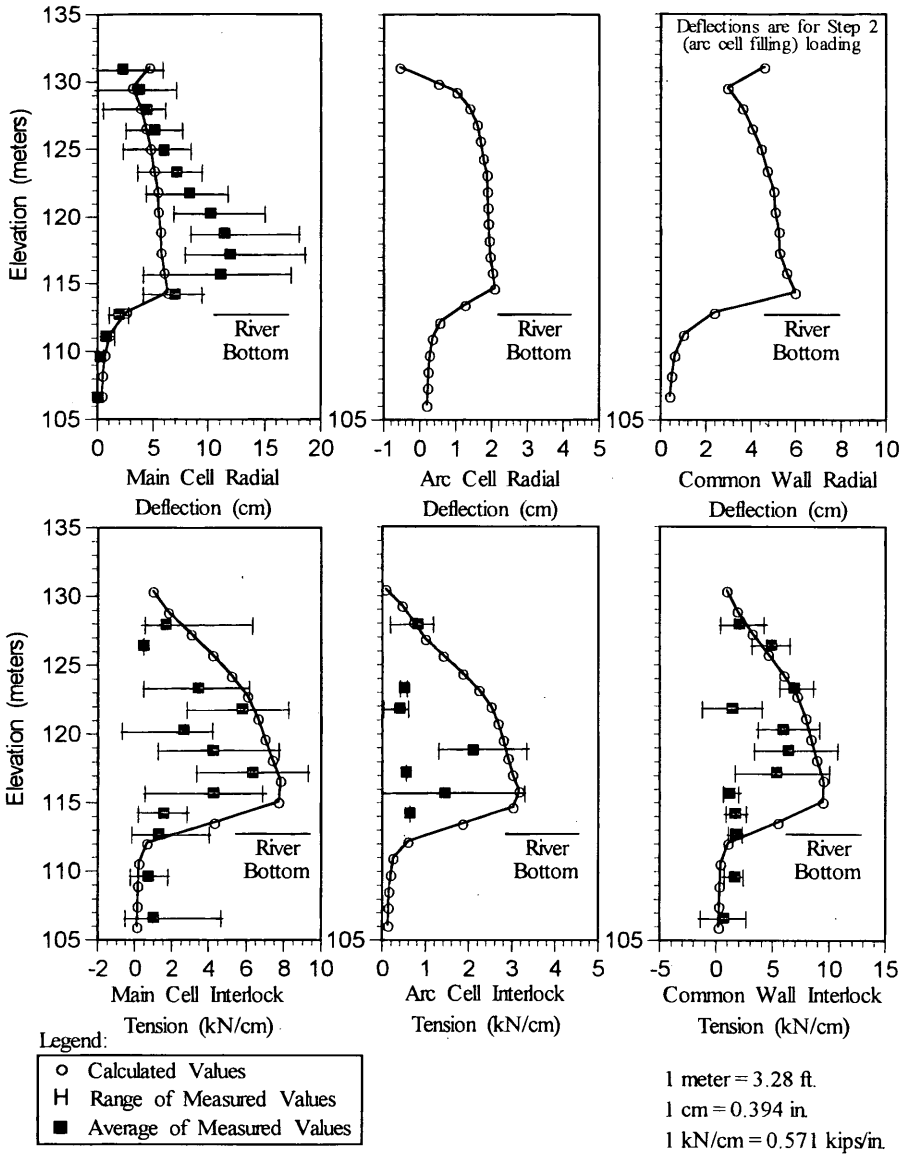


**FIGURE 6 Lock and Dam 26 (R): sheetpile deflections and interlock tensions for bilinear sheetpile response from laboratory tests.**

Common wall interlock tensions predicted by the TVA secant and Swatek methods are compared with three-step finite element analyses and average strain gage results in Figure 11. For simplicity, the TVA main cell procedures for the coefficient of lateral earth pressure and point of maximum tension were used to find the maximum lateral earth pressure. For the upper portion of the Trident cells, it can be seen that the TVA method generally provides relatively good predictions, whereas the Swatek method modestly underestimates common wall tensions in comparison with the trend in strain gage data. Both methods, however, provide locations of maximum common wall tension that are too high in comparison with the trend in Trident cell strain gage data. This is because both methods rely on main cell tension prediction procedures to find the point of maximum tension. For the upper portion of the Lock and Dam 26 (R) cells, it can be seen that the Swatek method provides a reasonable prediction of common wall tension in comparison with the strain gage data. The TVA method slightly overpredicts maximum tension. Both methods provide locations of maximum common wall tension that are relatively close to that indicated by the strain gage data.

## CONCLUSIONS

Finite element analyses of cellular structures are advantageous because soil-structure interactions are modeled and insight into con-

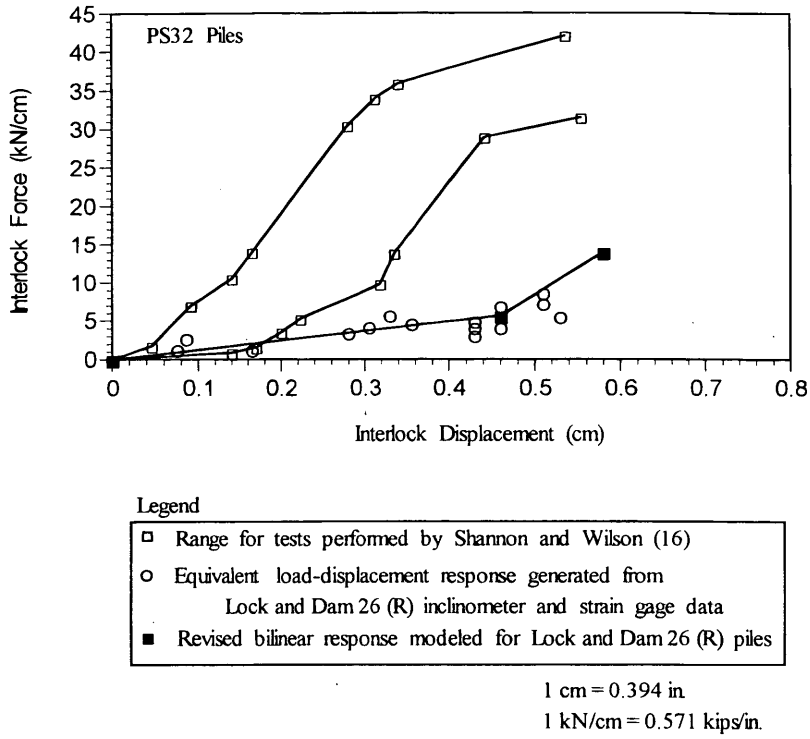


Legend

- Range for tests performed by Shannon and Wilson (16)
- Equivalent load-displacement response generated from Lock and Dam 26 (R) inclinometer and strain gage data
- Revised bilinear response modeled for Lock and Dam 26 (R) piles

1 cm = 0.394 in.
1 kN/cm = 0.571 kips/in.

**FIGURE 7 Lock and Dam 26 (R): revised sheetpile load-displacement curves.**

trolling mechanisms is gained. Conclusions based on the results of studies performed for two case histories can be summarized as follows:

1. Calculations of main and arc cell sheetpile displacements and interlock stresses that are in good agreement with measured values can be obtained from axisymmetric finite element analyses.

2. Computed sheetpile deflections and interlock tensions from the finite element model are sensitive to the sheetpile circumferential stiffness (E-ratio), which may be difficult to determine a priori.

3. A good match between computed and measured tensions was obtained for the Trident Drydock when the results of the laboratory sheetpile pull tests were used to determine sheetpile E-ratios. For Lock and Dam 26 (R), axisymmetric analyses performed with E-ratios from laboratory pull tests resulted in smaller computed radial deflections and larger computed interlock tensions than measured in the field. A better match between computed and measured sheetpile deflections and tensions was obtained for Lock and Dam 26 (R) when inclinom and strain gage results were used to determine the effective sheetpile assemblage E-ratio.

4. A new approach for determining common wall interlock tensions was found to provide good agreement with measured field data. The approach developed for this study calculates common wall tensions by: (a) performing an axisymmetric finite element analysis for main cell filling, (b) modeling the effects of placing fill within the arc cell area, and (c) superimposing arc cell tensions on the common wall.

5. In each of the cases examined, the finite element analysis provided the best match between the predicted and measured interlock tensions. However, with the exception of the Terzaghi method, the predictive capability of the simplified methods was practically equal to that of our finite element analysis. Both the Schroeder and Maitland and TVA methods gave very good results for both cases, with the possible exception that the TVA method underpredicted the maximum main cell tensions at Trident by about 20 percent. The Terzaghi method however, was found to largely overpredict tensions near the dredgeline because the restraint provided by the foundation is not considered.

6. The finite element analyses used in this work provided insight into the behavioral mechanisms associated with cellular structures and confirmed the importance of soil-structure interaction effects. Of particular significance, our finite element approach agreed well with measured field data and suggests that this technique can be used to model complicated cases in which simplified methods may be limited, or develop new simplified methods to predict other aspects of cellular behavior such as lateral movements.

## ACKNOWLEDGMENTS

This research was supported under the auspices of the U.S. Army Corps of Engineers. We wish to express their gratitude to G.W. Clough, University of Washington, and R. L. Mosher, U.S. Army Corps of Engineers, Waterways Experiment Station, for providing guidance for the work. A debt of gratitude is due E. B. Kinner, Haley and Aldrich, Inc., and Leland B. Jones, Vice President, Shannon and Wilson, Inc., for their invaluable comments and suggestions.

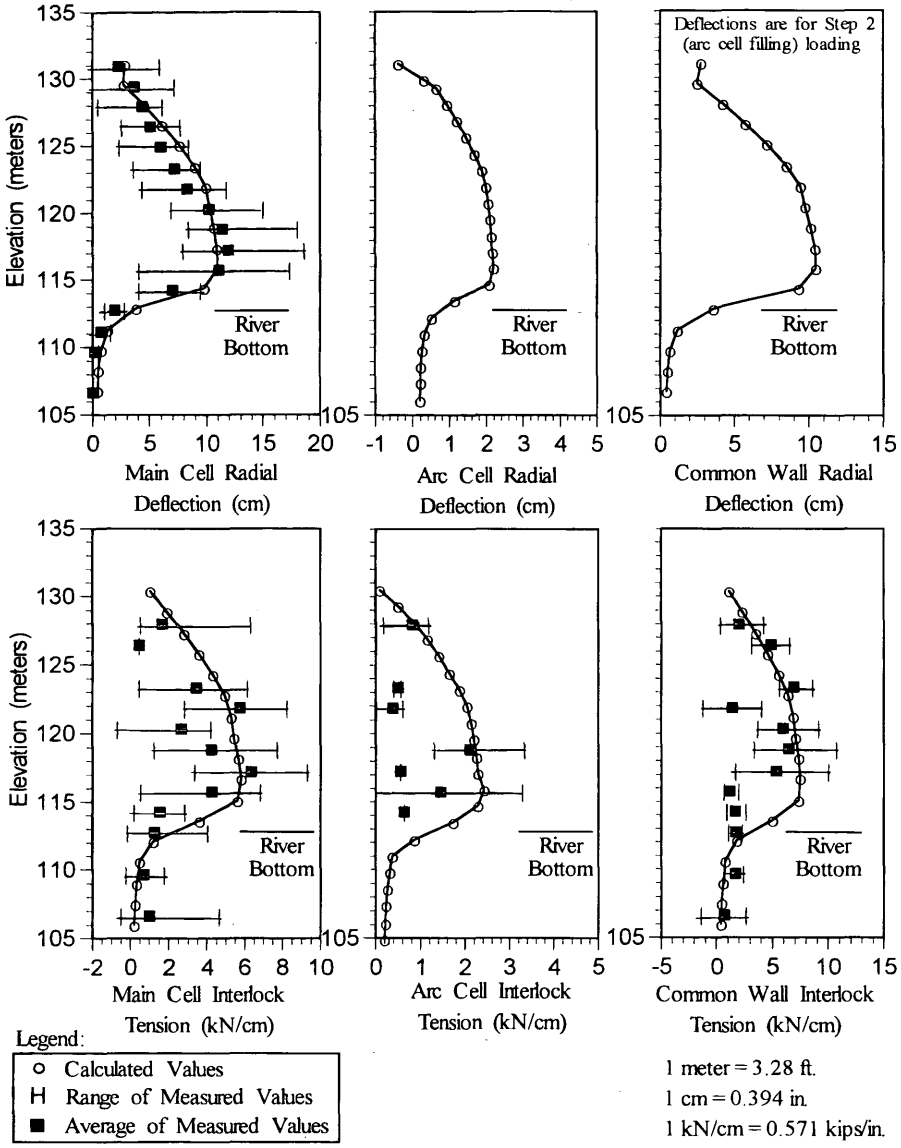


**FIGURE 8 Lock and Dam 26 (R): sheetpile deflections and interlock tensions for revised sheetpile response.**

**TABLE 2 Conventional Recommendations for K-Values During Cell Filling**

| Source | Coefficient of Lateral Earth Pressure (K) |
|---|---|
| Terzaghi (1) | 0.40 |
| Tennessee Valley Authority (3) | $K_a=\tan^2(45-\phi/2)$ |
| Schroeder and Maitland (17) | 1.2 to 1.6 Ka |

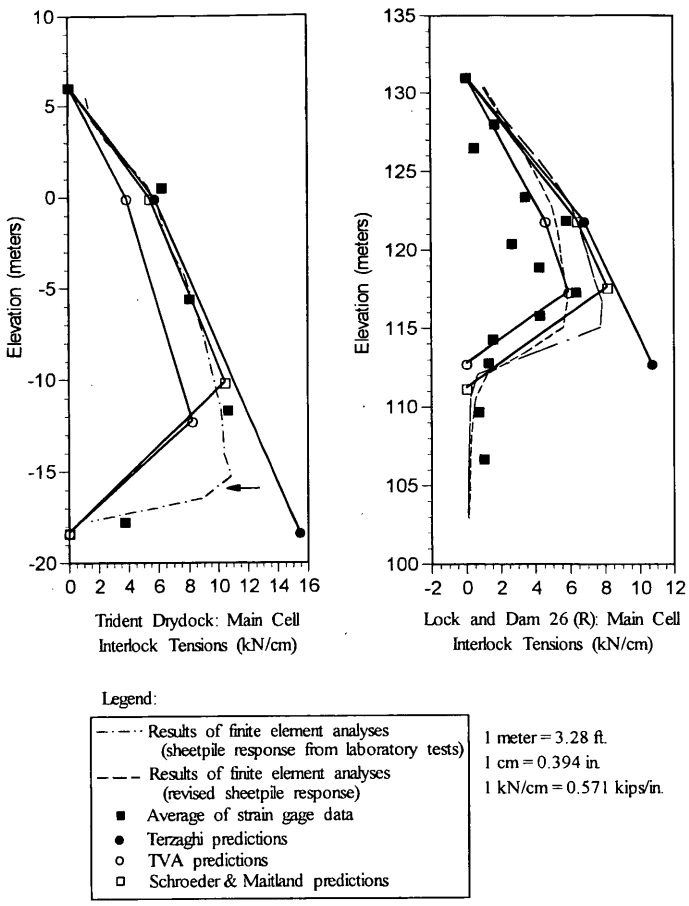


**FIGURE 9 Methods for predicting main cell interlock tensions.**

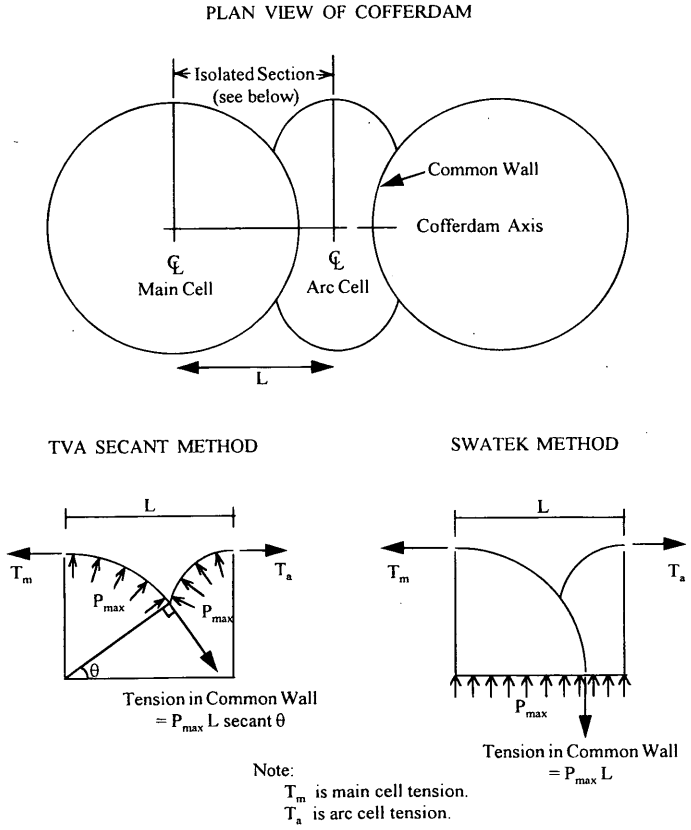


**FIGURE 10 Conventional methods for predicting common wall interlock tensions.**

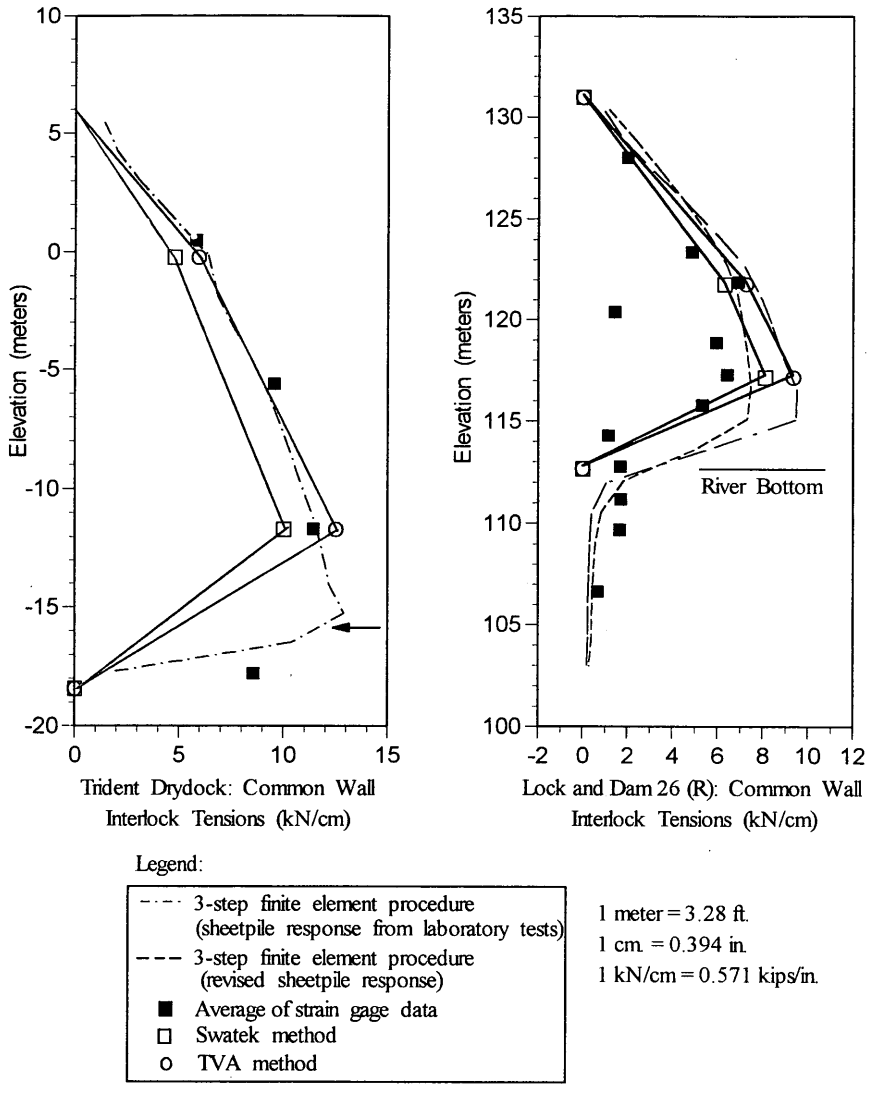


**FIGURE 11 Methods for predicting common wall interlock tensions.**

## REFERENCES


1. Terzaghi, K. Stability and Stiffness of Cellular Cofferdams. *Transactions, ASCE.* Vol. 110, 1945, pp. 1083-1119.
2. Clough, G. W., R. Mosher, Y. Singh, and T. Kuppusamy. Two and Three Dimension Finite Element Analysis of Cellular Cofferdams. Presented at Conference on Soil-Structure Interaction, Paris, France, 1987.
3. Tennessee Valley Authority. *Steel Sheet Cellular Cofferdams on Rock.* TVA Technical Monogragh No. 75, 1957.
4. Rossow, M., E. Demsky, and R. Mosher. *Theoretical Manual for Design of Cellular Sheet Pile Structures (Cofferdams and Retaining Structures).* Technical Report ITL-87-5, U.S. Army Corps of Engineers, Waterway Experiment Station, Vicksburg, Miss., 1987.
5. Hardin, K. O. *Finite Element Analysis of Cellular Steel Sheet Pile Cofferdams.* Ph.D. dissertation. Virginia Polytechnic Institute and State University, Blacksburg, 1990.
6. Sorota, M. D., and E. B. Kinner. Cellular Cofferdam for Trident Drydock: Design. *Journal of the Geotechnical Engineering Division, ASCE.* Vol. 107, No. GT12, December, 1981, pp. 1643-1655.
7. Sorota, M. D., E. B. Kinner, and M. X. Haley. Cellular Cofferdam for Trident Drydock: Performance. *Journal of the Geotechnical Engineering Division, ASCE.* Vol. 107, No. GT12, December, 1981, pp. 1657-1676.
8. Shannon and Wilson, Inc. *Analysis of Instrumentation Data, Interim report Task 3.1, Lock and Dam No. 26 (Replacement), Mississippi River.* Contract No. DACW43-82-C-0054. Department of the Army, St. Louis District, Corps of Engineers, St. Louis, Mo. 1982.
9. Shannon and Wilson, Inc. *Summary Report-Instrumentation Data Analysis and Finite Element Studies for First Stage Cofferdam, Lock and Dam No. 26 (Replacement), Mississippi River.* Contract No. DACW43-82-C-0054. Department of the Army, St. Louis District, Corps of Engineers, St. Louis, Mo. 1983.
10. Mosher, R. L. *Three-Dimensional Finite Element Analysis of Cellular Cofferdams.* Ph.D. dissertation. Virginia Polytechnic Institute and State University, Blacksburg, 1991.
11. Duncan, J. M., and C. Y. Chang. Nonlinear Analysis of Stress and Strain in Soils. *Journal of the Soil Mechanics and Foundations Division, ASCE.* Vol. 96, No. SM5, September, 1970, pp. 1853-1862.
12. Duncan, J. M., P. Byrne, P. Mabry, and K. S. Wong. *Strength, Stress-Strain, and Bulk Modulus Parameters for Finite Element Analyses of Stresses and Movements in Soil Masses.* Virginia Polytechnic Institute and State University, Blacksburg, 1980.

13. Barker, R., C. Lewis, W. Oliver, and K. Mould. *Sheetpile Interlock Connection Testing Program, Final Report–Task 1.1 Through 1.3*, Report No. VPI/CE-ST-85/01. Department of Civil Engineering, Virginia Polytechnic Institute and State University. Department of Army, Waterways Experiment Station, Corps of Engineers, 1985.
14. Shannon and Wilson, Inc. *Final Report, Tasks 6.1 through 6.7, Sheet Pile Interlock Testing, Lock and Dam No. 26 (Replacement), Mississippi River*, Contract No. DACW43-82-C-0054. Department of the Army, St. Louis District, Corps of Engineers, St. Louis, Mo., 1983.
15. Schroeder, W. L., and J. K. Maitland. Cellular Bulkheads and Cofferdams. *Journal of the Geotechnical Engineering Division, ASCE*. Vol. 105, No. GT7, July, 1979, pp. 823-838.

*Publication of this paper sponsored by Committee on Modelling Techniques in Geomechanics.*

# Centrifugal Modeling of Leaking Underground Storage Tanks

KUO-NENG G. CHANG, JAY N. MEEGODA, AND RAJ P. KHERA

Leaking underground storage tanks (UST) and contaminated soil must be removed to comply with environmental regulations. A major problem associated with removal of contaminated soils is the lack of a proven method to determine the extent of soil contamination. The movement of chemicals and the subsequent fate and transport of chemicals from the leaking UST are often estimated from field explorations coupled with mathematical models. A major difficulty in these modeling efforts has been a lack of information concerning the constitutive relationships governing multi-phase contaminant movement. Centrifugal modeling coupled with field investigation is an alternative way of simulating and estimating chemical movement and transport through soils. In centrifugal modeling an actual three-dimensional profile is created and the centrifuge, because of scaling laws, accelerates the chemical flow and transport processes such that a field event that lasts decades is simulated within hours or days. The centrifugal modeling technique was used to simulate the movement of gasoline through the vadose zone from leaky UST and to study the distribution of various constituents of gasoline. The results show that for granular soils the movement of gasoline was advective and the free product formed a pool on top of the water table directly below the UST. However, for fine grained soils, instead of the pooling of free products, spreading of components of gasoline at different rates was observed to be due to the movement and subsequent transport of gasoline in anisotropic soils.

Underground storage tanks (UST) and contaminated soil are often encountered during new highway construction and highway expansion projects. It is the responsibility of the transportation department that owns the site to remove the leaking UST and contaminated soils to comply with environmental regulations. The ground below the highway and the right of way should be free of soil contamination.

To address soil contamination caused by UST, the U.S. Congress (*1*) and most states proposed stringent regulations governing leaking UST and soils contaminated by them. To find the best clean-up option, the United States Environmental Protection Agency (USEPA) produced a comprehensive document to direct the users to select the most appropriate corrective action technology (*2*). However, this document did not address the extent or levels of contamination for sites nor the effectiveness and termination criteria for the corrective action technologies such as soil flushing, soil washing, vacuum extraction, slurry walls, soil cover, and others.

The following factors control the extent of soil contamination. The environmental factors are the volume and duration of leak and types of chemicals leaked including their transformations through degradation and volatilization. The hydrological factors are the amount of precipitation (rain, snow, and ice), evaporation and surface runoff. The geotechnical factors are soil layer thickness and inclination, anisotropy, soil type, soil properties (such as hydraulic conductivity), adsorption capacity that affects hydrogeological parameters, suction and capillary actions. Hydrogeological factors are the depth of water table, the rate and direction of groundwater movement and all the parameters of the vadose zone.

Field monitoring and gathering of field data, mathematical modeling, and physical modeling are the logical approaches that may be taken to determine the extent of contamination and most appropriate clean-up technology for sites contaminated from leaking UST. A combination of approaches may be used to find the extent of contamination and the most appropriate decontamination option. This will facilitate the decision making or judgment procedure with added confidence and will reduce the cost of the site investigation and subsequent chemical analyses. A detailed description of each approach is given below.

## Field Tests

The first approach is to gather field data through field monitoring. Though this approach is the best, it may not be feasible to create a complete picture because of the high cost of drilling, difficulties of obtaining undisturbed samples, sample contamination, loss of volatiles during transportation to a laboratory, and amount of time needed for such an investigation. However, such data is important in calibrating mathematical and physical models.

## Mathematical Models

Mathematical modeling of flow and fate and transport of contaminants in a multi-phase medium is another popular method. Numerical analyses of multi-phase pollutant migration have been presented by numerous researchers (*3,4*). The major difficulty in multi-phase modeling efforts has been a substantial lack of information concerning the constitutive relationships governing multi-phase contaminant movement such as the functional relationships between fluid pressures, saturation and permeability of coexisting phases, and separation of components because of different diffusion and adsorption values of components for fluids such as gasoline. Thus, most researchers have simplified the multi-phase problems to three-phase, two-phase, or even single-phase problems (*5,6*).

## 1-g Physical Models

Physical modeling (1-g), on the other hand, may give an insight to the problem and may provide data for the validation of a mathematical model. The movement of fluids immiscible with water has

K. G. Chang, SWK(PE), Inc., Stonehouse Road, P.O. Box 211, Millington, N.J. 07946. J. N. Meegoda and R. P. Khera, New Jersey Institute of Technology, Newark, N.J. 07102.

been physically modeled by numerous researchers (*7*). Most of the large scale physical models consisted of long one-dimensional columns or large soil box experiments (*8*). The soil box experiments yield interesting and useful data, but take considerable time and are expensive to construct.

### Centrifugal Models

The centrifuge modeling technique can be an improvement over the 1-g physical modeling technique because the size is made smaller and the time can be shortened through scaling. Because of a gravitational field of Ng (g is the acceleration due to gravity and N is the factor by which the centrifuge increases the intensity of gravity) generated by the centrifuge, the sample size is made 1/N of that in the prototype. The stress levels (which produce varying porosities) in the centrifugal models match the stress levels of the simulated sites. In addition to the stress levels the centrifuge can also simulate in situ capillary fringe, water tables, moving groundwater, any capillary trappings and many of the other features encountered in the field (*9*). The scaling laws for centrifuge modeling have been developed (*9,10*). During the past decade many researchers have used the centrifugal modeling technique to model subsurface flow (*9,11*).

### Centrifugal Modeling of Vadose Zone

The movement and subsequent transport of contaminants through unsaturated soils can be modeled in the centrifuge with the same scaling laws as that for saturated soils provided that the following are satisfied: (*a*) Richard's equation is valid, (*b*) the capillary fringe and capillary forces are simulated, and (*c*) suction pressures are simulated.

The unsaturated flow is governed by Richard's equation, which incorporates which Darcy's law and the condition of continuity. Darcy's law has been proved to be valid in the centrifuge for steady state flow (*12*), and it has been stated that "there is no strong evidence of the violation of unsaturated flow theory in the centrifuge," that is, Richard's equation is valid even for permeability values as low as $10^{-10}$m/s and under relatively dry conditions (*13*).

The capillary rise ($H_c$) in an unsaturated soil is given by:

$$H_c = \frac{2 \times T}{r_c \times d_w \times g}$$

where

$T$ = surface tension of pore fluid,
$r_c$ = radius of the capillary (or 0.2 times $D_{10}$ size of the soil), and
$d_w$ = density of water.

In a centrifugal model of size 1/N of the field model under a gravitational field of Ng, according to the above equation, the capillary head will be reduced to $H_c/N$ and hence it is simulated in the centrifuge models.

The total suction pressure that is equal to the sum of the matrix and osmotic suction (*14*) can also be simulated in a centrifuge. There is a unique water content and thus a degree of saturation versus the total suction relationship for remolded soils (*15*). The water content or degree of saturation profile for a given site can be simulated in the centrifuge under equilibrium of steady flow condition (*13*), so the total suction can also be simulated in a centrifuge. The centrifuge model simulates the total suction pressure and the model is N times smaller than the prototype, so the suction gradient is N times higher than that in the prototype. Therefore, hydraulic as well as suction gradients in the model are N times higher than that in the prototype.

The validity of the centrifugal modeling technique has been verified by: (*a*) modeling of one-dimensional contaminant transport in saturated soils using the modeling of models technique (*9*), and (*b*) comparing the one-dimensional centrifugal simulation of flow and transport of a LNAPL through unsaturated soils with prototype behavior and numerical simulation (*16*). Thus, the methodology can be applied to real world geo-environmental problems with complicated site conditions. One class of such problems is the simulation of an actual three-dimensional profile of a leaking UST contaminated site in a short duration, that is, to simulate events that occur over several decades in the field in a day or two inside the centrifuge. The goal of this research is to use the centrifugal modeling technique to study the three-dimensional movement of contaminants from leaking UST through the vadose zone to the groundwater table.

## EXPERIMENTAL PROCEDURE

### Soils Tested

The soils used consisted of a kaolin clay and a dredged residue from a gravel that represented a clay and a poorly graded fine sand, respectively. The liquid and plastic limits of kaolin were 48 and 36 percent, respectively. It had a clay fraction of 85 percent and a maximum dry density of 14.1 kN/m$^3$ at an optimum water content of 30 percent. The coefficients of uniformity and curvature of fine sand were 3.4 and 1.6 respectively. It had zero clay content, a $D_{10}$ of 0.117 mm and a maximum dry density of 14.6 kN/m$^3$ at an optimum water content of 10 percent. To make the aquifer, Ottawa C 30 sand was used.

### Gasoline Mixture

A commercial gasoline contains numerous organic compounds. Interpretation of data and making logical conclusions will be difficult with the use of commercial gasoline. Hence a synthetic gasoline that was reproducible and representative of the commercial gasoline was used in this research. Commercial gasoline is made of aliphatic, aromatic, and olefin. On average a middle grade gasoline contains 55 percent aliphatic, 42 percent aromatic, and 3 percent olefin. The synthetic gasoline was designed with 43 percent of aliphatic and 57 percent of aromatic but olefins were omitted. The aliphatic group consisted of 28.5 percent pentane and 28.5 percent hexane. Butane was omitted completely from the mixture because of difficulties in handling and because of chemical detection, and the potential fire hazard. The aromatic group consisted of 30.7 percent toluene, 6.1 percent *o*-xylene and 6.2 percent benzene. Instead of meeting the USEPA regulation that the benzene be below 2 percent, 6.2 percent benzene was used so that it would result in conservative predictions. The proportions and thermodynamic parameters of the various components of the synthetic gasoline are shown in Table 1. The gas chromtographs of the synthetic and commercial gasoline were compared (*17*).

TABLE 1 Chemical Parameters of Synthetic Gasoline and Its Components

| Chemicals | Percentage by weight | Molecular Weight | Saturated Vapor Concentration at 20° (mg/l) | Aqueous Solubility at 20° C (mg/l) | Henry's Law Constant** | Octanol/water Partition Coefficient at 20° ($logP_{oct}$) |
|---|---|---|---|---|---|---|
| Pentane | 28.5 | 72 | 1689* | N/A | 4299.67 | N/A |
| n-Hexane | 28.5 | 86 | 630** | 10** | 5663.95 | N/A |
| Benzene | 6.2 | 78 | 300** | 1780** | 18.07 | 2.13* |
| Toluene | 30.7 | 92 | 130** | 515** | 21.38 | 2.69* |
| o-Xylene | 6.1 | 106 | 30** | 152** | 21.60 | 2.77* |
| Commercial Gasoline | N/A | N/A | 411** | 156** | N/A | N/A |
| Synthetic Gasoline | 100 | N/A | N/A | N/A | N/A | N/A |

## Equipment

The centrifuge at the New Jersey Institute of Technology is a 5-g ton machine. It is equipped with 16 slip-rings and two hydraulic glands. It can reach a maximum speed of 450 rpm. The radius of the centrifuge is 0.65 m. The arms of the centrifuge are connected to swing-up buckets of internal dimension 32.0 cm × 25.4 cm × 20.3 cm. A special container was designed to maintain the inclined groundwater table that reduced the maximum size of the sample to 23 cm × 22 cm × 19 cm. This special container with several tubes in the inner walls was able to simulate the inclined groundwater table and the flowing groundwater. A video camera and a pre-amplifier were mounted inside the centrifuge. A 16-bit high-speed data acquisition card in a PC was used to acquire the data from the centrifuge. The speed of the centrifuge during each Test was maintained at 400 rpm. Therefore, the gravitational level for each test varied between 93 at the top of the sample and 114 at the bottom of the sample, times the actual gravity, with an average of 104 g ($N = 104$).

## Dimensions of Simulated Prototype

The plan area of each simulated site was 26 m × 25 m. The gasoline tank was a cylindrical drum of 2.0 m height and 6.4 m inside diameter. A hole was drilled at the center of the tank to simulate a leaking UST. The tank was installed at the middle of the site with its bottom at 2.0 m below the ground surface and top flush with the ground surface. The model dimension may be obtained by using a scale of 1/104. The geometrical symmetry of the site was taken advantage of to interpolate the data.

Three tests are reported in this paper. Test 1 consisted of 10.4 m of compacted kaolin on top of a 2.60 m thick aquifer consisting of Ottawa C30 sand. The water table was located at the top of the aquifer. Test 1 simulated 30 years [model time may be obtained by using a scale factor of $(1/104)^2$] of contamination. The total leakage was 24,747 L [model volume may be obtained by using a factor of $(1/104)^3$]. At the end of the simulation period, five borings extending to the top of the aquifer were made using a miniature boring tool. The borings were located at (*a*) the center of the tank (Point A); (*b*) 2.08 m (2 cm on model) north of point A (Point B); (*c*) 4.16 m east of A (Point C); (*d*) 6.24 m west of A (Point D); and (*e*) 8.32 m south of A (Point E). Five soil samples were taken from each boring, except for Point A, and were located at (*a*) the top of the soil layer; (*b*) a depth of 2.6 m (2.5 cm on model); (*c*) a depth of 5.2 m; (*d*) a depth of 7.8 m; and (*e*) the bottom of the soil layer. At Point A only four samples were taken at 2.6 m, 5.2 m, 7.8 m, and 10.4 m depths.

Test 2 consisted of 10.4 m of compacted sandy soil on top of a 2.60 m thick aquifer. The water table was located at the top of the aquifer. Test 2 simulated 28.7 years of gasoline contamination with total leakage of 44,995 L occurring over a period of 12.3 years as determined from the results of preliminary tests. There was no leakage for the rest of the 14.4 years. At the end of the simulation period five borings extending to the depth of the aquifer were made at (*a*) Point A located at the center of the tank; (*b*) Point B located 3.12 m (3 cm on model) north of Point A; (*c*) Point F located 6.24 m east of Point A; and (*e*) Point G located 9.36 m west of Point A; (*e*) Point H located 12.48 m south of Point A. Five soil samples were taken from each boring at the depths specified in Test 1.

In Test 3 the soil profile was the same as that in Test 2 except the water table was within the compacted soil layer and was located 5.7 m below the top of the soil layer. This test simulated 29.6 years of gasoline contamination. A total leakage of 17,998 L occurred over the first 6 years with no leakage for the rest of the 23.6 years. At the end of the simulation period five borings were made at the locations described in Test 2.

## Soil and Groundwater Sampling and Analysis

Before describing the procedure for soil and groundwater sampling, and chemical analyses, the field procedure is described. The soil samples from sites contaminated by leaking UST were obtained by boring. The groundwater samples were obtained from wells. In this centrifugal simulation a similar procedure was used to obtain the soil and groundwater samples. A miniature boring tool was fabricated to obtain the soil samples. It had an internal diameter of 0.95 cm and an external diameter of 1.27 cm. A sharp end was obtained by machining as in regular boring devices. The soil and groundwater samples from the field were usually analyzed using EPA Method 5030 (*18*). It was developed to measure the amount of volatile organic contaminants in the soil or water and was expressed as parts per million or parts per billion of soil or water.

When this research was first initiated, a purge-and-trap device was not available. Hence it was decided to modify the test proce-

dure for analysis. A soil sample containing roughly 0.8 g of wet soil extruding from the boring tool was put into a 5 ml vial with a Teflon septum. Methanol has a similar retention time as pentane and hexane, and carbon disulfide, so a solvent that did not produce a peak was used in this research. A predetermined volume of carbon disulfide was injected into each of the vials. Vials were shaken for 24 hours to extract all the gasoline from the solid, liquid and gaseous phases into the carbon disulfide. A 0.4 gml of solution extracted from each vial was directly injected into the GC equipped with FID for analysis.

### Centrifugal Simulation

The four main items of this phase were: (*a*) sample preparation, (*c*) spinning of the centrifuge, (*c*) soil sampling and GC analysis of soil samples, and (*d*) interpolation and contouring of data.

#### *Sample Preparation*

The site was prepared by adding water and maintaining the water table at the desired level. To form the aquifer Ottawa sand was wet pluviated to obtain a final height of 2.6 m (2.5 cm in the model). The top of the sand layer was leveled. For Test-1 air dried kaolin was mixed with 35 percent by weight of water and was compacted to a final unit weight of 13.8 kN/m$^3$ in four equal layers. Care was taken to make the clay homogeneous in the transverse direction. For Test 2 and Test 3 air dried sandy soil was mixed with 5 percent water by weight and was compacted to a final unit weight of 13.8 kN/m$^3$ in four equal layers. The empty gasoline tank was installed after excavating the compacted soil.

#### *Spinning and Soil Sampling*

The container with the prepared site model was installed in the centrifuge and the centrifuge was spun for 20 hours (actual time) for the sample to consolidate and further compact under centrifugal gravity (104 g). After 1 day the centrifuge was stopped. To conform to the design water table, water had to be removed in Test 1 and added in Test 2 and Test 3. The centrifuge was spun again for an additional day for the sample to reach hydrogeological equilibrium (i.e., suction, capillary fringe, and degree of saturation). At the end of 20 hours, if the sample met the desired prototype conditions synthetic gasoline was added to the tank, the centrifuge was accelerated to reach 400 rpm, and the clock was started to account for gasoline leakage. At the end of the simulation time corresponding to the desired prototype, the centrifuge was stopped and borings were made and soil samples were taken at the locations and depths described earlier. A total of 25 soil samples was taken with each sample containing roughly 0.8 g of wet soil, and was placed into 5 ml vials with Teflon septums.

#### *GC analysis*

Three milliliters of carbon disulfide were injected into each of the vials from Test 1, and 1 ml was injected into each of the soil samples obtained from Tests 2 and Test 3. The clay soil required a larger quantity of the solvent because of large surface area. Vials were shaken for 24 hours to extract all the gasoline from the solid, liquid and gaseous phases into the carbon disulfide. A 0.4 gml of solution extracted from each vial was injected into the GC for analysis.

#### *Data Interpolation and Contouring*

To generate the contours of gasoline and chemical fractions (concentrations) interpolation of the data points was made at the symmetrical points. For this purpose the z-axis or vertical axis was located at the center of the tank, which is also the source of leakage. Because of the symmetry about the z-axis the mirror image of a data point was assumed to have the same chemical fractions (concentration) as the data point itself. Thus the 24 real data points yielded a total of 44 data points because the data points along the z-axis yielded points that were coincidental with their respective images. These 44 data points served as input data to generate the contours of chemical fractions (concentrations).

## EXPERIMENTAL RESULTS AND DISCUSSION

Figure 1 shows the contours of total gasoline fraction (concentration) in the soil expressed as ppm for Test 2 at the end of a simulation period of 28.7 years. The leaked gasoline moved as a front and accumulated as a pool of free product above the capillary fringe. In a laboratory physical model test (*7*) it was reported that in a sand with a permeability of 0.4 cm/s gasoline seeped vertically down and accumulated above the capillary fringe when the water table was stationary, that is, when there was no groundwater flow. Furthermore, a substantially higher fraction (concentration) of gasoline was observed directly below the leakage source. The contours depicting the thickness of the gasoline in the mound showed decreasing thickness with increasing radial distance from the center. Also these contours were symmetrical about the source. The contour plot in Figure 1 corroborates these findings. Gasoline was nonexistent at the source of leakage because it was exhausted at the end of the first 12.3 years. Thus, the hydrocarbon fraction (concentration) decreased from the top of the aquifer toward the UST. The borings did not extend into the aquifer; therefore no information is available for the aquifer. The residual gasoline fractions within the silt layer for all the points except for the points shown in Figure 1 were below 0.01 percent or 100 ppm. The above data suggest that the gasoline infiltrated the soil as a front and became accumulated above the capillary fringe.

The contours for Test 3 are plotted in Figure 2. Note that the contours are quite similar to those in Test 2. Although the total amount of gasoline was about 60 percent less than Test 2, it took 6 years for the leakage to occur. Although there was dissolved gasoline in the water below the water table its maximum gasoline fraction was less than 0.015 percent or 150 ppm. The transport of gasoline below the water table appears to be dominated by the physical process of diffusion.

The contours of total gasoline fraction and its components after 30 years of continuous leakage for Test 1 are shown in Figure 3. Note that the gasoline has moved laterally to a considerable distance and has gone above the location of the leakage source (against gravity) which can occur only because of molecular diffusion. The clay soil is compacted wet of optimum ($S_r$ = 60 percent), and the hydraulic conductivity of the clay was very low ($k_w = 2 \times 10^{-7}$ cm/sec), so the physical process of advection played a minor role in

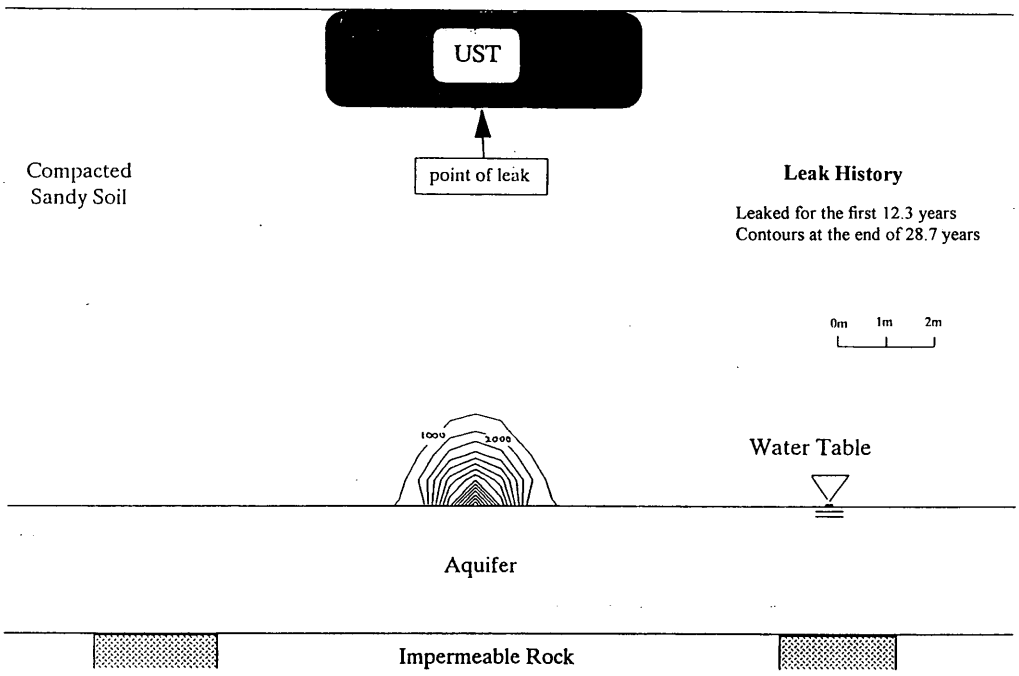


**FIGURE 1 Gasoline concentration profile for Test 2 (contour lines in ppm).**

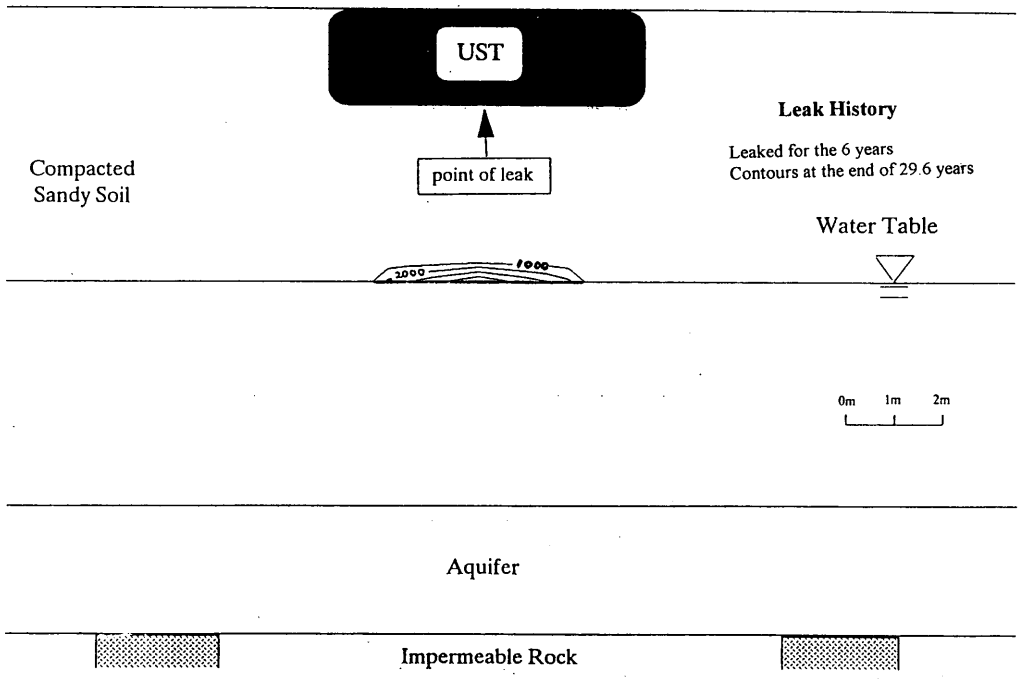


**FIGURE 2 Gasoline concentration profile for Test 3 (contour lines in ppm).**

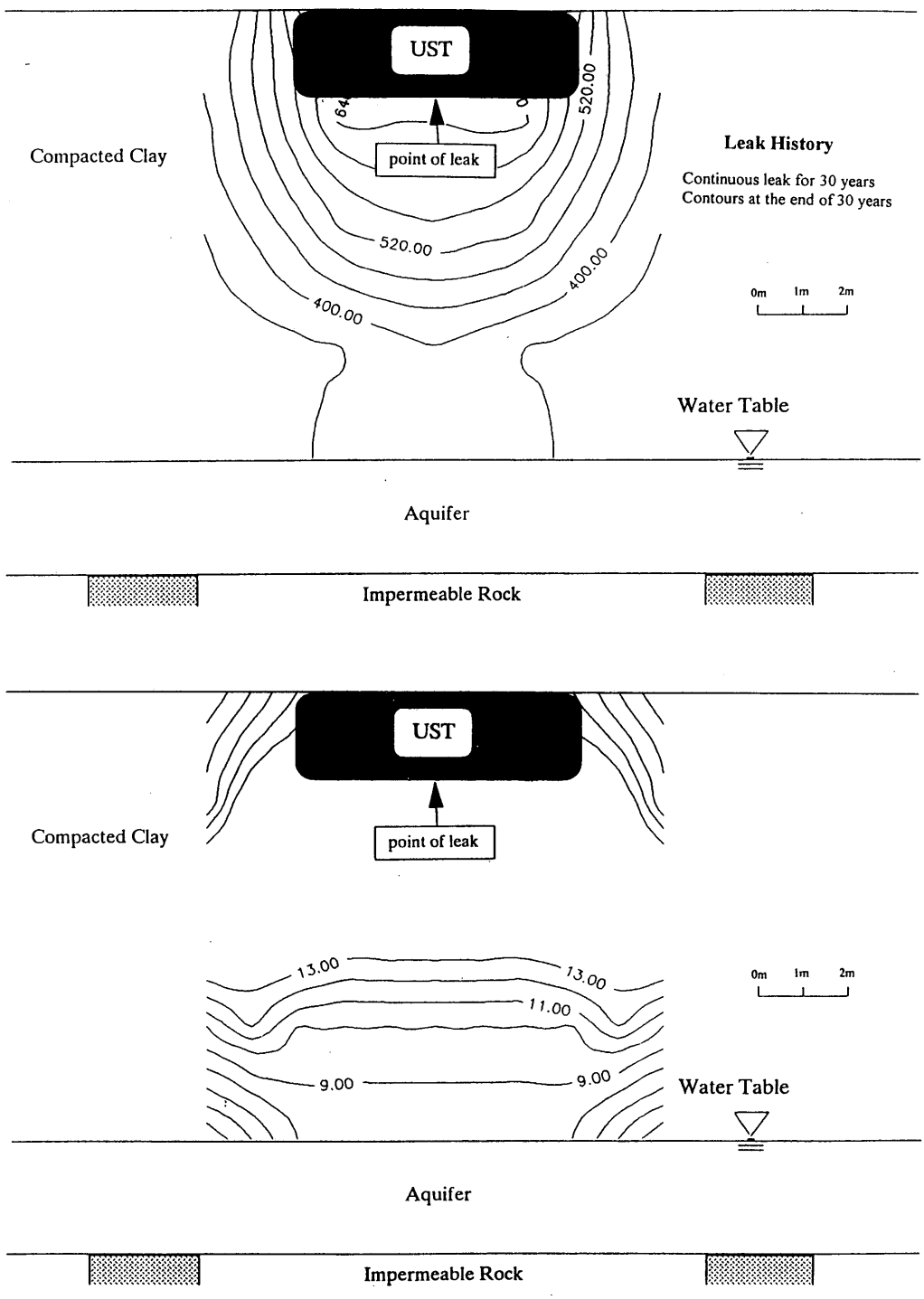


(*a*)

**FIGURE 3 Gasoline concentration profile for Test 1 (all contour lines in ppm). (a) Pentane concentration profile for Test 1. (b) Hexane concentration profile for Test 1. (c) Benzene concentration profile for Test 1. (d) Toluene concentration profile for Test 1. (e) Xylene concentration profile for Test 1.**

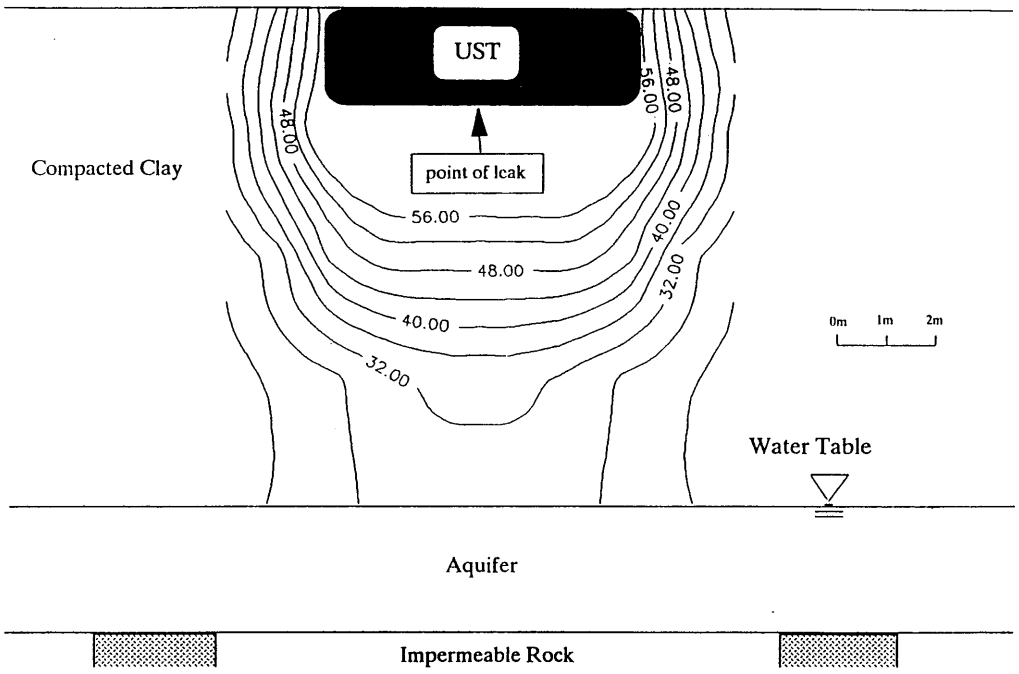


(*b*)

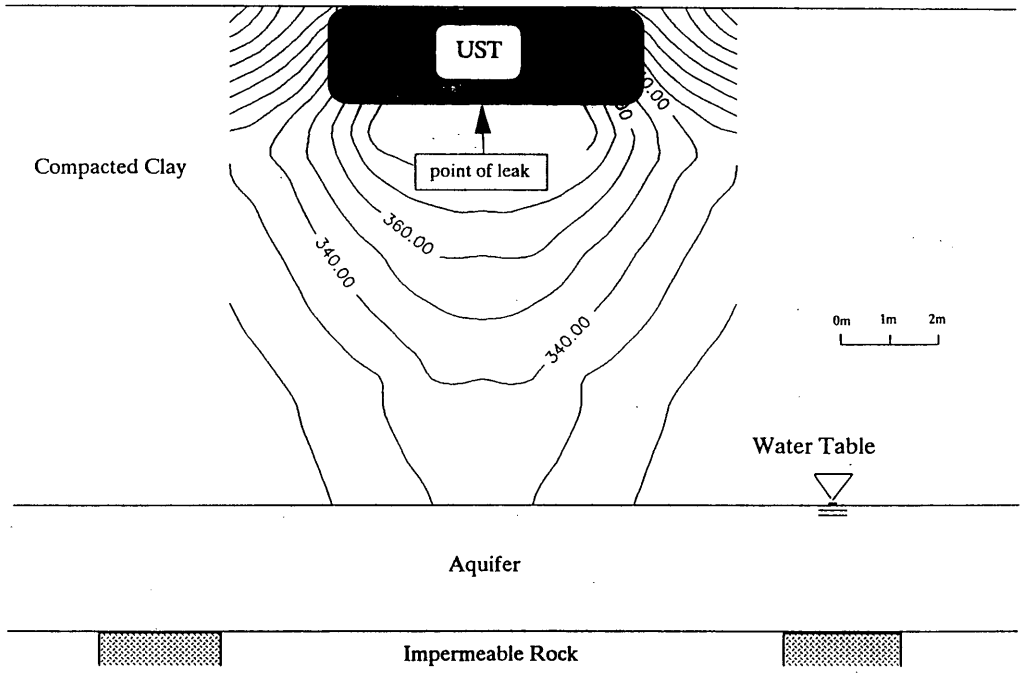


(*c*)

**FIGURE 3** *continued*

(*Continued on next page*)

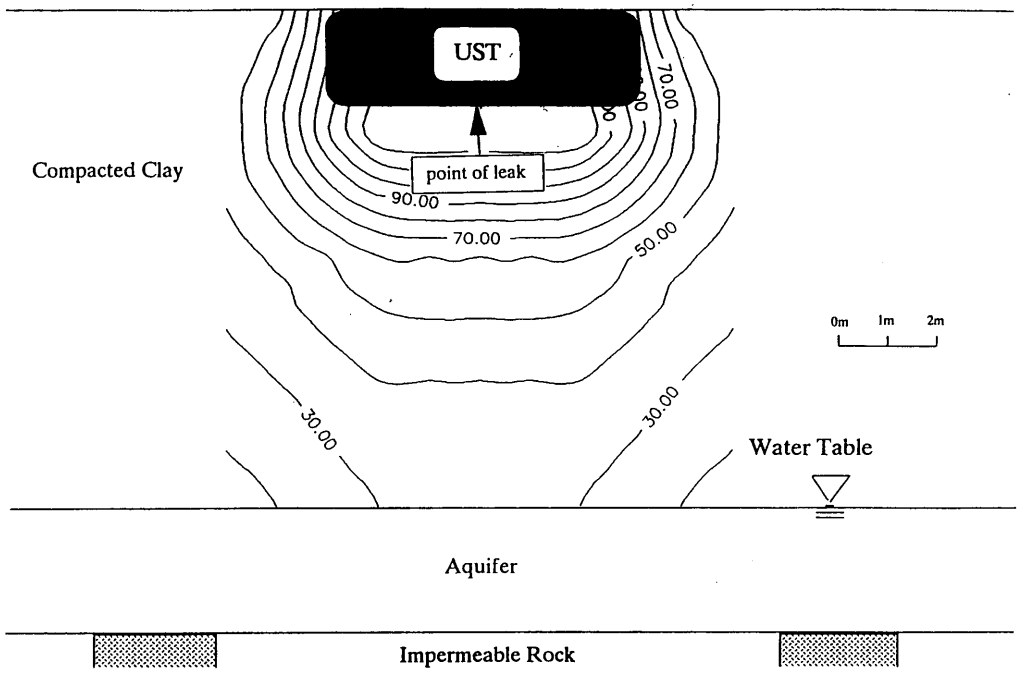


(*d*)

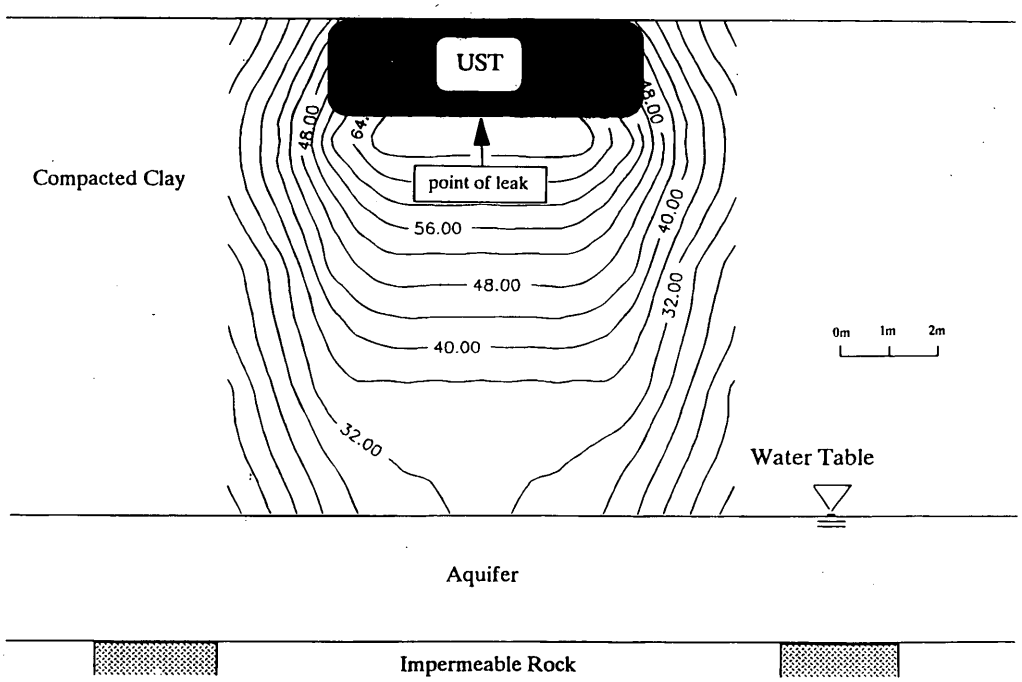


(*e*)

**FIGURE 3** *continued*

the movement of contaminants through the clay. The greater spread in lateral directions may be due to the anisotropy of the clay layer resulting from lower tortuousity of the path in the lateral direction as the result of manual and centrifugal compaction of the clay. Even though the same volume of gasoline was stored in this tank as that in Test 2, nearly one-third did not leak. This indicates that the rate of leakage may be governed by both the soil type underneath a UST and the size of the hole.

As seen in Figure 3*a*, contours for pentane had the lowest level of all of the chemicals present even though its proportion in the tank was among the highest. Its partition coefficient was not available, so no further comments can be made about these contours. It is also believed that the higher vapor pressure resulted in evaporation of most of the pentane leaving only residual values in the soil.

Although the benzene fraction was the second lowest in the synthetic gasoline, as shown in Figure 3*c*, it yielded the highest levels in the soil. Below the center of the tank at 3 m and 6 m depths the benzene fractions were 360 ppm and 340 ppm, respectively. Even though the amount of toluene in the UST was five times more than benzene (Table 1) it showed the lowest levels of 65 ppm and 39 ppm at the corresponding depths as shown in Figure 3*d*. Table 1 shows that the water solubility of benzene is more than three times that of toluene. The water content of the soil was about 35 percent, so the higher water solubility of benzene facilitated its movement.

Figures 3*a* and *e* show contours for hexane and xylene fractions and both chemicals have essentially identical amounts of about 52 ppm and 34 ppm at 3 m and 6 m depths, respectively. The proportions of free hexane to xylene in the synthetic gasoline were almost the same as that of toluene to benzene but the water solubility of xylene is about 16 times that of hexane (Table 1). Apparently the larger proportion of available hexane has overcome its much lower water solubility.

As seen in Figures 3*b* and *d*, hexane showed slightly lower value in the soil than toluene even though both of them comprised about the same fraction in the synthetic gasoline. Note that the water solubility of toluene is 51.5 times greater than that of hexane. The much higher water solubility of toluene did not have as profound an effect on its movement as was observed for benzene. Clearly there is high correlation between water solubilities and the movement of chemicals in soil. Other factors, such as selective transport and saturated vapor pressures, contribute to the movement of chemicals in soils. Therefore, additional experimental investigations are needed to understand mechanisms behind the movement of a group of chemicals through fine grained soils to accurately model their movement and subsequent fate and transport. There was a considerable spread of contaminants in the lateral direction, bulging of contours in the lateral direction, suggesting the contribution of soil anisotropy to movement of chemicals. This is an observation that cannot be simulated in a column test.

The difficulties commonly encountered in obtaining samples during field explorations were also present in this modeling technique. Even when care was taken during soil sampling, there was soil contamination from the boring/sampling device when samples were obtained from different depths. To minimize soil contamination because of sampling, the sampling was started from points with the lowest contamination levels and proceeded to higher levels. Baking the capillary column between GC analyses reduced cross-interference.

## CONCLUSIONS

Three sites with leaking UST were simulated in the centrifuge to determine the movement and subsequent fate and transport of gasoline and its components in the vadose zone. The test results on the sandy or coarse-grained soil showed that gasoline moved because of the physical process of advection and was retained as a pool of free product above the water table. These test results corroborate data reported from laboratory physical models. Therefore it may be concluded that the centrifuge looks feasible to be used as a research/design tool to generate data for unsaturated sites with coarse-grained soils contaminated by leaking UST.

The test results on the clay or fine-grained soil provided the following conclusions:

- The rate of leakage depends on both the type of soil underneath the UST and the amount of corrosion, that is, a UST with a higher corrosion rate may not have larger leakages in fine grained soils.
- The movement of gasoline is not dominated by the physical process of advection as for coarse-grained soils and hence pooled free product was not observed at the water table depth even after 30 years of simulated leakage.
- The movement is not dominated by the physical process of advection, so the contour profile of a given chemical within the soil depends on its water solubility and its fraction in the gasoline.
- There was a considerable spread of contaminants in the lateral direction, an observation that cannot be simulated in a column test.
- The spread of gasoline strongly depends on the anisotropy of the soil through which it travels as indicated by the bulging of contours in the lateral direction.

## ACKNOWLEDGMENTS

The authors acknowledge Antony Tafuri and C. Y. Fan of the USEPA, Angel Perez-Cobo of the Caltrans, Bonnie DuBose and Lobo Huang of NJIT.

## REFERENCES

1. USEPA. Must for USTs: A Summary of the New Regulations for the Underground Storage Tank Systems. Report EPA/530/UST-88/008. Office of Underground Storage Tanks, USEPA, Washington, D.C., 1988.
2. Rosenberg, M. S., D. Noonan, and C. Y. Fan. Assessing UST Corrective Action Technologies, Risk Reduction Engineering Laboratory, Office of Research and Development, USEPA, Cincinnati, Ohio, 1988.
3. Baehr, A. L. Selective Transport of Hydrocarbons in the Unsaturated Zone due to Aqueous and Vapor Phase Partitioning. *Water Resources Research*, Vol. 23, No. 1, 1987, pp. 1926–1938.
4. Ryan, P. A., and Y. Cohen. 1-D Subsurface Transport of a NAPL Containing Sparingly Water Soluble Organics: A Front Tracking Model. *Water Resources Research*, Vol. 27, No. 7, 1991, pp. 1487–1500.
5. Parker, J. C., R. J. Lenhard, and T. Kuppusamy. A Parametric Model for Constitutive Properties Governing Multiphase Flow in Porous Media. *Water Resources Research*, Vol. 23, No. 4, 1987, pp. 618–624.
6. Reible, D. D., T. H. Illangasekare, D. V. Doshi, and M. E. Malheit. Infiltration of Immiscible Contaminants in the Unsaturated Zone. *Groundwater*, Vol. 28, No. 5, 1990, pp. 685–692.
7. Schwille, F. Groundwater Pollution in Porous Media by Fluids Immiscible with Water. *The Science of the Total Environment*, Vol. 21, 1981, pp. 173–185.
8. Parmer, C. D. Characterization of Subsurface Physicochemical Process, USEPA Seminar on Site Characterization for Subsurface

Remediation. Report CER1-89-224. USEPA, Washington, D.C., 1989.
9. Arulanandan, K., P. Y. Thompson, B. L. Kutter, N. J. Meegoda, K. K. Muraleetharan, and C. Yogachandran. Centrifugal Modeling of Transport Processes for Pollutants in Soils. *ASCE, GTE*, Vol. 114, No. 2, 1988, pp. 185–205.
10. Celorie, J. A., T. S. Vinson, S. L. Woods, and J. D. Istok. Modeling Solute Transport by Centrifugation. *ASCE, EED*, Vol. 115, No. 3, 1989, pp. 513–526.
11. Meegoda, N. J., and K. G. Chang. Discussion on "Modeling Solute Transport by Centrifugation." *ASCE, EED*, Vol. 117, No. 3, 1991, pp. 388–389.
12. Nimmo, J. R., J. Rubin, and D. P. Hammermesiter. Unsaturated Flow in a Centrifugal Field: Measurement of Hydraulic Conductivity and Testing of Darcy's Law. *Water Resources Research*, Vol. 23, No. 1, 1987, pp. 124–134.
13. Nimmo, J. R. Experimental Testing of Transient Unsaturated Flow Theory at Low Water Content in a Centrifugal Field. *Water Resources Research*, Vol. 26, No. 9, 1990, pp. 1951–1960.
14. Krahn, J., and D. G. Fredlund. On Total, Matric and Osmotic Suction. *Soil Science*, Vol. 114, No. 5, 1972, pp. 339–348.
15. Croney, D., and J. D. Colman. Pore Pressure and Suction in Soils. Butterworths, London, 1960.
16. Illangasekare, T. H., D. Znidarcic, M. Al-Sheridda, and D.D. Reible. Multiphase Flow in Porous Media. *Proc., International Conference—Centrifuge 1991*, Boulder, Colo., June 13–14, 1991, pp. 517–523.
17. Meegoda, N. J., S. Gunasekera, S., and R. Hyjack. A New Method to Model Transport and Fate Gasoline from Leaking USTs. *Proc., Twenty-first Mid-Atlantic Industrial Waste Conference*, Harrisburg, Pa., June, 1989, pp. 582–595.
18. USEPA. Test Methods for Evaluating Solid Waste: Physical/Chemical Methods. Report SW-846. USEPA, Washington, D.C., 1986.
19. Verschueren, K. Handbook of Environmental Data on Organic Chemicals. Van Nostrand Reinhold Company, N.Y., 1983.
20. Bruell, C. J., and G. E. Hoag. The Diffusion of Gasoline-Range Hydrocarbon Vapors in Porous Media, Experimental Technologies. *Proc., NWWA/API Conference on Petroleum Hydrocarbons and Organic Chemicals in Ground Water*, November, 12–14, Houston, Tex, 1986.

*Publication of this report sponsored by Committee on Modelling Techniques in Geomechanics.*

# Response of Pavement Systems to Dynamic Loads Imposed by Nondestructive Tests

RAFAEL FOINQUINOS, JOSE M. ROESSET, AND KENNETH H. STOKOE II

Dynamic nondestructive testing of pavements can be grouped into two categories: (a) deflection basin tests and (b) wave propagation tests. Among the deflection basin tests, the Falling Weight Deflectometer test (FWD) has seen the most widespread use. Of the wave propagation tests, the Spectral Analysis of Surface Waves (SASW) test can be used with or serve as an alternative to deflection basin tests. The theoretical formulation used to analyze the dynamic response of pavement systems to dynamic loads imposed by such nondestructive testing techniques is presented. Analytical studies of the dynamic response of two generalized pavement systems (a flexible one and a rigid one) to the FWD and SASW tests were carried out. The results indicate that dynamic deflection basins due to the FWD load can be substantially different from those obtained under static conditions. The study shows that when complete time histories of FWD deflections are stored, the additional information can provide substantial insight into the properties of the pavement system and can significantly facilitate the inversion process. The dispersion curves obtained with the SASW test are very sensitive to the stiffness of the surface and subgrade layers but, unfortunately, are relatively insensitive to the properties of the base layer. These results are true even when bedrock is present at shallow depths.

Dynamic nondestructive testing techniques have been used for years to evaluate the structural capacity and integrity of highway and airfield pavements. These techniques can be grouped into two categories: (a) deflection basin tests and (b) wave propagation tests. Deflection basin tests are those in which maximum deflections are recorded along the surface of a pavement subjected to a steady-state harmonic load or a transient dynamic load. Typical of this group are the Dynaflect and Road Rater tests (steady-state loads) and the Falling Weight Deflectometer test (transient load) [Uddin (*1*)]. At present, interpretation of deflection basins, in order to backfigure the moduli of the pavement layers, is normally performed with static analyses and assuming that the subgrade extends to infinity. This approach neglects the dynamic nature of these tests and the fact that, in many cases, the soil will be underlain at some depth by much stiffer, rocklike material.

The second category of dynamic nondestructive tests is wave propagation tests. In these tests, the time histories of motion due to an applied dynamic load are recorded at two or more receivers on the pavement surface. By computing the surface wave travel time between adjacent receivers for different excitation frequencies, a dispersion curve is obtained relating phase velocities to frequencies (or wavelengths). Thicknesses and stiffnesses of the pavement layers are then obtained by an inversion process based on the propagation of generalized plane surface waves of the Rayleigh type. This type of test is represented by the Spectral Analysis of Surface Waves (SASW) method [Nazarian and Stokoe (*2*)].

Among these testing techniques, the Falling Weight Deflectometer (FWD) test has seen the most widespread use, largely because of its ability to impose on a pavement high-amplitude dynamic loads similar to those imposed by truck traffic. The FWD consists of a drop weight mounted on a vertical shaft and housed in a trailer that can be towed by most conventional vehicles. The drop weight is hydraulically lifted to predetermined heights ranging from 5 to 51 cm (2 to 20 in.). The weight is dropped onto a 30-cm-(11.8-in.-)in diameter loading plate resting on a 5.6-mm-(0.22-in.-)thick rubber buffer. The resulting load is a force impulse with a duration of approximately 30 msec and a peak magnitude ranging from about 9,000 to more than 90,000 N (2,000 to 20,000 lb), depending on the drop height and drop weight. The force and deflection signals at various points along the surface are measured by a load cell and a set of vertical velocity transducers. The position of the load and recording stations are shown in Figure 1(*a*).

In the SASW test, an impulsive load is applied at the surface, and the passage of the surface wave train is monitored at two vertical receivers, also located on the surface. A spectral analysis of the two recorded signals is performed, and the variation of the surface wave velocity with frequency or wavelength (dispersion curve) is found. The general arrangement of the source, receivers, and recording equipment is shown schematically in Figure 1(*b*). A piezoelectric shaker can be used to generate surface waves ranging from about 1 kHz to 50 kHz. The high frequencies are necessary to sample the stiff surface layer. A digital waveform analyzer, coupled with a microcomputer, is used to capture and process the output from the receivers. Compared with the FWD test, the SASW test imposes smaller loads on the pavement surface, but data analysis is more complex, and automation is less well-developed in the SASW test than in the FWD test.

An analytical study of the dynamic response of pavement systems to forces simulating the excitations of the FWD and SASW tests is presented. The FWD deflection basins obtained with a dynamic model and those computed with static analyses are compared. The effects of the depth to bedrock on the deflection basins (FWD) and on the dispersion curves (SASW) are investigated. The sensitivity of both types of tests to the properties and thicknesses of the various layers is also discussed.

## THEORETICAL FORMULATION

To understand how a pavement system responds to dynamic loads applied to the surface, a review of the theoretical studies that deal with the dynamic response of uniform and layered systems is necessary.

### Dynamic Loads on a Semi-Infinite Medium

Lamb (*3*) was the first to study the effect of a pulse on a uniform elastic half-space. Lamb treated four basic problems: surface line

Department of Civil Engineering, The University of Texas at Austin, Austin, Texas 78712-1076.

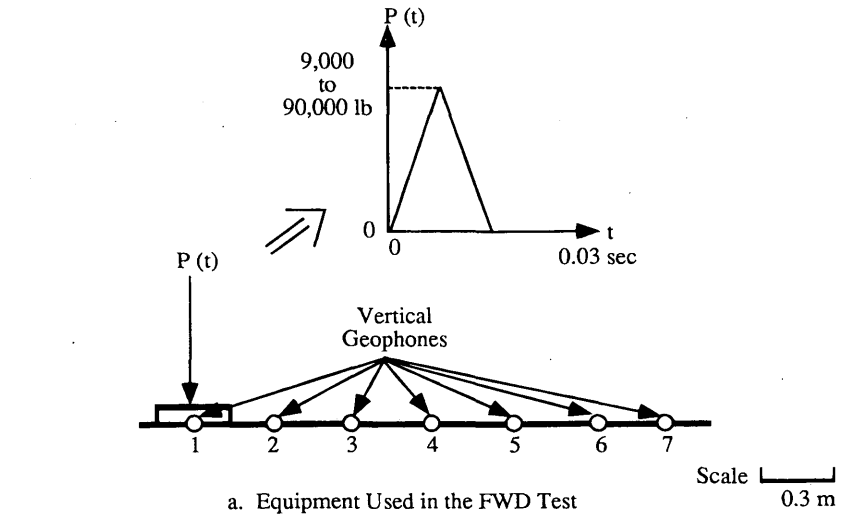


a. Equipment Used in the FWD Test

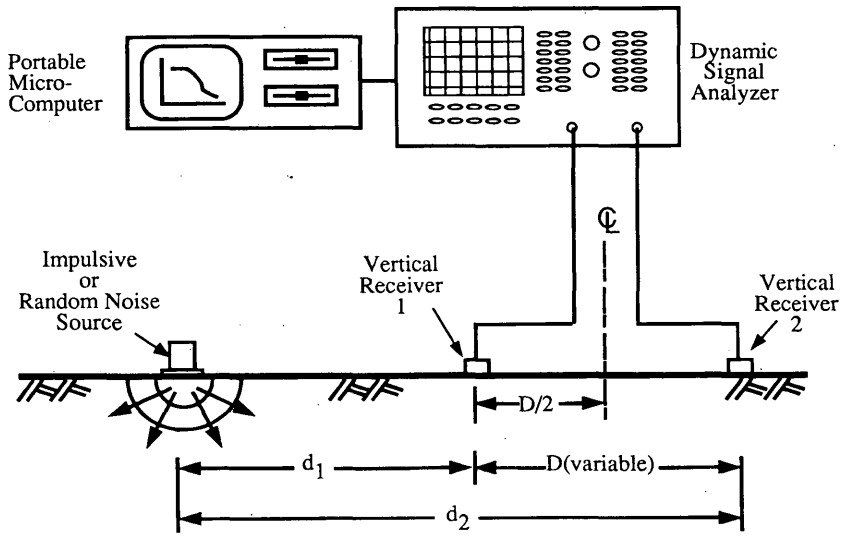


b. Equipment Used in the SASW Test

**FIGURE 1 General configuration of equipment used in FWD and SASW testing of pavements.**

and point load sources, and buried line and point load sources. He derived a solution to these problems through Fourier synthesis of the steady-state propagation solution. For the surface source problem, Lamb evaluated the surface displacements (horizontal and vertical), and noted that the largest disturbance in the far field is the Rayleigh surface wave. He noted the nondispersive nature of the solution, and that for a point-load excitation, the displacement decays as $\sqrt{r}$, where $r$ is the distance from the source. Through the years these problems have taken on the name, Lamb's problem.

The first closed-form solution for Lamb's problem in three-dimensional space was provided by Pekeris (*4*) for the case a material with Poisson's ratio of 0.25. A generalization for arbitrary values of Poisson's ratio is due to Mooney (*5*) and also can be found in Eringen and Suhubi (*6*); however, the Green's functions (in the time domain) for this case are available only for a vertical point pulse with a step time-function acting on the free surface.

Miller and Pursey (*7*) considered the case of a circular disk vibrating harmonically and normally on the free surface of a half-space. They found explicit expressions for the displacements at points at large distances from the loaded area. These expressions for the horizontal and vertical ($u$, $w$) displacements at the surface of the medium due to a unit disk load are of the form

$$f(\nu) \cdot \frac{R^2}{G} \cdot \sqrt{\frac{\omega}{Cr \cdot r}} \cdot e^{-i\frac{\omega \cdot r}{Cr}}$$

where

$R$ = the radius of the disk load,
$G$ = the shear modulus of the medium,
$\omega$ = the circular frequency of excitation,
$Cr$ = the Rayleigh wave velocity of the medium, and
$r$ = the distance to the source.

The term $f(\nu)$ is a complex function of Poisson's ratio, for instance, for $\nu = 1/3, f(\nu) = -0.182(\sqrt{2}/2 + i\sqrt{2}/2)$ for the horizontal displacement, and $0.286(\sqrt{2}/2 - i\sqrt{2}/2)$ for the vertical displacement.

While closed-form solutions to Lamb's problem have significant theoretical uses, it is improbable that exact solutions will become available soon for more complicated material or load configurations because of the mathematical difficulties involved. Thus, for the solution of dynamic problems in layered media such as pavement systems, numerical techniques must be used.

## Dynamic Loads on Layered Media: Application to the Dynamic Analysis of Pavements

Consider a pavement system that consists of horizontal layers. The mass densities and elastic moduli of the pavement system change with depth, from layer to layer, but are (assumed to be) constant over each layer. For the present application, the top layer represents the pavement surface layer (assuming it extends to infinity in both horizontal directions); the second layer is the base; and the remaining layers are the subbase layer, the soil subgrade, or both. Determining how this system responds to dynamic loads applied on the surface (or at any point within the profile) falls mathematically in the realm of wave propagation theory.

Formulation of these problems starts normally by considering steady-state harmonic forces and displacements at a given frequency. For an arbitrary transient excitation (case of the FWD test), the time history of the specified forces must be decomposed into different frequency components using a Fourier series, or more conveniently a Fourier transform. Results are then obtained for each term of the series (each frequency) and combined to obtain the time history of displacements (inverse Fourier transform).

For an isolated layer with uniform properties, the stresses and displacements along the top and bottom surfaces can be expanded in a double Fourier series (or Fourier transform) in the two horizontal directions for Cartesian coordinates, or in a Fourier series in the circumferential direction and a series of modified Bessel functions in the radial direction for cylindrical coordinates. For each term of these series corresponding to a given wave number, closed-form analytical expressions can be determined in the form of a transfer matrix relating amplitudes of stresses and displacements at the bottom surface to the corresponding quantities at the top (or vice versa). This approach [Thomson (*8*) and Haskell (*9*)] has served as the basis for most studies on wave propagation through layered media in the past 35 years. An alternative is to relate the stresses at both surfaces to the displacements, obtaining a dynamic stiffness matrix for the layer [Kausel and Roesset (*10*)], which can be used and understood in much the same way as in dynamic structural analysis. For a half-space, the stiffness matrix directly relates stresses and displacements at the top surface because the bottom surface is pushed to infinity.

For FWD and SASW testing of pavements with an axisymmetric load, only one term of the Fourier series is needed. The displacements $\overline{U}$ and forces $\overline{P}$ in the wave number domain are then related by

$$K\overline{U} = \overline{P} \tag{1}$$

where $K$ is the dynamic stiffness matrix of the profile obtained by assembling the stiffness matrices of the layers and the underlying half-space. For a uniform vertical load applied at the surface over a disk of radius $R$, the only nonzero term of the vector $\overline{P}$ is the second term, which is equal to

$$\frac{q \cdot R}{k} \cdot J_1(kR)$$

where

$q$ = the magnitude of the uniformly distributed load,
$k$ = the wave number, and
$J_1$ = the first order Bessel function.

If $\overline{u}_1$, and $\overline{w}_1$ are the first two terms of the vector $\overline{U}$, obtained by solving Equation 1 for a vector $\overline{P}$ with all components 0 and a 1 as the second term (for every value of $k$), the surface displacements as a function of the distance $r$ to the center of the loaded area become

$$u = q \cdot R \int_0^\infty \overline{u}_1 \cdot J_1(kR) \cdot J_1(kr)dk \tag{2a}$$

$$w = q \cdot R \int_0^\infty \overline{w}_1 \cdot J_1(kR) \cdot J_0(kr)dk \tag{2b}$$

The solution of the problem thus requires assembling the dynamic stiffness matrix $K$ of the layered medium, solving the system of Equation 1 for many different values of $k$ and evaluating numerically the integrals of Equation 2. The numerical integration is performed through shifting the poles of the integrand by including a small attenuation in the materials (for materials with damping, all of the poles are complex, so that no singularities are encountered along the real axis of integration). However, for systems with sharp variations in material properties between layers, the integrands may exhibit considerable waviness, making it difficult to evaluate the integrals. The solution of the equations also is time-consuming when there is a large number of layers. The procedure is convenient when dealing with a homogeneous half-space or a small number of layers.

An alternative can be obtained by expanding the terms of the dynamic stiffness matrix of a layer in terms of $k$ and keeping terms only up to second-degree (the terms of the transfer or stiffness matrices of each layer are transcendental functions). It can be shown that this is equivalent to assuming that the displacements have a linear variation with depth over each layer using standard finite element techniques to derive the layer matrix. The stiffness matrices of each layer, the half-space, and the total profile can then be expressed in the form

$$K = Ak^2 + Bk + G - \omega^2 M \tag{3}$$

The expressions for the matrices A, B, G, and M are given by Kausel and Roesset (*10*). By computing the in-plane modes of propagation as the solution of a quadratic eigenvalue problem (*11,12*) and keeping only the modes propagating outward, Kausel (*13*) has shown that the displacements $\overline{u}_1$, $\overline{w}_1$ in Equation 2 can be expressed as

$$\overline{u}_1 = \sum_{i=1}^{2n+2} \overline{u}_{i1}\,\overline{w}_{i1}\,\frac{k}{k_i(k^2 - k_i^2)} \tag{4a}$$

$$\overline{w}_1 = \sum_{i=1}^{2n+2} \overline{w}_{i1}^2\,\frac{1}{(k^2 - k_i^2)} \tag{4b}$$

for a system with $n$ layers, where $\bar{u}_{i1}$ and $\bar{w}_{i1}$ denote the horizontal and vertical displacements at the surface in the $i$th mode and $k_i$ is the eigenvalue, or wave number, in the $i$th mode. By substituting Equation 4 in Equation 2, the integrals can be evaluated analytically in closed form (*13*).

This formulation requires a subdivision of the layers (thin layers are needed to accurately reproduce the variation of displacements with depth with a piece-wise linear approximation). It is particularly convenient when dealing with a large number of layers, such as when obtaining a detailed variation of soil properties with depth is desired. Furthermore, since the fundamental solutions (or Green's functions) are known explicitly, the displacements or strains at many locations can be determined without significant additional computation.

Both continuous and discrete formulations had been implemented at the University of Texas at Austin [Roesset and Shao (*14*), and Roesset, Stokoe, and Foinquinos (*15*)] to simulate the FWD and SASW tests. Although a large number of sublayers must be used in the discrete formulation to obtain satisfactory results, this formulation has been found in general to be much more efficient computationally than the continuous formulation. Therefore, the results were obtained using the discrete formulation.

## ANALYTICAL STUDIES

Two generalized pavement profiles, a flexible one and a rigid one, were selected to illustrate the dynamic response of the pavement systems to the application of FWD and SASW. Because variations in total unit weight ($\gamma$), Poisson's ratio ($\nu$), and damping ratio ($D$) have minor effects on the dynamic response (within ranges of logical values) compared with changes in the stiffnesses of the layers, they were assumed to be the same for all the layers; that is, $\gamma$ = 18,850 N/m$^3$ (120 lb/ft$^3$), $\nu = 0.35$, and $D = 0.02$. The elastic properties and thicknesses of the layers in both profiles are given in Table 1.

### FWD Testing

#### *Flexible Pavement*

First the dynamic response to the FWD load of a flexible pavement with rigid rock at 6.1 m (20 ft) was computed. Figures 2(*a*) and 2(*b*) show the amplitude of the transfer function of displacements (amplitude of displacements due to a unit harmonic load as a function of frequency) at Station 1, located at the center of the load, and at Station 7, which is the farthest measurement point. For low frequencies, the system behaves as if the load were applied statically. As the frequency increases, the displacements increase until they reach a peak at the same frequency at all stations. The low amplitudes of displacements at high frequencies are a result of inertial effects. These transfer functions are multiplied by the Fourier transform of the excitation and then inverted to obtain the displacement-time histories. Figure 2(*c*) shows the time history of displacements at each station. The main pulse is followed by oscillations with decaying amplitude, which represent the free vibrations of the complete pavement system and the soil subgrade layer in particular. These free oscillations have a well-defined period (which lies between the natural period of the subgrade for shear and compressional waves) and are essentially the same for all the recording stations. The frequency of the free vibration coincides with the frequency of the peak in the transfer functions. Chang et al. (*16*) have suggested a simple formula to estimate the depth to bedrock based on the free vibration period from the displacement-time records. This figure also shows that there is a time offset at the start of the motion and at the occurrence of the peak displacements at the different stations. Seng (*17*) has suggested the use of the offset time to find the shear velocity of the subgrade. Figure 2(*d*) shows the dynamic peak displacement at each station (deflection basin), obtained from the maximum displacement recorded at each receiver.

**TABLE 1 Values of Elastic Properties and Layer Thicknesses of Generalized Pavement Profiles**

| Type of pavement | Layer | Thickness cm (in.) | Young's Modulus MPa (ksi) | Shear wave velocities m/sec (fps) |
|---|---|---|---|---|
| Flexible | Surface | 15 (6) | 3013 (436.7) | 762 (2500) |
| | Base | 30 (12) | 483 (70) | 305 (1000) |
| | Subgrade | variable | 124 (18) | 152 (500) |
| Rigid | Surface | 22.5 (10) | 39020 (5660) | 2743 (9000) |
| | Base | 15 (6) | 3013 (436.7) | 762 (2500) |
| | Subbase | 30 (12) | 483 (70) | 305 (1000) |
| | Subgrade | variable | 124 (18) | 152 (500) |

The effect of depth to bedrock on the FWD deflection basins is considered next. The analysis for the flexible pavement with different depths to bedrock is shown in Figure 3. Figures 3(*a*) and 3(*b*) show the transfer functions at Stations 1 and 7, respectively. As the depth to bedrock decreases, the peak displacement and the frequency at which it occurs increase, but the static displacement decreases. It also can be seen that the dynamic effect is more important at the farthest stations. Figures 3(*c*) and 3(*d*) show the displacement-time histories when the depth to bedrock is 6.1 m (20 ft) and when it extends to infinity. In the second case, the free oscillations are no longer present because there are no reflections from bedrock. Figure 3(*e*) shows that the static displacements are very sensitive to bedrock depth. However, the dynamic deflection basins are nearly independent of the depth to bedrock for depths greater than 3 m (10 ft), as shown in Figure 3(*f*).

#### *Rigid Pavement*

The same type of analysis was performed for the rigid pavement, and the results are shown in Figure 4. It can be observed again that the static displacements are very sensitive to the depth to bedrock, but the dynamic deflection basins are insensitive to this depth. Also, the shape and magnitude of the static and dynamic deflection basins are quite different from the ones for the flexible pavement.

#### *Dynamic Amplification*

The ratio of dynamic to static displacements (amplification factor) at the different stations was computed as a function of depth to bedrock. The results are shown in Figures 5(*a*) and 5(*b*) for flexible and rigid pavements, respectively. For these profiles the maximum amplification occurs at a depth to bedrock of about 2.1 to 3 m (7 to 10 ft). This means that for shallow profiles the use of a back-calcu-

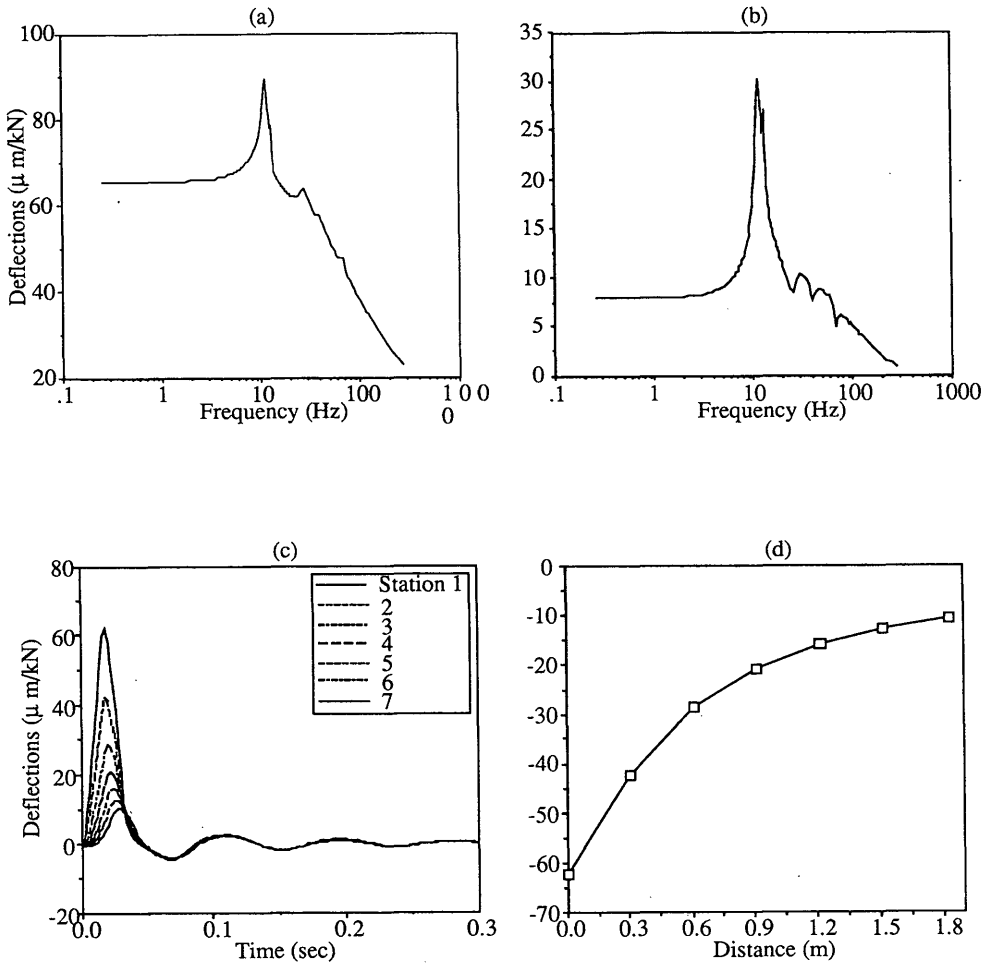


**FIGURE 2 Dynamic response of a flexible pavement with bedrock at 6.1 m to FWD loading: (a) and (b) transfer functions at recording Stations 1 and 7, (c) displacement-time histories and (d) measured deflection basin.**

lation process based on static analysis (with a known depth to bedrock) would lead to an underestimation of the stiffness of the subgrade layer and associated complications in evaluating the other layers. For the rigid pavement, the deflection ratio becomes less than 1 for depths greater than about 4.5 m (15 ft). In this range a static back-calculation procedure would lead to an overestimation of the stiffness of the subgrade layer and associated complications in evaluating the other layers.

In static back-calculation procedures it is often assumed that the subgrade is an elastic half-space. It is therefore more interesting to compare the dynamic results for a given depth to bedrock with the static deflections for an infinite depth to bedrock. The ratios of these deflections are shown in Figures 5(*c*) and 5(*d*) for flexible and rigid pavements, respectively. The results indicate that the dynamic deflections are smaller than the static deflections for a half-space (although they can be larger than the static deflections for the same profile with a finite bedrock depth). This implies that the static back-calculation process as normally applied will lead to an overestimation of the stiffness of the layers, particularly for shallow profiles. It can also be observed that the dynamic peak displacements remain constant for a depth to bedrock greater than about 4.5 m (15 ft). This depth depends mainly on the properties of the subgrade (Seng, 1992).

## SASW Testing

The effect of depth to bedrock on the theoretical dispersion curves obtained with the SASW test are shown in Figure 6 for the flexible pavement. Figure 6(*a*) shows the case in which the subgrade extends to infinity. For very short wavelengths (high frequencies), the phase velocity is approximately equal to the Rayleigh wave velocity of the surface layer and remains almost constant until the wavelength approximately equals the thickness of the surface layer. For long wavelengths (low frequencies), the phase velocity approaches the Rayleigh wave velocity of the subgrade. Figure 6(*b*) shows the dispersion curve with a finite depth to bedrock [6.1 m (20 ft)] and Figure 6(*c*) shows the variation of the dispersion curves for different depths to bedrock [the rock was considered to have a shear wave velocity of 1,524 m/sec (5,000 ft/sec)]. Figure 6(*c*) shows that the dispersion curves start bending upward at a wavelength which is approximately equal to the depth to bedrock.

Therefore, bedrock does not affect any of the measurements performed at wavelengths shorter than the depth to bedrock. The same type of analysis was performed for the rigid pavement, and the results are qualitatively the same as those of the flexible pavement.

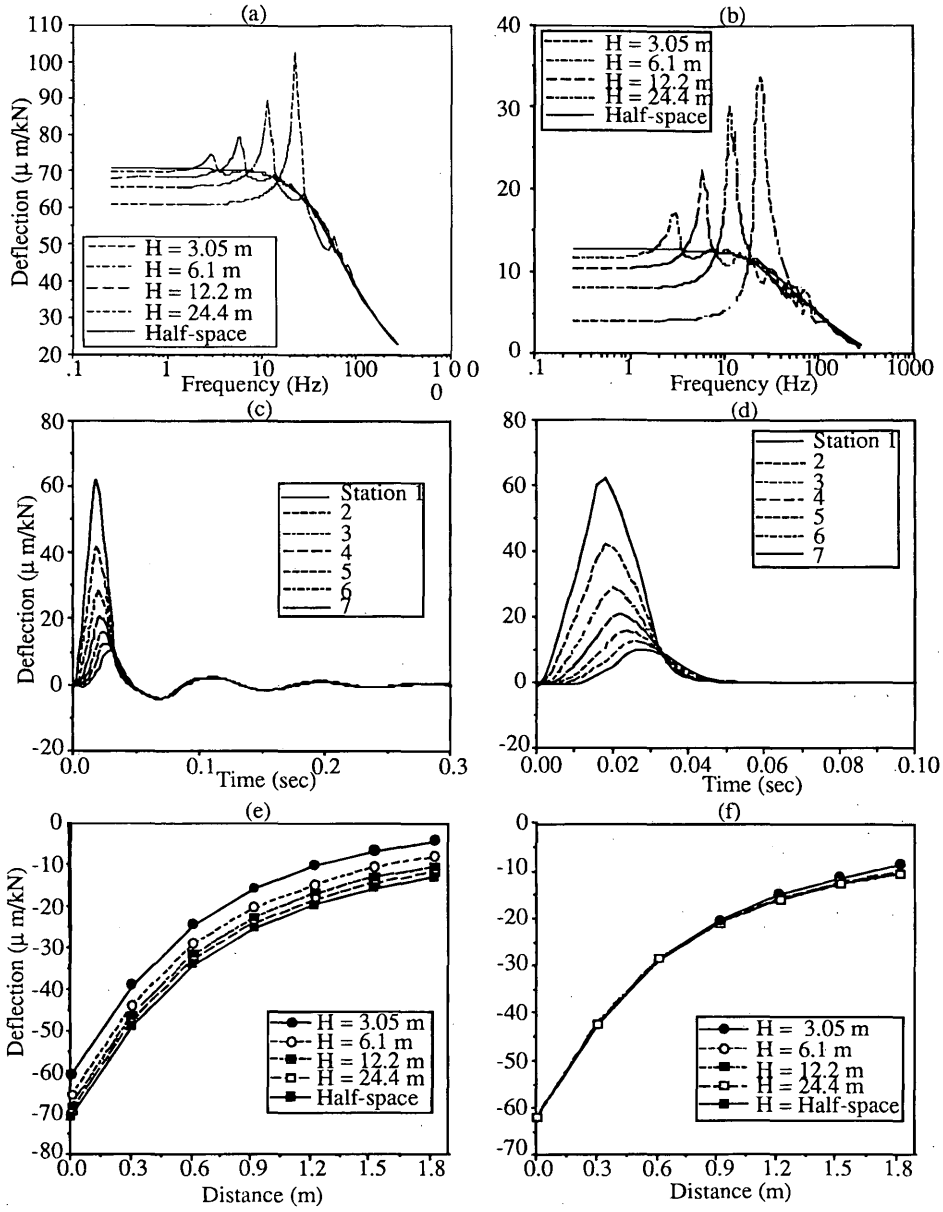


**FIGURE 3 Dynamic response of a flexible pavement with different depths to bedrock to FWD loading: (a) and (b) transfer functions at recording Stations 1 and 7, (c) and (d) displacement-time histories for depth to bedrock of 6.1 m and infinity, (e) static displacements and (f) measured deflection basins.**

## Parametric Studies

The sensitivity of the deflection basins and dispersion curves to variations in the stiffnesses of the pavement layers was investigated next. The flexible pavement given in Table 1 with a subgrade extending to infinity was analyzed first. The stiffness of each layer was varied independently. Figures 7(*a*) and 7(*b*) show the deflection basins and dispersion curves for shear wave velocities of the surface layer of 381, 762, and 1,143 m/sec (1,250, 2,500, and 3,750 ft/sec), which correspond to soft, medium, and stiff pavement surface layers, respectively. Figure 7(*a*) indicates that the displacement under the load is influenced by the properties of the surface layer, but this influence becomes negligible at the outer stations. Figure 7(*b*) shows that the dispersion curves are very sensitive to the properties of the surface layer for short wavelengths.

The deflection basins and dispersion curves when the shear wave velocities of the base are 152.4, 304.8, and 457.2 m/sec (500, 1,000, and 1,500 ft/sec) (corresponding to soft, medium, and stiff bases, respectively), are shown in Figures 7(*c*) and 7(*d*). Changes in the properties of the base affect the displacements under the load and at the next two stations, but have a negligible effect on the displacements at the last three stations. The dispersion curves are affected to some degree, but those effects are difficult to evaluate. Changes in the properties of the subgrade layer, on the other hand, affect the

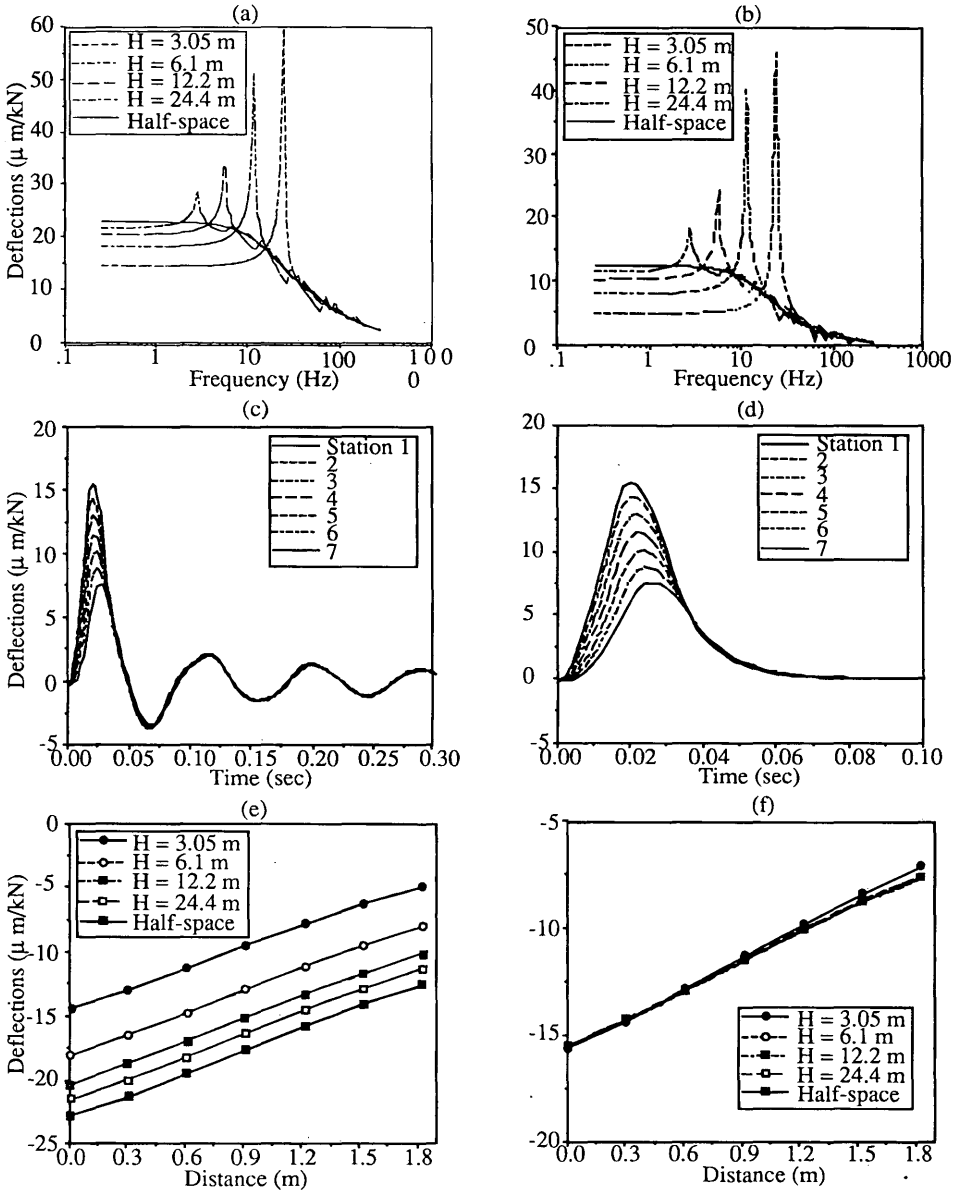


**FIGURE 4 Dynamic response of a rigid pavement with different depths to bedrock to FWD loading: (a) and (b) transfer functions at recording Stations 1 and 7, (c) and (d) displacement-time histories for depth to bedrock of 6.1 m and infinity, (e) static displacement and (f) measured deflection basins.**

displacements at all stations to about the same degree as shown in Figure 7(*e*). The dispersion curves for this case [Figure 7(*f*)] are very sensitive to the properties of the subgrade for long wavelengths. For the deflection basins, the displacements at the outer stations (particularly Station 7) are governed almost entirely by the properties of the subgrade layer; and for the dispersion curves, the phase velocity for short wavelengths is governed by the surface layer. The deflection basins computed with a finite depth to bedrock [6.1 m (20 ft)] were almost identical to those of Figures 7(*a*), (*c*), and (*e*).

The same type of parametric studies were performed for the rigid pavement. The results are qualitatively the same as those for the flexible pavement and therefore are not shown because of space limitations.

The sensitivity of the deflection basins and dispersion curves to changes in the thicknesses of the surface and base layers was also considered. The results indicate that the deflection basins are sensitive to these changes under the load and at the near stations, but that the effect is negligible at the outer stations. The dispersion curves are sensitive to the thickness of the surface layer, but they are quite insensitive to the thickness of the base layer (within the range of logical values).

Finally, the strains were computed at various depths below the load. The results indicate that the dynamic strains are almost iden-

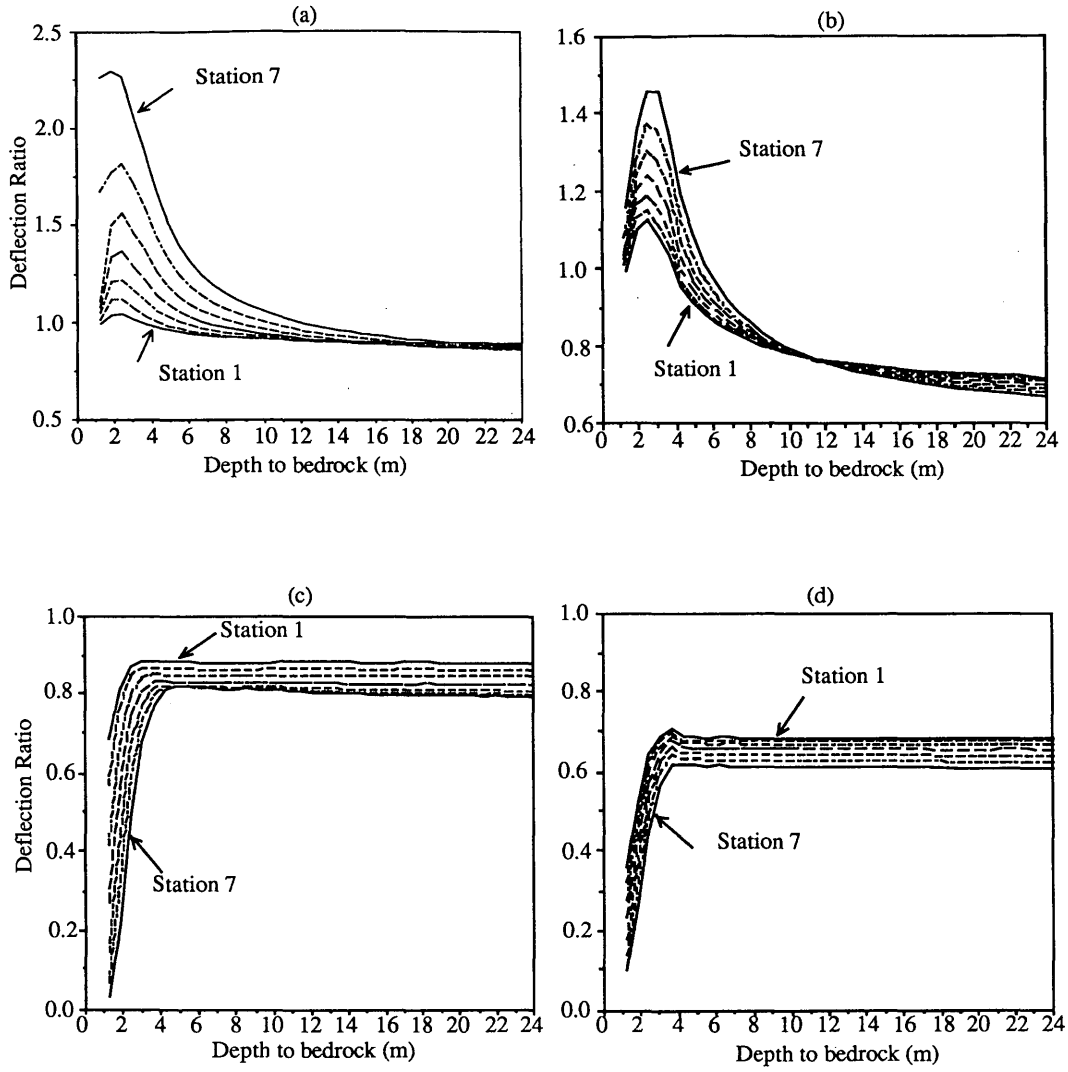


**FIGURE 5 Ratio of dynamic to static displacement: static displacements with a finite depth to bedrock for (a) flexible and (b) rigid pavements; static displacements with an infinite subgrade depth for (c) flexible and (d) rigid pavements.**

tical to the static ones over the top part of the pavement system and are insensitive to the depth of bedrock over this section. As the depth increases, the strains in the subgrade show more pronounced dynamic effects and a greater effect of the depth to bedrock.

## ADDITIONAL CONSIDERATIONS

Two of the main assumptions in the dynamic modeling of the pavement system were that the layers extend to infinity in both horizontal directions and that they are linear elastic. An accurate solution requires consideration of the finite width of the pavement and possible nonlinear behavior. These two effects were investigated in several studies conducted under the supervision of Roesset and Stokoe. Kang et al. (*18*) studied the effect of the finite width on the dynamic deflections of pavements and concluded that the loading position with respect to the edge of the pavement can influence (a) the amplitude of the deflections and (b) the shape of the deflection basin obtained with the FWD test. They also showed that finite pavement width can cause some fluctuations in the dispersion curves obtained with the SASW test. However, they found that for most pavements the error committed by assuming that the pavement extends to infinity will not be serious if the load is placed more than 0.6 m (2 ft) from the edge of pavements at level sites, or 1.2 m (4 ft) from the edge when the pavement is on an embankment or a ramp with concrete retaining walls.

Chang et al. (*19*) studied nonlinear effects in FWD testing using an approximate nonlinear analysis procedure (a linear iterative approach in the frequency domain) and a true nonlinear incremental analysis with a generalized cap model to reproduce the nonlinear material behavior. They showed that nonlinear behavior can be significant and localized around the loaded area if testing is performed on a flexible pavement with a rather thin surface layer and a soft subgrade. However, they also showed that nonlinear effects can be neglected for small to intermediate loads for many pavement systems and that very little nonlinearity will normally be generated

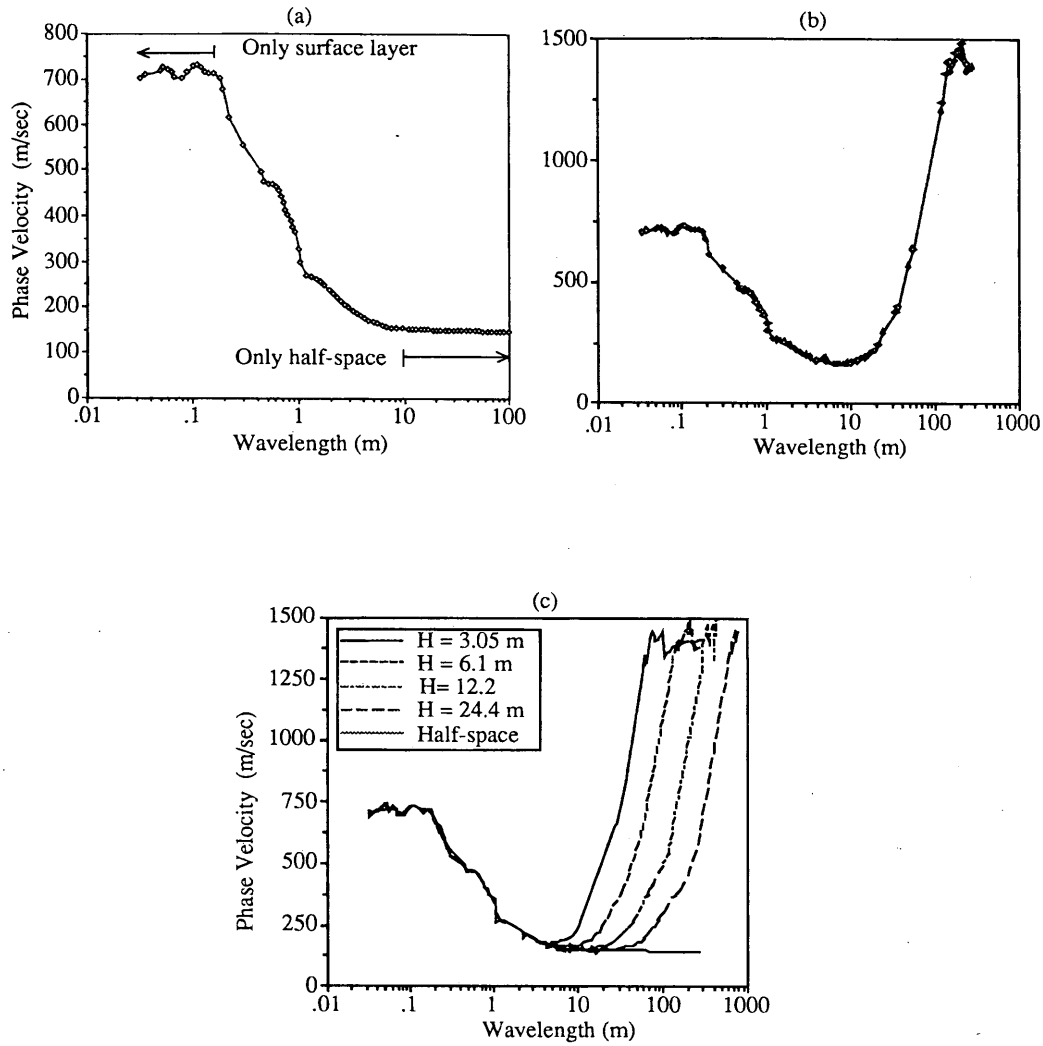


**FIGURE 6 Effect of depth to bedrock on the dispersion curves measured in SASW testing of a flexible pavement.**

in thick, rigid pavements. They did not study the SASW test because the small magnitude of the applied load creates only linear behavior in the pavement system.

## CONCLUSIONS

The results confirm that the dynamic response of the pavement system affects the magnitude and shape of the deflection basins obtained with the FWD test, and that these basins can be substantially different from those obtained under static conditions. When the dynamic deflection basins are compared with the static ones as a function of the assumed depth to bedrock, significant dynamic amplification is found for some range of depths to bedrock [typically less than 6.1 m (20 ft)]. However, dynamic deflections also can be smaller than the static ones over a wide range of depths to bedrock [typically depths greater than 15 m (50 ft)]. The use of a static back-calculation procedure with the known bedrock depth will result in an underestimation of the stiffness of the subgrade layer in the first case and an overestimation in the second case. The stiffnesses evaluated for the other layers will be complicated by the errors in the subgrade layer. On the other hand, current static back-calculation practice is to consider that the subgrade extends to infinity (because the depth to bedrock is not normally known). In this case, the static back-calculation procedure will result in a general overestimation of the stiffness of the pavement system.

The current method for interpreting FWD test results fails to utilize the test's true potential because the method does not consider the dynamic nature of the pavement response. Recording a longer time history of the dynamic response of the pavement system would yield a simpler and faster estimation of the subgrade stiffness from the offset times. The depth to bedrock also could be estimated from the period of the pavement's free vibrations, which follow the passage of the FWD pulse. This information and the history of the force are needed if a dynamic back-calculation procedure is to be used for system identification.

Computation of strains under the axis of the FWD load reveals that the static and dynamic strains are almost the same in the upper layers and that the effect of depth to bedrock is negligible for the strains in the top part [the upper 0.6 m (2 ft)] of the pavement. The dynamic

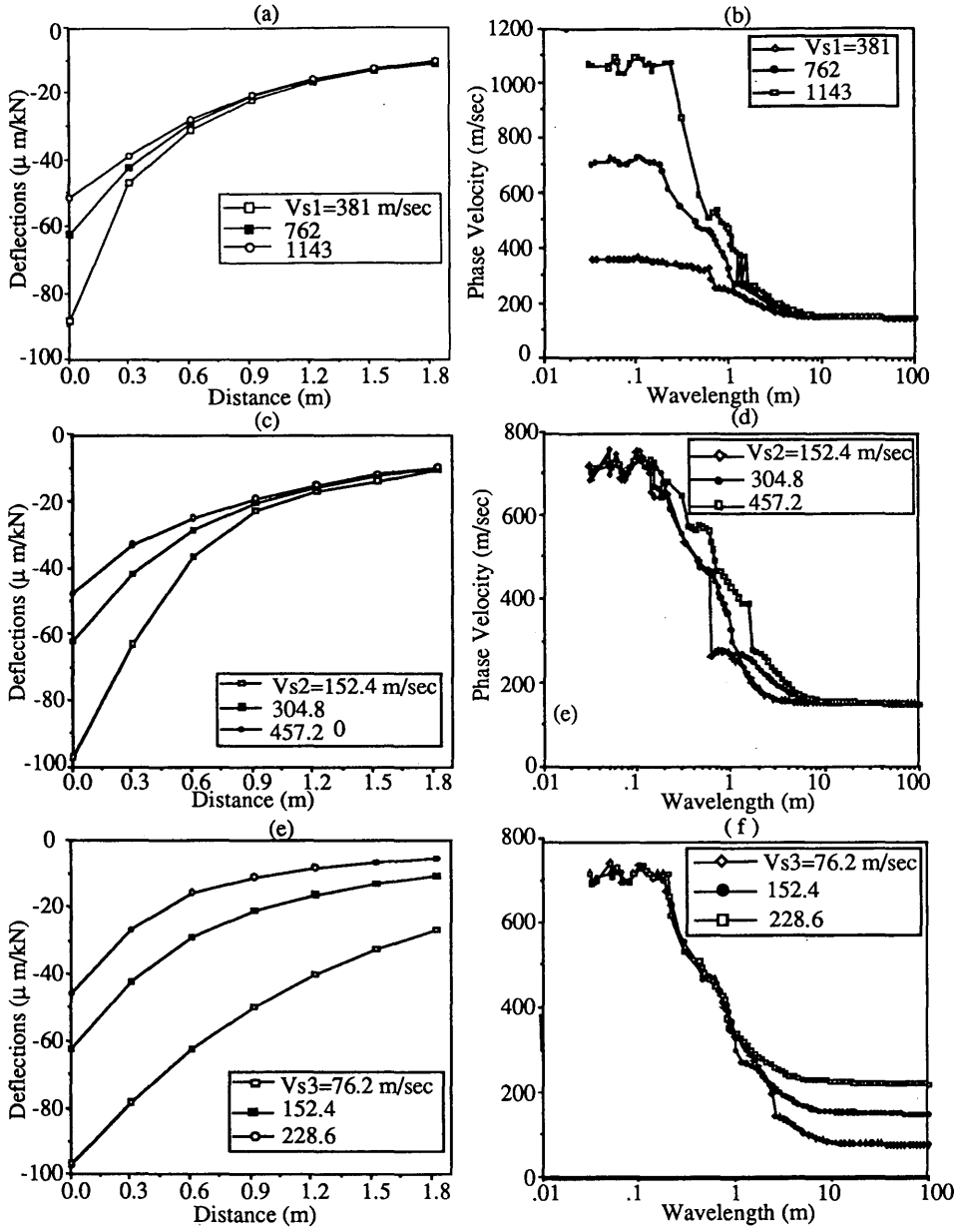


**FIGURE 7 Sensitivity of deflection basins and dispersion curves to changes in the stiffness of the layers: (a) and (b) surface layer, (c) and (d) base layer, (e) and (f) subgrade layer.**

effect on the strains increases with depth. The parametric studies clearly indicate that the dynamic deflections at the outer receivers are governed almost exclusively by the subgrade properties.

The SASW test, on the other hand, is particularly efficient in determining the properties of the top layer (stiffness and thickness). For long wavelengths, the phase velocity approaches the Rayleigh wave velocity of the subgrade. If there is a rocklike material at some depth, the dispersion curve starts bending upward at a wavelength of the order of the depth of the bedrock, and its presence is clearly seen in the dispersion curve. Unfortunately, SASW dispersion curves are relatively insensitive to the properties of the base material.

Using both the FWD and SASW tests is advised, since the research shows that the two tests complement each other.

## ACKNOWLEDGMENTS

The work described has been conducted at the University of Texas at Austin, supported for a number of years by the Texas Department of Transportation. The authors wish to express their appreciation for this support.

## REFERENCES

1. Uddin, W. A Structural Evaluation Methodology for Pavements Based on Dynamic Deflections. Ph.D. dissertation. The University of Texas at Austin, Austin, Texas, 1984.
2. Nazarian, S. and K. H. Stokoe II. Use of Surface Waves in Pavement Evaluation. *Transportation Research Record 1070,* 1986, pp. 132–144.

3. Lamb, H. On the Propagation of Tremors over the Surface of an Elastic Solid. Phil. Transactions Royal Society of London, Series A, Vol. 203, 1904, pp. 1–42.
4. Pekeris, C. The Seismic Surface Pulse. *Proc., National Academy of Science,* 1955, p. 41.
5. Mooney, H. M. Some Numerical Solutions for Lamb's Problems. Bulletin of the Seismological Society of America, Vol. 64, No. 2, 1974.
6. Eringen, A. C., and S. Suhubi. *Elastodynamics,* Vol. 2, Academic Press, New York, N.Y., 1975.
7. Miller, G. F., and H. Pursey. The Field and Radiation Impedance of Mechanical Radiators on the Free Surface of a Semi-Infinite Isotropic Solid. *Proc. Royal Society of London A223,* 1954.
8. Thomson, W. T. Transmission of Elastic Waves Through a Stratified Soil Medium. *Journal of Applied Physics,* Vol. 21, 1950.
9. Haskell, N. A. The Dispersion of Surface Waves on Multilayered Media. Bulletin of the Seismological Society of America, Vol. 43, No. 1, 1953.
10. Kausel, E. and J. M. Roesset. Stiffness Matrices for Layered Soils. Bulletin of the Seismological Society of America, Vol. 71, No. 6, 1981.
11. Waas, G. Linear Two-Dimensional Analysis of Soil Dynamics Problems on Semi-Infinite Layered Media. Ph.D. dissertation. University of California, Berkeley, Calif., 1972.
12. Kausel, E. Forced Vibrations of Circular Foundations on Layered Media. Research Report R74-11. Department of Civil Engineering, Massachusetts Institute of Technology, Cambridge, 1974.
13. Kausel, E. An Explicit Solution for the Green Functions for Dynamic Loads in Layered Media. Research Report R81-13. Massachusetts Institute of Technology, Cambridge, Mass., 1981.
14. Roesset, J. M. and K. Shao. Dynamic Interpretation of Dynaflect and Falling Weight Deflectometer Tests. *Transportation Research Record 1022,* 1985, pp. 7–16.
15. Foinquinos, R., J. M. Roesset, and K. H. Stokoe II. Dynamic Interpretation of FWD Deflection Basins. XII Congreso Mundial de IRF, Madrid, Spain, 1993.
16. Chang, D. W., V. Y. Kang, J. M. Roesset, and K. H. Stokoe II. Effect of Depth to Bedrock on Deflection Basins Obtained with Dynaflect and FWD Tests. *Transportation Research Record 1355,* 1992, pp. 8–16.
17. Seng, C. R. Effect of Depth to Bedrock on the Accuracy of Backcalculated Moduli Obtained with Dynaflect and FWD Tests. M.S. thesis. The University of Texas at Austin, Austin, Texas, 1992.
18. Kang, V. K., J. M. Roesset, and K. H. Stokoe II. Effect of the Finite Width of Pavements on Deflection Basins Obtained with Dynaflect and FWD Tests. Transportation Research Board, 1990, pp. 1–26.
19. Chang, D. W., J. M. Roesset, and K. H. Stokoe II. Nonlinear Effects in Falling Weight Deflectometer Tests. *Transportation Research Record 1355,* 1992, pp. 1–7.

*Publication of this paper sponsored by Committee on Modelling Techniques in Geomechanics.*

# Determination of Depth to Bedrock from Falling Weight Deflectometer Test Data

JOSE M. ROESSET, KENNETH H. STOKOE II, AND CHIA-RAY SENG

Depth to bedrock can have a significant effect on the moduli of the surface layer, base, and subgrade back-calculated from Falling Weight Deflectometer (FWD) tests when the calculations are performed using a static analysis. On the other hand, when the back calculation is based on dynamic analysis of the FWD test, the resulting moduli are quite insensitive to the depth to bedrock if this depth is larger than about 3 m (10 ft). When only the peak deflections at the seven receivers are recorded, there is little that can be done analytically to account for the depth to bedrock. However, when the time histories of the motions at the various receivers are stored, one can estimate both the depth to bedrock and the modulus of the subgrade rather easily from the time histories. These estimations are most correctly applied to time histories of 0.12 sec or longer rather than the 0.06 sec conventionally recorded. In this article, the results of a number of parametric studies simulating the FWD test on three flexible pavements and one rigid pavement are presented. From these results, approximate expressions were developed for (*a*) estimating the depth to bedrock, (*b*) computing the natural period of vibration of the pavement system, which is nearly equal to that of the subgrade layer, and (*c*) estimating the wave propagation velocity and modulus.

Deflection basins caused by the dynamic loads imposed by the Falling Weight Deflectometer (FWD) are nearly independent of depth to bedrock if this depth is larger than about 3 m (10 ft). Deflection basins caused by the same load applied statically are, on the other hand, affected by the existence of bedrock to depths of 15 m (50 ft) or more. As a result, if the back-calculation procedure used to determine the elastic moduli of the surface layer, base, and subgrade employs a static analysis, the results will depend on the depth to bedrock as shown by several studies over the last decade. The objective of this article is to discuss procedures by which the depth to bedrock and the modulus of the subgrade can be estimated directly from the FWD results, without back calculation, when the time history of the motions recorded at the various receivers is provided rather than only the peak deflections.

Analytical simulations of the FWD test were conducted using the UTFWD program (*1,2*). The four pavement profiles shown in Figure 1 were studied. The main purposes of these studies were as follows:

1. To determine the depth to bedrock at which resonance may occur for various stiffnesses of the subgrade, including unsaturated and saturated conditions;
2. To develop equations for estimating this resonant depth to bedrock;
3. To develop a method for estimating the depth to bedrock based on the free vibrations of the pavement system created in the FWD test; and
4. To develop an approach for estimating the stiffness of the subgrade layer based on the phase shift between the first pulses in the deflection-time records of the FWD test at two measurement stations.

The deflection basins presented in this article are normalized with respect to the load. Therefore, actual deflections under any load are simply calculated by multiplying the normalized deflection by the desire load.

J. M. Roesset and K. H. Stokoe, II, Department of Civil Engineering, University of Texas at Austin, Austin, Tex. 78712. C.-R. Seng, United Geotechnical Consultants, Taipei, Taiwan.

## MODEL PARAMETERS

Only the subgrade stiffness and thickness were varied in this study. The stiffnesses of the other pavement layers were kept constant as listed.

1. Continuously reinforced concrete (CRC):
   - shear wave velocity, $V_s$ = 2,593 m/sec (8,500 fps)
   - Young's modulus, $E$ = 37.4 MN/m$^2$ (5,425 ksi)
2. Asphalt concrete (AC):
   - $V_s$ = 915 m/sec (3,000 fps)
   - $E$ = 4.8 MN/m$^2$ (690 ksi)
3. Base material:
   - $V_s$ = 305 m/sec (1,000 pfs)
   - $E$ = 0.46 MN/m$^2$ (67 ksi)

The thickness of each of these upper pavement layers varied between the four profiles but it was kept constant in each profile.

The shear wave velocity of the subgrade layer in Profiles 1 to 4 was varied from 150 to 450 m/sec (500–1,500 fps), and the corresponding Young's modulus varied from 0.11 to 0.98 MN/m$^2$ (16 to 142 ksi). In addition, the depths to bedrock of the four pavement profiles (Figure 1) were varied from 1.65 to 27 m (5.5–90 ft), which simply means that the thickness of the subgrade was varied. The stiffness of the bedrock beneath the subgrade was assumed to be infinite.

To simulate an unsaturated subgrade, a Poisson's ratio of 0.33 was used. The material properties of the four pavement profiles with unsaturated subgrade conditions are given in Table 1. To simulate a saturated subgrade, the compression (P-wave) velocity of the subgrade was set equal to 1,525 m/sec (5,000 fps). This velocity represents typical field conditions for uncemented saturated soils (*3*). The shear wave (S-wave) velocities of the saturated subgrades were varied from 150 to 450 m/sec (500–1,500 fps), as in the unsaturated subgrade condition. As a result, Poisson's ratio varied from 0.495 to 0.451 as the S-wave velocity of the subgrade varied from 150 to 450 m/sec (500–1,500 fps). Hence, Young's modulus (which is equal to the resilient modulus) for the saturated subgrade varied from 0.12 to 1.07 MN/m$^2$ (18–155 ksi). The material properties of the four pavement profiles with saturated subgrades are given in Table 2.

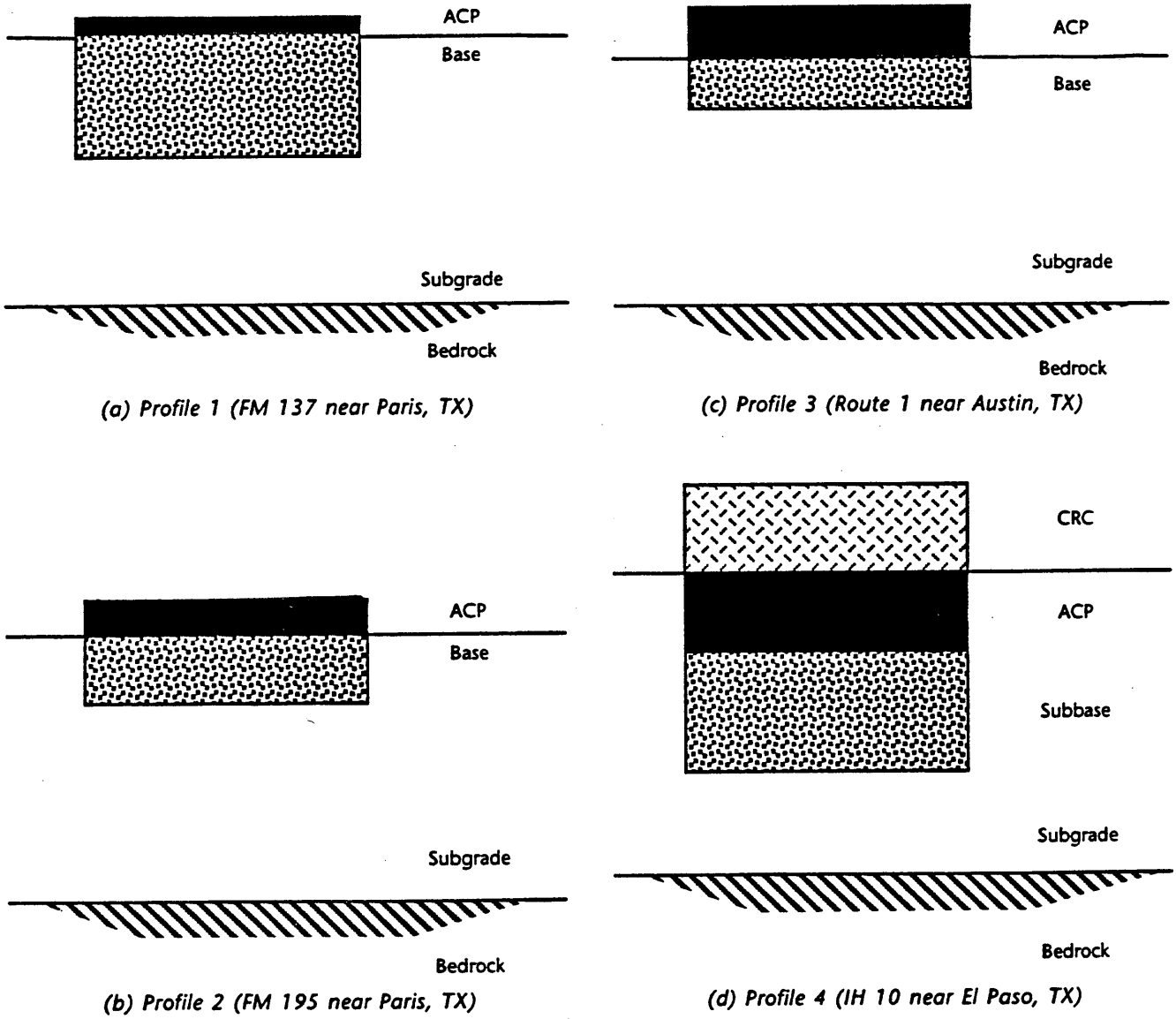


**FIGURE 1 Idealized cross-section of the four pavement profiles.**

## DEFLECTION BASINS

A typical example of the deflection basins created by the FWD test as a function of depth to bedrock is shown in Figure 2. These results correspond to Profile 1 with a soft, unsaturated subgrade. The dynamic deflections at all seven measurement stations (receivers) used in conventional testing vary only at shallow bedrock depths of less than 3 m (10 ft) as shown in Figure 2(*a*). An important observation is that the deflection at the first measurement station (under the load) remains nearly constant throughout the entire range of bedrock depths. Only at depths less than about 2 m (7 ft) is this deflection affected. On the other hand, the dynamic deflections at shallow bedrock depths are influenced more (relative to Station 1) as the distance from the load point increases.

The static deflections at all seven measurement stations for Profile 1 with an unsaturated subgrade are shown in Figure 2(*b*). As can be seen comparing Figure 2(*a*) and 2(*b*), static deflections are influenced more by shallow bedrock than dynamic deflections. In addition, they are influenced over a wider range of bedrock depths than dynamic deflections. These two observations are critical points when considering the dynamics in the FWD test.

An easy way to view the effect of bedrock depth on the FWD test is in terms of deflection ratio; that is, the ratio of dynamic deflections to static deflections. The deflection ratios for Profile 1 with an unsaturated subgrade are shown in Figure 2(*c*). In this case, there is a peak in the deflection ratios at a depth of about 1.8 m (6 ft). The depth to bedrock corresponding to the maximum deflection ratio is called the resonant depth to bedrock (*4*). It is at this depth where back calculation using a procedure that assumes static loading in the FWD test would be most in error.

A typical set of plots showing the combined effects of subgrade stiffness and depth to bedrock on the deflection ratios measured at

TABLE 1 Simplified Equations for Estimating Depth to Bedrock with Unsaturated Subgrade Conditions

a) FM137 (Profile 1)

| Material Type | Thickness (in.) | Poisson's Ratio | Unit Weight (pcf) | Damping Ratio | S-wave Velocity (fps) | P-wave Velocity (fps) | Young's Modulus (ksi) |
|---|---|---|---|---|---|---|---|
| ACP | 1 | 0.27 | 140 | 0.02 | 3,000 | 5,345 | 690.4 |
| Base | 12 | 0.25 | 125 | 0.02 | 1,000 | 1,732 | 67.4 |
| Subgrade* | h** | 0.33 | 110 | 0.02 | 500 | 993 | 15.8 |
| | | 0.33 | 110 | 0.02 | 750 | 1,488 | 35.5 |
| | | 0.33 | 110 | 0.02 | 1,000 | 1,985 | 63.1 |
| | | 0.33 | 110 | 0.02 | 1,500 | 2,978 | 142.0 |

b) FM195 (Profile 2)

| Material Type | Thickness (in.) | Poisson's Ratio | Unit Weight (pcf) | Damping Ratio | S-wave Velocity (fps) | P-wave Velocity (fps) | Young's Modulus (ksi) |
|---|---|---|---|---|---|---|---|
| ACP | 4 | 0.27 | 140 | 0.02 | 3,000 | 5,345 | 690.4 |
| Base | 6 | 0.25 | 125 | 0.02 | 1,000 | 1,732 | 67.4 |
| Subgrade | h | 0.33 | 110 | 0.02 | 500 | 993 | 15.8 |
| | | 0.33 | 110 | 0.02 | 750 | 1,488 | 35.5 |
| | | 0.33 | 110 | 0.02 | 1,000 | 1,985 | 63.1 |
| | | 0.33 | 110 | 0.02 | 1,500 | 2,978 | 142.0 |

c) Route 1 (Profile 3)

| Material Type | Thickness (in.) | Poisson's Ratio | Unit Weight (pcf) | Damping Ratio | S-wave Velocity (fps) | P-wave Velocity (fps) | Young's Modulus (ksi) |
|---|---|---|---|---|---|---|---|
| ACP | 7 | 0.27 | 145 | 0.02 | 3,000 | 5,345 | 715.1 |
| Base | 6 | 0.25 | 130 | 0.02 | 1,000 | 1,732 | 70.1 |
| Subgrade | h | 0.33 | 130 | 0.02 | 500 | 993 | 18.7 |
| | | 0.33 | 130 | 0.02 | 750 | 1,489 | 42.0 |
| | | 0.33 | 130 | 0.02 | 1,000 | 1,985 | 74.6 |
| | | 0.33 | 130 | 0.02 | 1,500 | 2,979 | 167.9 |

d) IH 10 (Profile 4)

| Material Type | Thickness (in.) | Poisson's Ratio | Unit Weight (pcf) | Damping Ratio | S-wave Velocity (fps) | P-wave Velocity (fps) | Young's Modulus (ksi) |
|---|---|---|---|---|---|---|---|
| CRC | 10 | 0.2 | 145 | 0.02 | 8,500 | 13,880 | 5424.2 |
| ACP | 6 | 0.27 | 145 | 0.02 | 3,000 | 5,345 | 715.1 |
| Base | 12 | 0.25 | 125 | 0.02 | 1,000 | 1,732 | 67.4 |
| Subgrade | h | 0.33 | 110 | 0.02 | 500 | 993 | 15.8 |
| | | 0.33 | 110 | 0.02 | 750 | 1,488 | 35.5 |
| | | 0.33 | 110 | 0.02 | 1,000 | 1,985 | 63.1 |
| | | 0.33 | 110 | 0.02 | 1,500 | 2,978 | 142.0 |

* There are four different S-wave velocities for each subgrade.
** Thickness of subgrade (h) was varied from 5.5 to 90 ft.

all seven stations in the FWD test is presented in Figure 3. These results are for Profile 1 with an unsaturated subgrade. As seen in the figure, the resonant depth to bedrock increases as the stiffness of the subgrade increases. Also, it should be noted that Station 7 in the FWD test is most affected by shallow bedrock and Station 1 (at the center of the load) is least affected.

Dynamic and static deflection basins as a function of distance from the source obtained at the peak deflection ratio (the resonant depth to bedrock) are shown in Figure 4 for Profile 1 (flexible pavement) with unsaturated and saturated subgrade conditions, respectively. As can be seen, there is little difference at the source between dynamic deflections and static deflections for Profile 1 with the softest subgrade [Figure 4(*a*)]. The differences between dynamic deflections and static deflections become larger as the distance from the source increases. This behavior explains why the deflection ratio at the nearest station is the smallest and the deflection ratio at the farthest station is the largest, as illustrated in Figures 2(*c*) and 3.

For the stiffest subgrade condition, there is little difference between the dynamic deflections and the static deflections, as shown in Figure 4(*b*). For the saturated subgrade conditions at Profile 1, the trends are similar to those first described for the unsaturated subgrade conditions, as shown in Figure 4(*c*) and 4(*d*).

TABLE 2 Simplified Equations for Estimating Depth to Bedrock with Saturated Subgrade Conditions

a) FM 137 (Profile 1)

| Material Type | Thickness (in.) | Poisson's Ratio | Unit Weight (pcf) | Damping Ratio | S-wave Velocity (fps) | P-wave Velocity (fps) | Young's Modulus (ksi) |
|---|---|---|---|---|---|---|---|
| ACP | 1 | 0.270 | 140 | 0.02 | 3,000 | 5,345 | 690.4 |
| Base | 12 | 0.250 | 125 | 0.02 | 1,000 | 1,732 | 67.4 |
| Subgrade* | h** | 0.495 | 110 | 0.05 | 500 | 5,000 | 17.4 |
| | | 0.489 | 110 | 0.05 | 750 | 5,000 | 39.5 |
| | | 0.479 | 110 | 0.05 | 1,000 | 5,000 | 69.8 |
| | | 0.451 | 110 | 0.05 | 1,500 | 5,000 | 154.8 |

b) FM 195 (Profile 2)

| Material Type | Thickness (in.) | Poisson's Ratio | Unit Weight (pcf) | Damping Ratio | S-wave Velocity (fps) | P-wave Velocity (fps) | Young's Modulus (ksi) |
|---|---|---|---|---|---|---|---|
| ACP | 4 | 0.270 | 140 | 0.02 | 3,000 | 5,345 | 690.4 |
| Base | 6 | 0.250 | 125 | 0.02 | 1,000 | 1,732 | 67.4 |
| Subgrade | h | 0.495 | 110 | 0.05 | 500 | 5,000 | 17.7 |
| | | 0.489 | 110 | 0.05 | 750 | 5,000 | 39.5 |
| | | 0.479 | 110 | 0.05 | 1,000 | 5,000 | 69.8 |
| | | 0.451 | 110 | 0.05 | 1,500 | 5,000 | 154.8 |

c) Route 1 (Profile 3)

| Material Type | Thickness (in.) | Poisson's Ratio | Unit Weight (pcf) | Damping Ratio | S-wave Velocity (fps) | P-wave Velocity (fps) | Young's Modulus (ksi) |
|---|---|---|---|---|---|---|---|
| ACP | 7 | 0.270 | 145 | 0.02 | 3,000 | 5,345 | 715.1 |
| Base | 6 | 0.250 | 130 | 0.02 | 1,000 | 1,732 | 70.1 |
| Subgrade | h | 0.495 | 130 | 0.05 | 500 | 5,000 | 21.0 |
| | | 0.489 | 130 | 0.05 | 750 | 5,000 | 46.7 |
| | | 0.479 | 130 | 0.05 | 1,000 | 5,000 | 82.5 |
| | | 0.451 | 130 | 0.05 | 1,500 | 5,000 | 183.0 |

d) IH 10 (Profile 4)

| Material Type | Thickness (in.) | Poisson's Ratio | Unit Weight (pcf) | Damping Ratio | S-wave Velocity (fps) | P-wave Velocity (fps) | Young's Modulus (ksi) |
|---|---|---|---|---|---|---|---|
| CRC | 10 | 0.200 | 145 | 0.02 | 8,500 | 13,880 | 5424.2 |
| ACP | 6 | 0.270 | 145 | 0.02 | 3,000 | 5,345 | 715.1 |
| Base | 12 | 0.250 | 125 | 0.02 | 1,000 | 1,732 | 67.4 |
| Subgrade | h | 0.495 | 110 | 0.05 | 500 | 5,000 | 17.7 |
| | | 0.489 | 110 | 0.05 | 750 | 5,000 | 39.5 |
| | | 0.479 | 110 | 0.05 | 1,000 | 5,000 | 69.8 |
| | | 0.451 | 110 | 0.05 | 1,500 | 5,000 | 154.8 |

* There are four different S-wave velocities for each subgrade.
**Thickness of subgrade (h) was varied from 5.5 to 90 ft.

Similar plots of deflection basins as a function of distance from the source for Profile 4 (rigid pavement) are shown in Figure 5 for unsaturated and saturated subgrade conditions. The amplitudes of the deflection basins are much smaller than those obtained with Profile 1, because the surface layer of Profile 4 is much thicker and stiffer than that of Profile 1. There is also less variation in the deflection basins with distance from the FWD load than in Profile 1. This response can be most easily seen by comparing Figures 4(*a*) and 5(*a*). This difference occurs because Profile 4 represents a rigid pavement, whereas Profile 1 represents a very flexible pavement. For saturated subgrade conditions [(Figure 5(*c*)], the trends for the rigid pavement are similar to those just described for the unsaturated subgrade conditions [(Figure 4(*c*)].

## RESONANT DEPTH TO BEDROCK

The analytical simulations of the FWD tests for the four pavement profiles were expressed in terms of deflection ratios as a function of depth to bedrock. The resonant depth to bedrock, $RD_b$, for each pavement profile with each subgrade stiffness was determined as the depth to bedrock corresponding to the maximum deflection

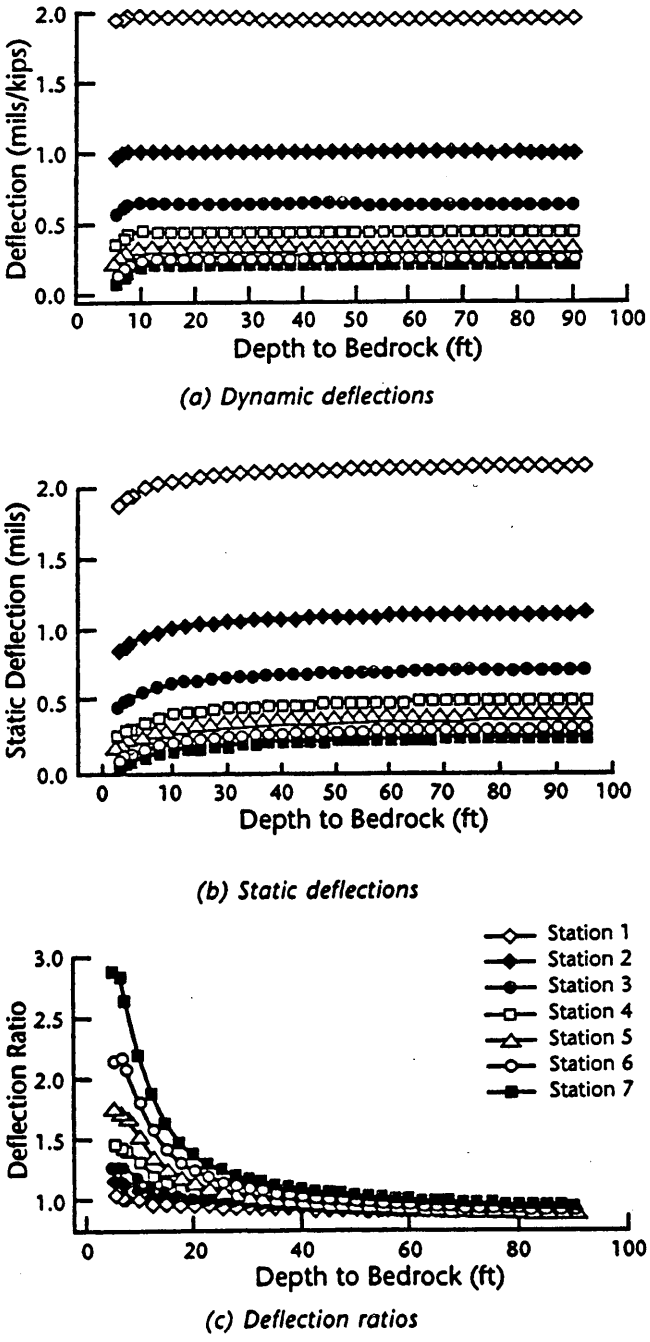


**FIGURE 2 Deflection basins obtained with FWD testing for Profile 1 with unsaturated subgrade conditions [$V_s$ of subgrade = 500 fps (155 m/sec) and $E$ = 16 ksi (0.11 MN/m$^2$)].**

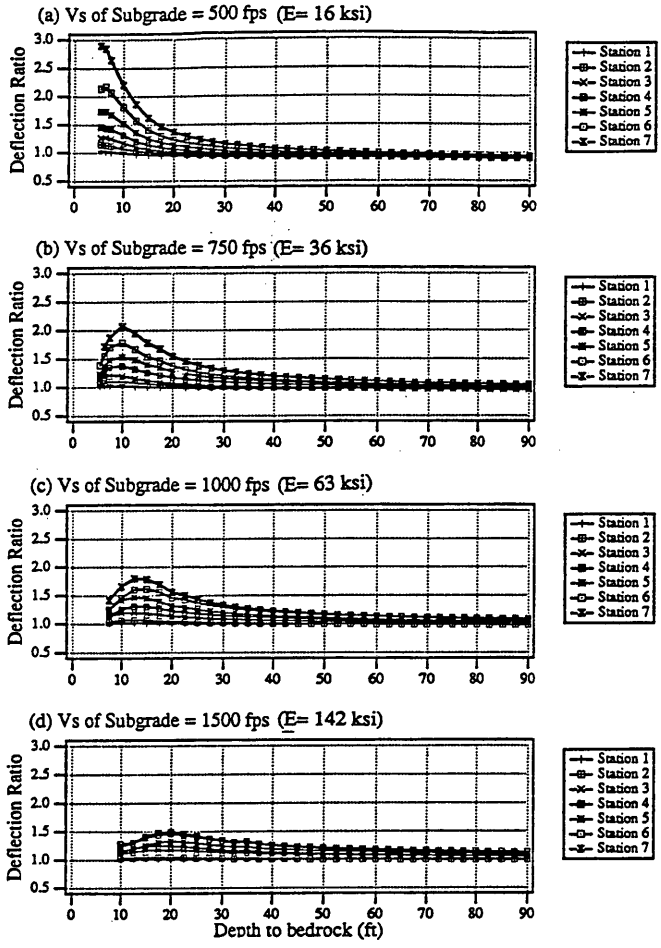


**FIGURE 3 Deflection ratio versus depth to bedrock for FWD tests at Profile 1 with unsaturated subgrade conditions.**

ratio. The values of $RD_b$ as a function of various subgrade stiffnesses for the four pavement profiles are summarized in Figure 6. The resonant depths to bedrock obtained with the FWD test varied from 1.7 to 6.2 m (5.5–20 ft). The values of $RD_b$ were plotted versus subgrade stiffness, and the results are presented in Figure 7.

As seen in Figure 7, the resonant depths to bedrock form two groups; one for flexible pavements (Profiles 1, 2, and 3) and the other for the rigid pavement (Profile 4). For flexible pavements, a straight line was fitted to the data, which results in:

$$RD_b = 0.013V_s \quad (1)$$

For the rigid pavement, the fitted line was:

$$RD_b = 0.011V_s \quad (2)$$

In Equations 1 and 2, $RD_b$ and $V_s$ can be expressed in any consistent set of units. It is easy to see that the resonant depth to bedrock can be predicted from the subgrade stiffness. Equation 1 can also be expressed in terms of Young's modulus ($E$) as:

$$RD_b = 0.00018\sqrt{E} \quad (0.0043\sqrt{E}) \quad (3)$$

for flexible pavements with the unit weight of the subgrade assumed to be 19 800 N/m$^3$ (110 lb/ft$^3$) and Poisson's ratio of the subgrade assumed to be 0.33. Likewise, Equation 2 can be expressed as:

$$RD_b = 0.00015\sqrt{E} \quad (0.0036\sqrt{E}) \quad (4)$$

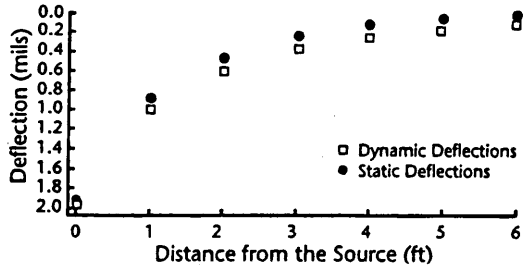


*(a) Unsaturated subgrade with S-wave velocity = 500 fps (E = 16 ksi)*

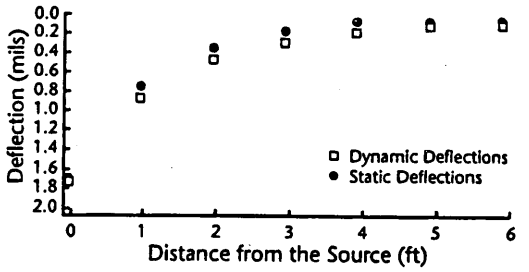


*(c) Saturated subgrade with S-wave velocity = 500 fps (E = 16 ksi)*

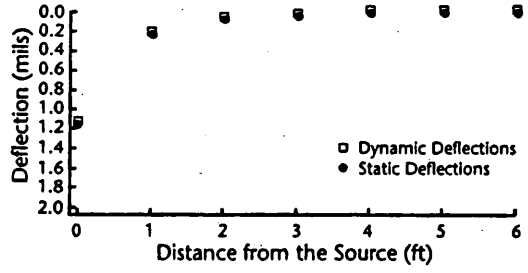


*(b) Unsaturated subgrade with S-wave velocity = 1,500 fps (E = 142 ksi)*

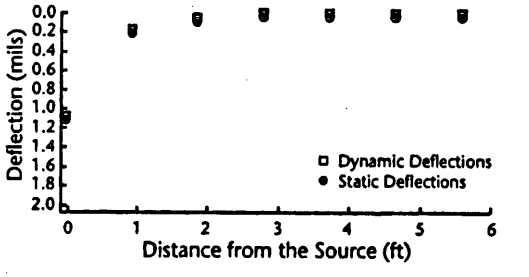


*(d) Saturated subgrade with S-wave velocity = 1,500 fps (E = 142 ksi)*

**FIGURE 4** Deflection basins as a function of distance from the FWD source for Profile 1 with saturated subgrade conditions.

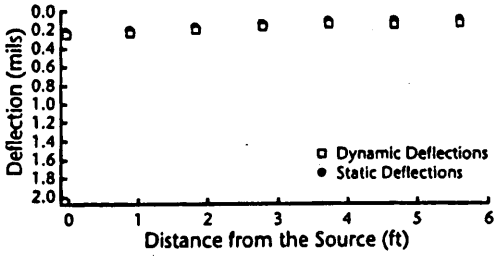


*(a) Unsaturated subgrade with S-wave velocity = 500 fps (E = 16 ksi)*

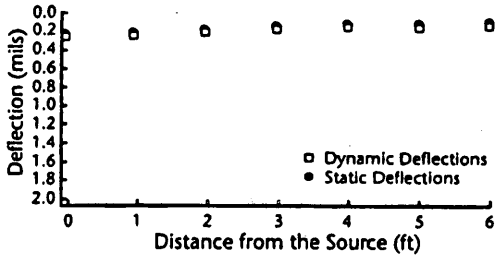


*(c) Saturated subgrade with S-wave velocity = 500 fps (E = 16 ksi)*

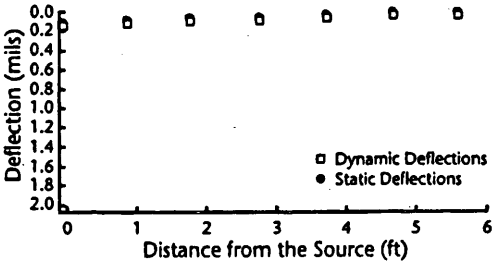


*(b) Unsaturated subgrade with S-wave velocity = 1,500 fps (E = 142 ksi)*

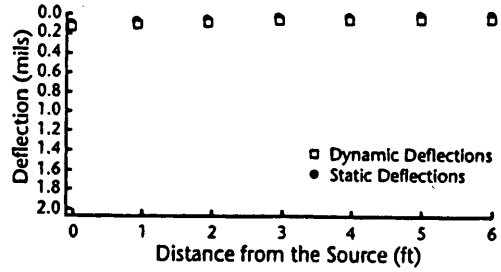


*(d) Saturated subgrade with S-wave velocity = 1,500 fps (E = 142 ksi)*

**FIGURE 5** Deflection basins as a function of distance from the FWD source for Profile 4 with unsaturated subgrade conditions.

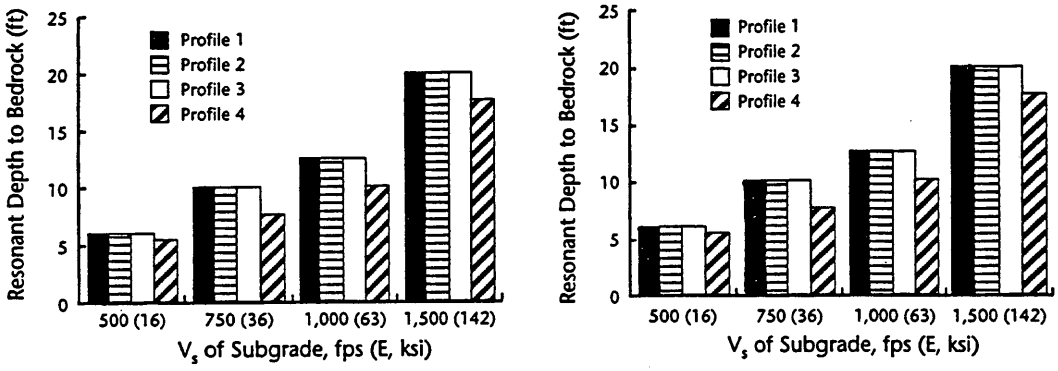


**FIGURE 6 Resonant depths to bedrock for FWD testing at the four pavement profiles with various subgrade stiffnesses.**

for the rigid pavement. In Equations 3 and 4, $E$ is in N/m$^2$ (or psf) and $RD_b$ in m (or ft).

## AMPLITUDE OF MAXIMUM DEFLECTION RATIO

The amplitude of the deflection ratio at each measurement station is an important index of the potential error generated in any static interpretation procedure (*4*). Figure 8 shows the maximum deflection ratios as a function of various subgrade stiffnesses for the four pavement profiles. It should be noted that the maximum deflection ratio of the FWD test always occurs at the farthest measurement station (Station 7).

As can be seen in Figure 8, the amplitudes of the maximum deflection ratios of the four pavement profiles decrease as the stiffness of the subgrade increases for both unsaturated and saturated subgrade conditions. This means that the accuracy of back calculated layer moduli based on a static interpretation method should improve as the subgrade stiffness increases (*4*).

The estimated amplitudes of the maximum deflection ratios of the four pavement profiles obtained with saturated subgrade conditions are generally larger than those obtained with unsaturated subgrade conditions. This indicates that the back-calculated layer moduli obtained at pavement sites with unsaturated subgrade conditions based on a static interpretation method should be more

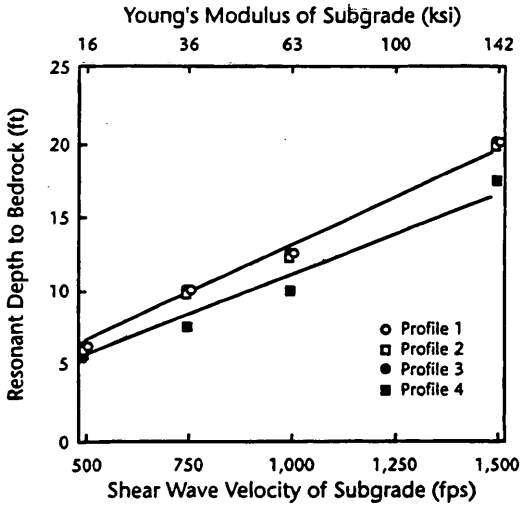


**FIGURE 7 Curve fitting of the resonant depth to bedrock for FWD testing at the four pavement profiles with various subgrade stiffnesses.**

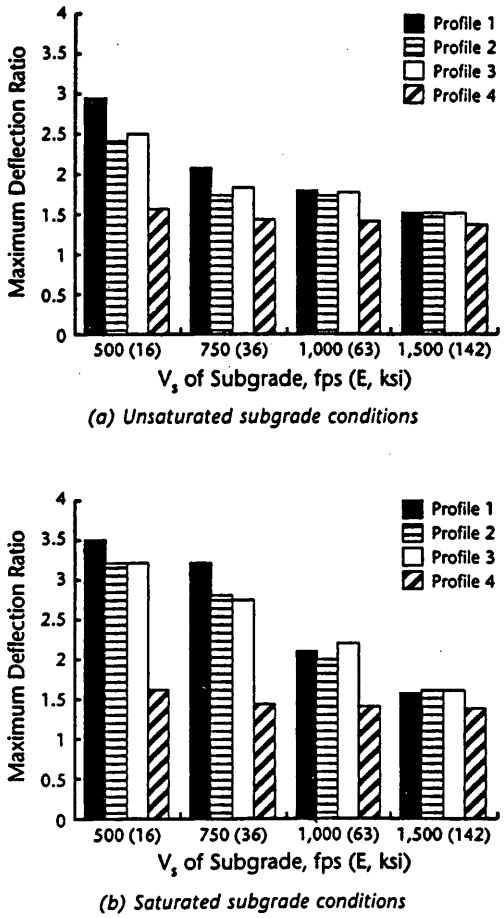


**FIGURE 8 Maximum deflection ratios for FWD testing at the four pavement profiles with various subgrade stiffnesses.**

accurate than those obtained at sites with saturated subgrade conditions (*4*).

## ESTIMATION OF DEPTH TO BEDROCK FROM FWD TEST

Chang et al. (*2*) developed a procedure for predicting the depth to bedrock based on the natural period of free vibrations of the pavement system immediately after FWD loading. Figure 9 illustrates the natural periods in the time-deflection records obtained from FWD tests with four shallow depths to bedrock at Profile 1

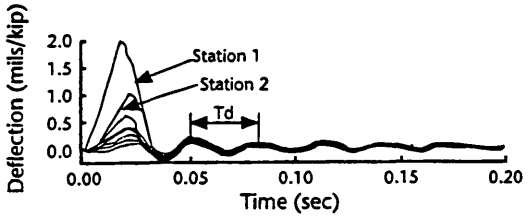


*(a) Depth to bedrock = 5 feet*

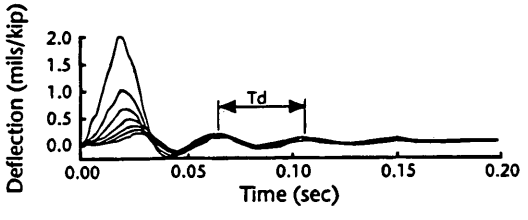


*(b) Depth to bedrock = 7.5 feet*

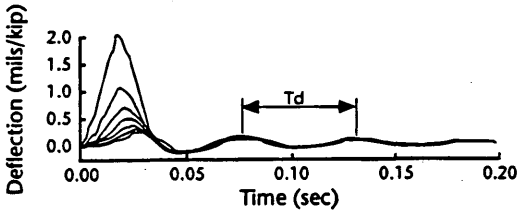


*(c) Depth to bedrock = 10 feet*

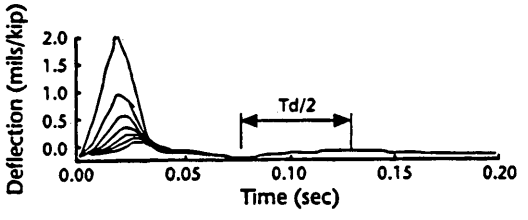


*(d) Depth to bedrock = 20 feet*

**FIGURE 9 Deflection-time histories in FWD testing and damped natural periods (Td) for Profile 1 with various depths to bedrock [$V_s$ of subgrade = 500 fps (155 m/sec) and $E$ = 16 ksi (0.11 MN/m$^2$)].**

for unsaturated subgrade conditions. It should be noted that a longer time interval (~ 0.12 to 0.20 sec) than normally recorded in FWD testing (0.06 sec) must be measured to record the free vibrations with confidence. FWD equipment is often set to record 60 msec of motion a 0.1-msec intervals. Increasing $\Delta t$ to 0.2 or 0.4 msec would increase the duration without loss in accuracy. Care may be necessary to avoid drift but even this might be relatively unimportant.

Additional studies that are presented in this article have been conducted beyond those performed in Chang et al. (*2*). In these studies, various stiffnesses of the subgrade layer and different subgrade saturation conditions were examined. This work was performed to provide a more complete evaluation of the estimation of bedrock depth. Three different degrees of saturation for unsaturated subgrade conditions were simulated by using Poisson's ratio of 0.20, 0.33, and 0.40 representing dry, moist, and wet (but unsaturated) conditions, respectively, while keeping the shear wave velocity constant. The remaining material properties are the same as those in Table 1 (except for the compression wave velocity). The material properties for the case of saturated subgrade conditions are shown in Table 2.

Four different shallow depths to bedrock of 1.5, 2.3, 3.1, and 6.1 m (5, 7.5, 10, and 20 ft, respectively) were studied. These depths were selected because the resonant depth to bedrock for the FWD test was always within 6 m (20 ft) of the pavement surface as shown in Figure 3, unless a very stiff subgrade [$V_s > 458$ m/sec (1500 fps)] was encountered.

### Unsaturated Subgrade Conditions

The depth to bedrock versus natural period, $T_d$, of the free vibrations for an unsaturated subgrade with Poisson's ratio of 0.20 is shown in Figure 10(*a*) and 10(*b*) for flexible and rigid pavements, respectively. The same set of plots for an unsaturated subgrade with Poisson's ratio of 0.33 is shown in Figure 10(*c*) and (*d*). These two sets of subgrade conditions can be considered to represent subgrades on the dry side of the optimum moisture content. For the case of the subgrade having Poisson's ratio equal to 0.40 (subgrade at or wet of the optimum moisture content), the linear relationship between depth to bedrock and the natural period of each profile is shown in Figure 11(*a*) and (*b*). There is a linear (or nearly linear) relationship between depth to bedrock and natural period for each stiffness and state of saturation of the subgrade in these figures. It should be noted that depth to bedrock is defined as the total depth from the top of the pavement to the top of the bedrock.

The equations of the straight lines for the flexible pavements with different Poisson's ratios ($\upsilon$) of the subgrade can be combined into one equation as:

$$D_b = \frac{V_s T_d}{(\pi - 2.24\,\upsilon)} \tag{5}$$

The equations for the rigid pavement with the subgrade having a range in Poisson's ratios ($\upsilon$ can also be combined into one equation as:

$$D_b = \frac{V_s T_d}{(\pi - 1.44\,\upsilon)} \tag{6}$$

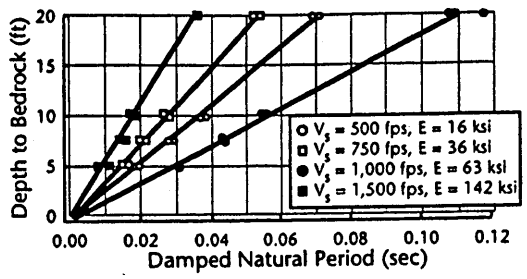


*(a) Flexible pavements with Poisson's ratio of the unsaturated subgrade = 0.20*

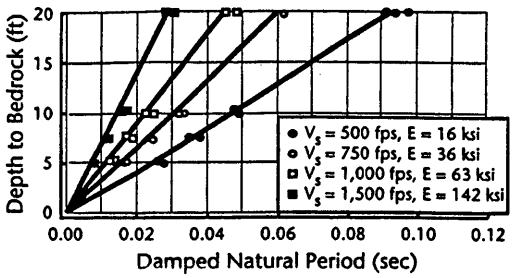


*(c) Flexible pavements with Poisson's ratio of the unsaturated subgrade = 0.33*

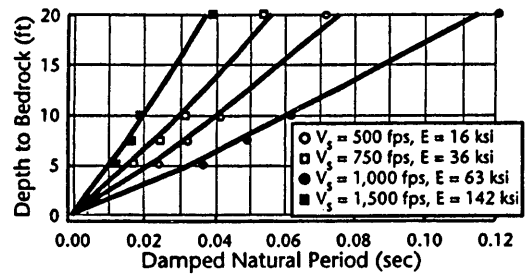


*(b) Rigid pavements with Poisson's ratio of the unsaturated subgrade = 0.20*

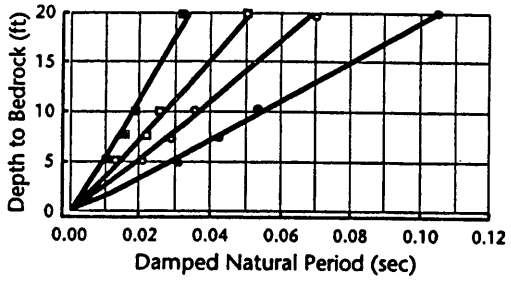


*(d) Rigid pavements with Poisson's ratio of the unsaturated subgrade = 0.33*

**FIGURE 10** Depth to bedrock versus damped natural period for FWD testing of pavement systems with subgrades having low to medium degree of saturation.

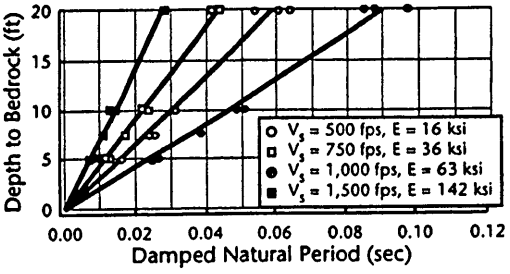


*(a) Flexible pavements with Poisson's ratio of the unsaturated subgrade = 0.40*

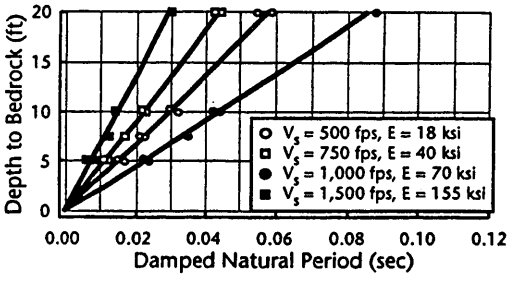


*(c) Flexible pavements with a saturated subgrade*

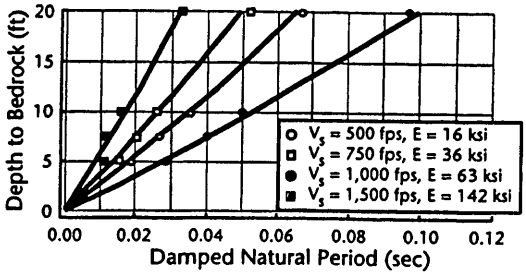


*(b) Rigid pavements with Poisson's ratio of the unsaturated subgrade = 0.40*

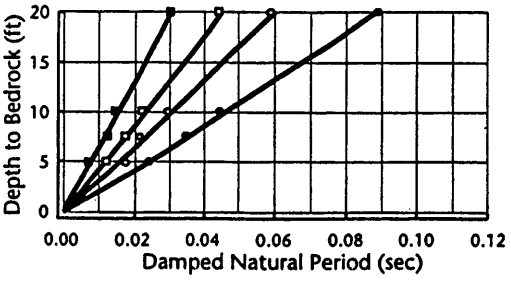


*(d) Rigid pavements with a saturated subgrade*

**FIGURE 11** Depth to bedrock versus damped natural period for FWD testing of the pavement systems with nearly saturated and saturated subgrades.

In Equations 5 and 6, $D_b$ and $V_s$ can be expressed in any consistent set of units. Equations 5 and 6 can be expressed in terms of Young's modulus of the subgrade instead of its shear wave velocity assuming a value of the mass density as before. Using a density of 2 000 kg/m$^3$ (or a unit weight of 110 pcf in British units) the expression substituting for $V_s$ becomes:

$$V_s = \frac{\sqrt{E}}{63\sqrt{1+\upsilon}} \qquad \left(\frac{\sqrt{E}}{2.6\sqrt{1+\upsilon}}\right) \tag{7}$$

### Saturated Subgrade Conditions

For saturated subgrade conditions, four different values for Poisson's ratios were used (0.495, 0.489, 0.479, and 0.451), which correspond to the four stiffnesses of the subgrade that result in the compression wave velocity equaling 1 525 m/sec (5,000 fps) (see Table 2). Figure 11(*c*) and 11(*d*) show the depth to bedrock versus natural period in this case. The equation for the flexible pavement is:

$$D_b = \frac{V_s T_d}{2.22} \tag{8}$$

The fitted equation for the rigid pavement can be expressed as:

$$D_b = \frac{V_s T_d}{2.31} \tag{9}$$

The expressions in terms of the Young's modulus can be obtained again using Equation 7.

## ESTIMATION OF SUBGRADE STIFFNESS FROM FWD TESTS

To use the above equations, a good estimate of the stiffness of the subgrade is required. The stiffness of the subgrade can be estimated by in situ seismic testing, by dynamic laboratory tests on undisturbed samples, or possibly even by experience. However, a more convenient and accurate way to estimate subgrade stiffness was developed in this study. It was observed that one could measure the offset time ($T_o$) of the first pulse in the time-deflection records as shown in Figure 12. The offset time is related to the Rayleigh wave velocity of the subgrade. With the assumptions discussed in the following section, and knowing the distance between two measurement stations, the shear wave velocity can be determined.

There are several assumptions that must be made to use the offset time method. First, the subgrade should be able to be approximated as a uniform material. Second, the wavelength should be long enough so that the surface, base, and sub-base layers have little effect on the Rayleigh wave velocity. Generally, this means that the wavelength should be at least 10 times the total thickness of the surface, base, and sub-base layers for untreated bases and sub-bases (*5*). Third, the bedrock needs to be deep enough so that it has little effect on the Rayleigh wave velocity. This condition is usually met if the bedrock depth is greater than 0.5 times the Rayleigh wavelength in the subgrade. Fourth, it is assumed that near-field effects are small and that they can be ignored. Fifth, the first pulses of Stations 5 and 7 were used to measure the offset time because the deflections obtained at the stations away from the source should better represent the properties of the subgrade. Finally, the difference between the Rayleigh wave velocity and the shear wave velocity is less than 10 percent if Poisson's ratio of the material is greater than 0.2 (*3*) so that it can be ignored. (Note: these assumptions may not apply in many test situations.)

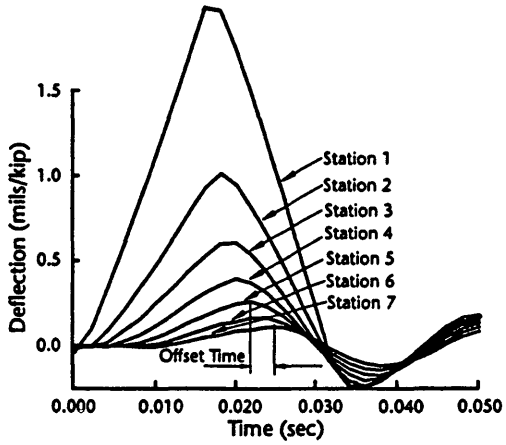


**FIGURE 12 Offset time of the first pulses between Stations 5 and 7 for FWD testing at Profile 1 [$V_s$ of subgrade = 500 fps (155 m/sec), $E$ = 16 ksi (0.11 MN/m$^2$) and depth to bedrock = 1.6 m (5 ft)].**

Table 3 illustrates an example of comparisons between the estimated shear wave velocity of the subgrade and the actual shear wave velocity for Profile 1 with an unsaturated subgrade having a Poisson's ratio equal to 0.20. Good estimations of the shear wave velocity of the subgrade are made in the case of the softest subgrade. However, as the stiffness of the subgrade increases and as the stiffnesses and thicknesses of the upper pavement layers increase, there are cases in which estimations cannot be made. This happens because the first pulses in the deflection-time records were distorted and the peaks could not be determined.

## SUMMARY

Analytical simulations of the FWD test were conducted using the computer program UTFWD (*1,2*). Four pavement profiles ranging from flexible to rigid were studied. The stiffness of the subgrade layer and the depth to bedrock (thickness of the subgrade) were the only parameters varied to simulate typical ranges in pavement systems that could be tested using the FWD.

Equations for estimating the resonant depth to bedrock, $RD_b$, were developed for both the flexible and rigid pavements. Depths to bedrock at which resonance effects may occur were found to vary from 1.7 to 6.2 m (5.5–20 ft), depending on the stiffness of the subgrade. Saturated subgrade conditions gave the same trend in resonant depth to bedrock with subgrade stiffness.

Equations for estimating the depth to bedrock based on the natural period of free vibrations of the pavement system immediately after FWD load application have been presented. In these equations, effects of stiffness and degree of subgrade saturation were taken into account. One important aspect in applying these equations is that complete time histories recorded for 0.12 sec or longer are desired.

**TABLE 3 Estimated Shear Wave Velocity of Subgrade from Offset Time of the First Pulses for FWD Testing at Profile 1**

Units: Vs (fps), E (ksi)

| Depth to Bedrock | Actual Vs of Subgrade (E of Subgrade) | | | | | |
|---|---|---|---|---|---|---|
| | 500 (16) | | | 750 (36) | | |
| | To | Estimated Vs | Error** | To | Estimated Vs | Error |
| (ft) | (sec) | (fps) | (%) | (sec) | (fps) | (%) |
| 5 | 0.0035 | 571 | 14% | na*** | na | na |
| 7.5 | 0.0039 | 513 | 3% | 0.0028 | 714 | -5% |
| 10 | 0.0040 | 500 | 0% | 0.0029 | 690 | -8% |
| 20 | 0.0042 | 476 | -5% | 0.0030 | 667 | -11% |

| Depth to Bedrock | Actual Vs of Subgrade (E of Subgrade) | | | | | |
|---|---|---|---|---|---|---|
| | 1000 (62) | | | 1500 (142) | | |
| | To | Estimated Vs | Error | To | Estimated Vs | Error |
| (ft) | (sec) | (fps) | (%) | (sec) | (fps) | (%) |
| 5 | na | na | na | na | na | na |
| 7.5 | na | na | na | na | na | na |
| 10 | 0.0020 | 1000 | 0% | na | na | na |
| 20 | 0.0021 | 952 | -5% | 0.0013 | 1538 | 3% |

* Poisson's Ratio of Subgrade equals 0.20.
** Error=[(Estimated Vs/Actual Vs)-1]*100%
*** Offset Time is not available because the first pulses in FWD tests are distorted.

A method to estimate the stiffness of the subgrade from the offset time of the first pulses of the deflection-time records at two measurement stations in the FWD tests has been proposed. The shear wave velocity of the subgrade can be estimated dividing the offset time into the distance between these two stations. At present, it seems that this approach is more appropriate in cases in which the stiffness of the subgrade is soft to moderate, $V_s$ = 155 to 233 m/sec ($V_s$ = 500–750 fps) [$E$ = 0.11 to 0.25 MN/m$^2$ ($E$ = 16–36 ksi)] and the bedrock depth is 3.1 m (10 ft) or more.

## ACKNOWLEDGMENTS

We thank the Texas Department of Transportation for partial support of the study under project 1175. The support of the Advanced Technology Program of the State of Texas is also sincerely appreciated.

## REFERENCES

1. Chang, D. W., J. M. Roesset, and K. H. Stokoe, II. Nonlinear Effects in Falling Weight Deflectometer Tests. *Transportation Research Record 1355*, TRB, National Research Council, Washington, D.C., 1992, pp. 1–7.
2. Chang, D. W., V. Y. Kang, J. M. Roesset, and K. H. Stokoe, II. Effect of Depth to Bedrock on Deflection Basins Obtained with Dynaflect and FWD Tests. *Transportation Research Record 1355*, TRB, National Research Council, Washington, D.C., 1992, pp. 8–16.
3. Richart, F. E., Jr., R. D. Woods, and J. R. Hall. *Vibrations of Soils and Foundations*. Prentice Hall, Englewood Cliffs, N.J., 1970.
4. Seng, C. R., K. H. Stokoe, II, and J. M. Roesset. *Effect of Depth to Bedrock on the Accuracy of Backcalculated Moduli Obtained with Dynaflect and FWD Tests. Research Report 1175-5*. Center for Transportation Research, University of Texas at Austin, Austin, Tex. 1993.
5. Aouad, M. *Evaluation of Flexible Pavements and Subgrades Using the Spectral-Analysis-of-Surface-Waves (SASW) Method*, Ph.D. dissertation. University of Texas at Austin, Austin, Tex. 1993.

*Publication of this paper sponsored by Committee on Soil and Rock Properties.*

# Determination of Resilient Modulus of Subgrades Using Bender Elements

SHAHRIYAR BAIG AND SOHEIL NAZARIAN

Resilient moduli of subgrades are becoming important input parameters in mechanistic pavement design. As such, test methodologies have been introduced by many highway agencies to estimate this parameter. These tests require several hours to perform. Therefore, only a small number of specimens can be tested for a given project. An alternative for rapidly determining the resilient modulus of subgrade soils—bender elements—is presented. Bender elements are thin sheets of piezo-ceramic material which are inserted in a specimen. When subjected to appropriate electric current, a Bender element bends and couples seismic energy to the specimen. A bender element can also be used to detect the coupled energy since it converts movement to voltage. For convenience, the end caps of a regular static triaxial test set-up can be retrofitted with a set of transmitting and receiving bender elements. The data reduction, which comprises of determining the arrival time of the seismic energy, is simple and can be carried out during the test. The limitation of the device is that the deviatoric stress cannot be varied and as such moduli at low strain levels are measured. Therefore, this method can be utilized parallel to resilient modulus tests when a large number of specimens of a similar subgrades has to be tested. Based on tests on over 30 different specimens, the bender elements can feasibly provide resilient moduli of subgrade materials at a fraction of time and at significantly lower investment in initial equipment costs. The bender element tests can be a compliment to the resilient modulus test systems.

In recent years, resilient modulus testing has gained tremendous popularity. This increased interest has been attributed to the American Association of State Highways and Transportation Officials (AASHTO) design procedure adopted in 1986. In the design procedure, the resilient modulus of subgrade soil is considered as one of the most important design parameters.

In general, the actual testing consists of more than a dozen loading steps. At each step either the confining pressure and/or the deviatoric stress is changed. The procedure requires tests at several confining pressures (ranging from 21 to 140 kPa for AASHTO) and several deviatoric stresses (ranging from 21 to 280 kPa for AASHTO). At each step, the specimen is subjected to a large number of cycles (100 cycles for AASHTO). The applied load, $F$, and the resulting resilient deformation of the specimen, $\delta$, are measured for the last five cycles. Knowing these two parameters as well as the cross-sectional area, A, and the height of the specimen, $L$, the resilient modulus, $M_R$, can be determined from

$$M_R = (F/A)/(\delta/L) \quad (1)$$

The test period for one specimen is approximately 3 hr. In addition the specimen preparation requires another 30–60 min.

The required equipment to perform resilient modulus tests is quite sophisticated and costly to acquire. A typical testing system consists of a closed-loop servo-valve system retrofitted with a triaxial cell, accurate load cells and linear variable differential transformers.

The use of piezo-ceramic bender elements in determining the dynamic properties of soil specimens in the geotechnical engineering area is becoming more popular (*1–4*). To respond to the level of interest, an ASTM subcommittee is developing standard procedure for this tests. Testing with the device is free from complicated data reduction procedures, is cost effective as well as rapid to perform.

The main limitation of the bender elements is that they yield moduli at low strain levels (less than 0.001 percent). Therefore, resilient modulus tests should still be carried out on the new subgrade specimens to determine their constitutive models. As done in the geotechnical engineering field, once the constitutive model for a given subgrade is developed, one can test similar subgrade soils with the bender elements as a rapid method for characterizing the variation in the moduli along a pavement or a highway.

Extrapolating the low-strain moduli from the bender elements to higher strain levels induced in the pavement is rather challenging. The study presented here is a feasibility study and as such does not address this important matter. However, this challenge with reasonable level of success has been addressed in geotechnical earthquake engineering [see Academy of Sciences (*5*) for an overview]. In that approach for a given soil, the variation in modulus with strain is normalized with respect to the modulus at a reference strain through comprehensive laboratory tests (resilient modulus in our case). This normalized curve, along with moduli from other test methods (bender elements in our case), are then combined during the analysis stages of the mechanistic pavement design.

## DESCRIPTION OF BENDER ELEMENT DEVICE

The bender elements have been mounted and used in various laboratory apparatus to measure shear or Young's modulus of soils (*1–3*).

Dyvik and Madshus (*4*) determined the shear modulus of five different offshore clays. They found that shear moduli obtained from bender elements and a resonant column device were practically identical for a wide range of soil stiffnesses.

Thomann and Hryciw (*6*) installed the bender elements in a new device called the Bender Element-Oedometer (BEO) device. They tested fine sands (Ottawa 100–200) and Glacierway silt. The purpose of these tests was to determine the shear moduli measured by the bender element technique and compare them with those obtained from a resonant column device at at-rest condition. In addition, bender elements were incorporated in a BEO device to study the effects of soil anisotropy on the small strain shear modulus.

A triaxial device incorporating bender elements was used in this research. A schematic of the device is shown in Figure 1. The

The Center for Geotechnical and Highway Materials Research, The University of Texas at El Paso, El Paso, Tex. 79968.

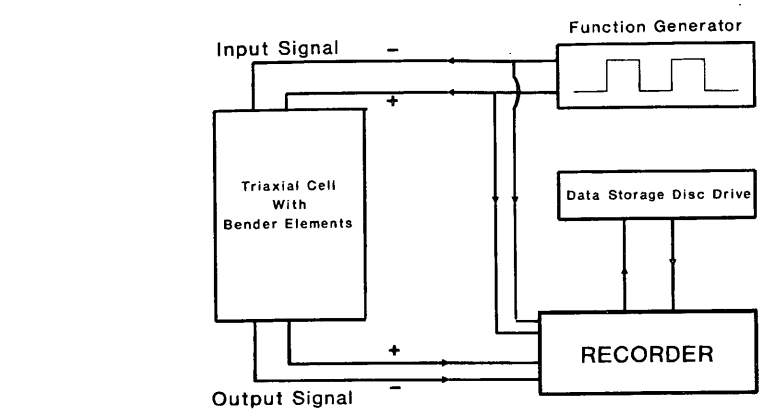


(*a*)

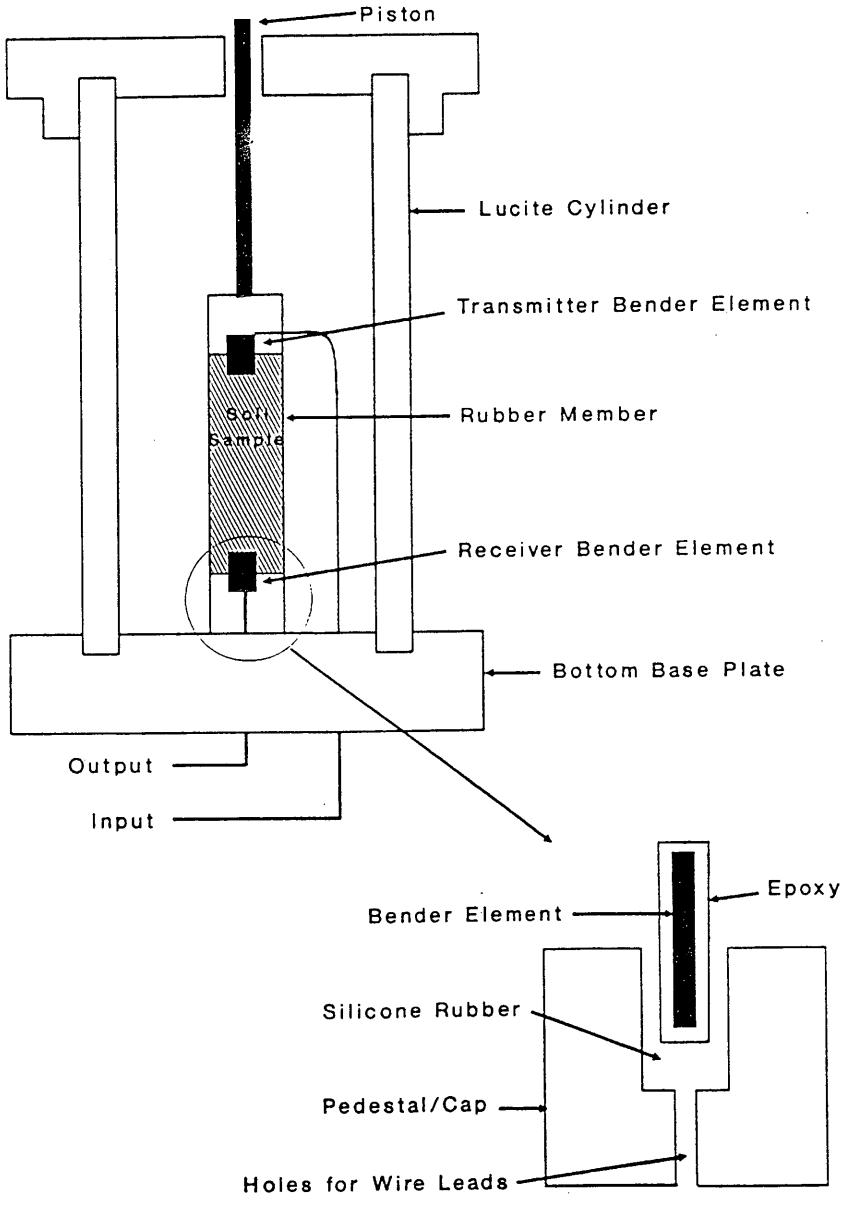


(*b*)

**FIGURE 1(*a*) Schematic diagram shows assembled testing devices. (*b*). Schematic of bender elements installed in triaxial device.**

receiver and transmitter bender elements were placed in the bottom and top caps of a triaxial device. The two end caps were specially designed and machined to accommodate the elements. The slots were then filled with silicone rubber and wire leads were run through the drainage holes in the bottom base plate of the triaxial cell. The elements were fixed in the caps such that at least two-thirds of their lengths were cantilevered. The cantilevered portion was inserted in the soil specimen to be tested. The triaxial load frame was used to apply very small seating loads to keep the specimens and the end caps in contact.

The major parameter measured with the bender elements is the travel time of seismic waves (especially shear waves) through the specimen along its longitudinal axis. Square wave pulses are applied to the transmitting element to couple body wave energy to one end of the specimen. The energy propagates within the specimen and is sensed by the receiving bender elements. A digital recorder was used to record the signals sensed by the receiving element. To enhance the quality of data recorded, tests were repeated 25 times, and their resulting signals were averaged. The signals were recorded at a sampling rate of 256 kHz which corresponds to an accuracy in travel time of approximately 2 μsec. As indicated by Baig (*7*), if the modulus of the material is less than 350 MPa, the modulus is known with an accuracy of better than 1.5 percent for a 150-mm long specimen. This level of accuracy is only due to travel time, and other factors such as mismeasurement of the length of the specimen may contribute to less accurate results.

Typical input and output traces are shown in Figure 2. One input and two output signals are shown. The two output signals correspond to two separate tests and are obtained by changing the polarity of the input voltage. When the polarity of the input is changed, the polarity of the propagated wave changes as well. The two outputs can be combined to minimize the ambiguity in the identification of the arrival time. The input record simply corresponds to the rise of the signal from zero to a maximum of about 10 volts. Some

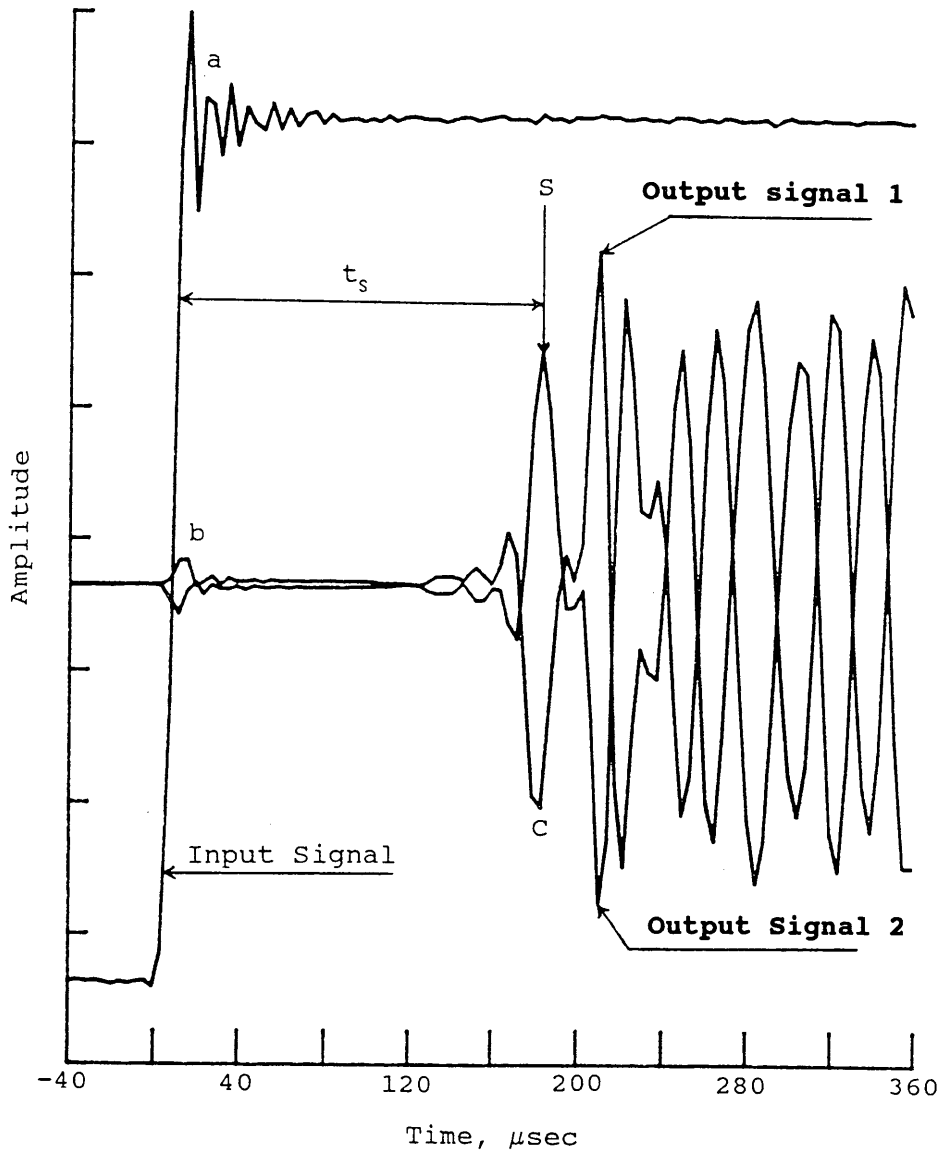


**FIGURE 2 Typical input and output signals.**

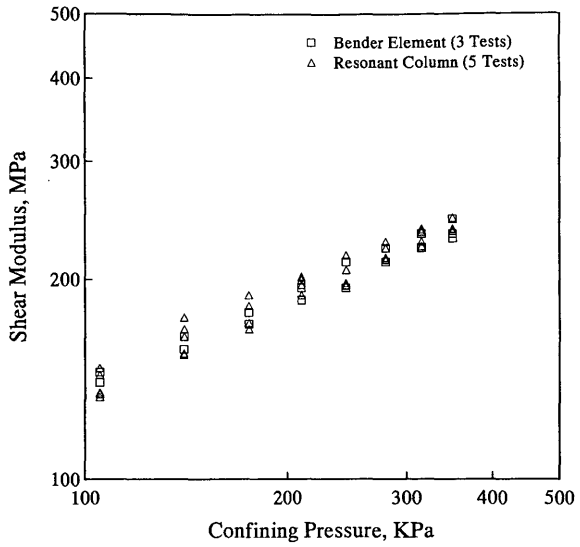


**FIGURE 3 Comparison of shear modulus results from bender elements and resonant column device.**

reverberation, marked *a* in the input signal is due to the nature of the wave generator.

The two output signals, aside from change in polarity, are similar. Before point *b*, the output is quiet and close to zero. This corresponds to pre-triggering events. At point *b*, some leakage of the input signal, probably through the recorder, occurs. This point coincides with the rise in the input. Point *S*, corresponds to the arrival of the shear wave. Therefore, the travel time, *t*[itinf]s[r], is the time interval between the rise of input record and Point *S*.

The shear modulus, *G*, can be calculated as follows.

$$G = (L/t_s)^2 \times \rho \quad (2)$$

where ρ is mass density, and *L* is the tip-to-tip spacing between the transmitting and receiving bender elements.

Young's modulus, *E*, can be easily calculated by assuming a Poisson's ratio, *v*, for the specimen using:

$$E = 2G(1 + v) \quad (3)$$

In the present study, a Poisson's ratio of 1/3 was assumed for calculation of Young's modulus.

## ACCURACY AND PRECISION

To determine the accuracy and precision of the bender elements setup used in this study, a series of test were carried out (*8*). A summary of the results are presented here.

Variations between moduli obtained with the resonant column and bender elements with confining pressure are compared in Figure 3. Resonant column tests are well established in the geotechnical-earthquake engineering area and are considered one of the most reliable and accurate methods for determining moduli of soils specimens (*9,10*).

The variation in modulus with confining pressure from three entirely different tests with the bender elements and five resonant column tests are shown in Figure 3. The results from the three bender element tests are quite similar. Based on more than 50 tests on sands and clays, Nazarian and Baig (*8*) reported that the precision (repeatability) of the bender element tests is better than 5 percent.

The moduli obtained with the resonant column device and the bender elements are typically within ±6 percent for most soils. Therefore, one can confidently utilize the bender elements to obtain accurate moduli.

## PRESENTATION OF RESULTS

### Test Program

To evaluate the feasibility of utilizing bender elements in determining the resilient modulus of subgrades, a test program was developed. A sand and a clay resident to El Paso, Tex., were selected. The index properties of these two materials are reported in the next section. Four different proportions of sands and clays were mixed to obtain a wide variety of compositions. The different proportions tested are presented in Table 1. The percentage of clay in different specimens varied from 30 to 90 percent. For each mixture, tests were carried out at three nominal water contents—optimum, 2 percent wet of optimum, and 2 percent dry of optimum. Tests were repeated two or three times for each mixture and at each water content to evaluate the repeatability.

A given specimen was first tested using the conventional resilient modulus tests following a modified version of the AASHTO T-274 protocol (*11*). The same specimen was then carefully transferred to the triaxial cell that contained the bender elements and tested at confining pressures of 14, 28, and 42 kPa, respectively. The results were then directly compared as discussed later in this report.

**TABLE 1 Total Quantity of Specimens Tested**

| Specimen Composition (percent) | | Number of Specimens | | |
|---|---|---|---|---|
| Clay | Sand | 2% Dry of Optimum | Optimum | 2% Wet of Optimum |
| 90 | 10 | 3 | 3 | 3 |
| 70 | 30 | 3 | 3 | 3 |
| 50 | 50 | 2 | 3 | 3 |
| 30 | 70 | 2 | 2 | 2 |

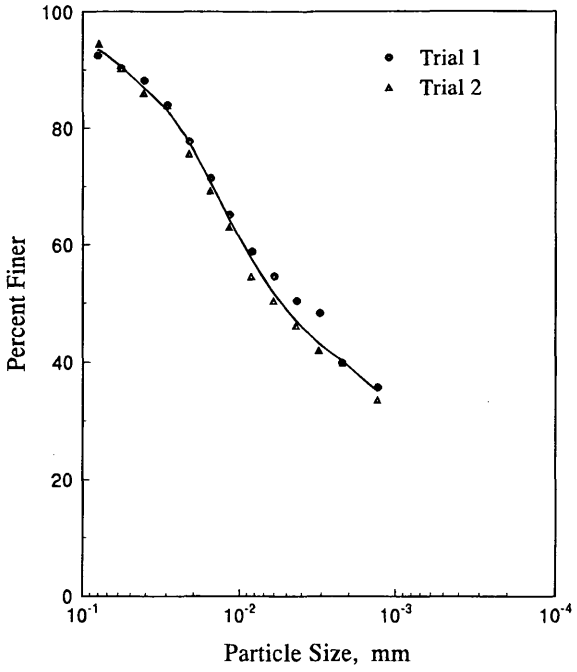


**FIGURE 4 Grain size distribution for clay.**

The main two modifications made to AASHTO T-274 are (*11*) fewer number of load repetition at each sequence (i.e., 25 cycles as opposed to 100 cycles for AASHTO), and less destructive loading sequence (i.e., smaller ratios of the deviatoric stress to confining pressure). Nazarian and Feliberti (*11*) indicated that the modified test program minimizes the degradation of the specimen due to the previous loading history.

## Index Properties of Materials

The grain size distribution of the clay is shown in Figure 4. The Atterberg limits were also obtained. The liquid limit and plasticity limit were 44.1 and 20.5 percent, respectively. The plasticity index is therefore 23.6 percent. Based on the Atterberg limits and gradation, the clay was classified as "CL" in the Unified Soil Classification System (USCS) and A-7-6 according to the AASHTO Classification System. The maximum dry density of the clay using the standard Proctor method was 1l699 kg/m$^3$ and the optimum water content was 16.0 percent.

The sand was first sieved. Only the fraction passing no. 40 sieve and retained on no. 60 sieve was utilized to minimize segregation. The maximum and minimum densities of the sand were 11713 and 11494 kg/m$^3$, respectively. The sand was classified as SP in the USCS and A-3 in the AASHTO Classification System.

As indicated before, the specimens tested were composed of a mixture of the sand and clay above. The Atterberg limits and Proctor moisture-density tests were performed on each mixture. The liquid limit, plastic limit, and plasticity index for each mixture are reported in Table 2. As expected, as the clay content increases the

**TABLE 2 Index Properties of Sand-Clay Mixtures**

| Mixtures Clay(percent)/ Sand (percent) | Liquid Limit (percent) | Plastic Limit (percent) | Plasticity Index (percent) | Classification (AASHTO/USCS) | Maximum Density (Kg/m$^3$) | Optimum Moisture Content (percent) |
|---|---|---|---|---|---|---|
| 100/0 | 44.7 | 20.5 | 24.2 | A-6/CL | 1699 | 16.0 |
| 90/10 | 37.5 | 18.6 | 18.9 | A-6/CL | 1953 | 18.4 |
| 70/30 | 30.5 | 16.3 | 14.2 | A-6/CL | 1696 | 16.9 |
| 50/50 | 23.2 | 15.7 | 7.5 | A-6/ML-CL | 1791 | 15.2 |
| 30/70 | 17.3 | 13.8 | 3.5 | A-2-4/SC | 1837 | 10.3 |
| 0/100 | -- | -- | Non Plastic | A-3/SP | 1697 | -- |

-- not applicable

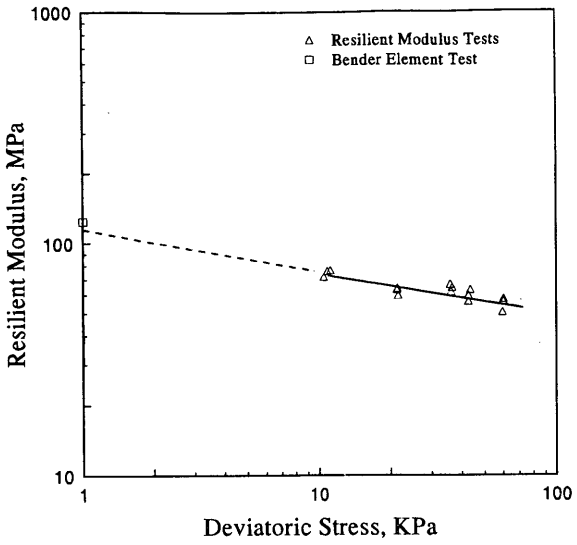


**FIGURE 5 Variation in resilient modulus with deviatoric stress for a 90 percent clay-10 percent sand specimen.**

liquid limit significantly increases, whereas the plastic limit only slightly increases.

The optimum moisture content and maximum dry density for each mixture are also shown in Table 2. As the clay content increases (up to a clay content of 70 percent) the maximum dry density decreases and the optimum water content increases. However, for a clay content of 90 percent, the maximum dry density sharply increases.

## Resilient Modulus

A typical variation in modulus with deviatoric stress from resilient modulus tests for a mixture of 90 percent clay and 10 percent sand at optimum moisture content is shown in Figure 5. There is not much scatter in the data. At each deviatoric stress, the variation in modulus is due to the variation in confining pressure. This trend more or less held true for the remaining mixtures (*12*).

Data obtained from bender element tests on identical specimen are also incorporated in Figure 5. These data were arbitrarily plotted at a deviatoric stress of 1 kPa, given the low deviatoric stresses exerted to the specimen. The results from the two techniques are in relatively good agreement.

A typical graph of variation in resilient modulus with clay contents for various sand-clay mix specimens are presented in Figure 6.

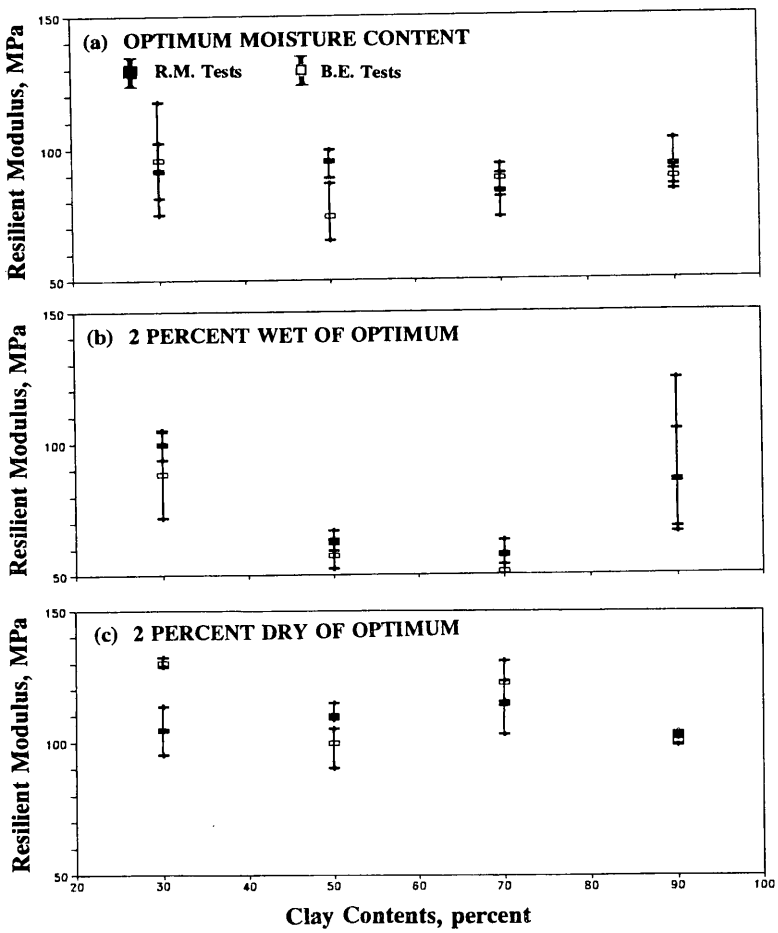


**FIGURE 6 Variations in resilient modulus with clay content from resilient modulus and bender element tests.**

Figures 6a, 6b, and 6c illustrate results for specimens prepared at optimum moisture content, 2 percent wet of optimum moisture content and 2 percent dry of optimum moisture content, respectively. The extreme values as well as the average resilient moduli are plotted for the three specimens tested at three confining pressures and different deviatoric stresses. The abbreviation R.M. is for resilient modulus, whereas B.E. is for bender elements in Figure 6.

Some scatter in the data is evident. The reasons for the scatter are several, and typically deal with the inherent problems with both testing techniques. With the bender elements, the major problems during these tests were: 1) the difficulty with inserting the bender elements into the specimen (especially for the specimens prepared at the dry of optimum, 2) inability to control the dynamic deviatoric stresses, and 3) the possibility of misestimating Poison's ratio.

The major problem with the resilient modulus tests is the typical levels of repeatability associated with the testing protocol. A repeatability of better than 10 percent is difficult when the specimen is not grouted (*12*). The major reason for the variability is the differences in the uniformity between the specimens tested for each mix due to difficulties in maintaining the uniformity in compaction.

One other factor ignored during this study is that the specimens were tested with the bender elements after they had already subjected to a stress history during the resilient modulus tests. As indicated above, studies performed by Nazarian and Feliberti (*11*) indicated that this parameter should not be of great significance if their proposed loading sequence is followed. However, it would have been desirable to verify this.

### Comparison of Results

The results from all tests are compared in Figure 7. Moduli obtained from resilient modulus tests at a given confining pressure are plotted on the *x*-axis and the moduli obtained from the bender elements at the same confining pressure are plotted on the *y*-axis. The line-of-equality and the best-fit line are also plotted on the same graph. In addition, the 95 percent confidence interval lines are also included. Moduli obtained from the two techniques are comparable. The best-fit line follows the line of equality fairly well. As indicated in the figure, the slope of the best fit line is about 1.02. This can be interpreted that in general the results are in reasonable agreement.

The 95 percent confidence interval lines bound the best-fit line with a relatively narrow band. The slope of the lines for lower and upper bounds are 0.91 and 1.11, respectively. This may be an indication that in most cases the bender elements can predict the resilient modulus of a specimen with sufficient and reasonable accuracy.

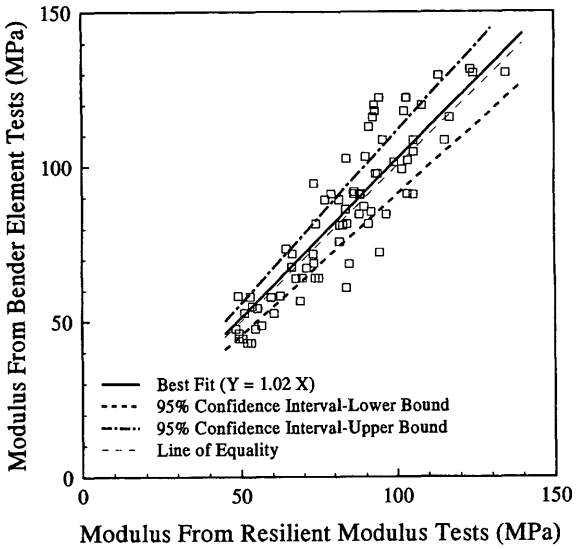


**FIGURE 7 Comparison of resilient moduli obtained from resilient modulus and bender element techniques.**

## SUMMARY AND CONCLUSIONS

This report contains a technique for rapidly determining the resilient modulus of subgrades. The resilient modulus determined with bender elements is only a function of travel time of body waves within the specimen and does not depend on several parameters as in other conventional methods. More tests are necessary to draw any definite conclusions.

Based on this study, the following conclusions can be drawn:

1) With the bender elements, the resilient modulus of subgrades can be predicted with a reasonable accuracy.

2) The method is cost-effective when resilient modulus values are needed for a large number of specimens in a short turn-around time.

3) The results obtained from both methods were in reasonably good agreement. Some variation in moduli are found due to various limitations related to both methods.

## ACKNOWLEDGMENT

The resilient modulus test results demonstrated here were performed by Mr. Manuel Feliberti for the Texas Department of Transportation under Project 1177. The support of that organization is appreciated.

## REFERENCES

1. Shirley, D. J., and L. D. Hampton. Shear Wave Measurement in Laboratory Sediments. *Journal of the Acoustical Society of America*, Vol. 63, No. 2, 1978, pp. 607–613.
2. Schultheiss, P. J. Simultaneous Measurements of P & S Wave Velocities During Conventional Laboratory Soil Testing Procedures. *Marine Geotechnology*, Vol. 4, No. 4, 1981, pp. 343–367.
3. Hamdi, F., and D. T. Smith. The Influence of Permeability on Compressional Wave Velocity in Marine Sediments. *Geophysical Prospecting*, No. 30, 1982, pp. 622–640.
4. Dyvik, R., and R. Madshus. Lab Measurement of $G_{max}$ Using Bender Elements. In *Advances in the Art of Testing Soils under Cyclic Conditions* (V. K. Khosla, ed.), American Society of Civil Engineering, New York, NY, 1985.
5. Academy of Sciences. *Liquefaction of Soils during Earthquakes*. National Academy Press, Washington, D.C., 1985.
6. Thomann, T. G., and R. D. Hryciw. Laboratory Measurement of Small Strain Modulus under $K_0$ Conditions. *Geotechnical Testing Journal*, Vol. 13, No. 2, 1990, pp. 97–105.
7. Baig, S. *Evaluation of Piezo-Ceramic Bender Elements for Measuring Low-Amplitude Shear Modulus of Various Soils*. Master's thesis. The University of Texas at El Paso, Tex.
8. Nazarian, S., and S. Baig. Evaluation of Bender Elements for Use with Coarse-Grained Soils. In *Third International Conference on Recent Advances in Geotechnical Earthquake Engineering and Soil Dynamics*, St. Louis, Mo., Vol. 1, 1995, pp. 89–94.

9. Drnevich, V. P. Recent Developments in Resonant Column Testing. Presented at Annual Meeting of the American Society of Civil Engineering, Detroit, Mich., October 1985, 29 pp.
10. Isenhower, W. M., K. H. Stokoe, and J. C. Allen. Instrumentation for Torsional Shear/Resonant Column Measurement Under Anisotropic Stresses. *Geotechnical Testing Journal*, Vol. 10, No. 4, 1987, pp. 183–191.
11. Nazarian, S., and M. Feliberti. Methodology for Resilient Modulus Testing of Cohesionless Subgrades. *Transportation Research Record 1406*, TRB, National Research Council, Washington, D.C., 1994, pp. 108–115.
12. Feliberti, M., S. Nazarian, and T. Srinivasan. *Critical Evaluation of Parameters Affecting Resilient Modulus Tests of Subgrades*. Research Report 1177-2, Center for Geotechnical and Highway Materials Research, The University of Texas at El Paso, Texas.

*Publication of this paper sponsored by Committee on Soil and Rock Properties.*

# Resilient Properties of Laboratory Compacted Subgrade Soils

LOUAY N. MOHAMMAD, ANAND J. PUPPALA, AND PRASAD ALAVILLI

The subgrade of road bed soils is generally constructed near the optimum moisture content-dry density combination standard Proctor tests. However, environmental and seasonal variations alter the design moisture contents and the resilient properties of subgrade soils. These changes influence structural performance of pavements. Recent pavement design guides, which use the resilient modulus for characterizing pavement materials, require additional information on seasonal moisture content variations and their influence on resilient properties. This report presents results from an experimental study which investigated the influence of moisture content variations on the resilient modulus of soils. Two soil types, sand and silty clay compacted at, above, and below optimum moisture content levels were tested using the AASHTO T-294 procedure. Two in-cell displacement measurement systems measured displacements with respect to the ends of the specimen and the middle one-third of the specimen. Results indicated that the influence of moisture content on moduli appears to be more evident in clays than in sands. The effect of moisture content on the resilient modulus computed from both measurement systems is discussed. The measurement coefficients used to convert end system moduli to middle system moduli are provided for various moisture content levels in both soils. The influence of conditioning confining stresses and moisture contents on accumulated plastic deformations is also evaluated. The regression model results for the tests conducted in the investigation are also included.

The 1986 AASHTO design guide recommends using a resilient modulus as the property for characterizing flexible pavement materials (*1*). The resilient modulus is defined as the ratio of repeated deviatoric stress to recoverable axial strain. The subgrade soils are usually tested in repeated load triaxial tests at the optimum moisture content since most embankment subgrade soils are compacted close to the optimum moisture content and the maximum dry density levels determined from standard Proctor tests. However, moisture content levels in the subgrade soils will vary as a result of seasonal and environmental fluctuations. The changes in moisture contents in the field will result in the variation of soil saturation levels, which in turn alter the strength and resilient properties of subgrade soils. Therefore, characterization based on resilient modulus ($M_r$) values at optimum moisture contents may not be accurate or reasonable enough to provide realistic designs for the design life of the pavement.

In addition, it is reported that most pavement failures occur as a result of wet and dry moisture content cycles of subgrade layers (*2*). Saturation due to flooding of underlying soil layers results in erosion of subgrades (*2*). On the other hand, extreme drying in summer periods causes shrinkage cracks in plastic clays. When wetted, the cracks soften the subgrade layers and decrease the strength of the pavement. Thus, it is important to identify the properties on the dry and wet side of the optimum moisture content levels which are more representative of field conditions. This is the rationale for the use of relative damage factors which represent moisture content fluctuations due to seasonal temperature variations in determining the effective resilient modulus. This modulus is used in the design of flexible pavements.

Two types of soils were tested at three different moisture contents. The soils were a blasting sand and a silty clay. The tests were conducted on the dry of optimum, at optimum and on the wet of optimum moisture content. This allowed to study of the influence of moisture content variation on the resilient modulus and plastic deformations developed during the conditioning and testing phases. Also, as a part of the laboratory investigations, the influence of the location of internally placed linear variable differential transformers (LVDTs) in providing accurate and realistic measurements is evaluated.

## BACKGROUND AND OBJECTIVE

Several investigators recognize moisture content as an important soil parameter for determining the resilient modulus of soils for the design and characterization of flexible pavements (*2–5*). Elliott et al. (*5*) listed drainability, hydraulic conductivity, soil type, geometry of the road, topography, water table depth, precipitation, and temperature as important factors that affect moisture contents in the field. Some of these factors and their influence on pavement performance are described below.

Cohesive subgrade soils pose a problem in practice, since the pore pressure developed during traffic loading will not be dissipated immediately due to the low hydraulic conductivity of soils. As a result, the effective stresses and subsequently the strength of the subgrade soils will be decreased. The resilient properties also decrease and may cause rutting failures in pavement when subjected to higher traffic loads. The hydraulic conductivity of the compacted soils depends on several factors like soil fabric, mineralogy, and moisture content or saturation level. The moisture content is the controlled variable in this study. Therefore, any factors that influence the moisture contents of soils will also influence the performance of pavement sections.

Several research studies in the past have attempted to investigate the influence of moisture content on resilient modulus results. Thompson (*3*) provided regression equations relating the breakpoint resilient modulus values at a deviatoric stress of 6 lb/in.$^2$ and the degree of saturation. These equations, which showed the combined effects of moisture contents and densities, become independent of the degree of saturation with an increase in clay content and plasticity. Pezo et al. (*6*) investigated influence of moisture content and plasticity indices by conducting $M_r$ tests on several subgrade soils

Louisiana Transportation Research Center, Baton Rouge, La. 70808.

from Texas. This investigation indicated that an increase in moisture content resulted in a decrease of the resilient moduli. It is also reported that the influence of moisture content is more significant on soils with lower plasticity indices than those with high plasticity indices.

Conclusions drawn from previous studies regarding the role of moisture contents are similar. This research study is also aimed at understanding the resilient behavior of two soils at various moisture contents. This investigation is, however, different from other studies. Previous studies utilized external or internal end measurements and the soil samples were tested under AASHTO procedures T-274 and T-292. This study utilized two types of internal measurement systems and the samples were tested using the recent AASHTO T-294 procedure (*7*). The results are used to understand the influence of moisture contents on the resilient modulus and plastic deformations of soils, as well as to determine the influence of internal measurement systems in obtaining realistic measurements. It should be noted that the relative compaction level of dry, wet, and at optimum moisture contents varied between 98 and 100 percent, which indicates that the effect of dry density is not a controlling factor in this study.

## EQUIPMENT AND SOIL DESCRIPTION

### Loading System

An MTS model 810 closed loop servo-hydraulic material testing system was used for applying repeated loading. A detailed description of the equipment is presented elsewhere (*8–10*). An automated test software was developed and used for conducting tests, and performing data acquisition, reduction, and analysis tasks.

### Measurement Systems

One of the aspects of interest in this study is the location of LVDTs on the specimens. It should be mentioned that the T-294-1992 procedure, which was used for conducting tests in the present program, suggests the use of an external LVDT system while the T-292-1991 procedure requires the use of both external and internal LVDT systems. The internal LVDT system located inside the chamber is a better system than those used outside the chamber since the measurements by internal systems are less influenced by system compliance errors.

This study used two diametrically placed internal LVDTs fixed on a Plexiglas clamp system. One system measured the deformations with respect to the ends of the specimen and the other measured the deformations in the middle one-third of the specimen. These systems are referred to as end system and middle systems, respectively.

### Description of Soils and Specimen Preparation

Two locally available soils, a uniform blasting sand and a silty clay, were used in this study. The blasting sand exhibited dry densities of $\gamma_{max}$ = 17.7 kN/m$^3$ (110.9 lb/ft$^3$) and $\gamma_{min}$ = 15.8 kN/m$^3$ (99.0 lb/ft$^3$). The silty clay had an optimum water content of 20.6 percent, a maximum dry density of 16.3 kN/m$^3$ (101.6 lb/ft$^3$) and a plasticity index (PI) of 22. The silty clay and blasting sand were classified as A-7-6 and A-3 using AASHTO classification. Figure 1 presents standard Proctor density curves of these soils. Sand specimens were compacted in-place in the triaxial cell to reduce sample disturbance. Cohesive specimens were compacted in molds and carefully extruded for testing. Both specimens were 71.1 mm (2.8 in.) in diameter and 142.2 mm in height. Specimens were compacted at three different moisture contents and dry density combinations which cover the optimum, dry of optimum, and wet of optimum ranges. A list of these levels is given in Table 1.

### Conditioning and Testing Procedure

The specimens were first subjected to a conditioning phase, followed by testing at various confining and deviatoric stress levels. The prescribed deviatoric load of haversine shape was applied in both conditioning and testing phases. The tests on both materials were performed at the confining and deviatoric stress levels recommended in the latest versions of AASHTO T-294-92. Detailed description of the AASHTO testing procedure can be found elsewhere (*8–10*). The data obtained from the acquisition were analyzed and reduced to determine resilient strains, plastic strains, and the moduli values for each of the confining and deviatoric stresses.

## ANALYSIS OF RESULTS

### Sands

Table 2, a, b, and c, presents the resilient modulus test results for each moisture content level. The data include the end and middle resilient modulus, along with their means, standard deviations (*STD*), and coefficient of variations (*CV*) for each set of five tests. The coefficient of variation varied between 0.1 and 15.0 with most of the values being around 3.0. This implies that the test results are highly repeatable. The higher coefficients of variations (*CV* values around 10) were obtained for the end resilient moduli data from tests conducted above and below optimum moisture contents at low confining stresses.

Figure 2 shows the variation of end resilient moduli at different moisture contents and dry densities for various confining stresses of 21 kPa (3 lb/in.$^2$), 70 kPa (10 lb/in$^2$), and 140 kPa (20 lb/in.$^2$), respectively. It should be noted that the resilient modulus increases with an increase in the confining pressure. This is attributed to the stiffness properties which increase with an increase in confining pressure (*9*). The decrease in dilational behavior at higher confining pressures also results in lesser axial strains and higher moduli values.

The influence of deviatoric stress can also be deduced from Figure 2. The deviatoric stress increase resulted in a slight increase in the end moduli values at each confining pressure. Overall, the deviatoric stress has a minor influence on resilient properties when compared with the confining pressure. This is because the deviatoric load levels applied are lesser than the peak deviatoric loads which can induce significant changes and deformations in the specimens. Therefore, the deformation responses in these tests are directly proportional to the applied deviatoric loading which results in slightly higher $M_r$ values.

The compaction moisture content appears to have some influence on $M_r$ results at low confining pressures. Figure 2 also indicates that higher moduli values are obtained at dry and wet of optimum moisture content level. An increase in strength at dry of optimum resulted in a slight increase in $M_r$ values over the optimum $M_r$ values. This is in agreement with those reported by other investiga-

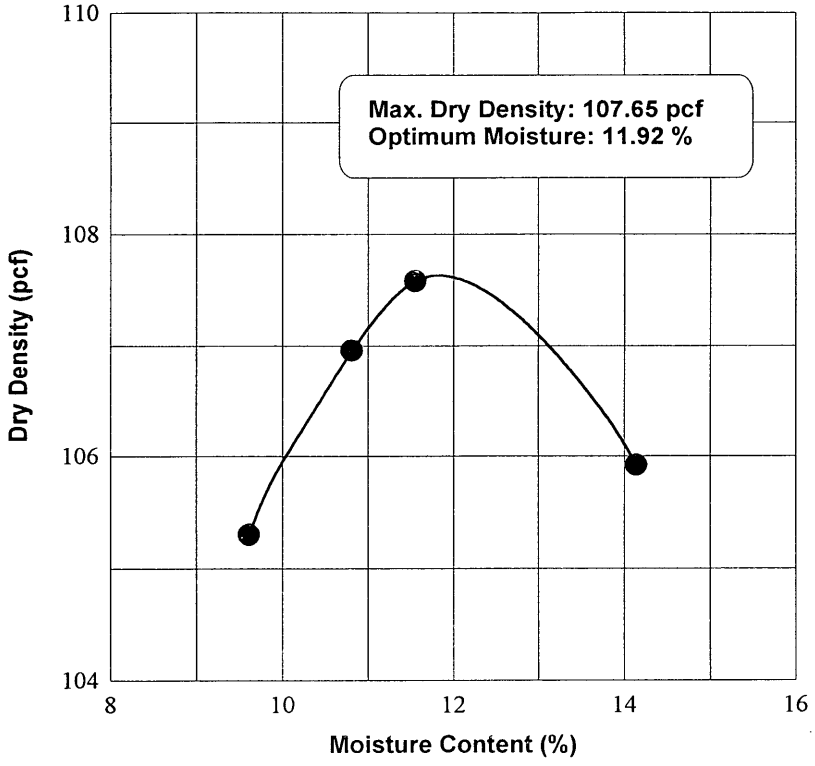


(a) Blasting Sand

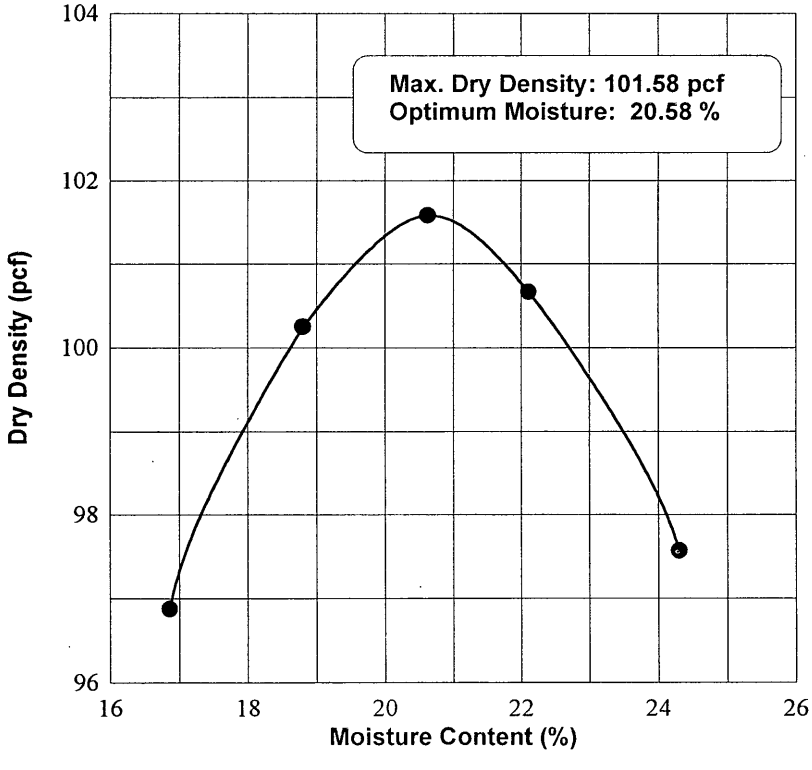


(b) Silty Clay

**FIGURE 1** Standard proctor curves.

TABLE 1 Density-Moisture Content Levels of the Soil Specimens

| Soil | Description (Optimum) | Dry Density (pcf) | Moisture Content (%) | Relative Compaction (%) |
|---|---|---|---|---|
| Blasting Sand | Dry | 105.5 | 9.67 | 98 |
| | Near | 107.65 | 11.92 | 100 |
| | Wet | 106.65 | 13.50 | 99 |
| Silty Clay | Dry | 96.50 | 18.00 | 98 |
| | Near | 101.58 | 20.58 | 100 |
| | Wet | 96.50 | 23.00 | 98 |

tions (*2,3,5*). On the other hand, the moduli at wet of optimum are higher than those of optimum at low confining pressures. This trend cannot be explained except for the fact that leakage problems were experienced during the wet of optimum specimen tests. This may have decreased the moisture contents in the soil specimens which probably resulted in higher resilient properties.

Results at higher confining pressures appear to provide similar resilient properties at all moisture contents. This is attributed to the small variations in relative compaction levels as well as the smaller role of moisture contents in sands at higher confining pressures. As mentioned earlier, the relative compactions at the moisture content-density levels vary from 98 to 100 percent which indicate that the corresponding relative densities of the sand do not vary considerably. This variation in relative density is not significant enough to provide distinctly different $M_r$ values.

## Clays

Table 3 presents the resilient modulus test results at dry of optimum, optimum and wet of optimum, respectively. The coefficients of variation of clay test results are higher than those obtained for sands. However, this number is relatively small when compared with the variations in modulus values. This indicates that the clay test results are also repeatable.

Figure 3 presents clay specimen results at dry, near, and wet of optimum moisture content levels. The end measurement results are depicted in this figure. An increase in confining pressure resulted in an increase in moduli values. This is attributed to an increase in stiffness with an increase in confining pressure. Results at three moisture content levels show that the $M_r$ values at dry and optimum levels are closer but significantly higher than those at wet of optimum.

TABLE 2 Sand Test Results

(a) Dry of Optimum

| $\sigma_3$ | $\sigma_d$ | Mr, ends (MPa) | | | Mr,middle (MPa) | | |
|---|---|---|---|---|---|---|---|
| kPa | kPa | Mean | STD | CV | Mean | STD | CV |
| 139.3 | 104.7 | 375.2 | 22.0 | 5.9 | 429.8 | 17.7 | 4.1 |
| 20.9 | 20.9 | 151.9 | 21.2 | 14.0 | 190.7 | 11.7 | 6.1 |
| 21.1 | 35.1 | 160.5 | 22.5 | 14.0 | 196.7 | 9.4 | 4.8 |
| 21.1 | 52.1 | 164.5 | 23.5 | 14.3 | 202.6 | 9.5 | 4.7 |
| 21.1 | 69.4 | 165.1 | 24.6 | 14.9 | 201.9 | 10.0 | 5.0 |
| 34.8 | 35.2 | 204.4 | 27.5 | 13.4 | 258.6 | 9.1 | 3.5 |
| 34.9 | 69.7 | 209.9 | 27.1 | 12.9 | 256.7 | 10.4 | 4.1 |
| 34.9 | 104.4 | 205.8 | 25.0 | 12.1 | 244.0 | 11.2 | 4.6 |
| 34.9 | 137.9 | 194.6 | 23.4 | 12.0 | 221.1 | 14.5 | 6.6 |
| 69.7 | 35.1 | 277.8 | 26.6 | 9.6 | 338.9 | 13.5 | 4.0 |
| 69.7 | 69.7 | 287.0 | 23.9 | 8.3 | 338.9 | 14.6 | 4.3 |
| 69.7 | 138.8 | 291.1 | 21.5 | 7.4 | 332.8 | 17.8 | 5.4 |
| 69.6 | 207.7 | 280.3 | 19.1 | 6.8 | 311.9 | 15.7 | 5.0 |
| 104.6 | 69.6 | 334.2 | 19.4 | 5.8 | 387.2 | 15.2 | 3.9 |
| 104.6 | 104.6 | 341.6 | 19.4 | 5.7 | 390.9 | 16.6 | 4.2 |
| 104.5 | 138.7 | 345.5 | 18.8 | 5.4 | 391.9 | 16.9 | 4.3 |
| 104.5 | 207.8 | 347.0 | 18.0 | 5.2 | 385.8 | 17.2 | 4.5 |
| 139.4 | 69.5 | 379.6 | 18.2 | 4.8 | 435.8 | 15.8 | 3.6 |
| 139.4 | 104.5 | 387.8 | 18.3 | 4.7 | 438.5 | 17.0 | 3.9 |
| 139.4 | 138.7 | 393.2 | 17.7 | 4.5 | 443.8 | 18.5 | 4.2 |
| 139.4 | 276.9 | 396.7 | 17.5 | 4.4 | 434.1 | 19.1 | 4.4 |

TABLE 2 *(continued)*

(b) Optimum

| $\sigma_3$ (kPa) | $\sigma_d$ (kPa) | Mr, ends (MPa) | | | Mr, middle (MPa) | | |
|---|---|---|---|---|---|---|---|
| | | Mean | STD | CV | Mean | STD | CV |
| 139.0 | 104.5 | 351.4 | 9.0 | 2.6 | 434.3 | 20.6 | 4.8 |
| 20.4 | 20.7 | 122.3 | 4.1 | 3.3 | 193.1 | 13.1 | 6.8 |
| 20.4 | 34.9 | 130.5 | 3.0 | 2.3 | 196.5 | 12.4 | 6.3 |
| 20.4 | 51.7 | 137.5 | 1.9 | 1.4 | 205.4 | 14.3 | 7.0 |
| 20.4 | 69.2 | 143.5 | 1.3 | 0.9 | 211.8 | 14.8 | 7.0 |
| 34.2 | 35.1 | 177.9 | 1.9 | 1.1 | 263.9 | 15.6 | 5.9 |
| 34.2 | 69.6 | 184.3 | 2.1 | 1.2 | 265.1 | 14.1 | 5.3 |
| 34.2 | 104.4 | 188.9 | 2.4 | 1.3 | 258.9 | 15.3 | 5.9 |
| 34.1 | 138.3 | 193.2 | 3.0 | 1.6 | 252.7 | 15.5 | 6.2 |
| 69.1 | 35.1 | 266.3 | 3.5 | 1.3 | 355.2 | 15.7 | 4.4 |
| 69.1 | 69.6 | 278.3 | 2.7 | 1.0 | 352.1 | 13.1 | 3.7 |
| 69.2 | 138.8 | 289.7 | 3.7 | 1.3 | 351.4 | 11.4 | 3.3 |
| 69.2 | 207.8 | 286.5 | 4.6 | 1.6 | 339.1 | 12.8 | 3.8 |
| 104.0 | 69.6 | 331.9 | 5.3 | 1.6 | 406.9 | 13.8 | 3.4 |
| 104.0 | 104.5 | 341.8 | 4.6 | 1.4 | 410.0 | 13.3 | 3.2 |
| 104.0 | 138.7 | 348.7 | 4.7 | 1.4 | 412.0 | 13.7 | 3.3 |
| 104.0 | 207.7 | 355.0 | 5.0 | 1.4 | 411.6 | 13.3 | 3.2 |
| 139.0 | 69.5 | 385.5 | 4.2 | 1.1 | 464.5 | 15.7 | 3.4 |
| 139.0 | 104.4 | 394.1 | 4.5 | 1.1 | 466.0 | 13.9 | 3.0 |
| 139.0 | 138.7 | 402.2 | 5.2 | 1.3 | 469.7 | 14.2 | 3.0 |
| 138.9 | 276.9 | 412.5 | 4.7 | 1.1 | 468.2 | 15.4 | 3.3 |

(c) Wet of Optimum

| $\sigma_3$ (kPa) | $\sigma_d$ (kPa) | Mr, ends (MPa) | | | Mr, middle (MPa) | | |
|---|---|---|---|---|---|---|---|
| | | Mean | STD | CV | Mean | STD | CV |
| 139.5 | 104.7 | 373.4 | 11.2 | 3.0 | 439.1 | 17.1 | 3.9 |
| 21.0 | 20.7 | 149.4 | 17.7 | 11.9 | 200.7 | 13.6 | 6.8 |
| 21.0 | 35.0 | 158.2 | 19.1 | 12.1 | 201.6 | 8.9 | 4.4 |
| 20.9 | 51.9 | 166.2 | 20.8 | 12.5 | 206.7 | 6.4 | 3.1 |
| 21.0 | 69.2 | 171.4 | 21.4 | 12.5 | 210.4 | 5.5 | 2.6 |
| 34.6 | 35.1 | 208.4 | 25.2 | 12.1 | 267.1 | 10.8 | 4.1 |
| 34.8 | 69.6 | 213.8 | 24.2 | 11.3 | 263.0 | 8.1 | 3.1 |
| 34.8 | 104.3 | 212.3 | 21.8 | 10.3 | 253.4 | 6.9 | 2.7 |
| 34.8 | 138.0 | 212.2 | 19.9 | 9.4 | 247.3 | 9.1 | 3.7 |
| 69.8 | 35.1 | 289.2 | 22.7 | 7.9 | 380.0 | 41.9 | 11.0 |
| 69.8 | 69.6 | 296.0 | 20.1 | 6.8 | 361.7 | 21.3 | 5.9 |
| 69.7 | 138.8 | 301.9 | 17.5 | 5.8 | 348.9 | 12.8 | 3.7 |
| 69.8 | 207.8 | 295.3 | 13.3 | 4.5 | 331.6 | 9.4 | 2.8 |
| 104.7 | 69.6 | 343.8 | 13.5 | 3.9 | 416.0 | 25.1 | 6.0 |
| 104.7 | 104.6 | 351.8 | 13.0 | 3.7 | 412.0 | 19.0 | 4.6 |
| 104.7 | 138.7 | 357.5 | 11.9 | 3.3 | 411.1 | 16.1 | 3.9 |
| 104.7 | 207.7 | 361.1 | 10.6 | 2.9 | 404.8 | 11.5 | 2.8 |
| 139.3 | 69.5 | 390.3 | 10.8 | 2.8 | 470.6 | 34.2 | 7.3 |
| 139.2 | 104.4 | 399.8 | 9.7 | 2.4 | 466.6 | 24.7 | 5.3 |
| 139.4 | 138.7 | 407.4 | 10.2 | 2.5 | 467.0 | 19.6 | 4.2 |
| 139.4 | 276.9 | 413.5 | 10.8 | 2.6 | 456.5 | 12.9 | 2.8 |

Note:

$\sigma_3$ = Confining Pressure
$\sigma_d$ = Deviatoric Stress
STD = Standard Deviation in MPa
CV = Coefficient of Variation in percent

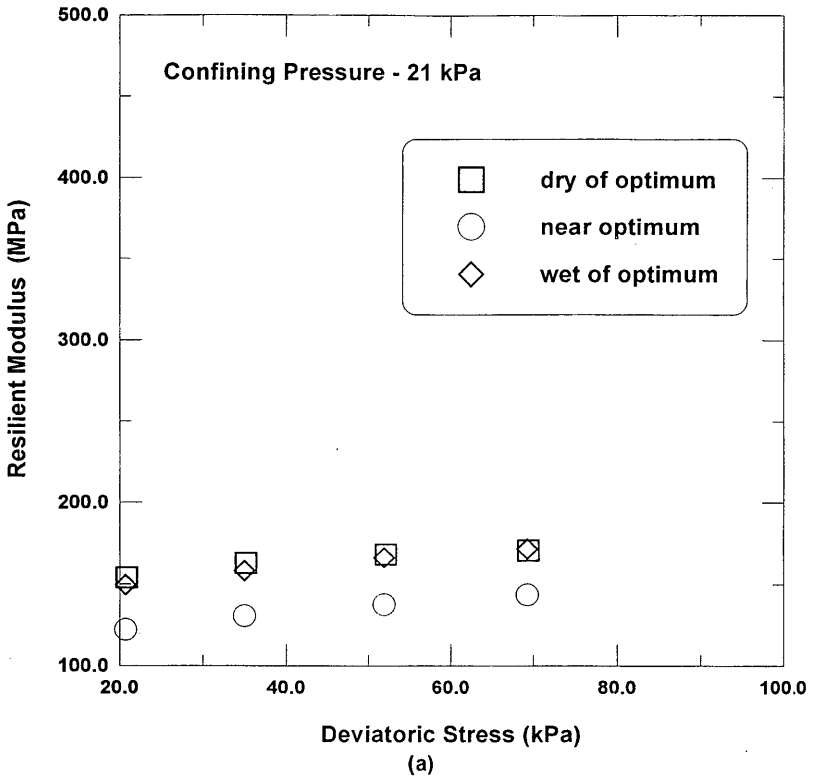


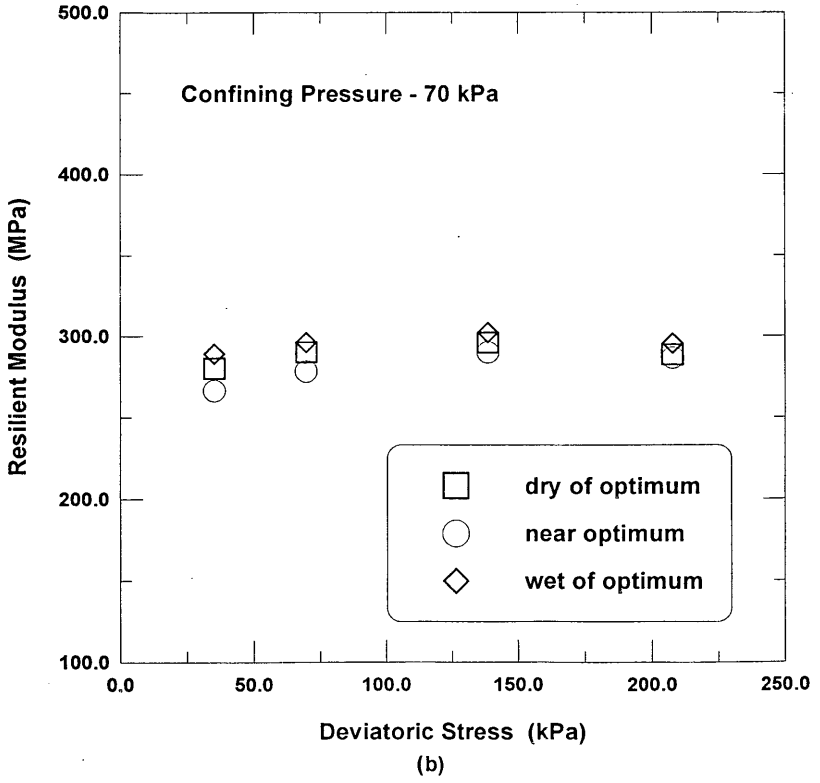


**FIGURE 2** Influence of confining stress on resilient modulus of sands at various moisture contents.

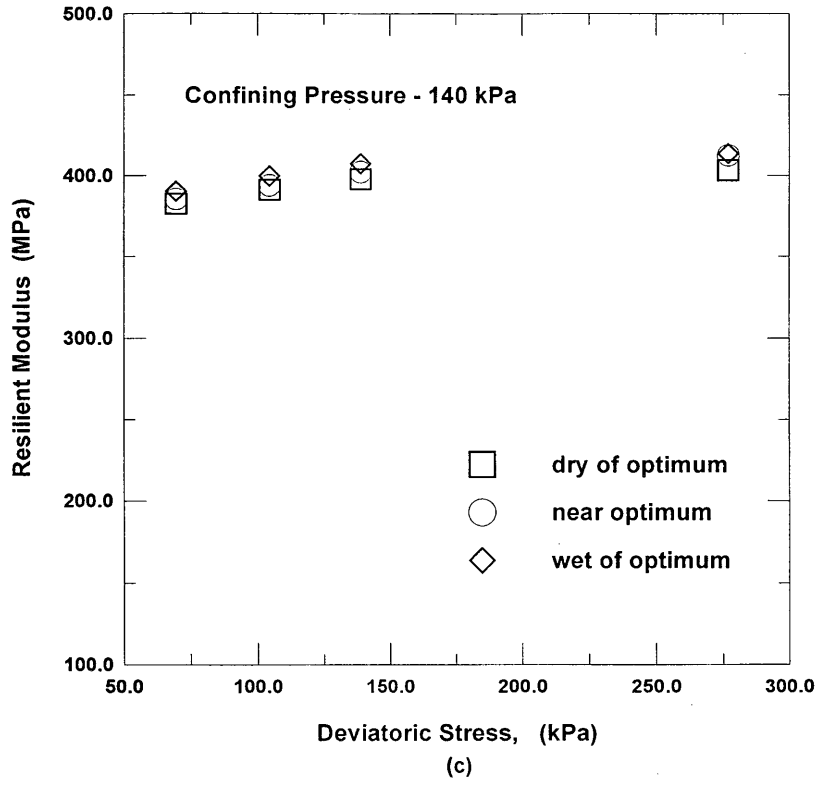


FIGURE 2 (*continued*)

The decrease in $M_r$ at wet of optimum is attributed to the strength decrease at a higher saturation level as a result of smaller cohesion and friction angles and higher pore pressure developments.

An increase in the deviatoric stress resulted in a reduction of moduli values. This observation is consistent with those reported in other studies (*2–4*). This phenomenon is attributed to factors such as positive pore pressure development and fabric changes due to stress cycles. The pore pressures which increase with deviatoric load magnitudes, cycles and saturation levels of the specimens result in the reduction of overall strength. The lower strength specimens provide lower moduli values.

The fabric describes the arrangement of particles, particle groups, and pore spaces in a soil and its influence on mechanical properties of cohesive soils are well documented (*11*). It is assumed that the

TABLE 3 Silty Clay Test Results

(a) Dry of Optimum

| $\sigma_3$ (kPa) | $\sigma_d$ (kPa) | Mr, ends (MPa) | | | Mr, middle (MPa) | | |
|---|---|---|---|---|---|---|---|
| | | Mean | STD | CV | Mean | STD | CV |
| 42.1 | 28.3 | 302.9 | 64.7 | 21.4 | 380.9 | 135.8 | 35.7 |
| 42.2 | 14.0 | 315.2 | 63.5 | 20.2 | 436.9 | 157.2 | 36.0 |
| 42.1 | 28.3 | 303.8 | 63.7 | 21.0 | 379.1 | 130.6 | 34.4 |
| 42.2 | 41.7 | 286.4 | 68.5 | 23.9 | 340.6 | 122.3 | 35.9 |
| 42.2 | 55.7 | 272.1 | 72.4 | 26.6 | 308.7 | 117.3 | 38.0 |
| 42.2 | 69.7 | 258.6 | 74.8 | 28.9 | 284.9 | 114.3 | 40.1 |
| 21.2 | 14.0 | 276.5 | 47.6 | 17.2 | 406.4 | 141.4 | 34.8 |
| 21.4 | 28.3 | 265.4 | 54.7 | 20.6 | 347.3 | 124.2 | 35.8 |
| 21.4 | 41.8 | 254.2 | 60.0 | 23.6 | 316.5 | 115.7 | 36.6 |
| 21.4 | 55.9 | 244.1 | 63.5 | 26.0 | 294.2 | 114.0 | 38.7 |
| 21.4 | 69.9 | 236.3 | 67.1 | 28.4 | 276.0 | 111.8 | 40.5 |
| 0.0 | 13.9 | 211.1 | 28.2 | 13.4 | 383.9 | 139.4 | 36.3 |
| 0.0 | 28.2 | 199.9 | 33.4 | 16.7 | 326.7 | 118.8 | 36.4 |
| 0.0 | 41.7 | 193.3 | 39.2 | 20.3 | 296.5 | 112.6 | 38.0 |
| 0.0 | 55.7 | 190.2 | 45.4 | 23.9 | 276.2 | 110.4 | 40.0 |
| 0.0 | 69.7 | 190.1 | 50.0 | 26.3 | 259.9 | 108.9 | 41.9 |

(*continued on next page*)

TABLE 3 (*continued*)

(b) Optimum

| $\sigma_3$ (kPa) | $\sigma_d$ (kPa) | Mr, ends (MPa) | | | Mr, middle (MPa) | | |
|---|---|---|---|---|---|---|---|
| | | Mean | STD | CV | Mean | STD | CV |
| 42.1 | 27.4 | 224.5 | 25.8 | 11.5 | 261.0 | 48.9 | 18.8 |
| 42.1 | 13.5 | 240.0 | 22.8 | 9.5 | 288.5 | 65.7 | 22.8 |
| 42.1 | 27.6 | 226.8 | 24.9 | 11.0 | 261.3 | 49.1 | 18.8 |
| 42.1 | 40.7 | 203.5 | 26.4 | 13.0 | 232.9 | 43.5 | 18.7 |
| 42.2 | 54.3 | 185.6 | 26.4 | 14.3 | 208.1 | 40.0 | 19.2 |
| 42.2 | 67.8 | 171.1 | 27.0 | 15.8 | 187.6 | 39.3 | 20.9 |
| 21.5 | 13.5 | 218.3 | 19.4 | 8.9 | 271.4 | 56.0 | 20.6 |
| 21.4 | 27.4 | 199.9 | 22.2 | 11.1 | 238.8 | 44.2 | 18.5 |
| 21.3 | 40.6 | 182.5 | 23.4 | 12.8 | 215.9 | 41.5 | 19.2 |
| 21.4 | 54.3 | 167.2 | 24.3 | 14.5 | 196.2 | 39.8 | 20.3 |
| 21.4 | 67.8 | 155.6 | 25.4 | 16.3 | 180.0 | 40.0 | 22.2 |
| 0.0 | 13.3 | 178.1 | 15.9 | 8.9 | 254.7 | 52.3 | 20.5 |
| 0.0 | 27.1 | 159.9 | 18.1 | 11.3 | 222.4 | 44.0 | 19.8 |
| 0.0 | 40.1 | 145.1 | 19.9 | 13.7 | 200.5 | 42.2 | 21.0 |
| 0.0 | 53.8 | 134.6 | 21.1 | 15.7 | 182.6 | 42.0 | 23.0 |
| 0.0 | 67.3 | 127.9 | 22.3 | 17.4 | 167.1 | 41.6 | 24.9 |

(c) Wet of Optimum

| $\sigma_3$ (kPa) | $\sigma_d$ (kPa) | Mr, ends (MPa) | | | Mr, middle (MPa) | | |
|---|---|---|---|---|---|---|---|
| | | Mean | STD | CV | Mean | STD | CV |
| 42.3 | 28.1 | 164.5 | 15.2 | 9.3 | 187.1 | 21.4 | 11.4 |
| 42.3 | 14.0 | 187.3 | 12.7 | 6.8 | 221.3 | 22.4 | 10.1 |
| 42.3 | 28.1 | 166.8 | 14.2 | 8.5 | 189.0 | 20.5 | 10.8 |
| 42.3 | 41.3 | 138.3 | 17.6 | 12.7 | 154.3 | 22.4 | 14.5 |
| 42.3 | 54.7 | 116.3 | 19.0 | 16.3 | 125.8 | 23.0 | 18.3 |
| 42.3 | 68.2 | 100.1 | 18.8 | 18.8 | 104.1 | 21.8 | 20.9 |
| 21.3 | 13.9 | 174.4 | 13.1 | 7.5 | 202.4 | 25.2 | 12.5 |
| 21.2 | 28.1 | 148.6 | 16.3 | 11.0 | 164.2 | 22.7 | 13.8 |
| 21.2 | 41.4 | 123.9 | 18.6 | 15.0 | 134.4 | 23.9 | 17.8 |
| 21.2 | 55.0 | 103.7 | 19.3 | 18.6 | 110.7 | 23.7 | 21.4 |
| 21.2 | 68.3 | 89.4 | 18.2 | 20.4 | 93.7 | 22.0 | 23.5 |
| 0.0 | 13.8 | 144.4 | 11.1 | 7.7 | 180.5 | 24.9 | 13.8 |
| 0.0 | 28.0 | 118.7 | 13.4 | 11.3 | 142.9 | 23.9 | 16.7 |
| 0.0 | 41.1 | 98.0 | 15.4 | 15.8 | 115.3 | 24.6 | 21.3 |
| 0.0 | 54.5 | 83.3 | 15.8 | 19.0 | 95.0 | 23.1 | 24.3 |
| 0.0 | 68.0 | 73.3 | 15.2 | 20.8 | 80.4 | 20.6 | 25.7 |

Note:
$\sigma_3$ = Confining Pressure
$\sigma_d$ = Deviatoric Stress
STD = Standard Deviation in MPa
CV = Coefficient of Variation in percent

fabric at the end of conditioning is far more dispersed (a state at which no face-to-face association in particles exist) than at the beginning of conditioning. The tests which start at the end of conditioning are therefore conducted on specimens with dispersed fabric. The fabric becomes further dispersed with the deviatoric load and the number of cycles. The increasing dispersion results in the decline of resilient properties since this type of orientation generally exhibits lower shear strength components, cohesion and friction angle of soils. Experimental verification of this assumption is beyond the scope of this investigation, but still needs to be assessed.

## Measurement Coefficients

Resilient deformations are considerably small and should be measured as accurately as possible by reducing sources of errors in the test. The influence of the location of the LVDT systems in providing accurate measurements was evaluated by using two types of internal measurement systems placed at different locations on the specimen.

The influence of the measurement system is presented in the form of measurement coefficients (*MC*) (*9,10*). The measurement coeffi-

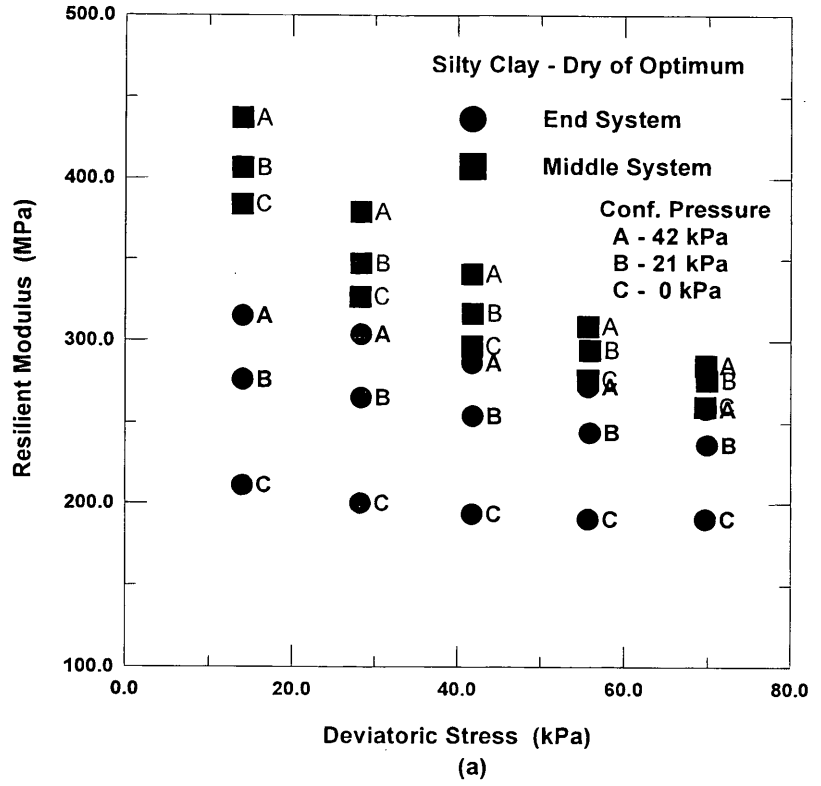


(a)

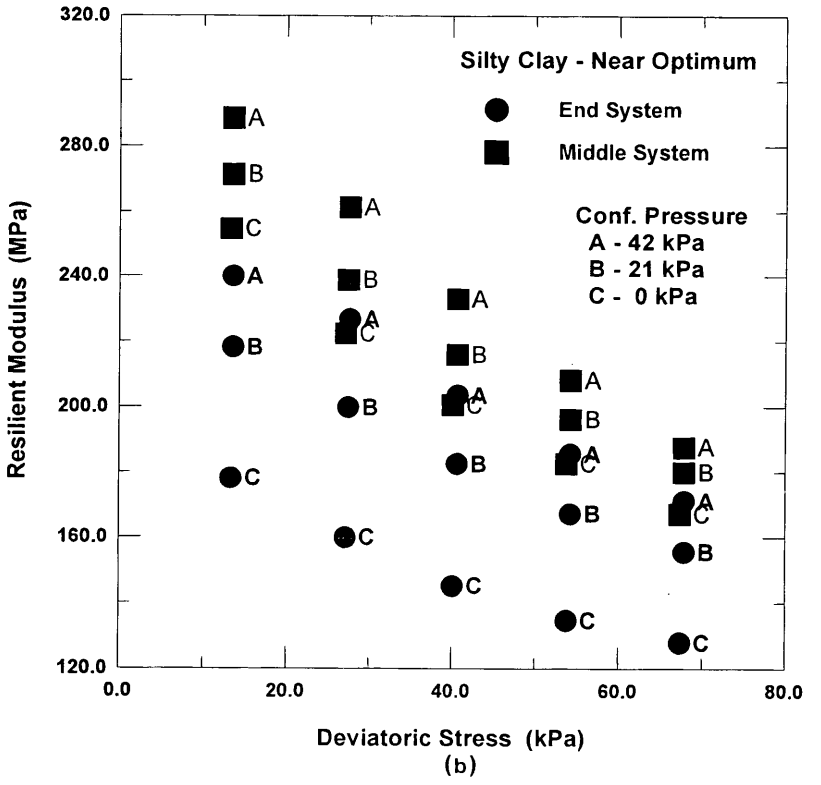


(b)

**FIGURE 3** Influence of moisture content on resilient modulus test results of silty clay.

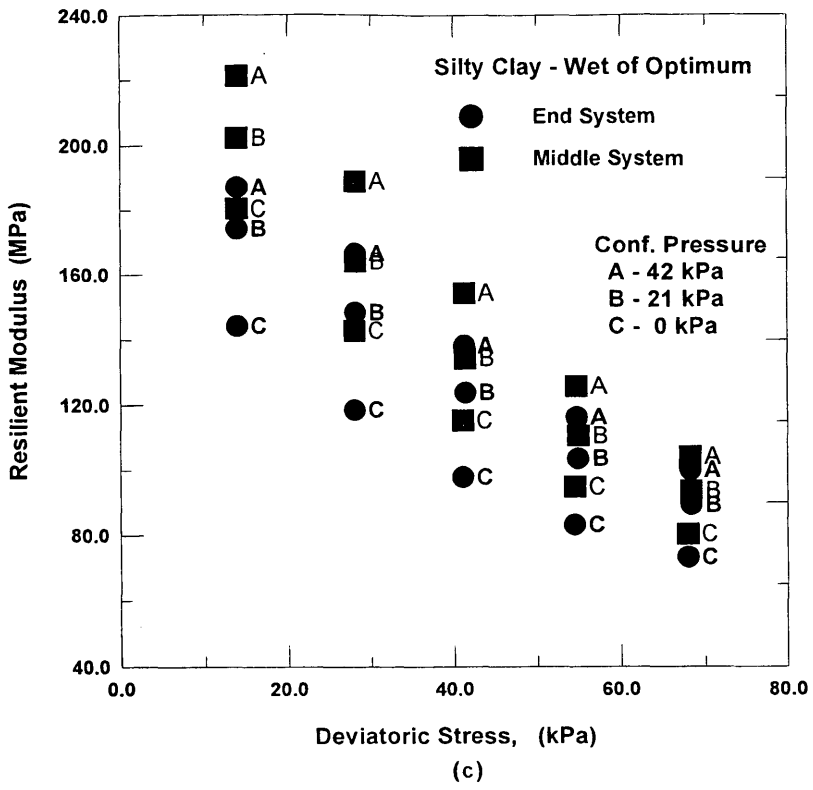


**FIGURE 3** *(continued)*

cient is defined as the ratio of the resilient modulus determined by the middle system to that determined by the end system. The coefficient values are determined for various confining and deviatoric stresses. The coefficients can be used to convert the end measurement results to more realistic middle measurement system results. The middle system is assumed as a more appropriate and realistic method since its measurements are not influenced by end friction effects and system compliance errors. Measurement coefficients are calculated for the tests conducted in this study and are presented in Figures 4 (sand) and 5 (silty clay).

Figure 4 shows the relationships between $M_r$ values from the middle measurement system and the end measurement system. The three moisture content levels and their results are plotted in the same figure. The slopes of these lines represent the measurement coefficients. The influence of the stresses on measurement coefficients was not considered in this case since the stresses did not alter the *MC* values considerably. The *MC* values are presumed to depend on the relative stiffness variation between samples and the Plexiglas clamps used for holding middle measurement LVDT clamp system. In other words, a softer sample allows the clamps to slip which induces significant errors into the measurements, while a stiff sample may not permit free movement of the LVDTs of middle system. Therefore, variations in soil stiffness during testing may affect the performance of middle measurement system and thus the measurement coefficients.

The measurement coefficients of sands obtained from Figure 4 are 1.15 (at dry of optimum), 1.22 (at optimum), and 1.18 (at wet of optimum). The differences in *MC* values obtained at various moisture contents are small. This indicates that the moisture content of the sand does not significantly affect the measurement system capabilities. This is attributed to the permeable nature of sands which immediately dissipates the developed pore pressures during testing, thereby keeping the stiffness properties intact during testing.

Figure 5 compares the measurement coefficients of clays at different deviatoric stresses for various confining pressures (0 to 42 kPa or 0 to 6 lb/in.$^2$). The influence of confining pressure appears to be more evident and, therefore, the stresses were included in the analysis to provide expressions for *MC* values. Higher *MC* values were obtained for an unconfined state and low deviatoric stress. The values decreased with an increase in the confining stress. This indicates that higher confining pressures provide better contact between LVDTs and the specimens which allows more precise and accurate measurements.

Linear regression analysis on the clay results provided the following measurement coefficient equations as a function of confining ($e_3$) and deviatoric stresses ($e_d$).

$$MC = (0.00335 * \sigma_3 - 0.051)\,\sigma_d + (1.83 - 0.0702 * \sigma_3) \quad (dry) \quad (1)$$

$$MC = (0.00032 * \sigma_3 - 0.013)\,\sigma_d + (1.43 - 0.0402 * \sigma_3) \quad (opt) \quad (2)$$

$$MC = (0.000298 * \sigma_3 - 0.017)\,\sigma_d + (1.26 - 0.0124 * \sigma_3) \quad (wet) \quad (3)$$

Increasing in moisture content levels decreased the *MC* values in the clay test results as opposed to the similar values obtained in the sand tests. Higher variation of *MC* values was obtained in the dry state than at the wet of optimum (Figure 5). This is attributed to pore

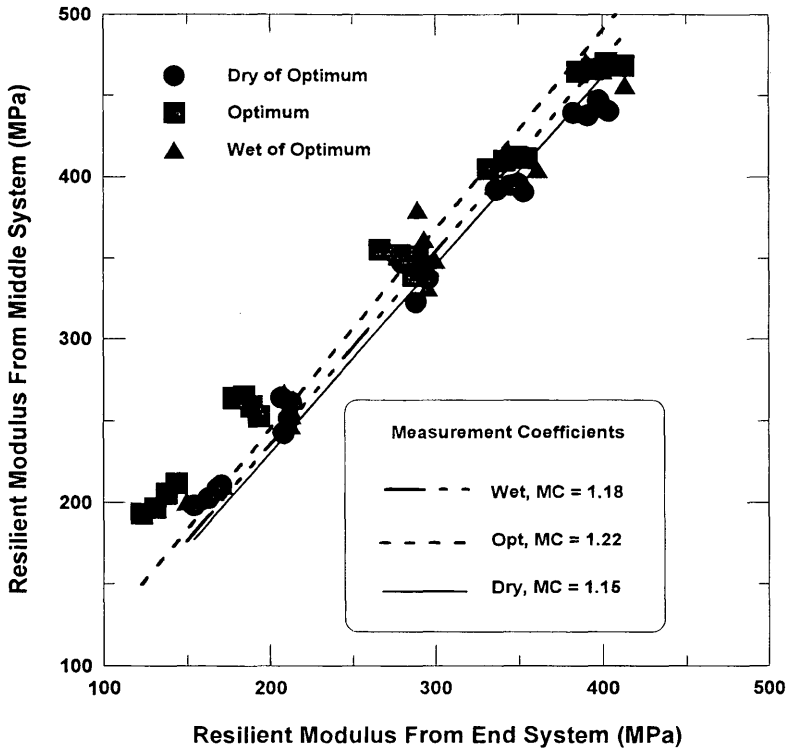


**FIGURE 4 Measurement coefficients for sands.**

pressure developments and fabric changes in the clay specimen. Although the tests were conducted in drained conditions, semi-drained conditions prevailed during testing due to low hydraulic conductivity of clays. This resulted in the development of pore pressures in the specimen. The wet of optimum state of a soil, which has a higher degree of saturation than at dry and optimum states, produces higher and more uniform pore pressures in the specimen. The uniform distribution of pore pressures may have resulted in uniform measurements at wet of optimum and smaller measurement coefficients.

Also, the fabric at the wet of optimum state is more dispersed structure, whereas the fabric at the dry of optimum state is more of flocculated (*11*). The flocculated structure can undergo greater particle dispersions or orientations than the dispersed structure during repeated loading. Therefore fabric changes in the specimen during testing are more significant at the dry of optimum than at the wet of optimum. Changes in particle orientations at dry level results in variations in measurements and the corresponding higher coefficients.

## Plastic Deformation Development

Figure 6 presents the plastic deformations of sands measured by the end system during the conditioning and the testing phases. All three moisture content levels are reported in this figure. The plastic deformations reported in the figure represent the accumulated deformations of one thousand cycles during conditioning and four hundred cycles for each confining stress during testing phase. The testing phase four hundred cycles were obtained by summing the deformations from individual sets of cycles (one hundred each) for four sets of deviatoric loads.

These results provided significant understanding of the conditioning role in this kind of testing since one of the objectives of conditioning, as reported by the AASHTO T-292 procedure, is to reduce plastic deformation developments in the specimens. The deviatoric stress influence is apparent since higher deviatoric loads usually resulted in larger plastic deformations. The influence of confining pressure on plastic deformations is more intricate and requires further scrutiny and attention.

For sands, lower plastic deformations were obtained at all testing confining stresses, 21, 70, 105, and 140 kPa with the exception of 35 kPa. This indicates that conditioning not only reduced the plastic deformations in the first test confining pressure (which is 21 kPa), but also in the case of three upper confining stresses, 70, 105, and 140 kPa which are somewhat closer to the conditioning confining stress of 140 kPa. This is a significant finding since no specific guidelines are available in the literature for determining the magnitudes of conditioning confining stresses for granular field core samples based on the plastic deformation criterion. The conditioning confining stress for cores should be greater than the lateral confining pressure of the depth at which the soil samples are retrieved. In cases when the soil sample represents a significant depth of subgrade (either a sample from a deeper depth or samples retrieved from a range of depths), the lateral pressure of the bottom layer of the subgrade or the deepest depth should be used as the confining pressure for conditioning.

Higher plastic deformations were observed at confining stress of 35 kPa, possibly due to significant fluctuations in the confining pressures in the preceding two stages, 140 kPa (conditioning) and 21 kPa (first level of testing).

Figure 6 also presents the plastic deformations developed during testing of the clay specimens. Results from three moisture

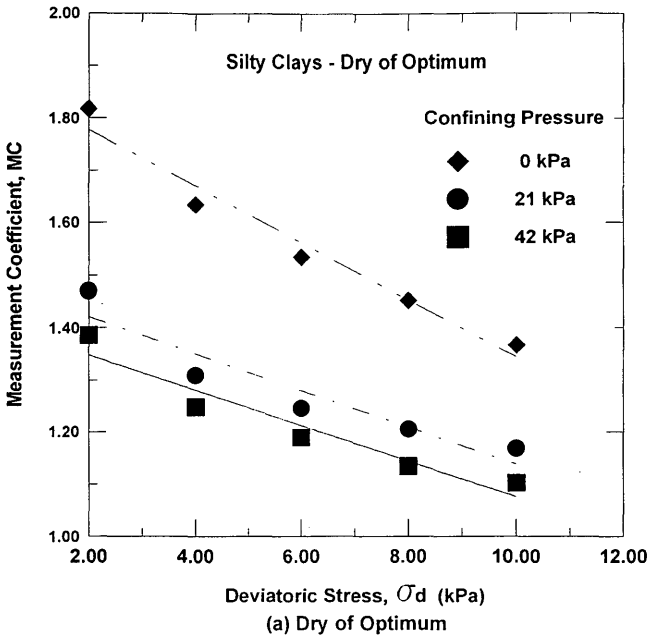


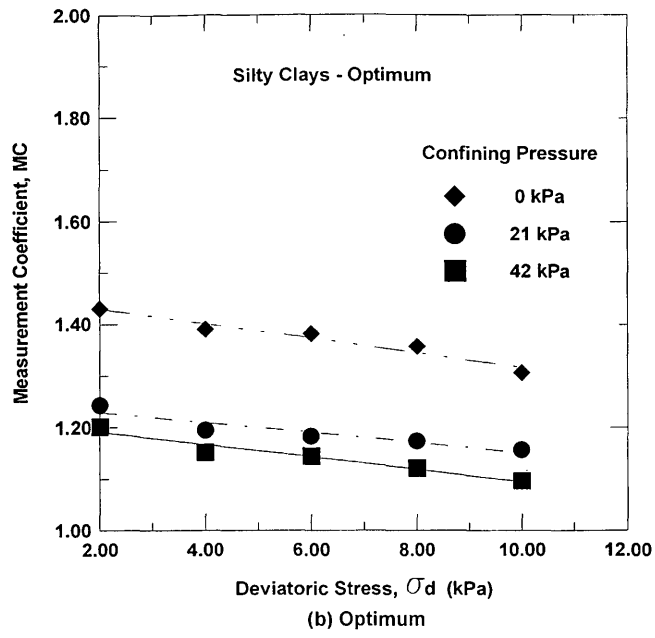


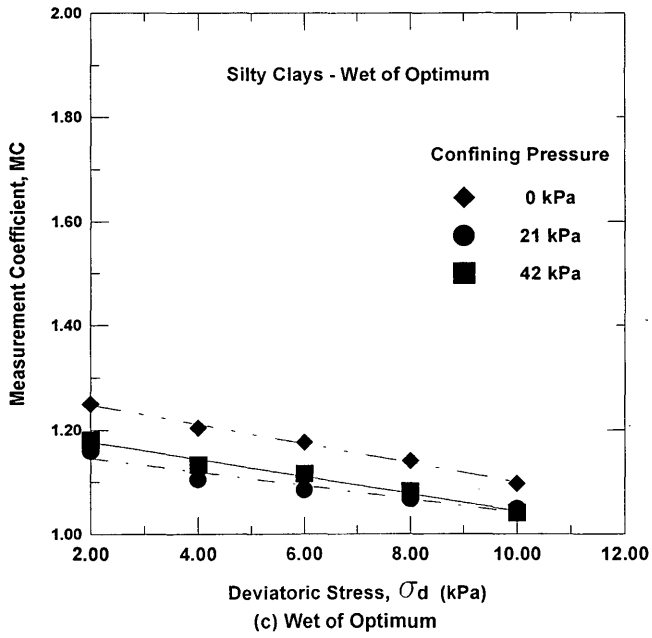


**FIGURE 5 Measurement coefficients for silty clay.**

contents and densities are depicted in this figure. The clay samples were conditioned at 42 kPa and the first test was conducted at the same confining pressure. This is followed by the testing at other confining pressures of 21 and 0 kPa. The figure suggests that the accumulated plastic deformations were larger at a confining pressure of 42 kPa (6 lb/in.$^2$) and then decreased with decreasing confining stresses. Even though conditioning did not result in the reduction of plastic deformations at first testing confining pressure (42 kPa), it significantly decreased the plastic deformations at other confining pressures (21 and 0 kPa). The purpose of conditioning in clays is probably achieved at confining stresses lower than the conditioning confining stress. Reason for this is attributed to the stiffening or over-consolidation of the specimen at a conditioning confining pressure of 42 kPa. The stiffened specimen, therefore, appears to induce smaller strains at lower confining pressures. This implies that the field cohesive core samples require a conditioning confining stress that is significantly higher than the lateral confining pressure corresponding to the retrieval depth location.

Smaller plastic deformations were measured by the middle system than the end system, possibly due to the differences in the lengths of the specimens that these systems were accounted for.

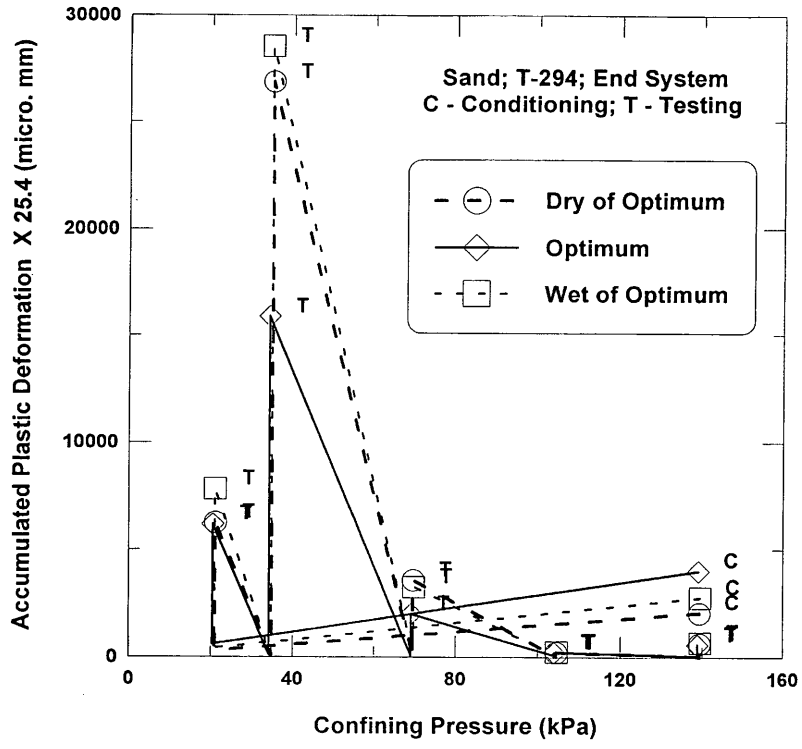


(a) Blasting Sand

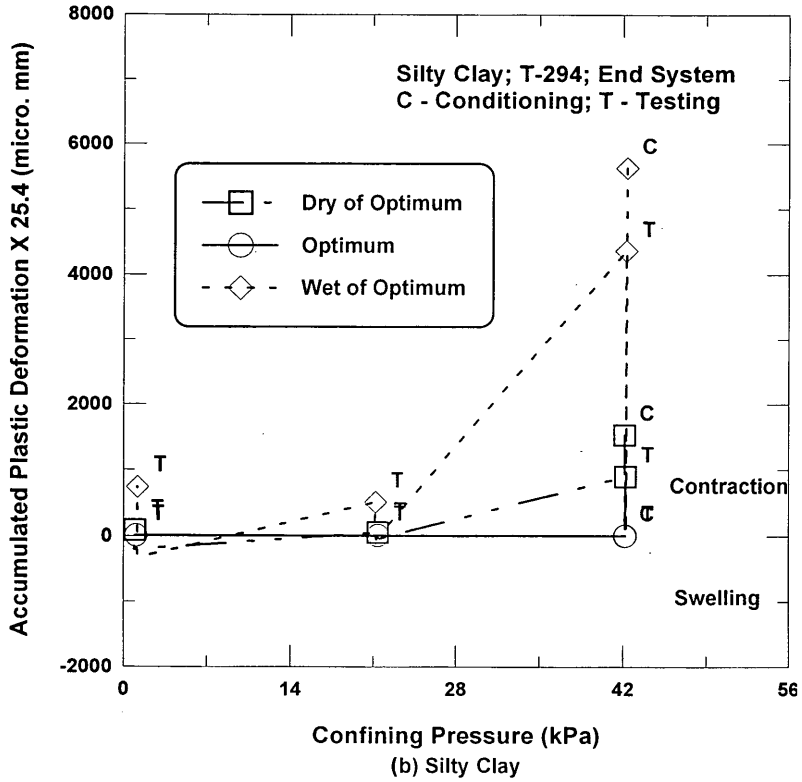


(b) Silty Clay

**FIGURE 6** Accumulated plastic deformations versus confining stresses for sands.

### Regression Model Analysis

Regression models are generally used in the form of equations for predicting the moduli values. Theta (θ) or bulk stress and deviatoric stress are used in the models as predictors based on whether the soil is cohesionless or cohesive. These models are recommended in AASHTO procedures:

$$Mr = k_1 * \theta^{k2} \quad \text{for grandular soils} \tag{4}$$

$$Mr = k_3 * \sigma^{k4} \quad \text{for cohesive soils} \tag{5}$$

where $k_1$ and $k_2$ (granular soils) and $k_3$ and $k_4$ (cohesive soils) are regression coefficients.

The regression coefficients are determined from the test results for both soils and are reported in Table 4a and b (sands and silty clays). Typical model results for sands and clays at wet of optimum are depicted in Figure 7. It is interesting to note that $k_2$ and $k_4$, which represent the slopes of the lines in the respective models, appear to be dependent on the type of soil and the moisture content level. The constants $k_1$ and $k_3$, which represent the intercepts in the figures, depend on the measurement systems, the moisture contents and density levels. As expected, higher $k_1$ and $k_3$ values are obtained for the middle system because of higher resilient moduli measurements. Although these constants varied with moisture content, no particular trend is observed in both soils.

## SUMMARY AND CONCLUSIONS

The resilient modulus test results provided the following conclusions:

1. Sands exhibited higher resilient moduli at dry and wet of optimum than at optimum moisture content. Higher $M_r$ values at dry of optimum over optimum is attributed to the higher strengths. The same at wet of optimum, on the other hand, did not follow a consistent trend possibly due to leakage problems associated during the wet of optimum tests. Overall, the statistical variation between the results at all three moisture content levels is insignificant, probably due to very small range of relative compactions used and lesser influence of moisture contents in sands.

2. The moduli values of clays decrease with an increase in moisture content. This is attributed to the increase in positive pore pressure development with an increase in moisture content or degree of saturation. Higher pore pressures decrease the effective stresses and the shear strength of the clay specimens, thereby resulting in smaller resilient moduli.

3. The measurement coefficients of the sand tested are 1.15 (dry of optimum), 1.22 (optimum), and 1.18 (wet of optimum). The small variations in these coefficients indicate that moisture contents in sands did not influence the measurement systems.

4. The measurement coefficients of clays for each moisture content level are expressed as a function of confining and deviatoric stresses. Higher values are produced for the dry of optimum moisture content level. Lesser fabric changes and uniform pore pressure developments at wet of optimum may have resulted in smaller variations between the end and middle measurements.

5. Conditioning resulted in smaller plastic deformations at most of the confining stress levels for sands and at confining stresses lower than the conditioning confining stress for clays.

6. The regression model constants appear to depend on the moisture content, density levels, and the measurement system. Though the model constants varied with respect to moisture contents, no particular or significant trends between them are noticed.

## ACKNOWLEDGMENTS

This work was supported by the Louisiana Transportation Research Center in cooperation with the Louisiana Department of Transportation and Development (LADOTD) state project no. 92-2GT. The authors express their appreciation for this support.

**TABLE 4 Regression Constants for Sand and Silty Clay**

(a) Sand

| Moisture Content (%) | Dry Density (pcf) | End System | | | Middle System | | |
|---|---|---|---|---|---|---|---|
| | | $\log(k_1)$ | $k_2$ | $R^2$ | $\log(k_1)$ | $k_2$ | $R^2$ |
| 9.67 | 105.50 | 4.44 | 0.43 | 0.90 | 4.20 | 0.50 | 0.94 |
| 11.92 | 107.65 | 4.38 | 0.48 | 0.92 | 4.91 | 0.63 | 0.96 |
| 13.50 | 106.65 | 4.39 | 0.46 | 0.88 | 4.15 | 0.52 | 0.95 |

(b) Silty Clay

| Moisture Content (%) | Dry Density (pcf) | End System | | | Middle System | | |
|---|---|---|---|---|---|---|---|
| | | $\log(k_3)$ | $k_4$ | $R^2$ | $\log(k_3)$ | $k_4$ | $R^2$ |
| 18.0 | 96.5 | 5.83 | -0.09 | 0.88 | 6.67 | -0.24 | 0.78 |
| 20.6 | 101.6 | 5.90 | -0.21 | 0.84 | 6.29 | -0.25 | 0.50 |
| 23.0 | 96.5 | 6.25 | -0.41 | 0.82 | 6.63 | -0.48 | 0.76 |

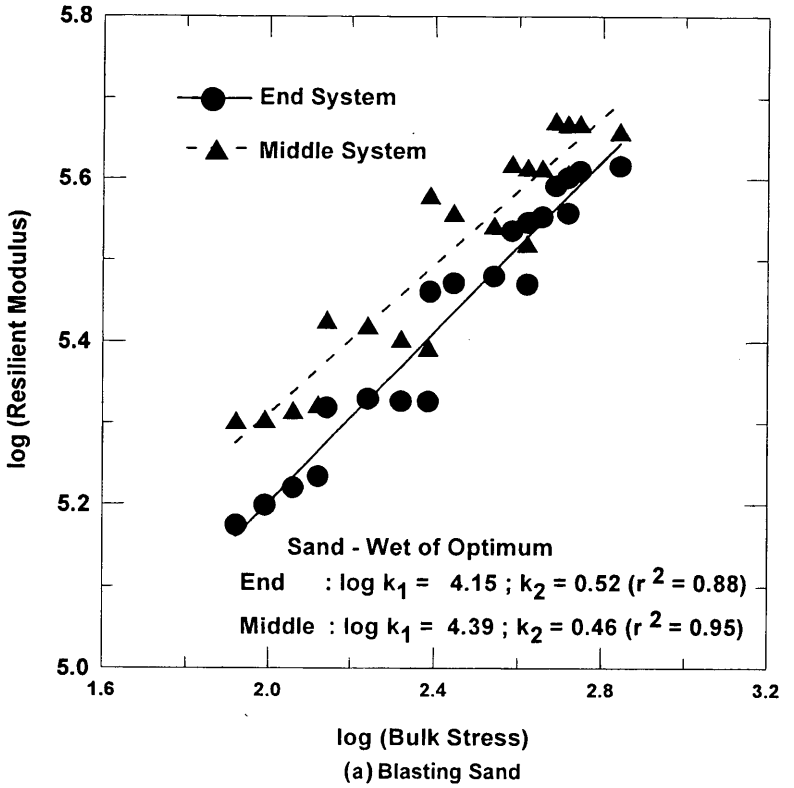


(a) Blasting Sand

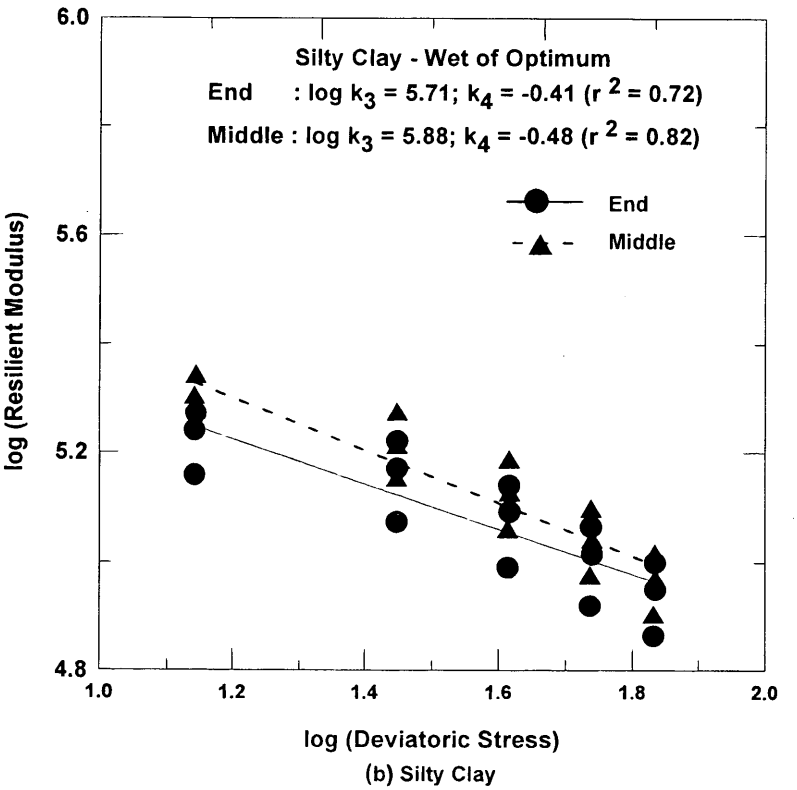


(b) Silty Clay

FIGURE 7 Typical regression model results.

## REFERENCES


1. *Guide for Design of Pavement Structures*. American Association of State Highway and Transportation Officials, 1986.
2. Barksdale, R. D., et al. *Laboratory Determination of Resilient Modulus For Flexible Pavement Design*. NCHRP Report 1-28, Georgia Institute of Technology, December 1990.
3. Thompson, M. R. Factors Affecting the Resilient Moduli of Soils and Granular Materials. *Proc., Workshop on Resilient Modulus Testing State-of-the-Practices*, Oregon State University, Corvallis, Ore., March 1989.
4. Thompson, M. R., and Q. L. Robnett. Resilient Properties of Subgrade Soils. *Transportation Engineering Journal*, pp. 71–89, January 1979.
5. Elliot, R. P., S. I. Thornton, K. Y. Foo, K. W. Siew, and R. Woodbridge. *Resilient Properties of Arkansas Subgrades*. Report No. FHWA/AR-89/004, Arkansas Highway and Transportation Research Center, University of Arkansas, Fayetteville, November 1988.
6. Pezo, R. F., G. Claros, W. R. Hudson, and K. H. Stokoe II. *Development of a Reliable Resilient Modulus Test for Subgrade and Non-Granular Subbase Materials for Use in Routine Pavement Design*. Research Report 1177-4f, Center for Transportation Research, University of Texas, Austin, Tex., January 1992.
7. *Interim Specifications for Transportation Materials and Methods of Sampling and Testing, Part II Interim Test Methods*. American Association of State Highway and Transportation Officials, 1992.
8. Mohammad, L. N., A. J. Puppala, and P. Alavilli. Effect of Instrumentation on Resilient Modulus of Sands. In *Dynamic Geotechnical Testing: Second Volume, ASTM STP 1213* (R. J. Ebelhar, V. P. Drnevich, and B. L. Kutter, eds.), American Society for Testing and Materials, Philadelphia, 1994.
9. Mohammad, L. N., P. Alavilli, and A. J. Puppala. Data Acquisition System for Determining the Resilient Modulus of Soils. *Advances in Site Characterization: Data Acquisition, Management and Interpretation*, ASCE Convention, Dallas, Tex., 1993.
10. Mohammad, L. N., P. Alavilli, and A. J. Puppala, *Influence of Testing Procedure and LVDT's Location on the Resilient Modulus of Soils*. TRB, National Research Council, Washington, D.C., 1994 (in press).
11. Mitchell, J. K. *Fundamentals of Soil Behavior*. John Wiley & Sons, Inc., New York, 1993.


*Publication of this report sponsored by Committee on Soil and Rock Properties.*

# Estimating Permeability of Asphalt-Treated Bases

JAY K. LINDLY AND ASHRAF S. ELSAYED

This report describes laboratory testing and statistical analysis of the resulting data to determine the effects of aggregate gradation and percent asphalt stabilization on the permeability of asphalt-treated roadway base layers. Three different types of aggregates were tested in the study. They are crushed limestone, crushed granite, and uncrushed river gravel. A top size of 38 mm (1.5 in.) was used for all gradations. Asphalt cement (AC-20 grade) at 2 percent and 3 percent was used to stabilize the aggregates. A total of 60 permeability tests were performed using a 15.2 cm (6-in.) diameter permeameter. A statistical method was used to arrive at a first-order multiple regression equation to predict the coefficient of permeability of asphalt-treated bases in the range of 0.2–0.7 cm/sec (500–2,000 ft/day) using the percentage of air voids in the sample, the percentage of asphalt cement used, and the percent by weight of materials that pass the 2.36-mm (no. 8) sieve.

Highway personnel agree that excess water in pavements is one of the primary reasons for premature roadway failures. Excess water reduces the frictional strength of the structural section and foundation materials by creating buoyancy within these materials (*1*). Excess pore water pressure can be created within subgrade and pavement structural elements by wheel impacts (*2*). These situations can produce excessive deflection, cracking, reduction in load-carrying capacity, raveling and disintegration of asphalt mixes, subgrade instability, pumping, and loss of support (*1,3*).

Water can enter the pavement structure by means of infiltration through the pavement surfaces and shoulders, melting of ice lenses during the freezing/thawing cycle, capillary action, and seasonal changes in the water table (*2,4,5*). It was the common belief that high water table and capillary water are the primary causes of excess water in pavement. However, recent studies indicated that surface (infiltration) water is the main cause of moisture accumulation in the subgrade (*2*).

## DAMAGE MINIMIZATION

Two methods are used to minimize the moisture-induced damage in pavement systems. The first method is to prevent the moisture from entering the pavement system by sealing the joints and using impervious surface layers. As pavements age and cracks multiply, this method becomes more impractical and expensive. The second method involves draining the excess moisture which enters the pavement system as quick as possible. Drainage is accomplished by employing high permeability base (or subbase) layers which are daylighted or which flow into discharge pipes (*4,5*). This method is dependent on the permeability of the base and/or subbase layer. Permeability is measured using Darcy's law. The more permeable the layer is, the quicker it drains the excess moisture.

Civil Engineering Department, University of Alabama, P.O. Box 870205, Tuscaloosa, Ala. 35487–0205.

Dense graded bases as currently specified do not have the required permeability to drain the pavements as quickly as designers wish. So, designers started using open-graded, highly permeable layers to provide the required drainage capabilities. However, a highly permeable layer can result in construction and rutting problems due to its low stability (*6,7*). One solution to that problem is to stabilize the open-graded layer with 2–3 percent asphalt cement to provide the necessary stability for construction and to minimize the future rutting under heavy traffic (*8–10*).

Many highway agencies have set permeability specifications for asphalt-treated permeable layers to be used in the drainage design of highway structures. The drainage design is usually based on a coefficient of permeability in the range of 0.18–0.36 cm/sec (500–1,000 ft/day). However, because of the variability involved in the testing and the construction of the drainage layers, the designers prefer that these layers have a much higher laboratory permeability than the range mentioned above.

Another reason for specifying a laboratory permeability much higher than the design range is that the coefficient of permeability is calculated in the lab in a 100 percent saturation condition, which gives higher coefficients than lower saturation conditions. One hundred percent saturation is rarely reached in the field. So, the drainage layers are usually developed based on a lab permeability of 0.4–2.0 cm/sec (1,000–5,000 ft/day), with the range of 0.8–1.2 cm/sec (2,000–3,000 ft/day) commonly used. Higher values of the coefficient of permeability are desired, but anticipated rutting and construction problems prevent the designers from using higher permeability layers.

To save time, the designer may want to estimate the laboratory coefficient of permeability of the drainage layer under specified gradation, density, and porosity conditions to use for the analysis and the design of a drainage system. (He can later perform laboratory tests on the final gradation and asphalt content he has selected.) There have been a number of charts and nomograph developed for estimating permeability of untreated aggregates. Two of the most well known are a chart by Cedergren (Figure 1) (*11*) and a nomograph by Moulton (Figure 2) (*12*). The only tool for predicting permeability of asphalt-treated bases found in the literature is Table 1 from Lovering and Cedergren (1962) (*11*). No study was found which employed the typical gradations used in today's treated bases or which varied the asphalt content.

## PURPOSE OF THIS RESEARCH

The purpose of this research is to find a method to predict the laboratory coefficient of permeability of asphalt-treated bases for different aggregates, at a range of 2–3 percent asphalt, and at gradations typical of those used in modern construction.

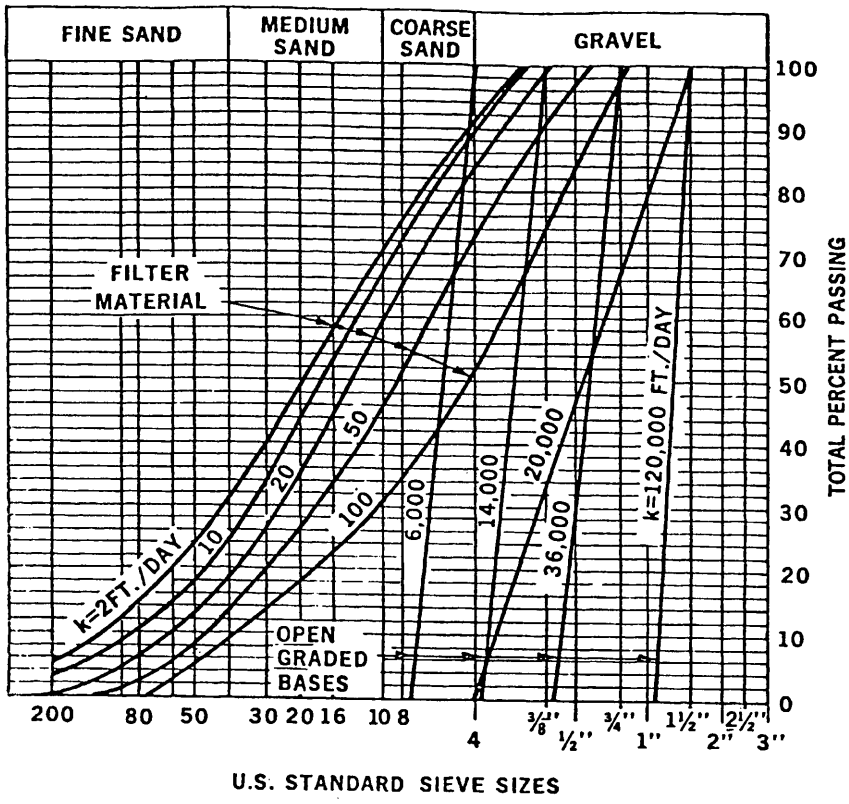


**FIGURE 1** Cedergren chart.

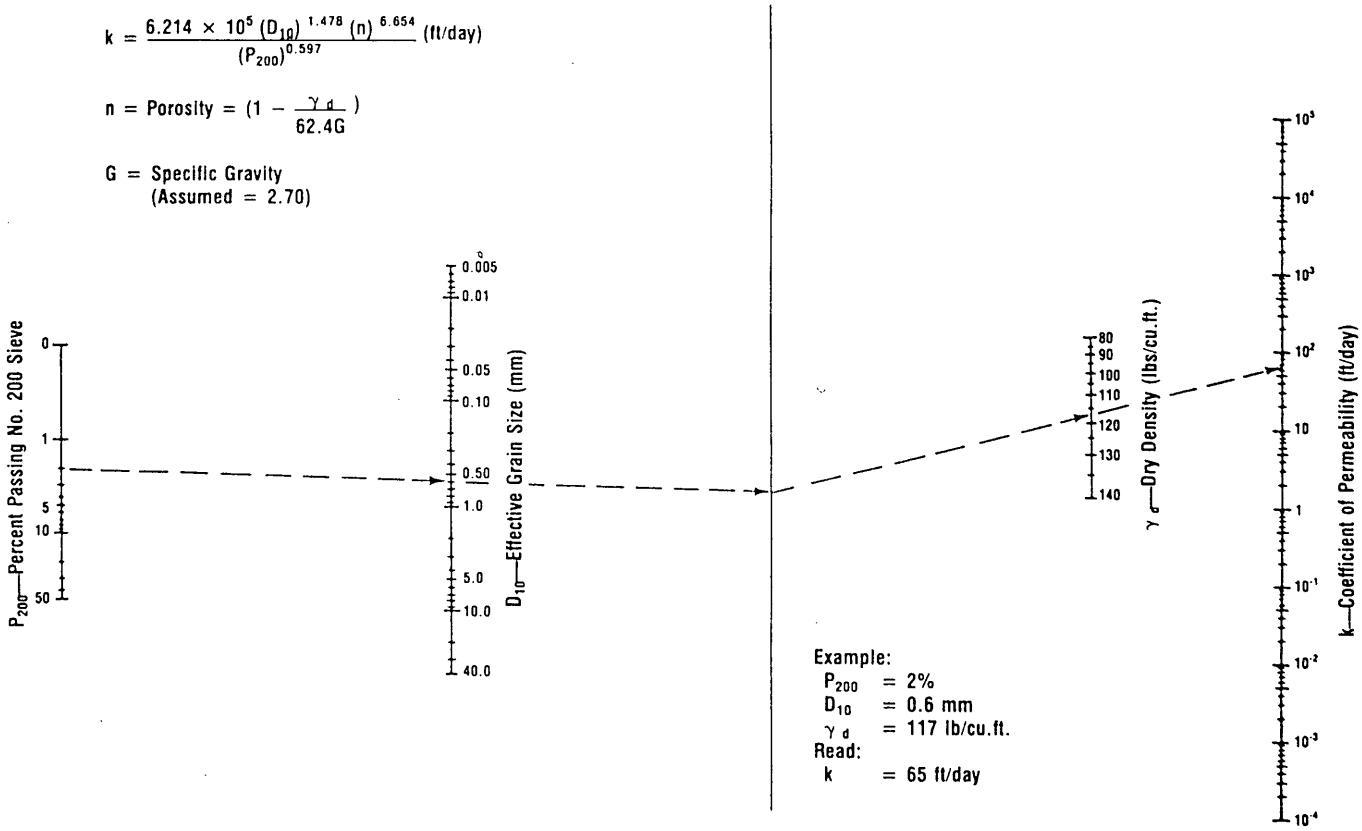


**FIGURE 2** Moulton nomograph.

**TABLE 1 Laboratory Permeability of Untreated and Asphalt-Stabilized Open-Graded Aggregates**

| Average size range | Permeability (ft/day) | |
|---|---|---|
| | Untreated | Bound with 2% asphalt |
| 1.5 to 1 in. | 140,000 | 120,000 |
| 3/4 to 3/8 in. | 38,000 | 35000 |
| No. 4 to No. 8 | 8,000 | 6,000 |

(Lovering and Cedergren, 1962)

## MATERIALS, DESIGN OF EXPERIMENT, AND TEST PROCEDURES

The materials tested, the number and type of tests, and the design of the experiment can be described under the following headings.

### Materials

All aggregates used in the study were provided by Vulcan Materials Company (VMC) in Birmingham, Ala. Three aggregates were tested:

a. Dolcito limestone from VMC quarries near Birmingham, Ala. It has a specific gravity of 2.71 and a top size of 38 mm (1.5 in.).
b. Crushed granite from VMC quarries in Georgia. It has a specific gravity of 2.67 and a top size of 38 mm (1.5 in.).
c. Uncrushed river gravel from VMC quarries in Chattanooga, Tenn. It has a specific gravity of 2.44 and a top size of 25 mm (1.0 in.).

The asphalt cement used in the study was AC-20 grade. It was provided by Hunt Refinery in Tuscaloosa, Ala.

### Permeameter

The permeameter used in the study was built in the machine shop of the University of Alabama College of Engineering. This permeameter was designed to determine the coefficient of permeability under the low hydraulic gradient conditions found in highways and was introduced by Barber and Sawyer (*13*) in 1951. This permeameter has also been successfully used in the Pennsylvania Department of Transportation research facilities (*14*). The permeameter built had a 15.2 cm (6 in.) inside diameter, which is suitable for testing materials up to 38 mm (1.5 in.) top size. Figure 3 shows the permeameter and the associated equations used to determine the coefficient of permeability. The derivation of these equations was explained by E. G. Yemington (*15*) in 1963.

### Gradation Selection

Two gradations were developed to be used in the study. The first gradation was developed to give a coefficient of permeability of 0.18 cm/sec (500 ft/day). This gradation is similar to the gradation developed by the New Jersey DOT (*16*) which has a permeability of 0.36–0.54 cm/sec (1,000–1,500 ft/day). Then, the 0.18 cm/sec (500 ft/day) gradation was modified (mainly by reducing fines) to produce a 0.71 cm/sec (2,000 ft/day) gradation. The two gradations are shown in Table 2.

### Design of Experiment

The design of experiment can be summarized as follows:

a. Asphalt percentages of 2 and 3 percent were used.
b. Three different aggregates were used (as mentioned before).
c. Two different gradations were used (as discussed before).
d. Five repetitions were performed at each asphalt content and gradation. This provides a full factorial experiment, resulting in 60 test specimens.
e. An average of six measurements of the coefficient of permeability were taken for each test specimen.

### Test Procedure

The procedure described in the Asphalt Institute MS-2 (*17*) was followed for combining the aggregates and asphalt cement into test specimens. Because of the lack of fines in the test specimens, the standard hammer was not used for compaction, as it would have crushed the large aggregate pieces as well as pumped the asphalt to the surface of the sample. Instead, a static load of 20,000–22,000 kg (55,000–60,000 lb) was applied using a hydraulic jack to arrive at the required compaction. The load was applied until the sample reached a pre-set height, calculated to give a unit weight in the desired range. This range was 2,040–2,220 kg/m$^3$ (125–140 lb/ft$^3$) for the limestone, 1,950–2,100 kg/m$^3$ (120–130 lb/ft$^3$) for the granite, and 1,700–1,800 kg/m$^3$ (105–115 lb/ft$^3$) for the uncrushed river gravel.

Before conducting the permeability test, the net weight and the average height of each sample were calculated so that the unit weight of the sample could be determined.

## TEST RESULTS

Test results were summarized in 12 tables: one for each combination of aggregate, gradation, and asphalt content. Table 3 is an example of one of these 12 tables. It shows the following data types:

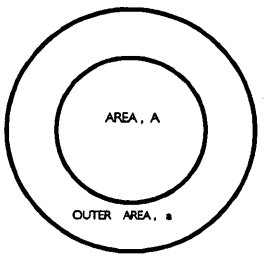


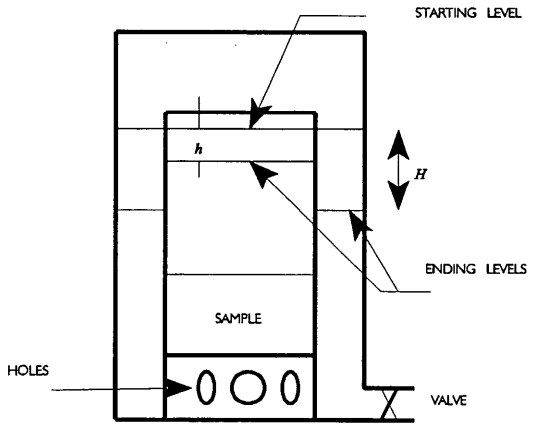


$$K = \frac{F}{1-\frac{hS}{Q}} * \frac{ad}{St}$$

F can be calculated using the equation:

$$\frac{hS}{Q} = 1 - \frac{F}{\ln\frac{1}{1-F}}$$

Q = the outflow volume caught in time t,
S = A + a,
h = the drop in water level inside the inner cylinder,
d = sample height,

**FIGURE 3 The permeameter used in the study.**

**TABLE 2 Gradations Used in the Study**

| Sieve Designation | 500 fpd gradation<br>% pass by wt. | 2000 fpd gradation<br>% pass by wt. |
|---|---|---|
| 1.5 | 100 | 100 |
| 1 | 93-100 | 89-100 |
| 3/4 | 80-90 | 70-80 |
| 1/2 | 60-72 | 50-62 |
| 3/8 | 52-62 | 38-52 |
| 4 | 33-41 | 13-34 |
| 8 | 15-22 | 2-18 |
| 16 | 0-7 | 0-6 |
| 30 | 0 | 0 |

**TABLE 3 Example of Test Results**

| Permeability Testing | | | | | |
|---|---|---|---|---|---|
| 500 fpd Trial | | | | | |
| Dolcito Limestone-3% A.C. | | | | | |
| Summary of Lab Results | | | | | |
| 1-Grain Size Distribution | | | | | |
| | Sample 1 | Sample 2 | Sample 3 | Sample 4 | Sample 5 |
| Sieve | % Passing | % Passing | % Passing | % Passing | % Passing |
| 1.5 | 100 | 100 | 100 | 100 | 100 |
| 1 | 94 | 94 | 94 | 94 | 93.9 |
| 3/4 | 79.9 | 79.9 | 79.9 | 80 | 79.8 |
| 1/2 | 61.8 | 61.7 | 61.8 | 61.9 | 61.7 |
| 3/8 | 51.7 | 51.7 | 51.7 | 51.9 | 51.6 |
| 4 | 33.6 | 33.5 | 33.6 | 33.9 | 33.4 |
| 8 | 17.4 | 17.4 | 17.5 | 17.9 | 17.3 |
| 16 | 4.4 | 4.3 | 5.5 | 3.8 | 4.2 |
| 30 | 0 | 0 | 0 | 0 | 0 |
| Permeability Values in cm/sec (fpd) | | | | | |
| cm/sec | 0.196 | 0.173 | 0.044 | 0.245 | 0.212 |
| fpd | 557 | 491 | 126 | 695 | 600 |
| Dimension, cm | | | | | |
| Ht. | 13.2 | 13.06 | 12.73 | 13.32 | 13.0 |
| Diam | 15.2 | 15.2 | 15.2 | 15.2 | 15.2 |
| Unit Weight | | | | | |
| pcf | 132.9 | 134.2 | 138.5 | 132.3 | 134.7 |
| $g/cm^3$ | 2.13 | 2.15 | 2.22 | 2.12 | 2.16 |
| A.C. % | 2.7 | 2.7 | 3.1 | 2.7 | 2.7 |

a. The table heading contains the target permeability, the type of aggregate tested, and the desired asphalt content.

b. Each column in the body of the table contains the data for one of the five replicates of this combination of asphalt content, gradation, and aggregate type. The grain-size distribution, the average calculated coefficient of permeability, the average height, the diameter, the unit weight, and the exact asphalt percentage (by aggregate weight) for each sample are given.

## DATA ANALYSIS AND RESULTS

The researchers listed the factors they thought might significantly affect the laboratory determination of the coefficient of permeability:

a. The percent air voids in each sample.

b. The percent asphalt in each sample, by total weight.

c. The crush factor (crushed versus uncrushed aggregate).

d. The percent passing, by weight, through sieves 0.6, 1.18, 2.36, 4.75, 9.5, 12.5, and 19.0 mm (nos. 30, 16, 8, 4; 3/8, 1/2, and 3/4 in.).

The viscosity of water was not taken into consideration since it depends on the water temperature, which was constant and equal to the laboratory temperature (25°C).

The percent air voids accounts for the total volume through which water can flow inside the sample and was assumed to be a very important factor in the experiment. Air void values were calculated following the procedure described in the Asphalt Institute MS-2 specifications.

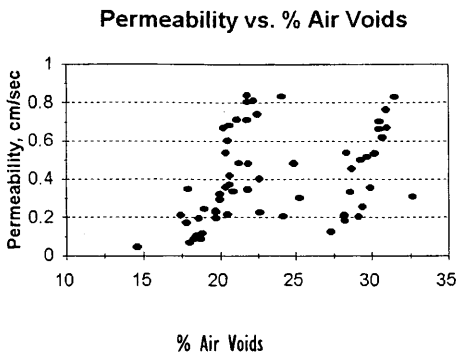


**FIGURE 4 Permeability versus percent air voids.**

The crushed materials were assigned a crush factor of 3, whereas the uncrushed materials were assigned a crush factor of 2. However, statistical analysis (described later) indicated that the crush factor has no significant effect on the coefficient of permeability, perhaps because the asphalt coating eliminated the angularity effect and made the aggregates behave as semi-angular or round aggregates in the permeability tests.

The statistical analysis also indicated that the percentage of coarser material (the amount retained on the 4.75-mm (no. 4) sieve did not have a significant effect on the permeability. The finer part (the amount passing the 4.75-mm (no. 4) sieve) is the part that affects the volume of voids inside the sample and consequently affects the coefficient of permeability. So, only the percentages passing 4.74-, 2.36-, 1.18-, and 0.6-mm (nos. 4, 8, 16, and 30) sieves were taken into consideration as statistical analysis continued.

In this manner, the insignificant factors were eliminated, and only the important factors were included in the reminder of the statistical analysis:

a. Percent air voids.
b. Percent asphalt.
c. Percent passing 0.6-, 1.18-, 2.36-, 4.75-mm (nos. 30, 16, 8, and 4) sieves.

A computer program called EXACUSTAT was used to conduct the regression analysis. A permeability coefficient was chosen as the dependent variable, and the other factors were treated as independent variables. First, each factor was plotted against the coefficient of permeability, $k$, to find if there was a trend in the relationships between $k$ and the different factors. Figure 4 is an example of these plots, and it shows the relationship between $k$ and the percent air voids. Figure 4 also shows a trend for two groups of points around 20 and 30 percent air voids. To investigate this observation, a correlation analysis was run on all the independent variables that were used in the regression analysis (discussed later). The results of the correlation analysis, which are shown in Table 4, indicated almost no correlation between percent asphalt and percent passing 2.36 mm (no. 8) sieve (correlation coefficient of $-0.0453$), slight correlation between percent air voids and percent asphalt (correlation coefficient of $-0.1388$), and a considerable correlation between percent air voids and percent passing 2.36-mm (no. 8) sieve (correlation coefficient of 0.4184). Although the last value appears high, the regression analysis, which will be discussed later, did not suggest the elimination of any of the dependent variables used.

The analysis continued by running a simple regression analysis of the coefficient of permeability as a dependent variable against each independent variable separately. Each factor was included in a simple regression and in a polynomial regression of second and third degrees. The square root, the exponent, and the log of each factor were also tested. Table 5 shows $R^2$ values for all different forms of the independent variables. The table shows no $R^2$ value higher than 0.45 was reached, which meant that $k$ could not be accurately estimated by using just one variable.

The next step in the analysis was to run a multiple regression using different combinations of the independent variables. A

**TABLE 4 Correlation Analysis Results**

| | PrcntAC | PrcntAIR | Pass8 |
|---|---|---|---|
| PrcntAC | | -0.1388 | -0.0453 |
| PrcntAIR | -0.1388 | | 0.4184 |
| Pass8 | -0.0453 | 0.4184 | |

**TABLE 5 $R^2$ Values for Simple Regression**

| variable | X | $X^2$ | $X^3$ | $e^x$ | logx | $X^{0.5}$ |
|---|---|---|---|---|---|---|
| prcntAIR | 0.11 | 0.18 | 0.25 | 0.02 | 0.13 | 0.12 |
| prcntAC | 0.06 | 0.17 | 0.26 | - | 0.05 | 0.05 |
| pass16 | 0.28 | 0.29 | 0.29 | 0.08 | 0.16 | 0.27 |
| pass8 | 0.40 | 0.43 | 0.44 | 0.06 | 0.42 | 0.42 |
| pass4 | 0.35 | 0.39 | 0.41 | 0.02 | 0.38 | 0.37 |

few nonlinear formulas were also tested but the analyses were mainly conducted using linear forms. The multiple regression computer runs showed that combining some of the independent variables in a linear form gave $R^2$ values higher than the summation of the $R^2$ values of the simple regression run on each variable separately. An example of this type of run combined percent air voids and percent passing the 1.18-mm (no. 16) sieve in a linear multiple regression, which gave an $R^2$ of 0.63. The simple regression had given $R^2$ values of 0.11 and 0.28 for percent air voids and percent passing the 1.18-mm (no. 16) sieve, respectively.

The following multiple regression equation gave the highest $R^2$ values:

$$k = 852.298 - 248.665 \times \text{prcntAC} + 97.507 \times \text{prcntAIR} - 95.521 * \text{pass8} \quad (R^2 = 0.873)$$

where

$k$ = coefficient of permeability in feet per day. (The associated values shown in the tables as cm/sec can be obtained by dividing this foot per day value by 2,835)

pass8 = percent by weight passing 2.36-mm (no. 8) sieve.
prcntAC = percent asphalt cement by total weight of sample.
prcntAIR = percent air voids by total volume of sample.

The $R^2$ value of 0.873 indicates that the equation is doing a good job of predicting permeability. Table 6 shows both measured and predicted permeability values using the equation. It indicates that the equation can be successfully used in estimating lab permeability values for asphalt-treated bases, especially in the range of 0.25–0.70 cm/sec (700–2,000 ft/day), where the coefficient of permeability is desired. Figure 5 shows a plot of predicted versus measured values of coefficients of permeability. Both Table 6 and Figure 5 indicate that the equation is less accurate in estimating permeability below 0.2 cm/sec (500 ft/day).

The next step was to study the residuals which are the difference between the measured and the predicted coefficients of permeability. First, all the residuals and the studentized residuals were calculated. The studentized residual is the difference between the fitted line and an observation in terms of standard deviation. Then a table of the unusual residuals and their corresponding studentized residuals was prepared. The unusual residuals are the ones that have studentized values higher than 2.0 or less than −2.0. It would be expected that about 5 percent of the residuals are unusual

**TABLE 6 Actual and Predicted Permeability Values Using the Three-Term Regression Equation**

| Test No. | Actual Value | Pred. Value | Test No. | Actual Value | Pred. Value | Test No. | Actual Value | Pred. Value |
|---|---|---|---|---|---|---|---|---|
| 1 | 610 | 758 | 21 | 914 | 1118 | 41 | 353 | 625 |
| 2 | 560 | 666 | 22 | 836 | 1029 | 42 | 1009 | 1042 |
| 3 | 672 | 623 | 23 | 990 | 871 | 43 | 515 | 627 |
| 4 | 650 | 657 | 24 | 1016 | 1124 | 44 | 581 | 716 |
| 5 | 955 | 769 | 25 | 984 | 1167 | 45 | 603 | 675 |
| 6 | 557 | 348 | 26 | 1526 | 1571 | 46 | 1525 | 984 |
| 7 | 491 | 273 | 27 | 1185 | 1189 | 47 | 579 | 854 |
| 8 | 126 | -142 | 28 | 1369 | 1436 | 48 | 945 | 955 |
| 9 | 695 | 341 | 29 | 1372 | 1287 | 49 | 723 | 1084 |
| 10 | 600 | 243 | 30 | 1059 | 1179 | 50 | 877 | 1439 |
| 11 | 2096 | 2136 | 31 | 190 | 375 | 51 | 2165 | 1729 |
| 12 | 3480 | 2361 | 32 | 247 | 370 | 52 | 1897 | 1640 |
| 13 | 2363 | 2432 | 33 | 331 | 454 | 53 | 1752 | 1728 |
| 14 | 2281 | 2179 | 34 | 254 | 64 | 54 | 1880 | 1693 |
| 15 | 2300 | 2216 | 35 | 296 | 359 | 55 | 2352 | 1770 |
| 16 | 2023 | 2124 | 36 | 583 | 1185 | 56 | 1460 | 1327 |
| 17 | 1702 | 1709 | 37 | 855 | 1238 | 57 | 1418 | 1464 |
| 18 | 1894 | 1836 | 38 | 642 | 1051 | 58 | 1994 | 1627 |
| 19 | 2012 | 2085 | 39 | 1366 | 1273 | 59 | 1287 | 1248 |
| 20 | 1933 | 1876 | 40 | 1139 | 939 | 60 | 1515 | 1459 |

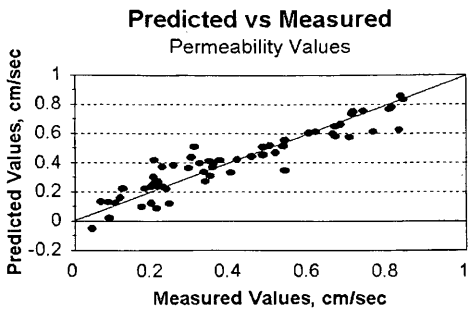


**FIGURE 5 Predicted values versus measured values of the coefficient of permeability.**

ones. Table 7 shows a list of the unusual residuals. Only four unusual residuals were observed (6.6 percent of the total residuals). No absolute studentized residual that is higher than 3.0 was observed.

The four points were then taken out of the database and the regression analysis was rerun. The rerun shows an improvement of 3.5 percent for $R^2$ (a new $R^2$ of 91.8 percent). A new table of the new unusual residual was prepared (Table 8). It shows a list of four unusual residuals, which have studentized values in the range of −2.35 to 2.51. These four points used to have lower values in the first analysis. However, their values went up in the new analysis due to the loss in the degrees of freedom (deleting four observation from the original database).

The influential points of the regression were also studied using a statistic called "leverage." The influential point is defined as a point that has a large influence on the fitted line. First, the average leverage of single data point was calculated as 0.066667. An influential point should have greater than 2.5 times the leverage of an average data point (*17*). The analysis indicated no influential points in either the first or the second run. Therefore, based on the facts mentioned above, the researchers conclude the regression equation mentioned before will be good for estimating the coefficient of permeability.

## SUMMARY AND BENEFITS

The research produced a regression equation which can be used to predict permeability of asphalt-treated bases. The regression equation was based on 38-mm (1.5-in.) top size aggregates and 2–3 percent asphalt stabilization. Most highway agencies use these values in their design of asphalt-treated drainage layers, so the results of this research can be used to estimate the lab permeability of these layers. That ability will allow designers to more quickly select the percent asphalt and aggregate gradation for their desired application. These results can also be used to estimate the coefficient of permeability of existing asphalt-treated permeable layers. The equation is not suitable for dense-graded bases because only open gradations were tested in the research.

## ACKNOWLEDGMENT

The authors would like to thank the Research Division of Vulcan Materials Company for providing the aggregates used in the research. Special thanks go to Dr. Chuck Marek and former Research Engineer Sandra Wood.

**TABLE 7 Unusual Residuals (First Run)**

| Row | Permeability | Predicted Perm. | Residual | Studentized Residual |
|---|---|---|---|---|
| 36 | 583 | 1185.92 | -602.923 | -2.72 |
| 46 | 1525 | 984.973 | 540.027 | 2.41 |
| 50 | 877 | 1439.71 | -562.709 | -2.57 |
| 55 | 2352 | 1770.33 | 581.673 | 2.64 |

**TABLE 8 Unusual Residuals (Second Run)**

| Row | Permeability | Predicted Perm | Residual | Studentized Residual |
|---|---|---|---|---|
| 36 | 855 | 1245.46 | -390.458 | -2.17 |
| 37 | 642 | 1062.45 | -420.468 | -2..35 |
| 48 | 2165 | 1722.16 | 442.8843 | 2.51 |
| 54 | 194 | 1615.6 | 378.402 | 2.10 |

## REFERENCES


1. Cook, M., and S. Dynkins, P. E. Treated Permeable Base Offers Drainage, Stability. *Roads and Bridges*, May, 1991.
2. Ridgeway, H. H. Pavement Subsurface Drainage Systems. *National Cooperative Highway Research Program 96*, Transportation Research Board, November, 1982.
3. Flen, L. Open Graded Bases May Lengthen Pavement Life. *Roads and Bridges*, September, 1991.
4. Magidzadeh, K., and R. Elmitiny. *Development and Implementation of Pavement Drainage Design Guidelines in Ohio*. Ohio Department of Transportation and FHWA, U.S. Department of Transportation, 1982.
5. Magidzadeh, K. *Evaluation of Pavement Subsurface Drainage Conditions in Ohio*. Ohio Department of Transportation and FWHA, U.S. Department of Transportation, 1979.
6. Forsyth, R. A., J. B. Hannon, and W. C. Gray. *Performance of Two Layer Asphalt Stabilized Drainage Blanket for Highway Subdrainage*. California Department of Transportation, Translab No. 632618, FHWA No. D-2-1, June 1974.
7. Smith, T., R. Forsyth, and W. Gray. *Performance of an Asphalt Treated Drainage Blanket in a Flexible Pavement Section*. California Department of Transportation, Interim Report, January 1970.
8. Baldwin, J. S. Use of Open-Graded, Free Draining Layers in Pavement Systems: A National Synthesis Report. In *Transportation Research Record*, TRB, National Research Council, Washington, D.C., 1990.
9. Foryth, R. A. *Asphalt-Treated Permeable Material—Its Evaluation and Application*. National Asphalt Pavement Association, 1990.
10. Poul, H. R. *Evaluation of Asphalt-Treated Drainage Blanket in a Rigid Pavement Section*. Louisiana Department of Transportation Research Project No. 72-8B(B), U.S. Department of Transportation, Federal Highway Administration, Report No. FHWA-LA-78-117, January 1978.
11. Cedergren, H. R. *Drainage of Highway and Airfield Pavements*. John Wiley & Sons, New York, 1977.
12. Moulton, L. K. *Highway Subsurface Drainage*. Federal Highway Administration, Report No. FHWA-TS-80-224, August 1980.
13. Barber, E. S., and C. L. Sawyer. Highway Subdrainage. *Public Roads*, Vol. 26, No. 12, 1952, pp. 251–268.
14. Highlands, K. L., and G. Hoffman. *Subbase Permeability and Pavement Performance*. Pennsylvania Department of Transportation, Research Project No. 79-3, Final Report, 1987.
15. Yemington, E. G. *A Low-Head Permeameter for Testing Granular Materials*. ASTM Special Technical Report No. 163, 1963.
16. Mottola, V. Design and Implementation of Internal Roadway Drainage. Presented at Conference on Crushed Stone for Road and Street Construction and Reconstruction, Arlington, Va., June 14–15.
17. The Asphalt Institute. *Mix Design Methods for Asphalt Concrete MS-2*, 1990.


*Publication of this paper sponsored by Committee on Subsurface Drainage.*

# Methodology for Functional Design of Low-Level River Crossings in South Africa

PEPRUS A. PIENAAR AND ALEX T. VISSER

With the renewed emphasis on low-volume roads in South Africa, the use of low-level river crossings (LLRC) will receive increased attention in the future. To evaluate low-level river crossings, it is necessary to know how often certain floods will occur and how long the structure can be expected to be submerged. From a functional design point of view, no guidelines exist on the size of openings required on an LLRC. The aim of the study is to quantify the extent of overtopping and provide a functional design method for the selection of LLRCs. The methodology is based on an analysis of historic river flow data obtained from the Department of Water Affairs of South Africa. Data were collected on several catchment areas with a variety of characteristics for a 20-year period. The 1-in-2-year flood was then determined for each catchment area. Considering various fractions of the 1-in-2-year flow, the number of times this flow as exceeded and the duration of excess flow were determined. This information was used as a basis for developing models to quantify the extent of overtopping. Based on these models, three levels of design were defined; namely 0.25, 0.5, and 1.0 times the 1-in-2-year flood. It was accepted that apart from passing under the structure, the design flood also may partially be accommodated over the structure. The acceptable flow depth for subcritical and supercritical flow during which a vehicle can pass over the structure was determined.

Since the first democratic elections in the history of South Africa in April 1994, policy makers have begun to focus more attention on the extensive disadvantaged rural areas of the country. The Reconstruction and Development Programme (RDP) (*1*) outlines the policies of the new government in this regard. In the transportation sector, low-volume roads are expected to play an increasingly important role in these areas. With renewed emphasis on low-volume roads, the use of low-level river crossings (LLRC) will also receive increased attention in the future. An LLRC, or low-water crossing, is a road-stream crossing designed to allow flooding during periods of high annual runoff (*2*). Compared with conventional high-level bridges, LLRCs are considered appropriate for tertiary roads mainly because of their low cost. These structures range from concrete slabs and causeways to submersible span structures. Eriksson (*2*) provides guidelines on structure type selection. During the development of South Africa's road network from the 1930s to 1950s, many of the main roads were constructed with these types of structures. After this initial development, high-level structures were generally used.

To evaluate LLRCs, it is necessary to know how often certain floods will occur and how long the structure is expected to be submerged. This information is needed to evaluate the impact on road users, who must use alternative routes while the structure is flooded or wait for the structure to become passable again. Without this information, an economic analysis of the investment decision required for the development of an LLRC is not possible.

From a functional design point of view, no guidelines exist on the size of openings required on an LLRC. Although some engineers design for the 1-in-2-year flood, others believe this is excessive, particularly for large catchment areas, relatively dry areas, or low-order roads where even unvented causeways may be acceptable.

The aim of the study is to quantify the extent of overtopping and provide a design method for the selection of LLRCs. The development of three models to describe the flooding of LLRCs and a design methodology are presented. The study is based on research that forms part of the research project, *Guidelines on Project Evaluation for Tertiary Roads* (*3*), done on behalf of the South African Roads Board.

## METHODOLOGY

The Department of Water Affairs of South Africa monitors river flow at several hydrological gauging stations throughout the country (*4*). Historic river flow data for the period August 1, 1972 to July 31, 1991 were obtained from the department for a number of catchment areas with a variety of characteristics. The flood with a 2-year recurrence interval was determined for each catchment area, using the rational, unit hygrograph, and two empirical methods (*5,6*). The number of times flow was exceeded and the duration of excess flow were then determined for various fractions of the 1-in-2-year flood.

This information was used as a basis for the models to be developed. Based on these models, three levels of design were defined; namely 0.25, 0.5, and 1.0 times the 1-in-2-year flood.

Besides passing under the structure, the design flood also may partially be accommodated over the structure provided that vehicles can still pass over the structure. The acceptable flow depth for subcritical and supercritical flow under which a vehicle can pass over the structure was determined.

## DATA COLLECTED

The study area includes drainage regions A, B, and X (*4*), shown in Figure 1. This area is in the northern part of the country and may be described as that part of the country north of an imaginary east-west line drawn through Johannesburg. After the methodology has been established, the study area may be extended to the whole of South Africa.

P. A. Pienaar, African Consulting Engineers Inc., P.O. Box 35007, Menlo Park, 0102, South Africa. A. T. Visser, Department of Civil Engineering, University of Pretoria, 0002, South Africa.

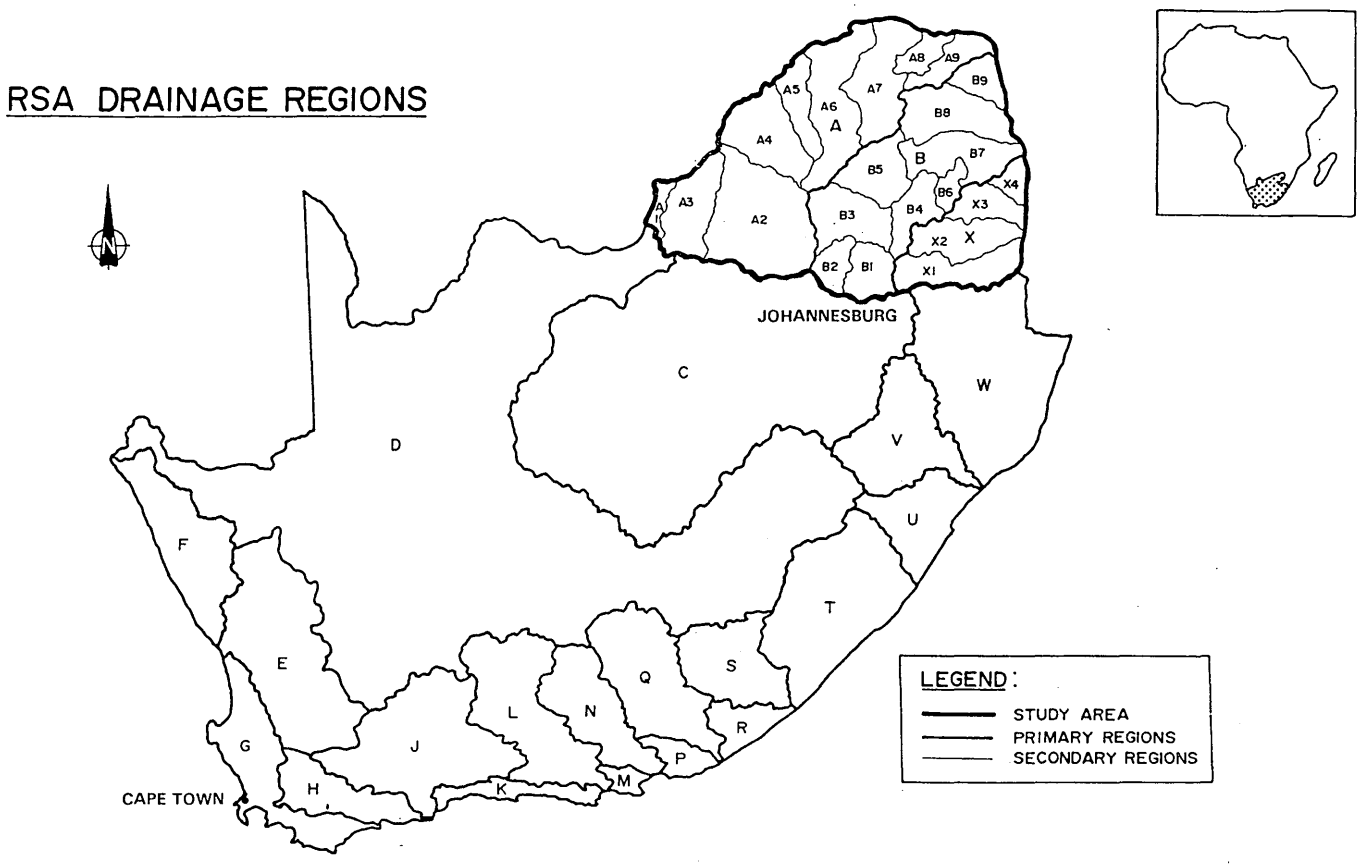


**FIGURE 1 Study area.**

The following criteria were used for the selection of gauging stations:

- In the development of the methodology, it was decided to focus on a limited number of drainage regions. Drainage regions A, B, and X were chosen because those areas are composed of mountainous, rolling, and flat terrain, and rainfall varies from 320 to 1,300 mm per year. Territories such as Lebowa, Venda, Gazankulu, Kwandebele, and large portions of Kangwane and Bophuthatswana (all former homelands where the need for the provision of low-level structures is high) are also in the area.
- Based on experience with low-level structures catchment areas were grouped as follows: less than 100 km$^2$, between 100 km$^2$ and 500 km$^2$, and between 500 km$^2$ and 1,200 km$^2$. In the case of catchment areas greater than 1,200 km$^2$ a detailed analysis was performed instead of using a generalized model as discussed in this study.
- Only gauging stations with complete or almost complete data for the past 20 years were considered.
- Only gauging stations serving rural catchment areas were considered.

## RESULTS

Each gauging station has a gauging weir, which measures the river flow on a continuous basis. A range of five flow values, expressed as a fraction of the 1-in-2-year flood, was selected for each gauging station. The range chosen depended on the capacity of the gauging station; for example, if the capacity was 1.4 times the 1-in-2-year flood, the range 0.25, 0.50, 0.75, 1.00, 1.25 was used. If the capacity was only 0.6 times the 1-in-2-year flood, the range 0.1, 0.2, 0.3, 0.4, 0.5 was used. For each of these flow values an analysis of the flow data was made to determine

- The total time period per year that the flow value was exceeded,
- The number of times per year that the flow value was exceeded, and
- The average duration flow was exceeded.

Two curves were then developed for each of the preceding characteristics: one serving as an envelope and one representing the mean values. Of the various relationships that were tested, the following was found to fit the data best:

$$Y = aX^b \tag{1}$$

where $Y$ and $X$ are as shown in Table 1 and $a$ and $b$ are regression coefficients.

The data and the curves fitted are shown in Figures 2, 3, and 4. The values of the regression coefficients for the various cases are provided in Table 1.

**TABLE 1 Value of Calibration Constants**

| DESCRIPTION | | AVERAGE CURVE | | ENVELOPE CURVE | |
|---|---|---|---|---|---|
| Y | X | a | b | a | b |
| Time exceeded per year (hrs) | Fraction of $Q_2$* | 2.58 | -1.38 | 12.00 | -1.30 |
| Number of times exceeded/year | Fraction of $Q_2$* | 0.47 | -0.74 | 1.40 | -0.80 |
| Average duration of excess flow (hrs) | Fraction of $Q_2$* | 3.41 | -0.70 | 6.00 | -1.15 |

* $Q_2$ is the 1 in 2 year flood

## DESIGN METHOD

After the models predicting the number of times certain flows will be exceeded and the duration of these flows were available, the design method was developed.

First, the design level (which provides an indication of the level of service to be expected from the structure) is chosen. Three design levels were defined, as shown in Table 2. If Design Level 1 is used, the design flow will be exceeded 1.3 times per year on average and the average flood duration will be 9 hr (as shown in Table 2, these values were as high as 4.2 times per year and 30 hr per flood for some of the gauging stations). If Design Level 3 is chosen, the design flow will be exceeded only 0.5 times per year on average, and the average flood duration will be 3.4 hr. Table 2 describes the implications of the three design levels in more detail. This table is based on the models developed.

Compared with criteria determined in other parts of the world, this approach represents an acceptable level of service. Coghlan (*7*)

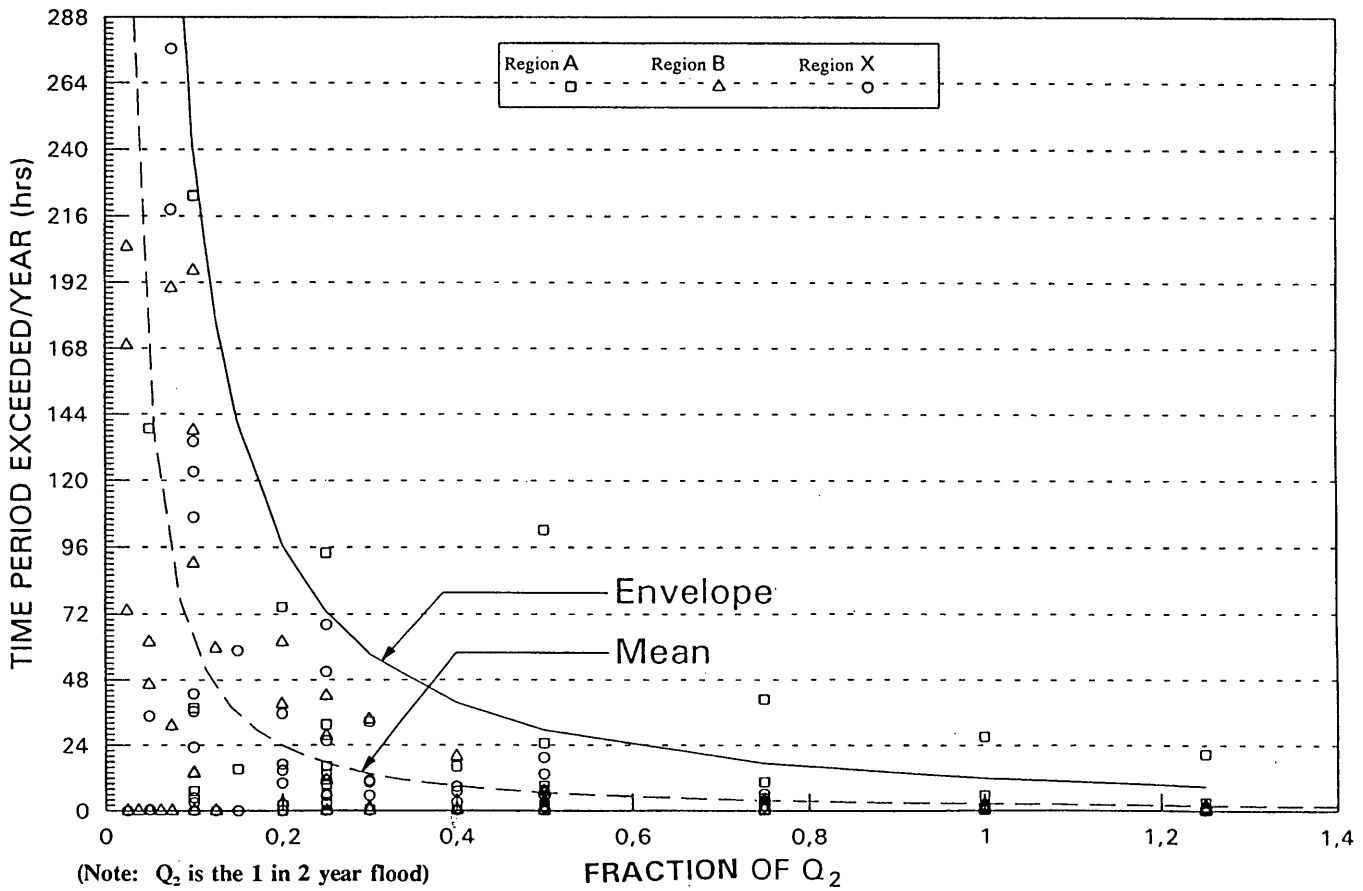


**FIGURE 2 Time certain flows were exceeded for three drainage regions.**

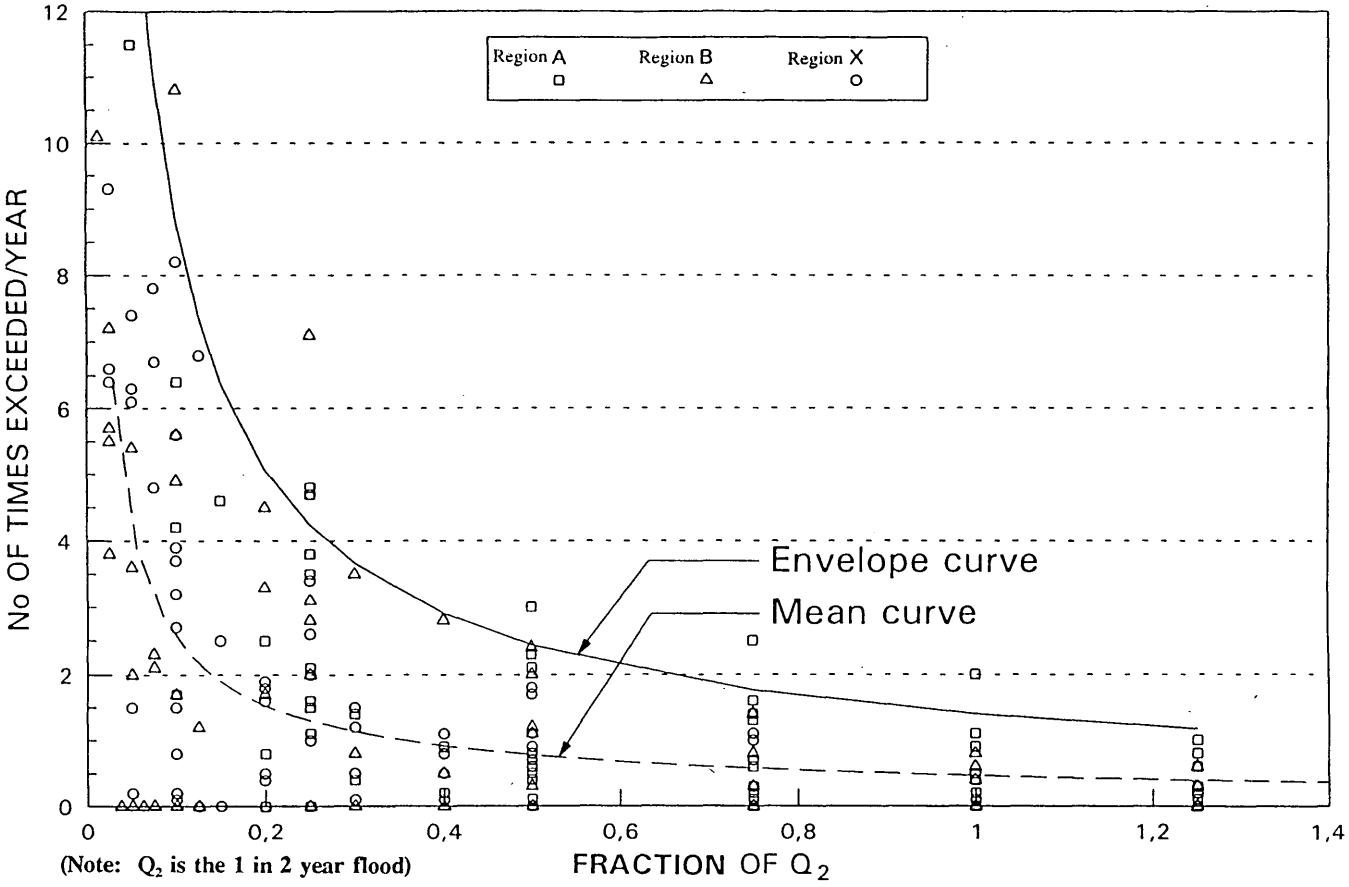


**FIGURE 3 Number of times certain flows were exceeded for three drainage regions.**

quotes criteria for access consisting of maximum closure of 1 to 3 days at a time, totaling not more than 15 days a year. Shen (*8*) established through an opinion survey the following (modified) absolute constraints for LLRCs:

- Average annual frequency of possible flooding: 5 to 10 times; and
- Duration of average traffic interruption: less than 48 to 72 hr.

The following approach is suggested for determining the design level:

- Design Level 1 is taken as the initial choice;
- The design level is increased to Level 2: if the traffic volume exceeds 250 vehicles per day or if the additional length of alternative routes exceeds 20 km;
- The design level is increased to Level 3: if the traffic volume exceeds 500 vehicles per day or if the additional length of alternative routes exceeds 50 km; and
- Should there be no alternative route available, or if the road is of strategic importance, the designer must choose the design level based on the implications described in Table 2.

When the design level is known, the design flood is determined as follows:

$$Q_{design} = f_i \times Q_2 \quad (2)$$

where

$Q_{design}$ = the design flood,
$f_i$ = a dimensionless factor related to the design level chosen and shown in Table 2, and
$Q_2$ = the flood with a 1-in-2-year return period.

It was assumed that accommodating the total design flood under the structure would not be necessary; such an approach would have ruled out unvented structures (e.g., concrete slabs). Part of the design flood may be accommodated over the structure provided it is still safe for a vehicle to pass over the structure.

The structure should therefore be designed such that

$$Q_o + Q_u \geq Q_{design} \quad (3)$$

where $Q_o$ is the flow that can be accommodated over the structure for flow depth less than the maximum acceptable and $Q_u$ is the flow capacity under the structure.

## FLOW DEPTH

It was accepted that a vehicle should not pass over an LLRC being overtopped if the depth of flow exceeds the underbody ground

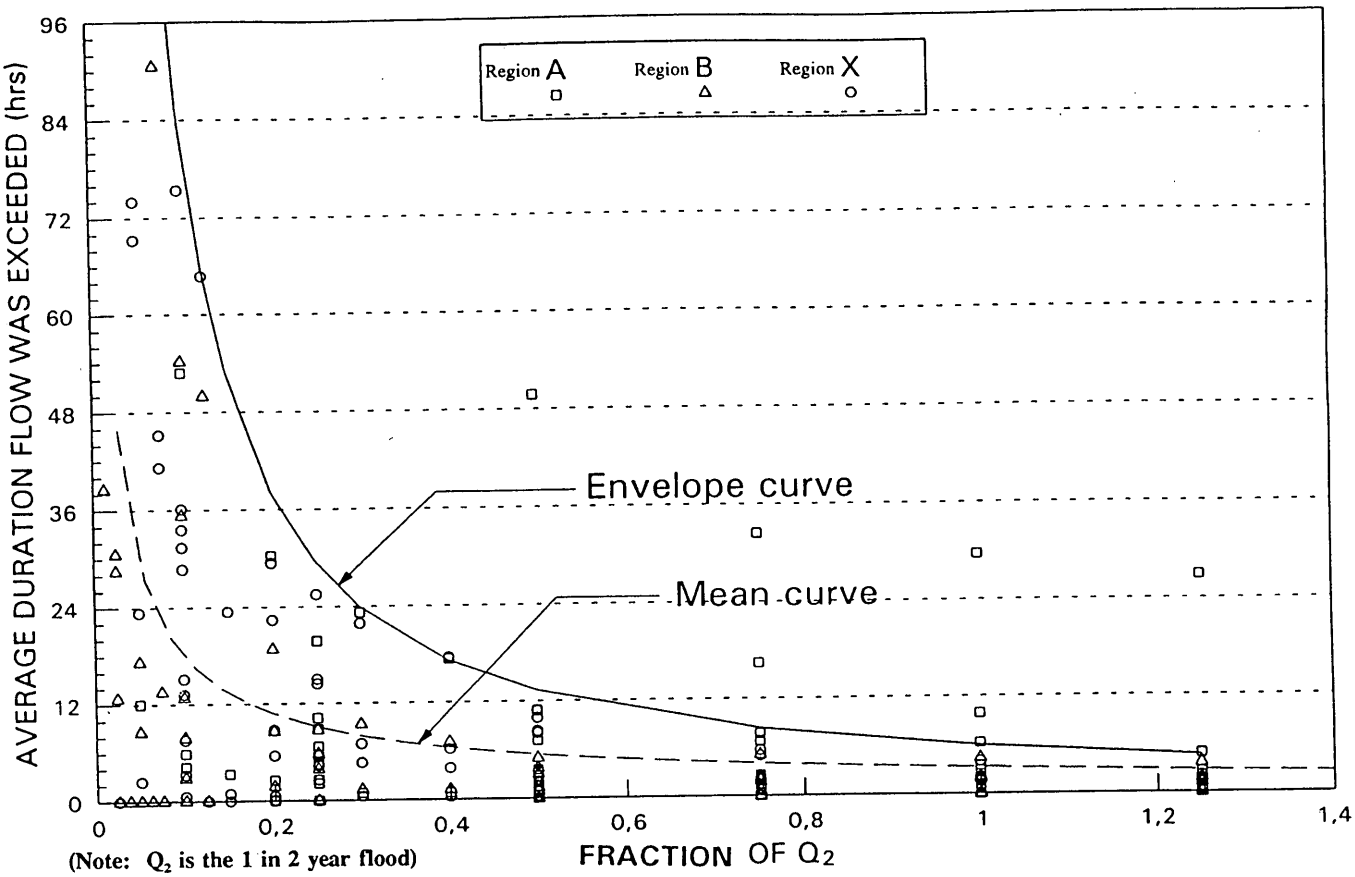


**FIGURE 4 Average duration flow was exceeded for three drainage regions.**

clearance height of the vehicle. The flow velocity, however, also must be considered.

The flow-depth relationship was determined for the following typical cross sections being used for low-level structures (Figure 5) (*9*):

- 5.5 and 8.5 m wide with a crossfall of 2 percent in the direction of flow,
- 8.5 m wide with a 2 percent camber, and
- 5.5 and 8.5 m wide with a zero-grade crossfall.

Based on the analysis, the following design values are recommended:

- Supercritical flow: maximum depth 100 mm, and
- Subcritical flow: maximum depth 150 mm.

The value of 100 mm was chosen for supercritical flow because at this depth, flow velocity was approaching 2 m/sec, which is relatively high. In the case of subcritical flow, 150 mm was chosen, as most passenger cars have this amount of clearance and flow velocities are generally less than 1 m/sec, which is not considered to present any danger to moving vehicles.

## USE OF THE METHODOLOGY: SUMMARY

The use of the methodology is summarized as follows:

1. Determine the design level ($f_i$), taking into account traffic volume, importance of the route, and the availability of alterna-

**TABLE 2 Levels of Design for Low-Level Structures**

| | | AVERAGE NO OF TIMES EXCEEDED PER YR PER GAUGING STATION | | | AVERAGE DURATION PER FLOOD (HRS) PER GAUGING STATION | | |
|---|---|---|---|---|---|---|---|
| DESIGN LEVEL | $f_i$ | MINIMUM VALUE | MAXIMUM VALUE | AVERAGE VALUE | MINIMUM VALUE | MAXIMUM VALUE | AVERAGE VALUE |
| 1 | 0.25 | 0 | 4.2 | 1.3 | 0 | 30 | 9.0 |
| 2 | 0.50 | 0 | 2.4 | 0.8 | 0 | 13 | 5.5 |
| 3 | 1.00 | 0 | 1.4 | 0.5 | 0 | 6 | 3.4 |

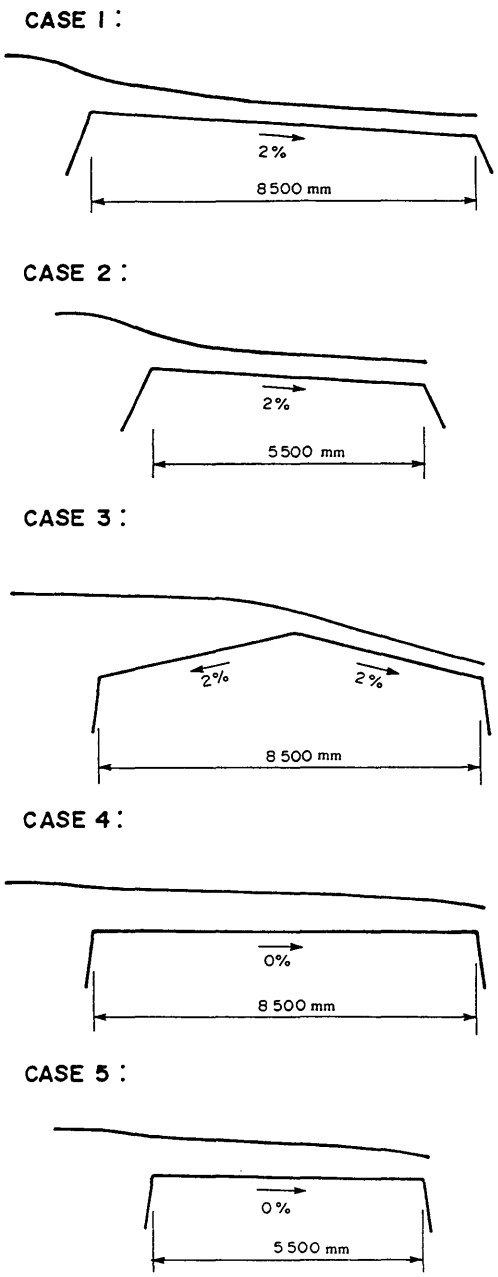


**FIGURE 5 Typical cross sections used for low level river crossings.**

tive routes. Table 2 quantifies the implications of the design level chosen.

2. Determine the 1-in-2-year flood ($Q_2$).
3. Determine the design flood: $Q_{design} = f_i \times Q_2$ (Equation 2).
4. Determine the road cross section and the (preliminary) road profile over the river.
5. Determine the flow that can be accommodated over the structure within the maximum acceptable flow depth ($Q_o$): 100 mm for supercritical and 150 mm for subcritical flow.
6. Determine the flow that must be accommodated underneath the structure: $Q_u \geq Q_{design} - Q_o$ (Equation 3).
7. Determine the dimensions of the opening(s) required underneath the structure if flow must be accommodated.
8. If it is necessary to adjust the road profile because of the dimensions of the opening(s), return to Step 4.

If the structure is outside the study area, the methodology should be applied with caution.

## CONCLUSION AND RECOMMENDATION

Recent political changes in South Africa have led to an increased emphasis on rural areas and on the use of low-level river crossings. The study addressed the quantification of the implications of these structures being flooded. A design method for the selection of LLRCs was presented.

The methodology proposed can be beneficial to practitioners involved with the design of LLRCs. The authors recommend that the study area be extended to the whole of South Africa and later to other regions.

## ACKNOWLEDGMENTS

The research was funded by the South African Roads Board, and permission by the Department of Transport for presenting this paper is gratefully acknowledged.

## REFERENCES

1. African National Congress. *The Reconstruction and Development Programme: A Policy Framework.* Umanyano Publications, Johannesburg, 1994.
2. Eriksson, M. O. Cost Effective Low-Volume-Road Stream Crossings. In *Transportation Research Record 898,* TRB, National Research Council, Washington, D.C., 1983.
3. Pienaar, P. A. *Guidelines on Project Evaluation for Tertiary Roads.* Research Report PR 91/232, South African Roads Board, Pretoria, Transvaal, Republic of South Africa, 1993.
4. *List of Hydrological Gauging Stations.* Vol. 1. Hydrological Information Publication No. 15. Directorate of Hydrology, Department of Water Affairs, Pretoria, Transvaal, Republic of South Africa, 1990.
5. National Transport Commission. *Road Drainage Manual.* Chief Directorate: National Roads, Department of Transport, Pretoria, Transvaal, Republic of South Africa, 1986.
6. Alexander, W. J. R. *Flood Hydrology for Southern Africa.* The South African National Committee on Large Dams, Pretoria, Transvaal, Republic of South Africa, 1991.
7. Coghlan, G., and Davis, N. Low Water Crossings. In *Transportation Research Record 702,* TRB, National Research Council, Washington, D.C., 1979.
8. Shen, H. W. Opinion Survey for Selection of Low-Water Crossing Structures. In *Transportation Research Record 898,* TRB, National Research Council, Washington, D.C., 1983.
9. Division of Road and Transport Technology (DRTT) and Jordaan & Joubert Inc. *Towards Appropriate Standards for Rural Roads: Discussion Document.* Report RR 92/466/1, South African Roads Board, Department of Transport, Pretoria, Transvaal, Republic of South Africa, 1993.

*Publication of this paper sponsored by Committee on Low-Volume Roads.*

# Portable Crossings for Weak Soil Areas and Streams

LOLA E. MASON AND PAUL H. GREENFIELD

To access forest products, streams typically need to be crossed by heavy equipment. In many cases, the access is only needed for a short time. The cost and time involved to construct a permanent crossing exceeds the need. Also, permanent access into the area is unwanted, making it necessary to remove the crossing that closes the road. Removal may cause pollution to the stream and continuous erosion problems, especially when culverts are used. A possible solution would be portable, temporary, reusable crossings made of readily available, inexpensive materials. The U.S. Department of Agriculture Forest Service has investigated this type of crossing option. Several products were considered as potential crossings. Five crossings were chosen for field trials: pipe mats, gratings, Terra Mats, wood pallets, and wood mats. All five crossings work well, although each has different strong and weak points. Most of the work has been performed in Florida. Conditions in other states will require different design modifications and improvements. Although quantitative information is still being analyzed, qualitatively, the crossings greatly reduce impact to weak soils of stream beds. This impact was observed to be lower particularly when compared with using no crossing or removing a permanent crossing.

The U.S. Department of Agriculture Forest Service constructs many miles of low-volume roads. These are primarily single lane, unsurfaced roads that are often used to access forest products (*1*). In some cases, the roads are built in areas that already have a high road density, which is open to the public. Often, small, intermittent streams with little or no water and weak stream bed soils must be crossed. These minor stream crossings can present a formidable problem for engineers, who must consider the environmental aspects of the surrounding ecosystem.

The Forest Service has been trying to decrease the open-road density by closing roads after the timber sale. One closure solution involves the removal of culverts at stream crossings, making the stream impassable. Both installation and removal of a culvert adds unwanted fill material to the stream. After removal, continuous erosion can occur.

Intermittent stream beds often consist of soil with poor load-bearing capacity and high moisture content or standing water. When the soil is dry, it can support vehicular loads. As the moisture content increases, the soil can no longer carry the load without the possibility of erosion.

A better solution might be the use of portable crossing products that are temporary and reusable. These products should be

1. Able to handle the anticipated traffic loads,
2. Designed to be moved with available labor and equipment at the site and easy to remove with minimal erosive impact,
3. Designed with adequate traction to perform well while immersed in water or mud,
4. Durable enough to withstand transfer to another site, possibly as often as every 3 months, and
5. Cost-effective and readily available.

It is also desirable to have a product capable of conforming to different lengths of a stream crossing.

Seeking to improve access while protecting streams, the San Dimas Technology and Development Center (SDTDC) began a study of portable crossings in 1990. The initial step was a literature review and market search, reported in the publication, *Portable Wetland Area and Stream Crossings* (*2*). The publication covers products available commercially and through the military. It includes a description of each product with photos and sketches; situations in which the product can be used; the testing and use that has been performed; and the potential problems that need to be addressed.

Over the past 4 years, some of the crossing products described in the publication have been field tested. For a product to be chosen for testing, it had to be new to this type of use, inexpensive, readily available, or any combination of these. Thus far, testing has entailed the crossing of three types of vehicles: log trucks (or similar heavy vehicles), light vehicles, and skidders. Testing began by locating possible sites, then determining which products would be the most suitable. Most of the field tests have been performed in the Osceola Ranger District (RD) near Jacksonville, Florida, where elevations are fairly constant and the soil is mainly a silty sand.

Before beginning the review of products, a word about the use of geotextiles is in order. Much literature currently exists on the use of geotextiles. Their connection with portable stream crossings relates to confinement of the material under the crossing product and its ease of removal. For most of the products tested, installation of geotextiles is recommended to limit the amount of local material permeating the installation. Geotextiles also facilitate the timely removal of the product.

Some concerns have been raised about leaving the geotextile behind. Ideally, an environmentally sensitive solution would require that the geotextile be removed or that a biodegradable type be used. The designer will need to determine the cost-effectiveness of the type of geotextile to use.

## PORTABLE CROSSING PRODUCTS EXAMINED

### Pipe Mat Crossing

One of the most interesting stream crossings found during the market search was the Pipe Fascine System (*3,4*). Designed by the British military, the system was specifically designed as a portable, reusable bridge for tank traps. Because of its design, logging equip-

USDA Forest Service, San Dimas Technology & Development Center, 444 East Bonita Avenue, San Dimas, Calif. 91773.

ment and loaders can easily install and retrieve the system. The Forestry Commission Kielder, United Kingdom, has performed field tests during timber harvests and intends to use the system on a regular basis. The system is excellent for alleviating the problem of one fixed bridging point because it is so easy to move. The Forestry Commission covers the system with logs or slash to protect it and provide a good running surface.

The SDTDC evaluated a pipe mat installation similar to the British Pipe Fascine System. The pipe mat crossing is constructed of schedule 40 polyvinyl chloride (PVC) pipes and steel wire rope (cable). Initial testing was conducted at SDTDC to verify adequate strength of the pipes under direct loading. A second set of loading tests was performed on pipes chilled to freezing temperatures. The pipe proved strong enough under direct loads up to 826 kPa (120 psi).

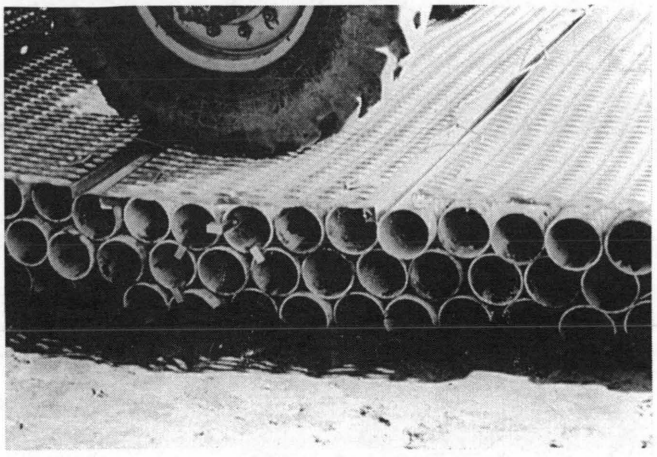

**FIGURE 1 Pipe mat crossing with grating surface.**

*Field Tests*

Field testing confirmed that connecting all of the pipe that comes in contact with vehicle tires is mandatory. Pipes are drilled at 0.3 m (1 ft) and 1.2 m (4 ft) from each end. Four 10-mm (3/8-in.) cables are threaded through the holes to connect the individual pipes. The cable ends are looped and secured with cable clamps to prevent individual pipes from rolling, shooting out the sides, or moving in other directions. This also reduces the time to install and retrieve the crossing. From field tests, 5-mm (3/16-in.) cable appeared to be sufficient, was much easier to work with, and was less costly than the larger-size cable.

Crossings were assembled into bundles made of 5.1-, 10.2-, 15.3-, and 20.4-cm (2-, 4-, 6-, and 8-in.) schedule 40 PVC pipe and proved very successful in crossing U-shaped channels. The main concern was damage to the banks due to gaps between the bank and the bundle. Because U-shaped channels are not typical, further testing was performed on broader, shallow channels. Bundles could not be placed to make an even surface. To alleviate this and completely fill the channel, thus reducing damage to the stream banks, loose pipe were placed in the channel. A single layer of pipe was connected along the surface, first using clamps, then cable. Sheets of grating were placed on top to protect the pipe and provide traction. The deck-span safety grating (described later) was placed with the 3.0-m (10-ft) edge perpendicular to the wheel lines and proved more stable than the expanded metal grating. The sheets were later connected to each other with 10-mm (3/8-in.) cable and clamped to the pipe (Figure 1). This crossing proved very successful with little pipe movement under a loaded log truck making 10 passes.

A field test on the Osceola RD was conducted at a site where a small, shallow stream required crossing by a skidder. Only a single layer of pipe connected to form a mat was needed. The mat was 2.7 m (9 ft) long by 6.1 m (20 ft) wide, providing the log skidder with plenty of maneuvering room. A nonwoven, needle-punched geotextile was placed along the stream bottom, with the crossing placed on top. Because of the short length, no additional surfacing material was needed for improvement of traction or protection of the crossing. The crossing materials cost approximately $602. Life expectancy is unknown. Construction and placement of the mat took approximately 3 hr. The skidder successfully completed 40 round trips with no movement or damage to the pipe mat crossing. Except for the slight indentation from the pipes, the stream showed no detrimental effects from the crossing. The only damage to the pipe mat crossing occurred after removal due to the skidder arm swinging back and hitting one pipe. The mat is still usable.

Another field test on the Osceola RD was conducted to measure changes to the stream bed and water quality. The channel was 10.6 m (35 ft) wide and 0.5 m (1.3 ft) deep at the center. A nonwoven, needle-punched geotextile was placed on the stream bottom followed by five loose pipes in the main channel used to even out the stream bottom. Then, two pipe mat crossings of 10.2-cm (4-in.) schedule 40 PVC and 5-mm (3/16-in.) cable were placed to cover 7.5 m (25 ft) of the span. A third 3.0-m-(10-ft-)long crossing was placed on top, at the center, to bring the crossing to the water surface level. Wood pallets (described later) were placed as the running surface. The entire crossing took approximately 1.5 hr to place. A loaded lowboy, 36 320 kg (80,000 lb), made a single pass. More passes were not attempted due to long stretches of weak soils on both sides.

Although test results are not yet available, several items appeared to affect water quality for the short duration of installation and removal. During installation, soil may be picked up with the crossing if the crossing has been stored directly on the ground. This soil is deposited in the stream with the pipes. Also, small fragments of pipe from cutting and drilling may remain inside the pipes and be deposited in the stream. With some care, both of these pollutants can be kept out of the stream.

During removal of the geotextile, sediment that had settled on the surface of the geotextile entered the stream mainly from disturbance when the fabric was dragged out. Care must be taken when placing and removing the crossing. Equipment can be a detriment to weak soils at the edges of streams. Measurements of changes to the stream bed are not yet completed, however, a slight indentation of approximately 12 mm (0.5 in.) was noticeable at the stream edges.

The pipe mat crossing has proven a very successful means of crossing a stream, provided the stream bottom has little, if any, grade. For all designs, it is important to place geotextile before pipe installation to ensure separation and prevent sinking, which causes impact to the stream and makes removal difficult. A layer of connected pipes should be placed along the stream bottom. If necessary, loose or connected pipes should then be placed to the desired height; then, a final layer of connected pipes should be placed. The top and bottom layers should be long enough to go beyond the stream edge to help protect the stream banks.

Typically, a tractive surface such as grating, Terra Mat, wood mats, or wood pallets should be connected to the top layer of pipe.

An important consideration is width. A 3.0-m (10-ft) width is too narrow for many vehicles, and 6.1 m (20 ft) (typical PVC length) may be excessive. It is possible to use shorter sections, end-to-end, between full length pipes making 4.2-m-(14-ft-)wide mats. This concept is shown in Figure 2.

Transport depends on the length and amount of pipe. In some cases, the drilled, individual pipes are transported by pickup truck and constructed on-site. Preconstructed mats may be too heavy for a pickup truck, requiring a lowboy or dump truck. Due to weight, equipment on-site (typically front-end loaders or skidders) is used to place the mats. Time to place depends on length and depth of the stream, amount of water, equipment available, and the amount of room needed for equipment to maneuver. The greatest consumption of time involves construction of the mat. To cut, drill, and cable together a 6.1-m-(20-ft-)long, 4.2-m-(14-ft-)wide mat can take three people about 3 hr.

The two main causes of pipe deterioration are impact (from dropping or hitting the mat) and ultraviolet (UV) light. Pipe with UV inhibitor is available, or the pipe may be kept covered as much as possible. The two main causes of vehicle damage occur when (a) loops at the end of the cables hook onto items on the underside of the vehicle and (b) the cross surfacing is not sufficiently connected to the pipe, possibly flipping up under the truck.

## Grating

During the market search, placing steel grating over geotextile was considered. Two types of steel grating were suggested for the initial field tests. One is deck-span safety grating. Made from 10-gauge, pre-galvanized sheet metal, it is 0.9 m (3 ft) by 3.0 m (10 ft) by 3.3 cm (1-5/16 in.) with the edges flat instead of bent into a channel. The plank has an 8-diamond design with a diamond opening size of 9.8 cm (3-7/8 in.) by 3.2 cm (1-1/4 in.). The other is a 1.8 kg (4 lb) regular expanded metal grating. It is made of non-galvanized carbon steel. The size is 1.2 m (4 ft) by 3.0 m (10 ft) by 13.0 mm (0.6 in.) with a diamond opening of 3.2 cm (1.3 in.) by 13.4 cm (5.3 in.).

### *Field Tests*

All the grating field tests were performed on the Osceola RD. The initial step was to smooth the area of rutting. The geotextile was then placed, followed by the grating. For one site, a woven, high-tensile strength geotextile was used. For the other tests, a standard nonwoven, needle-punched geotextile was used. For the other tests, a standard nonwoven, needle-punched geotextile was used. The woven geotextile has a slicker surface allowing more movement of the grating. The geotextile is critical to the success of this type of crossing and must be used.

Before placement of the grating, some of the deck-span safety grating was connected to reduce the amount of cold pressing. Cold pressing is the slow deformation (bowing) of the sheet metal over the 3.0-m (10-ft) length, which could catch under a vehicle, possibly damaging both. Cold pressing does not harm the grating, but would necessitate flipping the grating over occasionally. Connecting the grating was also considered to reduce installation time. Wing hinges were used to connect two sets of the grating. One set was connected along the 0.9-m (3-ft) edge, the other connected along the 3.0-m (10-ft) edge.

The grating was placed in the wheel paths with the 3.0-m (10-ft) edge parallel to the direction of travel. Only the set of safety grating connected along the 3.0-m (10-ft) edge was placed with the 3.0-m (10-ft) edge perpendicular to the direction of travel. The main problem with the connected grating during installation was its weight. It took six to eight people to lift, carry, and place the grating. Connecting did reduce bowing. Bowing is also reduced by placing the 3.0-m (10-ft) edge perpendicular to the direction of travel. The grating installation time was decreased very little, if any, by connecting the grating.

The initial use of the grating was for light-vehicle access through an intermittent stream with standing water. Only the two types of grating were used. Geotextile was not considered necessary. Approximately 200 vehicles traveled over the surfacing. It was very successful, with no problems or user complaints.

The first test with heavy vehicles occurred in March 1991. It took eight people 2 hr to place the geotextile and grating. After placement, an empty log truck made one round trip. Everything performed successfully, including a geotextile without grating section. Unfortunately, no further testing was performed at this site.

In March 1992, another opportunity arose when a 60-m (200-ft) section of continuously saturated soil conditions stopped timber harvesting. Four people installed the nonwoven, needle-punched geotextile and both types of grating in approximately 2 hr (Figure 3). The road was continuously used from March through May, equaling

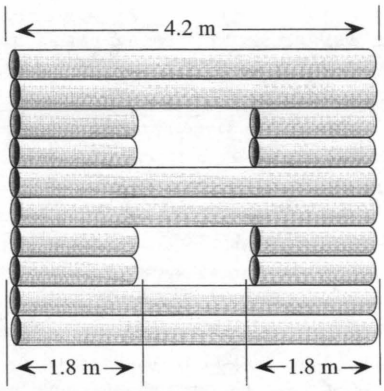


**FIGURE 2 Using shorter pipe sections, end-to-end, between full length pipes, to make 4.2-m-(14-ft-)wide mats.**

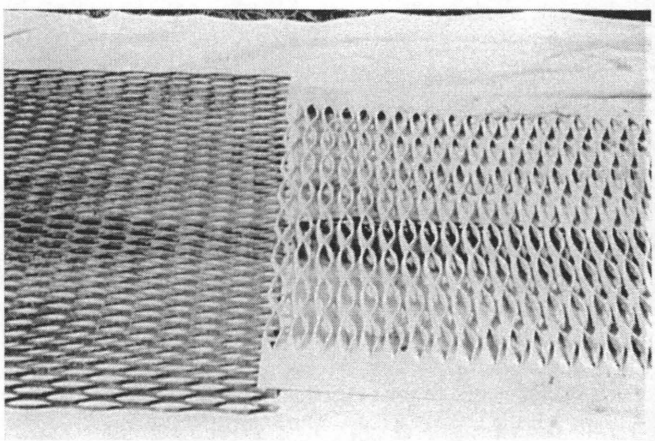

**FIGURE 3 Expanded metal and deck span safety grating.**

approximately 130 round trips of log trucks. The grating was quickly and easily removed by a nearby loader. The geotextile was still in good condition, however, it was saturated with water and sand. The weight of the fabric during removal resulted in fabric tears in several areas. A way to easily remove the fabric so it can be reused still needs to be determined.

The key to the system's success appears to be the geotextile. As the tires travel over the grating, the geotextile below it goes into tension, which helps distribute the load over the road surface between the tires. The geotextile allows the water to move to the surface while confining the sand beneath. The grating provides traction, keeps the geotextile from moving, and distributes the direct wheel load over a wider area of the geotextile.

A lower gauge (11-gauge) of expanded metal grating has also been used. It weighs less and costs only $32 for a 1.2-m (4-ft) by 2.4-m (8-ft) sheet. The problems with cold pressing of the deck-span safety grating and lateral movement of the expanded metal remain. Reinforcing bar, typically used in concrete, was shaped and used to anchor the grating. A 1.2-m (4-ft) section of 12.7-mm (0.5-in.) bar was bent into a U-shape. The center section would be 15.2 cm (6 in.) and the legs 0.5 m (1.7 ft) each. Thus far, it has worked well. It also helps reduce theft. Life expectancy information has been difficult to obtain due to theft of the grating before the end of its useful life.

Information concerning the reduction in surface impacts has been gathered and includes soil moisture content, strength, compaction, and surface deformation (mainly rutting). A comparison is made between two areas, one with the two types of grating and one without grating. The one with grating had about 1.3 to 2.5 cm (0.5 to 1 in) of deformation compared with up to 0.3 m (1 ft) of deformation in areas without grating (Figure 4). If the grating or other type crossing does not span the entire length of weak soil, deep rutting occurs at the ends. Vehicles begin to off-track, causing impact to the area.

## Terra Mat

Disposal of rubber tires has become a growing problem due to the tires' slow rate of deterioration. Because old tires are readily available and inexpensive, companies are beginning to look for ways to use this material. Tires are very durable and have long-life attributes, which make them suitable for a portable, reusable crossing. Terra Mat was developed specifically to help logging trucks cross weak soils. The mats are made to be portable and reusable.

Terra Mat is made of interconnected tire sidewalls. Maintenance is minimal and typically consists of replacing connectors. Although it was developed specifically for logging trucks, only limited experimentation with Terra Mat had been performed on Forest Service roads. The product has performed well, but more experimentation is needed.

These mats come in a variety of sizes depending on the width of road, length of area to be covered, and weight that can be handled by on-site equipment. Variations include double layers of sidewalls or a layer of treads topped by sidewalls. The standard mat [2.7 m (9 ft) by 6.1 m (20 ft)] weighs 680 kg (1,500 lb) and costs $200 (Figure 5).

The other basic type of mat is narrower and should be placed only in the wheel tracks. These are typically 0.9 m (3 ft) wide and 3.0 m (10 ft) long. The design tested in the field has two layers of tire treads topped with tire sidewalls. This mat weighs 360 kg (800 lb) and costs $125 for two sections.

### *Field Tests*

Several field tests have been performed, mainly with the standard and wheel track mats. In the Daniel Boone National Forest (NF), near Lexington, Kentucky, a standard mat was placed on a bridge deck. The timber bridge was being used by skidders. The surface had become slick due to rain and mud. The mat provided the necessary traction for the skidders to complete the remaining round trips over the bridge. It was transported by a pickup truck to the site. A skidder, chained to one end, dragged the mat into place, taking only a few minutes. By the end of the test, little remained of the mat. Trees dragged behind the skidders caught on the mat and pulled apart the center during the first pass. This continued throughout its use with only parts remaining along the deck edge in the wheel track areas.

A field test was performed on the Osceola RD using the wheel track mats. The site was for log truck use where no road previously existed. Using a feller buncher, trees and stumps were cleared. A nonwoven, needle-punched geotextile was placed over the existing

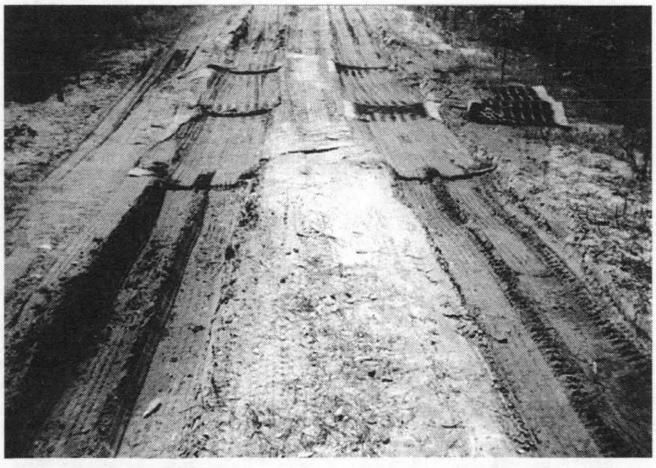

**FIGURE 4 Comparison of wheel path deformation, grating versus untreated surface.**

**FIGURE 5 Interconnected rubber tire sidewalls, Terra Mat.**

vegetation. A loader piled the Terra Mats for the skidder to drag to the road location. Each mat was then chained and placed by the feller buncher. The mats are heavy, very flexible, and have a tendency to curl under at the ends (Figure 6). Location of the chain is critical because people are not strong enough to help in placement. The mats took little time to place, 15 min per mat once on-site. Maneuvering room is critical to time of placement. Transport and chaining took the greatest amount of time. The mats performed successfully for 35 round trips. In the drier areas, without crossing materials, the trucks had to be assisted. Finally, due to the increased moisture conditions, the mats began moving out of place and the test ended. Impact to the crossing area was minimal when compared with the areas without crossings.

A field test was performed on the Apalachicola National Forest (NF) near Tallahassee, Florida. The site was a dry sand area with a grade of about 10 percent. The standard mat was placed directly on the sand. No means of holding the mat in place was used. A loaded log truck then tried to climb the grade. The mat was pulled out of place and the test was abandoned. This mat-crossing application may have been successful had the mat been anchored in place.

Without the proper equipment these mats are difficult to place. Because they are heavy, large, and very flexible, it can easily take an hour to place one mat. Although this makes them difficult to work with, they conform well to the area and their weight tends to keep them in place. With Terra Mat, use of geotextile is not as critical. Placement is easier without the geotextile because the mats can be dragged instead of lifted into place. Both are too narrow for typical forest road applications. Log trucks need at least 3.0 m (10 ft), preferably 3.6 m (12 ft) of width on straight stretches and more on curves. The 2.7-m (9-ft) by 6.1-m (20-ft) mat is too short in one direction and too long in the other. The 0.9-m (3-ft) mats can be spaced for the wheel tracks and are easy to drive off of. However, getting back on the mats can be difficult. Although the maximum grade has not yet been determined, anchorage of the Terra Mats should be considered for any grade greater than 5 percent. The Terra Mat does have a rough surface requiring a reduction in vehicle speed. Placement should be in areas where the speed is low or there is good visibility and plenty of distance to slow the vehicle. Their best quality is the very low cost.

The mats appear to cause little impact to the road surface. No direct measurements of the impact have yet been made. Unfortunately, the impact by the equipment placing the mats can be high and spread over a large area. This is mainly due to maneuvering to the side when lifting instead of dragging the mats into place. Proper equipment to handle the loads would help, and lighter mats would be desirable.

**FIGURE 6 Feller buncher installing Terra Mat.**

### Wood Pallets

Supreme International is a Louisiana company that produces a sturdy variation of a wood pallet. They are made up of 7.6-cm (3-in.) by 20.3-cm (8-in.) hardwood planks, nailed together to make a three-ply pallet. They interconnect to make roads and platforms typically used in oil fields. The individual pallets range from 2.4 m (8 ft) by 3.6 to 4.8 m (12 to 16 ft). The prefabricated pallets are made from lumber weighing 1,000 kg (2,200 lb) with approximately 250 nails, and cost $370.

The pallets should last at least 2 years. No nail points can surface, which eliminates the possibility of tire puncture. The mats are reversible and broken planks can easily be replaced, prolonging their life. Each end has an overlap area for connection between pallets. In some areas, such as road intersections and curves, the panels are placed with the 4.8-m (16-ft) width, providing ample maneuvering room for log trucks.

#### *Field Tests*

A field test has been carried out on the Osceola RD. The area was near a culvert, which increased the moisture content of the silty sand soil to more than 30 percent. Although the area needs to be fairly smooth to obtain an even surface and reduce stresses to the pallets, 10.2 to 15.3-cm (4 to 6-in.) ruts were present at the time of placement. A nonwoven, needle-punched geotextile was placed under the pallets to reduce sinking and improve separation, reducing stresses to the planks during removal. The pallet was cut in half to make two 1.2-m (4-ft) by 4.2-m (14-ft) pallets. This helped reduce the weight and made them less cumbersome and easier to place. Each pallet was placed in a wheel track, providing proper road width. Soil was then placed on both ends to reduce the abrupt edges, which decreased roughness.

The geotextile was unrolled by two people and the pallets placed by a backhoe. Transporting was the most time-consuming process. Picking up pallets was somewhat difficult. The planks were too close together to use a chain. Making loops with cables through the center of the pallets could permit chain use. After 1 week and approximately 150 round trips, the pallets were holding up well. Some deflection occurred due to pre-existing ruts. One plank edge broke off and vehicles had to slow down at the crossing due to roughness (Figure 7). The pallets deformed the road surface by only 12.7 mm (0.5 in.).

Another field test was performed in Florida using the pallets as surfacing for the pipe mat crossing. Due to the small equipment available to handle the pallets, they were cut in half. They were placed by a front-end loader and truck with a winch (Figure 8). Placement took less than 15 min per pallet. No noticeable movement occurred under a loaded lowboy.

### Wood Mats

Pallets work very well and have proven themselves in oil field applications. However, they are expensive, limited in size, and manu-

**FIGURE 7 Wood pallet installation.**

factured by only one company. Hence, they are not readily available and can be expensive to ship. As an alternative, wood mats using posts were constructed and tested. The posts were 10.2 cm (4 in.) by 10.2 cm (4 in.) and 15.3 cm (6 in.) by 15.3 cm (6 in.) in width and 3.6 to 4.2 m (12 to 14 ft) in length. Holes were drilled through each piece at 0.3 m (1 ft) and 1.5 m (5 ft) from each end. They were connected with 10-mm (3/8-in.) galvanized steel cable. Loops were made at the end of each cable and secured with cable clamps.

The connection between the lumber pieces was loose. Putting tension on the cable would help increase friction between the pieces so they would act as a unit and not individually. From the field tests, this does not appear to be necessary.

### *Field Test*

A field test was performed in the same area and at the same time as the one for the wood pallets. Because the crossing area was large, both pallets and mats were needed to cover it. The existing rutting was smoothed by a small dozer. Unfortunately, most of the rutting reoccurred during placement from the backhoe and the need to allow log truck traffic to continue during installation. The geotextile was rolled out and the mats were emptied by the dump truck onto the ground. The backhoe picked up each mat by the loops and laid it in place. The mats were moved to better cover the weak soil area. It would be wise to flag where the mats should be placed, based on the length of mats and area to be covered, so extra moves are not necessary. The 15.3-cm (6-in.) mats were placed in the center with the 10.2-cm (4-in.) mats on each end as ramps. The length of each mat was 1.2 to 1.8 m (4 to 6 ft) to reduce weight and ease placement. The mats could be connected to each other on-site, but this was not done for this test. If the surface becomes slick, grating can be connected to the surface.

**FIGURE 8 Front end loader installing wood mat.**

During the first pass of a loaded log truck, a loop caught on the disconnect valve of the fuel line. It pulled the mat up out of position and disconnected the valve. Although inexpensive and easy to repair, this occurrence highlights the importance of making sure all loops are tucked under the mats. In the 150 round trips since, no other vehicle damage occurred. Impact to the site has been minimal. The pallets have settled about 12 mm (0.5 in.) and make for a smooth road surface.

The surface has not become wet or muddy to the point of becoming slick. Initially the moisture content of the soil was so high that pumping of water through the geotextile onto the mat surface was visible. The 10.2-cm (4-in.) mats were considered the most critical in terms of strength and have proven to work well, at a lower cost and lighter weight than the 15.3-cm (6-in.) mats.

Information was gathered at a pallet crossing site and at an area without pallet crossings. Moisture content, cone penetrometer, and shear vane data were gathered as well as surface deformation. Although further analysis of the information must be completed, the site without pallets had a moisture content typically 5 to 10 percent less than the crossing site. The rutting that occurred at the non-crossing site was 15.3 to 25.4 cm (6 to 10 in.). At the pallet crossing, settlement was only about 12 mm (0.5 in.). The addition of wood pallets left no specific areas to hold and channelize water or specific areas of high compaction (rutting).

## Crossing Products Cost Comparison

Comparisons shown in Table 1 are made based on a crossing 4.3 m (14 ft) wide and 2.4 m (8 ft) long. Most of the crossings, except the 3-m-(10-ft-)long safety grating and Terra Mat, meet this criteria. For the pipe crossings, assume that the 6-m-(20-ft-)long pipes are cut to 4.3 m (14 ft) and that the extra 1.8-m (6-ft) pipes are used in the wheel tracks. None of the costs include labor to construct, install, or remove. Only the grating costs include the use of geotextile. No costs are included for surfacing over the pipe crossing. Shipping is not included in the costs (mainly for Terra Mat and wood pallets). Cost of rebar to pin down grating is not included.

## CONCLUSION

A number of options exist for portable, reusable stream crossings. All of these options need further evaluation under conditions relevant to their operating environment. All of the options identified have positive as well as negative characteristics; some have a higher initial cost yet provide a longer life expectancy, while others can be

TABLE 1 Cost and Weight Comparisons of Various Products

| Item | | Cost | Approx. weight |
|---|---|---|---|
| Pipe mat | 7.6 cm (3 in.)PVC | $331 | 275 kg (605 lb) |
| | 10.2 cm (4 in.)PVC | $346 | 295 kg (650 lb) |
| Terra mat | | $250 | 815 kg (1,800 lb) |
| Wood pallet | | $360 | 1 000 kg (2,200 lb) |
| Wood mat | 10.2 cm x 10.2 cm (4 in.x 4 in.) | $220 | 700 kg (1,540 lb) |
| | 15.3 cm x 15.3 cm (6 in.x 6 in.) | $340 | 950 kg (2,100 lb) |
| Grating | Expanded | $74 | 45 kg (100 lb) |
| | Safety | $580 | 80kg (180 lb) |

used only under certain conditions. All of the products need various design improvements.

The goal is to devise short-term, portable crossings that allow temporary access, result in the least amount of damage to the environment, and remain cost-effective. This paper identifies a variety of temporary crossings that can be used during timber harvest; as pioneer and access roads during construction; and for other temporary applications including floods and fires. An alternative to building permanent stream crossings, these products have been proven to protect the environment while providing access without rutting. Research should continue, and testing of the various choices should be expanded to determine the most advantageous stream crossings.

## REFERENCES

1. Shands, W. E. *U.S. Forest Service: Meeting Society's Changing Needs—Fact Book.* USDA Forest Service, Policy and Analysis Staff, Washington, D.C., 1994.
2. Mason, L. E. *Portable Wetland Area and Stream Crossings.* Report 9024 1203. USDA Forest Service, SDTDC, San Dimas, Calif., 1990.
3. Holtz, R. D. *Modern Corduroy and Fascines for Vehicle and Construction Mats.* Vol. 1, International Symposium, New Horizons in Construction Materials, Bethlehem, Pa., 1976.
4. Ongskul, S. *The Use of Fascines to Reinforce Fill Embankment on Very Soft Clay.* Thailand Department of Highways, Materials and Research Division, Bangkok, Thailand, 1973.

*Publication of this paper sponsored by Committee on Low-Volume Roads.*